ADDIS ABABA UNIVERSITY

COLLEGE OF TECHNOLOGY AND BUILT ENVIRONMENT

SCHOOL OF CHEMICAL AND BIOENGINEERING

ADVANCED OXIDATION PROCESS–DRIVEN DEGRADATION OF SELECTED EMERGING CONTAMINANTS IN WASTEWATER USING TITANIUM OXIDE- BASED PHOTOCATALYTIC NANOCOMPOSITE MATERIALS

PH.D. DISSERTATION

MOLALIGN EMIRIE HAILU

ADDIS ABABA, ETHIOPIA

February, 2026

ADVANCED OXIDATION PROCESS–DRIVEN DEGRADATION OF SELECTED EMERGING CONTAMINANTS IN WASTEWATER USING TITANIUM OXIDE-BASED PHOTOCATALYTIC NANOCOMPOSITE MATERIALS

by

MOLALIGN EMIRIE HAILU

A Ph.D. Dissertation

Submitted to the School of

Chemical and Bio-Engineering of the College of Technology and Built Environment, Addis Ababa University, Addis Ababa, Ethiopia

In Partial Fulfilment of the Requirements

for the Degree of

DOCTOR OF PHILOSOPHY

in

CHEMICAL ENGINEERING (ENVIRONMENTAL ENGINEERING)

February 2026

STATEMENT OF THE AUTHOR

By my signature below, I declare and affirm that this doctoral dissertation is entirely my own work. It has not been submitted, in whole or in part, for any degree or examination at any other university. I have complied with all ethical guidelines in accordance with the regulations of the university and in line with accepted standards of originality and academic integrity.

All sources of scholarly content incorporated into this thesis have been fully acknowledged through proper citation. I confirm that every reference used in the preparation of this thesis has been appropriately cited and listed. This thesis has been prepared with the utmost care to uphold academic honesty and to avoid any form of plagiarism.

Molalign Emirie Hailu		27/02/2026
Ph.D. Candidate	**Signature**	**Date**

APPROVAL SHEET

The dissertation entitled "**Advanced oxidation process–driven degradation of selected emerging contaminants in wastewater using titanium oxide- based photocatalytic nanocomposite materials**," prepared and submitted by Molalign Emirie Hailu in partial fulfilment of the requirements for the **Degree of Doctor of Philosophy in Chemical Engineering**, complies with the regulations of the University and meets the accepted standards of originality and academic quality.

Approved by the Examination Committee

Dr. Enyew Amare		
Internal Examiner	**Signature**	**Date**
Prof. Esayas Alemayehu		
External Examiner	**Signature**	**Date**
Prof. Dr.-Ing. Zebene Kiflie		
Major Advisor	**Signature**	**Date**
Dr. Shimelis Kebede		
Co-Advisor	**Signature**	**Date**
Dr. Anteneh Marelign		
Chairperson	**Signature**	**Date**
VEDAA, CTBE-AAU	**Signature**	**Date**

DEDICATION

I dedicate this dissertation to my family and many friends. I am profoundly grateful to my loving parents, Mr. Emirie Hailu and Mrs. Addis Alemayehu, whose unwavering support, encouragement, and love have guided me throughout every stage of my life.

This work is also dedicated to my wife, Mrs. Mulu Berihun; my daughter, Rediet Molalign; my older brother, Tsegaye Emirie; my younger sister, Edmialem Emirie; and to the many other family members and friends whose constant support, encouragement, and belief in me have strengthened my resolve. Your inspiration and presence by my side mean more to me than words can express.

ACKNOWLEDGEMENT

Above all, my deepest and highest gratitude is extended to the Almighty God, without whose grace and blessings none of this would have been possible. I am profoundly indebted to my supervisors, Prof. Dr Eng. Zebene Kiflie and Dr Shimelis Kebede of Addis Ababa University, Ethiopia, for their unwavering support and guidance throughout my doctoral journey. Their consistent and insightful suggestions, exceptional expertise, and extensive experience have been invaluable at every stage of my studies, significantly shaping my growth as a researcher and providing a solid foundation for my future academic career.

Furthermore, my profound and unreserved appreciation goes to Prof. Dr.-Ing. Zebene Kiflie, for her immense, insightful, and invaluable contributions throughout my studies. Prof. Dr.-Ing. Zebene, I will always cherish your daily guidance, thoughtful remarks, and constant words of encouragement; they will remain with me forever. The academic freedom you afforded me, coupled with your unwavering reassurance and hope, proved extraordinarily meaningful. Truly, words are insufficient to fully convey the magnitude of your contributions to this work and to my personal and academic growth. To Dr. Shimelis Kebede, I express my deepest gratitude for your immeasurable support and wise supervision. Your co-supervision left no void, and your dedicated efforts, invaluable guidance, and steadfast support have been instrumental to the successful completion of this study. I remain profoundly grateful for all that you have done.

For their exceptional support, I would also like to extend my heartfelt gratitude to Prof. Asnakech Laß-Seyoums of Faculty I, University of Applied Sciences (UAS) Berlin, Germany. My sincere appreciation also goes to my friend, Dr. Zinnabu Tassew of UAS Berlin, whose persistent assistance and unwavering commitment to providing essential chemical inputs made this study possible. Without their generous support, the initiation of this research would not have been feasible.

The successful completion of this study is also strongly attributable to the invaluable contributions of Prof. Dionissios Mantzavinos and his colleagues at the University of Patras, Patras, Greece; Prof. Won Sik Shin and Dr. Alam Venugopal Narendra Kumar of Kyungpook National University (KNU), Daegu, South Korea; and Prof. Zacharias Frontistis of the University of Western Macedonia, Greece. I take this opportunity to express my sincere and profound gratitude for their generous support and significant scientific input, which greatly enriched the quality and scope of this research.

I am especially and profoundly grateful to my employer, Addis Ababa University, for supporting my full-time doctoral studies. I would also wish to sincerely acknowledge and thank the academic and administrative colleagues of the School of Chemical and Bio-Engineering for their unwavering assistance and cooperation throughout my program.

Moreover, I extend my heartfelt gratitude to SIDA for providing the financial support that enabled me to undertake the three-month research stay, and to the Global Korean Scholarship (GKS) 2024 Program for awarding me the fully funded one-year scholarship, which was instrumental in the successful completion of this study.

I am especially indebted to Prof. Won Sik Shin in Daegu, South Korea, for his financial support beyond the GKS Scholarship program. Your assistance greatly facilitated my stay in South Korea and enabled me to successfully complete my studies. I am sincerely grateful for your generosity.

LIST OF ACRONYMS AND ABBREVIATIONS

Abbreviation	Description
AOP	Advanced oxidation process
ARGs	Antibiotic Resistance Genes
BBD	Box-Behnken Design
BET	Brunauer–Emmett–Teller analysis
BOD	Biological Oxygen Demand
CB	Conduction Band
CIP	Ciprofloxacin
COD	Chemical Oxygen Demand
DCF	Diclofenac
DMPO	5,5-Dimethyl-1-pyrroline N-oxide
DO	Dissolved Oxygen
DRS	Diffuse reflectance spectroscopy
ECs	Emerging Contaminants
EDCs	Endocrine Disrupting Chemicals
EIS	Electrochemical impedance spectroscopy
ESR	Electron Spin Resonance
FFA	Furfuryl Alcohol
FTRI	Fourier Transform Infrared Spectroscopy
GC	Gas Chromatography
HA	Humic Acid
HLB	Hydrophilic lipophilic balance
HPLC	High Performance Liquid Chromatograph
ICP-MS	Inductively coupled plasma mass spectrometry
IDL	Instrumental detection limit
IPA	Isopropanol
JCPDS	Join Committee on Powder Diffraction Standards
LC-MS	Liquid Chromatography Mass Spectroscopy
LOQ	Limit of quantification
MDL	Method detection limit

ME	Matrix effects
NOM	Natural organic matter
NORF	Norfloxacin
PL	Photoluminescence
PMS	Peroxymonosulfate
PFO	Pseudo-first-order
PPCPs	Pharmaceuticals and personal care products
PSO	Pseudo-second-order
PZC	Point of Zero Charge
rGO	Reduced graphene oxide
ROS	Reactive oxygen species
RSM	Response surface methodology
SEM	Scanning Electron Microscopy
SMX	Sulfamethoxazole
SPE	Solid phase extraction
TBA	t-butyl Alcohol
TC	Tetracycline
TDS	Total Dissolved Solids
TEM	Transmission Electron Microscopy
TEMP	Tetramethylpiperidine
TOCs	Total organic Carbons
TSS	Total Suspended Solids
TTIP	Titanium Tetra isopropanol
UASB	Up flow Anaerobic Sludge Blanket Reactor
UV	Ultraviolet
UV-Vis	Ultraviolet Visible
VB	Valence Band
WWTPs	Wastewater Treatment Plants
XPS	X-ray Photoelectron Spectroscopy
XRD	X-ray Diffraction

TABLE OF CONTENTS

APPROVAL SHEET ..... **iii**
DEDICATION ..... **iv**
ACKNOWLEDGEMENT ..... **v**
LIST OF ACRONYMS AND ABBREVIATIONS ..... **vii**
TABLE OF CONTENTS ..... **ix**
LIST OF TABLES ..... **xiii**
LIST OF FIGURES ..... **xiv**
LIST OF PUBLICATIONS ..... **xviii**
ABSTRACT ..... **xix**
CHAPTER ONE **1**
INTRODUCTION **1**
1.1 Background 1
1.2 Statement of the Problem 5
1.3 Scope of the Study 7
1.4 Limitation of the Study 7
1.5 Research Hypothesis 8
1.6 Objectives of the Study 8
1.6.1 General objective of the study 8
1.6.2 Specific objectives of the study 8
1.7 Expected Significance and Implications of the Study 9
1.8 Organisation of Dissertation 9
CHAPTER TWO **12**
LITERATURE REVIEW **12**
2.1 Wastewater and Contaminants 12
2.2 Emerging Contaminants 12
2.2.1 Impact of emerging contaminants 13
2.3 Wasteawter treatment 14
2.3.1 Conventional wastewater treatment technologies 14
2.3.2 Advanced oxidation processes for wastewater treatment 15
2.3.3 Advanced oxidation processes limitations 17
2.4 Photocatalytic oxidation processes 19
2.4.1 Principle 19

2.4.2 Parameters affecting the mechanism of photocatalysis 21
2.5 Latest development in TiO_{2-x} based photocatalysts for antibiotic degradation 23
2.6 Knowledge gap and research opportunities 26
CHAPTER THREE 29
Physicochemical Characterisation and Emerging Contaminant Analysis in Wastewater: A Case Study from Kality Treatment Plant, Ethiopia 29
3.1 Introduction 29
3.2 Materials and Methods 30
3.2.1 Study area and description of Kality WWTP 30
3.2.2 Chemicals and Standards 31
3.2.3 Sample collection and preparation 31
3.2.4 Physicochemical analysis 32
3.2.5 Heavy Metal Analysis 32
3.2.6 Solid Phase Extraction of Emerging Contaminants 33
3.2.7 Statistical Analysis 35
3.3 Results and discussion 35
3.3.1 Investigation of physicochemical variables 35
3.3.2 Analysis of Emerging Contaminants 40
3.4 Conclusions 43
CHAPTER FOUR 44
Response Surface Methodology-Based Optimisation of Triple KBN-Doped TiO_2 Synthesis Parameters for Ciprofloxacin Degradation 44
4.1 Introduction 45
4.2 Experimental 47
4.2.1 Synthesised catalyst 47
4.2.2 Characterisation of synthesised catalyst 48
4.2.3 An adsorption–photocatalytic degradation experiment 49
4.3 Results and Discussion 52
4.3.1 Best synthesised conditions for modified KBN@TiO_2 catalyst 52
4.3.2 Crystal phase composition 53
4.3.3 Specific surface area 54
4.3.4 Adsorption and photocatalytic degradation tests 55
4.3.5 Model verification and optimisation 59

4.3.6 Characterisation of the synthesised catalyst under optimum conditions. 60
4.3.7 Effects of operational parameters on CIP degradation 64
4.3.8 Reusability and degradation of other antibiotics 66
4.3.9 CIP degradation mechanism 68
4.4 Conclusions 69
CHAPTER FIVE 70
Highly efficient KBN@TiO_2@rGO composite for photodegradation of antibiotics under visible light irradiation 70
5.1 Introduction 71
5.2 Materials and Methods 73
5.2.1 Materials 73
5.2.2 Synthesis of KBN@TiO_2 74
5.2.3 Synthesis of GO and rGO 74
5.2.4 Synthesis of KBN@TiO_2@rGO composite 75
5.2.5 Photocatalytic degradation experiments 76
5.3 Results and Discussions 77
5.3.1 Characterisation of synthesised KBN@TiO_2@rGO 77
5.3.2 Effect of rGO content and photocatalytic activity of the composite 84
5.3.3 Adsorption kinetics and isotherms 93
5.3.4 CIP degradation mechanisms and pathways 95
5.3.5 Reusability and stability of the KBN@TiO_2@rGO system 97
5.3.6 Other antibiotic degradation and TOC removal 97
5.3.7 Photocatalytic process in KBN@TiO_2@rGO 100
5.4 Conclusions 100
CHAPTER SIX 102
Peroxymonosulfate Activation by KBN-Doped TiO_2@rGO: Multi-Site Radical and Non-Radical Degradation of Antibiotics 102
6.1 Introduction 103
6.2 Materials and methods 103
6.2.1 Materials 103
6.2.2 Design and preparation of the KBN@TiO_2@rGO composite nanoparticle 103
6.2.3. Characterisation of the KBN@TiO_2@rGO nanocomposite 103
6.2.4. Photocatalytic degradation experiments 103

6.2.5 Experimental design via response surface methodology (RSM) 104
6.3 Results and discussion 106
6.3.1 Characterisation of prepared photocatalyst 106
6.3.3 Evaluation of PMS activation performance and photocatalytic oxidation 112
6.3.4 Feasibility of practical application 117
6.3.5 Mechanisms of photocatalytic degradation in KBN@TiO_2@rGO/PMS 119
6.3.6 Statistical analysis using RSM 125
6.4 Conclusions 131
CHAPTER SEVEN 132
CONCLUSIONS AND RECOMMENDATIONS 132
7.1 Conclusions 132
7.2 Recommendations and Future Outlooks 133
References 135
LIST OF APPENDICES 168
Appendix A. Supplementary Information for Chapter Three 168
Appendix B. Supplementary Information for Chapter Four 174
Appendix C. Supplementary Information for Chapter Five 183
Appendix D. Supplementary Information for Chapter Sex 200

LIST OF TABLES

Table 2.1: Overview of antibiotic photocatalytic degradation by TiO_2-x based photocatalysts. 25

Table 2.2: Research Gaps and Proposed Questions/Hypotheses in Advanced Oxidation Processes Using Modified TiO_2. 27

Table 3.1: Instruments/methods used for the determination of Physicochemical Parameters. 33

Table 3.2: Quality parameters obtained for six selected pharmaceutical compounds. 35

Table 3.3: Physicochemical characterisation of wastewater sample from Kality MWWTP...37

Table 3.4: Heavy metal analysis and percentage removal from the Kality Municipal WWTP. 39

Table 3.5: Average values of selected pharmaceutical pollutants reported by previous studies. 42

Table 3.6: Concentrations and ranges in ($\mu g\ L^{-1}$) of treated effluent from large-scale WWTPs in different areas. 42

Table 4.1: Experimental variables and levels were determined for BBD based on an initial investigation. 50

Table 4.2: Actual and predicted BBD values for specific area (S_{BET}) and CIP degradation efficiency (R%) 51

Table 4.3: Doped and undoped TiO_2 model validation results were established under optimal conditions 59

Table 5.1: Surface area and pore size distribution of prepared samples. 79

Table 5.2: Effect of adsorption on CIP removal by the synthesised catalysts. 87

Table 5.3: Effect of photocatalysis on CIP degradation by the synthesised catalysts. 87

Table 5.4: The fitting constant of adsorption kinetics for CIP removal on KBN@TiO_2@rGO. 94

Table 5.5: The isothermal adsorption parameters for CIP on KBN@TiO_2@rGO. 95

Table 6.1: Experimental key study factors and levels. 104

Table 6.2: Experimental design matrix generated using BBD-RSM. 105

Table 6.3: Investigation of surface area and pore size distribution in synthesised samples. 109

Table 6.4: ANOVA of the response surface model for CIP photodegradation. 129

Table 6.5: ANOVA of the response surface model for TOC removal. 127

LIST OF FIGURES

Figure 2.1 Overview of research trends in antibiotic removal: adsorption, wastewater treatment, and photocatalysis 13
Figure 2.2 Schematic overview of the most used treatments based on AOPs. 19
Figure 2.3 The fundamental process through which photocatalysis degrades pollutants 20
Figure 2.4 Overview of the challenges and research gaps in the photocatalytic degradation of antibiotics 27
Figure 3.1 Schematic diagram of the Kality municipal WWTP. 31
Figure 3.2 Physicochemical characterisation of Kality Municipal WWTP. 38
Figure 3.3 Selected heavy metals analysis from Kality MWWTP. 40
Figure 3.4 LC-MS/MS analysis (a, c) Standard solution of each 10 mg L^{-1} amoxicillin, ciprofloxacin, and tetracycline, (b) influent; (d) effluent from Kality municipal wastewater. 41
Figure 3.5 Regional comparison of target pollutants in WWTP effluents 43
Figure 4.1 XRD patterns of KBN-doped TiO_2 samples calcinated at 500 ℃ for 3 h under a fixed concentration of 5 mol% N and 2 mol% K, with varying B/Ti molar ratio of 2mol%B, 5mol%B, and 8mol%B. 54
Figure 4.2 Three-dimensional interaction plots showing the effects of (a) calcination temperature and B/Ti molar ratio on surface area, (b) calcination temperature and calcination time on surface area, (c) calcination temperature and B/Ti molar ratio on CIP degradation efficiency, and (d) calcination temperature and calcination time on CIP degradation efficiency for the KBN@TiO_2 system. 55
Figure 4.3 Catalyst performances were evaluated through adsorption and photocatalysis at various dopant concentrations and calcination temperatures. Adsorption performance (a, b, and c) and photocatalytic oxidation performance (d, e, and f) were compared under identical conditions. 56
Figure 4.4 Effect of calcination time on (a) adsorption and (b) photocatalytic activity, and Effect of calcination temperature on (c) adsorption and (d) photocatalytic activity of 5%B-doped KN@TiO_2 nanocomposite. 58
Figure 4.5 Characterisation of the optimised synthesised samples: (a) X-ray diffraction (XRD) patterns of BN-TiO_2 and KBN-TiO_2, (b) FT-IR spectra of TiO_2, BN@TiO_2 and KBN@TiO_2, (c) N_2 adsorption-desorption isotherms (BET), (d) SEM image of Only TiO_2, (e) SEM image 61

Figure 4.6 XPS analysis of KBN@TiO_2 nanoparticles (a) Overall survey, (b) Ti 2p, (c) O 1s, (d) C 1s + K 2p, (e) B 1s, and (f) N 1s.....63
Figure 4.7 (a) UV–Vis DRS and (b) Tauc-plot of undoped TiO_2 and 5%B- 2%K-5%N-TiO_2……..66
Figure 4.8 Effects of (a) catalyst dosage, (b) initial [CIP], (c) initial pH, and (d) water matrices via photocatalytic degradation of CIP on the KBN@TiO_2 system.....65
Figure 4.9 (a) reusability of KBN@TiO_2, (b) reaction rate constants, (c) degradation of different antibiotics, and (d) TOC removal by the KBN@TiO2 system. 67
Figure 4.10 Schematic diagram of the CIP removal mechanism (adsorption–photocatalysis) by triple-doped KBN-TiO_2. 68
Figure 5.1 Schematic illustration of the synthesis process for the KBN@TiO_2@rGO nanocomposite. 75
Figure 5.2 Characterization of the synthesized materials: (a) XRD patterns; (b) FTIR spectra; (c) N_2 adsorption-desorption isotherms; FE-SEM images of (d) KBN@TiO_2 and (e) KBN@TiO_2@rGO; (f) TEM image of KBN@TiO_2@rGO composite; EDX spectra of (g) KBN@TiO_2 and (h) KBN@TiO_2@rGO; and (i) elemental mapping of KBN@TiO_2@rGO..79
Figure 5.3 XPS analysis of KBN@TiO_2@rGO NCs: (a) Overall survey, (b) Ti 2p, (c) O 1s, (d) C 1s + K 2p, (e) B 1s, and (f) N 1s.....82
Figure 5.4 UV-Vis diffuse reflectance spectra of (a) rGO, KBN@TiO_2, and KBN@TiO_2@rGO, (b) Tauc plots of rGO, KBN@TiO_2, and KBN@TiO2@rGO, and (c) PL spectra of KBN@TiO2 and KBN@TiO_2@rGO. (d) EIS Nyquist plot and (e) Mott-Schottky plot for different materials. 84
Figure 5.5 Evaluation of catalyst performance (a) adsorption, (b) pseudo-first-order rate constants for adsorption, (c) photocatalytic degradation, and (d) pseudo-first-order rate constants for photocatalytic degradation system. 85
Figure 5.6 Effects of (a) catalyst dose, (b) initial CIP concentration, (c) initial pH, (d) point of zero charge (pHpcz) for KBN@TiO_2@rGO, (e) cation effects, and (f) anion effects on photocatalytic degradation of CIP using the KBN@TiO_2@rGO system. 88
Figure 5.7 Effects of (a) humic acid, (b) rate constants at different concentrations of HA, (c) effects of water matrix, (inset) corresponding rate constant values, (d) quenching experiments, ESR spectra using (e) TEMP and (f) DMPO spin-trapping agents. 95
Figure 5.8 Possible degradation pathways of CIP in photocatalytic oxidation over the KBN@TiO_2@rGO system.....96

Figure 5.9 (a) Reusability and stability, (b) rate constants of five cycles, (c) the effect of multi-antibiotics, and (d) multi-antibiotics and TOC removal efficiency, degradation on KBN@TiO_2@rGO system. and (e) schematic illustration of the photocatalytic degradation of CIP process. 99
Figure 6.1 XRD patterns of the synthesised (a) KBN@TiO_2 and KBN@TiO_2@rGO, (b) FTIR spectra of KBN@TiO_2 and KBN@TiO2@rGO, (c) N_2 adsorption-desorption isotherms of rGO, fresh KBN@TiO_2@rGO and used KBN@TiO_2@rGO, (c) pore size distribution curves for rGO, fresh KBN@TiO_2@rGO, and used KBN@TiO_2@rGO, (d)FE-SEM images of the synthesised KBN@TiO_2@rGO composite, (e) EDX spectra of KBN@TiO_2@rGO, and (f) Tauc plots of rGO, KBN@TiO_2@rGO, and KBN@TiO_2@rGO. 108
Figure 6.2 XPS analysis of KBN@TiO_2@rGO Nanocomposite: (a) Overall survey, (b) Ti 2p, (c) O 1s, (d) B 1s, (e) N 1s, and (f) C 1s + K 2p. 112
Figure 6.3 Effects of (a) catalyst type, (b) PMS dose, (c) catalyst dose, (inset) corresponding rate constant values, (d) initial CIP concentration, (e) initial pH, (inset) corresponding final pH values and (f) anion effects on photocatalytic degradation of CIP using the KBN@TiO_2@rGO/PMS system. 114
Figure 6.4 Effects of (a) humic acid, (b) rate constants at different concentrations of HA, (c) effects of water matrix, (inset) corresponding rate constant values, (d) reusability and stability on the degradation of ciprofloxacin, (e) different pollutants, (inset) corresponding rate constant values, and (f) TOC removal from different pollutants on the KBN@TiO_2@rGO/PMS system. 118
Figure 6.5 Effects of (a) CIP degradation with the addition of various scavengers, (b) First-rate constants of in the CIP@ KBN@TiO_2@rGO/PMS system, (c) DMPO as a spin-trapping agent, (d) ESR spectra using TEMP, (e) LSV analysis, and (f) i-t curve experiment for Light/ KBN@TiO_2@rGO/PMS system. 122
Figure 6.6 Schematic illustration of the proposed reaction mechanism for ciprofloxacin (CIP) photodegradation over the KBN@TiO_2@rGO/PMS catalyst under solar light irradiation. .. 124
Figure 6.7 Proposed photodegradation pathway of CIP in aqueous solution using the KBN@TiO_2@rGO/PMS system. 125
Figure 6.8 3D surface plot of CIP photodegradation efficiency as a function of (a) Solution pH and reaction time, (b) Solution pH and catalyst dosage, (c) reaction time and catalyst dosage, (d) Initial CIP concentration and pH, and (e) catalyst dosage and Initial concentration of CIP in the KBN@TiO_2@rGO/PMS system. 129

Figure 6.9 3D surface plot of TOC removal as a function of (a) solution pH and reaction time, (b) solution pH and Initial concentration of CIP, (c) reaction time and catalyst dosage, and (d) reaction time and Initial concentration of CIP in the KBN@TiO_2@rGO/ PMS system. 130

LIST OF PUBLICATIONS

Peer–Reviewed Publications

1. **M. E. Hailu** et al., Physicochemical Characterisation and Emerging contaminants analysis in wastewater: A Case study from Kality Treatment plant, Ethiopia, Journal of Ethiopian Engineers and Architects, Accepted.
2. **M. E. Hailu** et al., Response surface methodology-based optimisation of Triple KBN-doped TiO_2 synthesis parameters for ciprofloxacin degradation, submitted.
3. **M. E. Hailu** et al., Highly efficient KBN@TiO_2@rGO composite for photodegradation of antibiotics under visible light irradiation, Sep Purif Technol, 380(2025)135352**.** https://doi.org/10.1016/J.SEPPUR.2025.135352.
4. **M. E. Hailu** et al., Peroxymonosulfate Activation by KBN-Doped TiO_2@rGO: Multi-Site Radical and Non-Radical Degradation of Antibiotics, Journal of Water Process Engineering, 82 (2026)109430. https://doi.org/10.1016/j.jwpe.2025.109430

ABSTRACT

Wastewater treatment plants are increasingly recognised as secondary sources of emerging contaminants due to the limitations of conventional treatment technologies. This study assessed the physicochemical characteristics of influent and effluent from the Kality Municipal Wastewater Treatment Plant (KMWWTP) in Ethiopia and evaluated its performance in removing nutrients, heavy metals, and selected pharmaceuticals. Influent and effluent analyses were conducted following APHA standard methods, while heavy metals were quantified using ICP-MS. The plant demonstrated partial compliance with the WHO and USEPA standards, with low removal efficiencies for total nitrogen, total phosphorus, and several heavy metals. Notably, concentrations of Ni, Cd, Pb, and As increased after treatment. Pharmaceuticals detected in the effluent using LC-MS/MS - including amoxicillin (2.54 μg L^{-1}), ciprofloxacin (2.43 μg L^{-1}), ibuprofen (8.21 μg L^{-1}), carbamazepine (0.82 μg L^{-1}), and caffeine (1.24 μg L^{-1})-confirmed the persistence of emerging contaminants in treated wastewater.

To address these challenges, a visible light–active triple KBN–doped TiO_2 nano photocatalyst was synthesised via the sol–gel method and optimised operation parameters using the Box–Behnken design (BBD). Boron (B) – to titanium (Ti) molar ratio, calcination temperature, and calcination time were selected as synthesis variables, while potassium (K) and nitrogen (N) doping ratios were kept constant at 2%K and 5%N, respectively. Characterisation using XRD, FTIR, BET, SEM-EDX, XPS, and UV-Vis revealed that calcination temperature and boron doping concentration significantly influenced the crystallinity, surface area, electron transfer properties, and photocatalytic activities of the materials. The optimised photocatalyst achieved a surface area of 66.48 m^2 g^{-1} and 84.3% ciprofloxacin (CIP) degradation, with the quadratic regression models showing high predictive accuracy ($R^2 > 0.98$).

Building on this optimisation, a novel KNB@TiO_2@rGO nano photocatalytic composite was synthesised through sol–gel processing, followed by hydrothermal deposition of TiO_2 nanoparticles on reduced graphene oxide. Comprehensive characterisation, including XRD, FTIR, XPS, SEM-EDS, UV–Vis, and photoluminescence (PL), confirmed successful composite formation with enhanced charge separation efficiency. The composite achieved 99.21% CIP degradation and 75.09% total organic carbon (TOC) removal under visible light (950 W m^{-2}). The influence of co-existing ions showed mild inhibition by Mg^{2+} and Ca^{2+}, enhancement by Cl^-, NO_3^-, and HCO_3^- and suppression by SO_4^{2-}, PO_4^{3-} and humic acid (HA). Electron spin resonance and radical scavenging tests confirmed the formation of •OH, $O_2^{\bullet-}$, and

$^1O_2$ reactive oxygen species, and using UPLC – MS/MS identified the intermediate byproducts and proposed the plausible degradation reaction pathways

To further enhance performance, peroxymonosulfate (PMS) activation was integrated with the photocatalytic process, forming the KBN@TiO_2@rGO/PMS system. This ternary system achieved complete (100%) CIP degradation and 74.23% TOC removal within 90 minutes, outperforming TiO_2/PMS and pristine TiO_2. The improved activity was attributed to synergistic effects from ternary (K, B, N) doping, rGO-mediated electron transfer, and PMS activation, which collectively promoted the generation of both radical (•OH, $O_2^{\bullet-}$, $SO_4^{\bullet-}$) and non-radical ($^1O_2$) species. Response Surface Methodology optimised operational conditions (pH 8.17, 101.2 min reaction time, 0.13 g L^{-1} catalyst, and 9.99 mg L^{-1} CIP), predicting 100% CIP degradation and 75.91% TOC removal with 100% desirability.

Overall, this work highlights the inadequacy of conventional wastewater treatment plants for removing persistent pollutants in Kality municipal wastewater treatment plant effluents and demonstrates the strong potential of advanced photocatalytic systems, particularly the KBN@TiO_2@rGO/PMS composite, for efficient and sustainable degradation of emerging contaminants across diverse water matrices.

Keywords: Advanced oxidation; Antibiotic degradation; Catalyst Characterisation; Composite photocatalysts; Doping Technology; Emerging pollutants; Municipal Wastewater; optimisation

CHAPTER ONE
INTRODUCTION

1.1 Background

Water is fundamental to life and sustainable development, yet its availability is increasingly constrained. Rapid industrialisation, urbanisation, population growth, and socioeconomic expansion have contributed to deteriorating water quality and escalating contamination [1, 2]. Concurrently, climate change has intensified the frequency and severity of droughts, further diminished freshwater resources and posed serious environmental and economic challenges [3].

In recent decades, contaminants of emerging concern (CECs) - including pharmaceuticals and personal care products (PPCPs), artificial sweeteners, endocrine-disrupting chemicals (EDCs), flame retardants, fuel additives, and various industrial organic compounds have attracted significant global attention due to their widespread occurrence and potential adverse effects on ecosystems and public health [4]. These substances enter aquatic systems primarily through municipal, hospital, and industrial wastewater discharges, sewage leakage, and agricultural or urban runoff. Wastewater treatment plants (WWTPs) are major pathways through which CECs are released into the environment, as many of these compounds are detected in influent and effluent at concentrations ranging from ng L^{-1} to μg L^{-1}, and they may transform into by-products that are even more persistent or toxic [5, 6, 7, 8].

Conventional municipal wastewater treatment plants are not designed to effectively remove CECs, resulting in their continuous discharge into receiving water bodies. This poses a range of ecological and human health risks, including antibiotic resistance, endocrine disruption, feminisation of aquatic organisms, neurotoxicity, and potential carcinogenicity [9]. In Ethiopia, wastewater generation has increased due to rapid population growth, unplanned urbanisation, inadequate sanitation infrastructure, and poorly regulated industrial activities. Moreover, current environmental legislation does not specify permissible limits for most ECs [10]. In Ethiopia, rapid population growth, inadequate sanitation infrastructure, poorly regulated industrial activities, and the absence of regulatory limits for most emerging contaminants have exacerbated water quality challenges [11].

Rivers and streams passing through major urban centres often become heavily polluted. The Kality Municipal Wastewater Treatment Plant (KMWWTP), the country's largest municipal

treatment facility, treats more than 34 million m³ of septic wastewater annually and discharges effluent into the Little Akaki River, which supports downstream irrigation. Despite growing international concern, the occurrence, fate, and removal efficiency of CECs in Ethiopian wastewater remain largely unexplored. Thus, generating baseline data on their presence and behaviour in municipal wastewater systems is critical for ensuring safe and sustainable wastewater reuse.

Advanced oxidation processes (AOPs), particularly heterogeneous photocatalysis, offer promising approaches for degrading recalcitrant organic pollutants due to their strong oxidising capability, low sludge production, and compatibility with solar energy [10, 11]. Titanium dioxide (TiO_2) is one of the most studied photocatalysts owing to its low cost, non-toxicity, photostability, and high catalytic potential [13,14]. However, practical applications are hindered by its wide band gap (3.2 eV for anatase), which restricts activation to UV light, and the rapid recombination of photogenerated electron–hole pairs [15,16]. To overcome these limitations, extensive research has explored metal and non-metal doping, heterojunction formation, and composite fabrication with graphitic materials [17, 18].

Doping with elements such as K, B, and N can significantly narrow the band gap, enhance charge separation, and improve visible-light response [19]. Metal-doped photocatalysts, such as those modified with silver (Ag) [20], iron (Fe) [21], potassium (K) [22], and boron (B) [23], exhibit superior photocatalytic performance due to the localised surface plasmon resonance (LSPR) and the electron-accepting capabilities of the metal dopants. These dopants capture electrons due to the altered Fermi level in the metallic oxide, facilitating the separation of photogenerated electron–hole pairs [24]. Similarly, non-metal doping involves the introduction of heteroatoms, such as nitrogen (N) [25], carbon (C) [26], and phosphorus (P) [27], into the metal oxide lattice by partially replacing oxygen atoms. The incorporation of non-metal dopants enhances charge carrier separation, creates non-metallic energy levels, and facilitates electron capture, thereby lowering the bandgap. Moreover, co-doping with multiple heteroatoms (C/N) [28] and (B/N) [29] can suppress the recombination of charge carriers by leveraging the electron-accepting properties of non-metals, further reducing the bandgap of bare TiO_2 by creating new energy levels. Additionally, ternary doping (KHB) [30] can significantly enhance photocatalytic activity, particularly for the degradation of antibiotics. Additionally, integrating TiO_2 with reduced graphene oxide (rGO) enhances photocatalytic activity due to rGO's high conductivity, superior surface area, and strong adsorption properties

[18,31]. The adsorption of organic contaminants onto rGO is facilitated by the presence of carboxylic acid (–COOH) at the edges and hydroxyl (–OH) and epoxide (C–O–C) groups on the basal plane [32].

Recent advances have highlighted the potential of the co-doped TiO_2-graphene system for degrading emerging contaminants [30]. However, the combined use of triple metal–non-metal doping (KBN) with rGO, particularly using sol–gel-assisted hydrothermal synthesis, remains underexplored. Furthermore, coupling photocatalytic nanomaterials with oxidants such as peroxymonosulfate (PMS) can generate multiple reactive oxygen species (ROS), promote synergistic degradation pathways, suppress charge recombination, and significantly improve antibiotic removal performance. Due to the generation of highly reactive species, AOPs are considered an effective strategy for removing emerging contaminants from wastewater as well. Peroxymonosulfate (PMS)/Peroxydisulfate (PS)- based AOPs exhibited superior antibiotic removal performance due to the generation of reactive oxygen species (ROS) upon activation by a heterogeneous catalyst [30]. Activation of the oxidants (PMS or PS) by photocatalyst materials proceeds through both non-radical and radical pathways mediated by electron transfer, which is fundamentally distinct from the homogeneous photocatalysis activation mechanism. The ROS generated could break the bonds in pollutants and proceed to the mineralisation process. PMS is a powerful oxidant widely applied in AOPs for surface water treatment and groundwater remediation [33]. PMS activation produces sulfate radicals ($SO_4^{\bullet-}$), which effectively oxidise both organic and inorganic pollutants present in water. PMS is activated through multiple approaches, such as thermal treatment, photocatalysis, ultraviolet (UV) irradiation, and the involvement of transition metal ions, among others [34, 35]. During PMS activation, there is a broken O-O bond, producing ($SO_4^{\bullet-}$) and (•OH) radicals, which abstract electrons from organic contaminants, leading to their oxidation [36, 37]. Additionally, PMS can also be activated using carbon catalysts, including graphite, activated carbon, biochar, and photocatalytic nanomaterials [38, 39]. Consequently, organic pollutants are degraded because of the generation of •OH and/or $SO_4^{\bullet-}$ radicals, while non-radical pathways are likewise substantially engaged in the PMS-photocatalytic nanomaterial system [40]. The non-radical pathways mainly involve: (1) the activation of PMS occurs through transfer of electrons from organic pollutants (donors) to PMS (acceptor), facilitated by graphitic structures, defects, and heteroatoms in photocatalytic materials, and (2) the generation of singlet oxygen ($^1O_2$) from

$SO_4^{\bullet-}$ and at reactive sites such as C=O groups [41]. Compared with •OH based AOPs, $SO_4^{\bullet-}$ based AOPs have received greater attention because $SO_4^{\bullet-}$ is reactive over a broader pH range, exhibit extended half-life, and possess a higher redox potential. Many studies have confirmed that TiO_2@rGO, metal-doped TiO_2, non-metal-doped TiO_2, and co-doped TiO_2@rGO composites hold great potential for the efficient remediation of emerging contaminants, due to the outstanding properties of graphene and doping elements [42, 43, 44].

Recently, we developed a metal-non-metal-doped TiO_2@rGO photocatalyst, which efficiently decomposes antibiotic organic pollutants under visible light irradiation [44], but unfortunately, the catalyst dose, reaction time, and accumulation of intermediates during the antibiotic photodegradation process have been observed to lower the overall performance of the KBN@TiO_2@rGO system. To overcome this issue, the addition of PMS not only generates multiple free radicals and non-radical species that synergistically enhance the photocatalytic degradation of emerging pollutants but also improves charge separation efficiency. Despite their promise, the synergistic interactions between KBN@TiO_2@rGO photocatalysts and PMS, as well as the dominant factors influencing system efficiency and deactivation, have not been systematically investigated. Therefore, it is meaningful to study in detail the synergistic impact of the KBN@TiO_2@rGO/PMS system and the dominant factors influencing photocatalyst deactivation, as well as to optimise the operating parameters. This is, to the best of our knowledge, the first study addressing the use of a triple metal–nonmetal (KBN)-doped TiO_2 composite integrated with rGO (KBN@TiO_2@rGO) as a photocatalyst for CIP photodegradation via PMS activation. The photocatalytic conditions were optimised to achieve maximum performance in natural wastewater, highlighting its potential to outperform conventional composites.

This study aimed to evaluate wastewater quality and treatment performance at the Kality MWWTP while establishing baseline data on emerging contaminants. It also focused on synthesising and characterising modified KBN-doped TiO_2 and KBN@TiO_2@rGO photocatalysts using sol–gel and hydrothermal methods. In addition, the research investigated the adsorption behaviour and visible-light-driven photocatalytic degradation of CIP, alongside optimising key operating parameters for both photocatalyst synthesis and CIP removal through response surface methodology (RSM) and the Box–Behnken design (BBD). Furthermore, the study explored the role of reactive oxygen species in the KBN@TiO_2@rGO/PMS system to

clarify the underlying degradation mechanisms, and assessed the reusability and performance of the photocatalyst in different water matrices to determine its practical applicability.

Overall, this work provides the first comprehensive investigation of a triple metal-non-metal-doped TiO_2 composite with KBN@TiO_2@rGO for PMS activated photocatalysis for degradation of emerging contaminants in municipal wastewater and optimisation of the key operating parameters. The findings offer valuable insights into developing sustainable and highly efficient treatment strategies for emerging organic contaminants in real-world conditions.

1.2 Statement of the Problem

Due to increasing concern about the potential risks emerging contaminants (ECs) pose to aquatic ecosystems and human health; there is a growing emphasis on developing cost-effective treatment technologies. In many developing countries, ECs remain unregulated, and their available treatment options are not well documented [45]. The widespread occurrence of ECs in surface water, groundwater, and municipal wastewater has prompted the tightening of regulatory standards for emerging contaminants [46]. Despite the guidelines established by local authorities, unregulated discharges continue to occur, largely due to weak legislation and insufficient ecotoxicity data on ECs [10].

The continuous release of emerging contaminants (ECs) into aquatic environments, primarily due to their inadequate removal by conventional wastewater treatment technologies, has intensified global research efforts to identify viable mitigation strategies. Most ECs are resistant to traditional treatment processes, allowing them to persist in effluents and subsequently enter natural water bodies. Once released into the environment, these contaminants can induce significant toxicological effects. For example, studies have shown that fish exposed to environmentally relevant concentrations of the lipid-lowering drug gemfibrozil and the non-steroidal anti-inflammatory drug diclofenac exhibit glutathione S-transferase (GST) inhibition, increased lipid peroxidation (LPO), and DNA damage. Such impacts highlight the urgent need for more advanced and effective treatment solutions to address this growing global concern [47]. Continuous discharge and chronic exposure to these chemicals may pose a risk to human health, even at trace levels [47]. Another concern is that the presence of ECs, such as antibiotics and antimicrobial agents, can result in the development of antibiotic resistance genes (ARGs) and bacteria, which reduce the therapeutic potential of

antibiotics against human and animal pathogens. For these reasons, the collection of information on the environmental occurrence and fate of ECs in the environment allows an accurate evaluation of the environmental risk associated with these chemicals, which target aquatic organisms as well as humans [48]. In Addis Ababa, a major potential source of emerging contaminants is the effluent discharged from the Kality Wastewater Treatment Plant (WWTP) into nearby aquatic environments, particularly the Little Akaki River, which ultimately flows into the Aba Samuel Reservoir. Communities surrounding these areas rely on the river and reservoir for irrigation, raising concerns about potential exposure to untreated or partially treated contaminants. However, the presence, concentration, and removal efficiency of emerging pollutants in this system have not been thoroughly identified or quantified, limiting the ability to implement corrective measures. To date, the issue has received insufficient attention in Ethiopia, and no comprehensive studies have examined the occurrence of emerging contaminants in the influent and effluent of the Kality WWTP or assessed the plant's capacity to remove them.

Emerging contaminants, including pharmaceuticals and personal care products, are difficult to remove using conventional water treatment methods because they occur at very low concentrations and are often chemically stable. Physical–chemical treatments, such as adsorption and filtration, typically move these pollutants to another medium, like sludge or filter material, rather than eliminate them, while coagulation and flocculation are generally ineffective for small dissolved organic compounds, and chlorination may not fully degrade them. Moreover, many of these compounds are resistant to biological treatment, so processes like activated sludge cannot efficiently break them down. Disinfection can also produce toxic by-products that may be as harmful as, or even more harmful than, the original contaminants [49]. However, advanced oxidation processes (AOPs) have been shown to effectively degrade trace organic contaminants in wastewater. Unlike conventional treatment methods, AOPs generate highly reactive species, such as hydroxyl radicals (•OH) and sulfate radicals ($SO_4^{\bullet-}$), which can non-selectively oxidise and break down a wide range of persistent organic pollutants. This capability allows AOPs to mineralise emerging contaminants that are otherwise resistant to biological or physicochemical treatment. Moreover, AOPs can be applied under various operational conditions, making them a versatile and promising solution for improving wastewater quality and reducing the environmental and health risks associated with emerging pollutants.

For these reasons, there is a pressing need to develop effective and practical technologies that can be implemented to improve wastewater effluent quality, such as composite photocatalyst-based advanced oxidation processes (AOPs). Titanium-based photocatalysts are commonly used in advanced oxidation processes (AOPs); however, their application is limited by a large bandgap and rapid electron–hole recombination, which reduces photocatalytic efficiency. To address these limitations, this study employs metal–nonmetal-doped TiO_2 integrated with reduced graphene oxide (rGO) and activated with peroxymonosulfate (PMS) to enhance photodegradation efficiency. This composite system is expected to improve charge separation, extend light absorption, and generate reactive species more effectively, thereby increasing the removal of emerging contaminants from wastewater.

1.3 Scope of the Study

The scope of this study is to conduct experimental research on a photocatalytic advanced oxidation process for the degradation of emerging contaminants in municipal wastewater. Within this framework, the main investigative components include: physicochemical characterisation of wastewater from the Kality Municipal Wastewater Treatment Plant and an assessment of its treatment performance, synthesis and characterisation of a composite photocatalyst, optimisation of the operating parameters for the synthesised KBN-doped TiO_2 photocatalyst, evaluation of its photocatalytic performance in the degradation of selected antibiotics, Investigation of the synergistic effects of multiple radical species involved in the degradation process, and final optimization of the operational parameters governing the photocatalytic degradation of antibiotics.

1.4 Limitation of the Study

One limitation of this study is that its emphasis on selected antibiotics as emerging contaminants reduces the applicability of the findings to other pharmaceutical or industrial pollutants. Since the research utilised wastewater solely from the Kality Municipal Wastewater Treatment Plant, the results may not be generalisable to other treatment facilities or regions with different wastewater characteristics. The photocatalytic experiments were also conducted under controlled laboratory conditions, which may not accurately reflect real environmental settings. Furthermore, the study did not provide a comprehensive assessment of the formation or potential toxicity of intermediate degradation by-products. Lastly, economic feasibility, energy requirements, and scale-up considerations were not examined, although these factors are essential for practical implementation.

1.5 Research Hypothesis

The composite photocatalytic process activated with peroxymonosulfate (PMS) can serve as an efficient and cost-effective advanced oxidation process (AOP) for municipal wastewater treatment. It is hypothesised that this integrated system will enhance the removal or mineralisation of emerging contaminants while reducing catalyst dosage and reaction time compared to using photocatalysis or PMS activation independently. The combined composite photocatalyst–PMS process generates both radical and non-radical oxidative species that synergistically improve contaminant degradation performance. The optimised operational parameters (e.g., Initial pollutant concentration, photocatalyst dose, pH, and reaction time) significantly influence the efficiency of emerging contaminant removal using the composite photocatalytic PMS system.

1.6 Objectives of the Study

1.6.1 General objective of the study

The overall objective of this study is to synthesise, characterise, and optimise photocatalytic composite nanomaterials and evaluate their advanced oxidation process–driven performance for the photodegradation of selected emerging contaminants in wastewater effluents.

To achieve this primary objective, four secondary specific objectives were formulated as follows:

1.6.2 Specific objectives of the study

The specific objectives of the study include:

- To assess physicochemical characteristics and emerging contaminant profiles of wastewater from the Kality wastewater treatment plant, Ethiopia
- To synthesise, characterise, and optimise the parameters of a triple KBN-doped TiO_2 photocatalyst for efficient ciprofloxacin degradation
- Synthesis and characterisation of highly efficient KBN@TiO_2@rGO composite for photodegradation of antibiotics under visible light irradiation.
- Peroxymonosulfate activation by KBN-Doped TiO_2@rGO for the multi-site radical and non-radical degradation of antibiotics: synergistic effects and optimisation of operational parameters.

1.7 Expected Significance and Implications of the Study

The present investigation focuses on experimentally evaluating the effectiveness of novel, sustainable composite photocatalysts for degrading emerging contaminants in wastewater. It also aims to develop low-cost and efficient catalytic materials (KBN@TiO_2 and KBN@TiO_2@rGO) to enhance the photocatalytic degradation of these pollutants, contributing to sustainable environmental remediation.

The study's conclusions are generally expected to be advantageous to several significant stakeholders:

A. **Academia.** Future studies on sophisticated oxidation processes, novel contaminants, and photocatalysis can use the results of this work as a scientific foundation. The synthesis, characterisation, and optimisation of the KBN@TiO_2 and KBN@TiO_2@rGO composites may facilitate the development of new materials and inspire further investigation into environmental remediation techniques.
B. **Policymakers/regulatory bodies.** The study provides essential insights for environmental policymakers on the presence and persistence of emerging pollutants in municipal wastewater. It underscores the vulnerability of natural water bodies and highlights the need to revise regulatory policies, strengthen discharge standards, and promote the use of advanced treatment technologies to protect both the environment and public health.
C. **Industrialists and Treatment plant operators.** The findings offer valuable guidance for industries that generate complex effluents and for wastewater treatment plants. By revealing the limitations of current treatment methods and demonstrating the effectiveness of sustainable photocatalytic technologies, the study encourages operators to implement more efficient, environmentally friendly, and socially responsible treatment practices that support long-term sustainability objectives.
D. **Community.** The community benefits indirectly through enhanced environmental protection, reduced exposure to harmful emerging contaminants, and improved water quality. The advancement of affordable and sustainable photocatalytic technologies promotes cleaner ecosystems, healthier living conditions, and broader efforts toward long-term environmental sustainability.

1.8 Organisation of Dissertation

This dissertation work is organised into seven major chapters, each addressing a key component of the study. The structure is designed to guide the reader from the introductory background

and research objectives through experimental methods, results, discussions, and finally, the conclusions and recommendations. A brief overview of each chapter is provided below to illustrate the logical flow and interconnectedness of the research.

Chapter One serves as the opening section of the general introduction. It outlines the background of the study, explains the rationale for focusing on the removal of emerging contaminants from municipal wastewater, and describes the scope and limitations of the research. It also presents the study's objectives along with the anticipated significance and broader implications of the work.

Chapter Two presents a comprehensive review of relevant literature conducted before initiating any experimental work. This review examines existing studies to identify related research and establish the current state of knowledge. With particular emphasis on the principles of both conventional and advanced wastewater treatment technologies, it also highlights global trends in photocatalytic advanced oxidation processes for the removal of emerging contaminants. The chapter provides valuable insights into contemporary environmental remediation technologies and concludes with a summary of the key findings from the literature.

Chapter Three presents the published work on a comprehensive physicochemical characterisation study conducted to identify and quantify selected pharmaceutical pollutants and other major contaminants in the effluents of the Kality Municipal Wastewater Treatment Plant. This assessment evaluates the treatment plant's performance and offers critical insight into the types and levels of emerging pollutants currently present in the system.

Chapter Four presents a submitted study on the synthesis of a metal-non-metal-doped photocatalyst designed to reduce the band gap energy and enhance light absorption. The synthesised material was further optimised using Response Surface Methodology (RSM) employing a three-level Box–Behnken Design (BBD). Finally, a comprehensive characterisation of the optimised photocatalyst was conducted to evaluate its structural, optical, and functional properties.

Chapter Five presents a published study in which the optimised KBN@TiO_2 nano catalyst developed in Chapter Four was further enhanced by compositing it with rGO to produce a highly efficient composite photocatalyst. The material was synthesised using a sol–gel method followed by hydrothermal treatment. A comprehensive characterisation of the composite was

conducted, and its performance was evaluated against various synthetic antibiotic contaminants as well as real wastewater samples.

Chapter Six presents a detailed investigation of the KBN@TiO_2@rGO composite photocatalyst activated by PMS, highlighting the synergistic multi-radical and non-radical reaction pathways responsible for contaminant degradation. Key operational parameters were systematically optimised using CIP and TOC removal as response variables, providing insights into both the mechanism and practical application of the advanced oxidation process for wastewater treatment.

Chapter Seven constitutes the final section of the dissertation, summarising the study's conclusions and providing recommendations and future perspectives for further research. Following this chapter, the bibliography section lists all references cited throughout the dissertation. Additionally, the document includes extensive supplementary material related to experimental studies, which can be accessed in the List of Appendices.

CHAPTER TWO
LITERATURE REVIEW

2.1 Wastewater and Contaminants

In recent decades, urbanisation and industrialisation have led to high production, consumption and disposal of a variety of chemicals with complex and diverse structures that offer improvements in industry, agriculture, medical treatment and household conveniences [50]. An increased volume of municipal or industrial wastewater has compounded concerns regarding the environmental impact of these chemicals. Little is known about the extent of environmental occurrence, transport and ultimate fate of many of these synthetic chemicals after their intended use [51].

2.2 Emerging Contaminants

Conventional wastewater treatment processes are effective in improving the quality of treated water; however, these technologies are only partially effective at removing certain organic contaminants, resulting in their discharge into natural water streams. Development of new analytical equipment and robust extraction techniques has allowed the detection of low-concentration organic contaminants in natural waters and wastewater at different stages of the treatment process. A growing concern over the last few years has been focused on the presence of chemicals now designated emerging contaminants (ECs), also known as chemicals of emerging concern (CECs), including pharmaceuticals, personal care products, hormones and pesticides in municipal wastewater effluents [52].

The main sources of these emerging contaminants are municipal wastewater, hospital effluents, chemical manufacturing plants where any of the classes of ECs are manufactured or used, leakages and leachates from landfills, storm water runoffs and wastewater from livestock and agriculture [52].

Typically, the concentration of these emerging contaminants in treated wastewater, surface water and groundwater is in the range of 0.1 - 20 μg/L [53]. A study on concentrations of ECs in treated wastewater effluents reported a range of 1.0 ng/L to 1.0 μg/L [54]. Antibiotics are among the most frequently detected emerging contaminants in a wide range of water matrices, including surface water, groundwater, municipal wastewater, hospital effluents, and even treated wastewater [55]. Figure 2.1 illustrates the keyword co-occurrence network associated

with research on antibiotic removal in aquatic systems, with photocatalysis emerging as one of the most prominent focal areas.

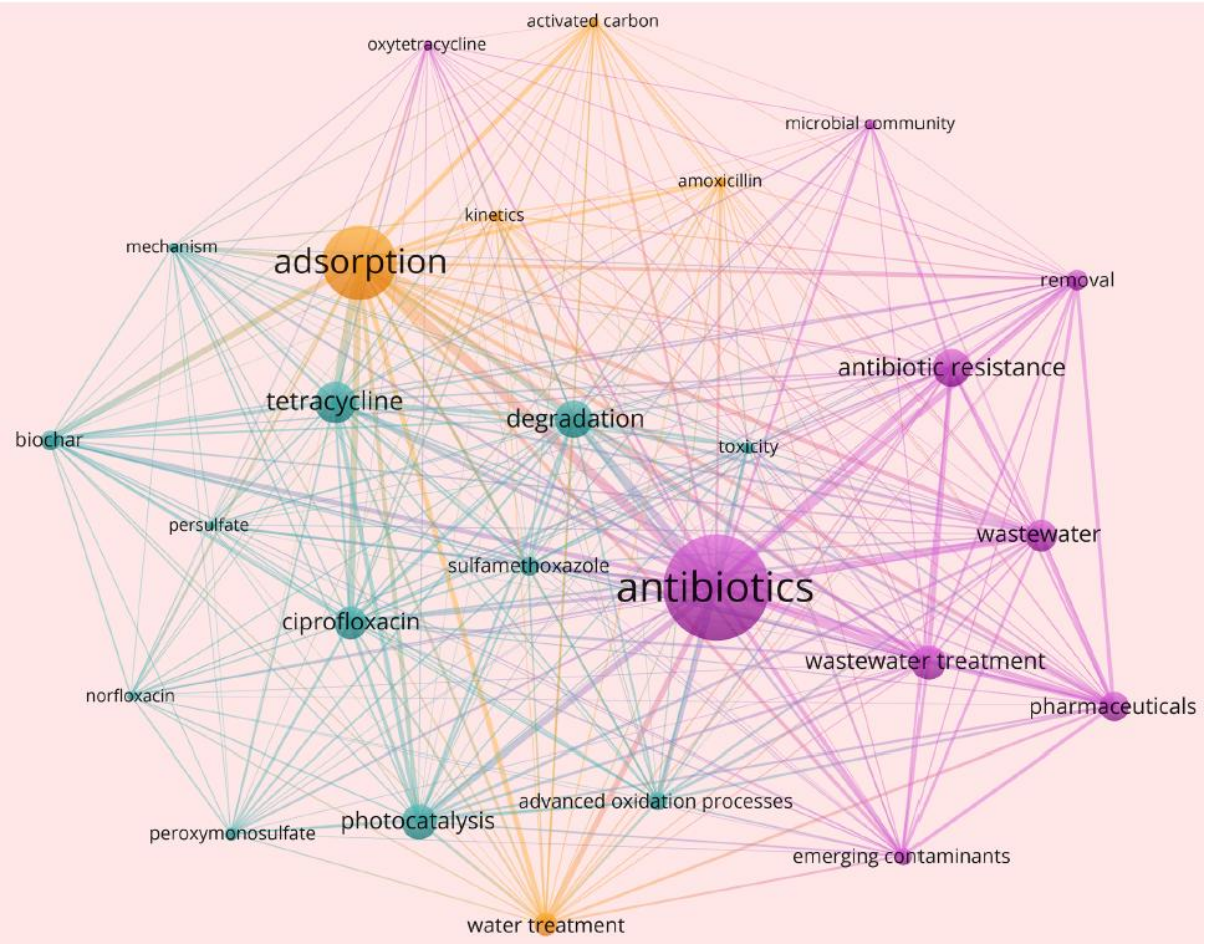

Figure 2.1 Overview of research trends in antibiotic removal: adsorption, wastewater treatment, and photocatalysis [56].

2.2.1 Impact of emerging contaminants

The effects of emerging contaminants (ECs) on animals are well documented, whereas their direct impacts on human health are still under investigation. Even at low concentrations, ECs pose significant potential risks to humans. The primary route of human exposure to endocrine-disrupting chemicals (EDCs) is through ingestion of food and beverages contaminated via soil, water, microorganisms, plants, and animals. Bioaccumulation and biomagnification are particularly concerned for species at the top of the food chain. However, data on the toxicity of heavy metals, EDCs, and bisphenol-A (BPA) originating mainly from surface runoff, WWTP effluents, seepage, and landfills remain limited [57].

EDCs can disrupt the endocrine system by mimicking, suppressing, or altering natural hormone functions. Even at low concentrations, these exogenous compounds interfere with normal hormonal activity. Human health effects include reduced male sperm counts, reproductive malfunctions, and increased risks of cancers such as testicular, prostate, ovarian, and breast cancer [58]. In children, exposure has been associated with delayed brain development and reduced intelligence quotient (IQ) [59]. Eliminating these contaminants is challenging due to their occurrence at trace levels, yet it is crucial given their chronic toxicity and endocrine-disrupting potential [60].

Evidence from animal studies shows that substances such as estradiol, estrone, estriol, and ethinyl estradiol can disrupt reproductive tissues and impair growth, reproduction, and development [4]. Pharmaceuticals and personal care products further influence species' growth, reproduction, and evolutionary patterns. The complex physicochemical properties of these pollutants across air, water, and soil hinder a comprehensive understanding. Researchers are working to trace these contaminants from their sources to receptors to better predict their long-term environmental and health impacts [61].

2.3 Wasteawter treatment

Various activities, including agricultural practices, domestic usage, and industrial discharges, introduce undesirable pollutants into water bodies, posing significant threats to biodiversity and aquatic ecosystems [7]. These hazardous waste streams often contain toxigenic microorganisms, suspended solids, heavy metals, and inorganic salts. In this context, wastewater treatment plants play a crucial role in removing such contaminants and improving effluent quality. Moreover, rapid population growth and increasing urbanisation have resulted in large volumes of sewage requiring treatment before discharge. In Europe, regulations have become progressively stricter, mandating that all municipal wastewaters be treated prior to release into the environment. Consequently, diverse treatment approaches must be considered to achieve optimal purification and decontamination outcomes [62].

2.3.1 Conventional wastewater treatment technologies

The main goals of conventional wastewater treatment facilities are to remove suspended particulates, easily degrade organic components, nutrients, and metal contaminants from wastewater. These purification systems often function through numerous phases that integrate physical, chemical, and biological processes, including coagulation, flocculation, ion-exchange, membrane filtration, and other electrochemical approaches [63]. However, conventional

wastewater treatment processes are often unable to fully eliminate persistent pollutants, allowing these compounds to pass through the system and enter the environment. Consequently, pharmaceuticals, one prominent group of recalcitrant contaminants, are frequently detected in surface waters receiving effluent treatment [64]. Numerous studies have reported the presence of various drugs in the outputs of traditional treatment methods. Several studies have examined the occurrence of pharmaceuticals in conventional wastewater treatment plants serving heavily populated urban areas and surrounding hospitals. These studies reveal a range of pharmaceutical residues in influent and effluent streams, underscoring the limitations of conventional treatment methods in completely removing these pollutants [65,66,67].

Monitoring results showed that conventional biological treatment techniques accomplished total or partial elimination for only roughly 50% of the detected pharmaceutical chemicals. The remaining half persisted throughout the treatment process, demonstrating insufficient removal and highlighting the ineffectiveness of conventional techniques for these recalcitrant contaminants [68]. Indeed, most pharmaceutical compounds possess low hydrophobicity, high water solubility, and typically carry a negative charge at neutral pH, resulting in minimal adsorption onto biological sludge. Because these characteristics hinder their removal by traditional treatment systems, significant attention has shifted toward advancing alternative, high-efficiency treatment technologies designed to fully eliminate such emerging contaminants [69]. In summary, wastewater treatment plants play a critical role within urban infrastructure, acting as the primary barrier for treating contaminated water. Conventional pollutants tend to be larger molecules and are typically more biodegradable, allowing them to be effectively removed through standard treatment stages. In contrast, emerging contaminants occur at much lower concentrations and often display strong resistance to these traditional processes [70]. This limitation highlights the importance of integrating advanced oxidation processes with existing WWTP systems to achieve comprehensive elimination of all pollutants.

2.3.2 Advanced oxidation processes for wastewater treatment

The persistence of hazardous and recalcitrant pollutants, even at trace concentrations, renders conventional treatment methods largely ineffective [71]. Over recent decades, various alternative strategies have been explored to address pollution caused by these resilient compounds. Among them, advanced oxidation processes (AOPs) have proven to be highly efficient and environmentally friendly approaches for degrading a broad range of organic contaminants in wastewater. AOPs are commonly employed to enhance biodegradability,

reduce overall organic content, and dismantle specific pollutant structures. These processes operate through the generation of reactive oxygen species (ROS), which oxidise contaminants and ultimately convert them into carbon dioxide (CO_2) and water. The hydroxyl radical (•OH), a primary ROS produced in AOPs, reacts rapidly and non-selectively, effectively eliminating a wide spectrum of pollutants [72]. Other reactive species, such as the sulfate radical ($•SO_4^-$), have gained considerable attention as potential alternatives in advanced oxidation processes due to their effectiveness over a broad pH range (2.0–8.0), high oxidation potential (2.5–3.1 V), and relatively long half-life (30–40 μs) [68].

2.3.2.1 Catalytic advanced oxidation processes

Catalytic advanced oxidation processes (cAOPs) have become a strong and efficient option for removing both newly discovered and persistent pollutants from wastewater [73]. In these systems, oxidants like hydrogen peroxide, ozone, persulfate, and peroxymonosulfate are activated by catalysts like metal oxides, doped semiconductor materials, carbon-based structures, and hybrid nanocomposites to produce reactive oxygen species that can degrade persistent organic pollutants. By stimulating both radical and non-radical oxidation mechanisms, cAOPs deliver faster degradation rates, increased mineralisation, and greater operational stability than conventional AOPs[74]. Their adaptability also facilitates integration with membrane filtration, photocatalysis, and adsorption processes, thereby enhancing overall efficiency. cAOPs are becoming recognised as sustainable, scalable, and cutting-edge technology for contemporary wastewater as industrial growth contributes to water pollution and increases the presence of pharmaceuticals, hormones, and other emerging contaminants[75]. To improve the production of •OH radicals, various catalysts have been incorporated into pollutant treatment systems. Among catalytic AOPs, homogeneous photo-Fenton reactions and heterogeneous photocatalytic processes are the most widely studied and applied approaches [76].

Homogeneous photo-Fenton process: Fenton-based technologies rely on the reaction between Fe^{2+} and H_2O_2 to produce •OH radicals, typically under acidic conditions. In the photo-Fenton process, exposure to UV or visible light accelerates the direct generation of •OH radicals and facilitates the regeneration of Fe^{2+} from Fe^{3+} (Eqs. 2.1– 2.4). This leads to the formation of additional •OH species and an increase in Fe^{2+} concentration, thereby improving the overall oxidation efficiency. Consequently, these methods can achieve complete mineralisation of pharmaceutical contaminants [68].

$$Fe^{2+} + H_2O_2 \rightarrow Fe^{3+} + \bullet OH + OH^- \quad (2.1)$$

$$Fe^{3+} + H_2O_2 \rightarrow Fe^{2+}HO_2^{\bullet} + H^+ \quad (2.2)$$

$$Fe(OH)^{2+} + hv \rightarrow Fe^{2+} + \bullet OH \quad (2.3)$$

$$H_2O_2 + hv \rightarrow 2(\bullet OH) \quad (2.4)$$

Heterogeneous photocatalysis process: This process can operate under UV or visible light, as well as natural solar irradiation. Upon illumination, a series of redox reactions are initiated on the surface of the photocatalyst, leading to the degradation of persistent pollutants [77]. Among advanced oxidation methods, heterogeneous photocatalysis is currently regarded as one of the most promising and environmentally friendly technologies for wastewater treatment [78]. Numerous studies have highlighted the effectiveness of advanced oxidation processes (AOPs) in treating wastewater and eliminating a wide range of emerging contaminants. The incorporation of catalysts such as TiO_2 is particularly important in these systems. In photocatalysis, TiO_2 significantly enhances reaction performance by facilitating the generation of reactive species, especially hydroxyl radicals under UV irradiation, which subsequently degrade pollutants. Its use not only accelerates contaminant removal but also provides environmental and economic advantages by lowering energy demands and operational costs [79]. In photo-Fenton processes, TiO_2 also plays a critical role, acting as a photocatalyst within the modified Fenton system that employs iron ions and hydrogen peroxide under UV or visible light. Overall, the presence of TiO_2 is indispensable due to its catalytic efficiency and its contribution to improved treatment outcomes.

2.3.3 Advanced oxidation processes limitations

Advanced oxidation processes (AOPs) are highly effective for degrading a wide range of persistent contaminants; however, several limitations hinder their widespread industrial application [80]. Many AOPs require significant energy input, especially those that rely on UV

irradiation, resulting in high operational costs. Processes such as Fenton and photo-Fenton are strongly pH-dependent and typically require acidic conditions, making pH adjustment necessary and adding complexity to treatment [42]. Additional challenges include catalyst deactivation, sludge generation, difficulties in catalyst recovery, and the formation of potentially harmful intermediate by-products [76]. Furthermore, real wastewater matrices containing inorganic ions, natural organic matter, or high turbidity can suppress radical formation and decrease treatment efficiency. Despite these drawbacks, AOPs have progressed into promising technologies capable of removing a broad spectrum of organic pollutants without generating secondary pollution [81]. They can be classified into two main categories: homogeneous and heterogeneous systems, each employing different activation pathways Figure 2.2.

As AOPs continue to advance, evaluating their economic and energy performance has become essential. Costs vary widely depending on the type of process, catalyst, oxidant, and equipment requirements, which is particularly important when considering full-scale implementation [82]. Improving energy efficiency is also critical for identifying sustainable treatment strategies. Integrating renewable and environmentally friendly energy sources such as solar, wind, and hydropower can significantly reduce both operational costs and environmental impact. Solar energy, for example, can directly power photocatalytic systems, reducing dependence on conventional electricity, while wind and hydropower can support other energy-intensive AOP configurations [80, 81].

Overall, the performance of AOPs is influenced by operational conditions, chemical consumption, and energy requirements. To address these challenges, combined or hybrid AOPs have been widely investigated and shown to enhance treatment efficiency while reducing drawbacks associated with single processes. Continued research is therefore needed to develop greener, simpler, and more cost-effective catalysts, as well as more sustainable treatment configurations. Among the various AOPs, heterogeneous photocatalysis remains one of the most promising technologies, particularly for the degradation of pharmaceutical compounds, due to its high efficiency, low secondary pollution, and strong potential for integration with renewable energy sources.

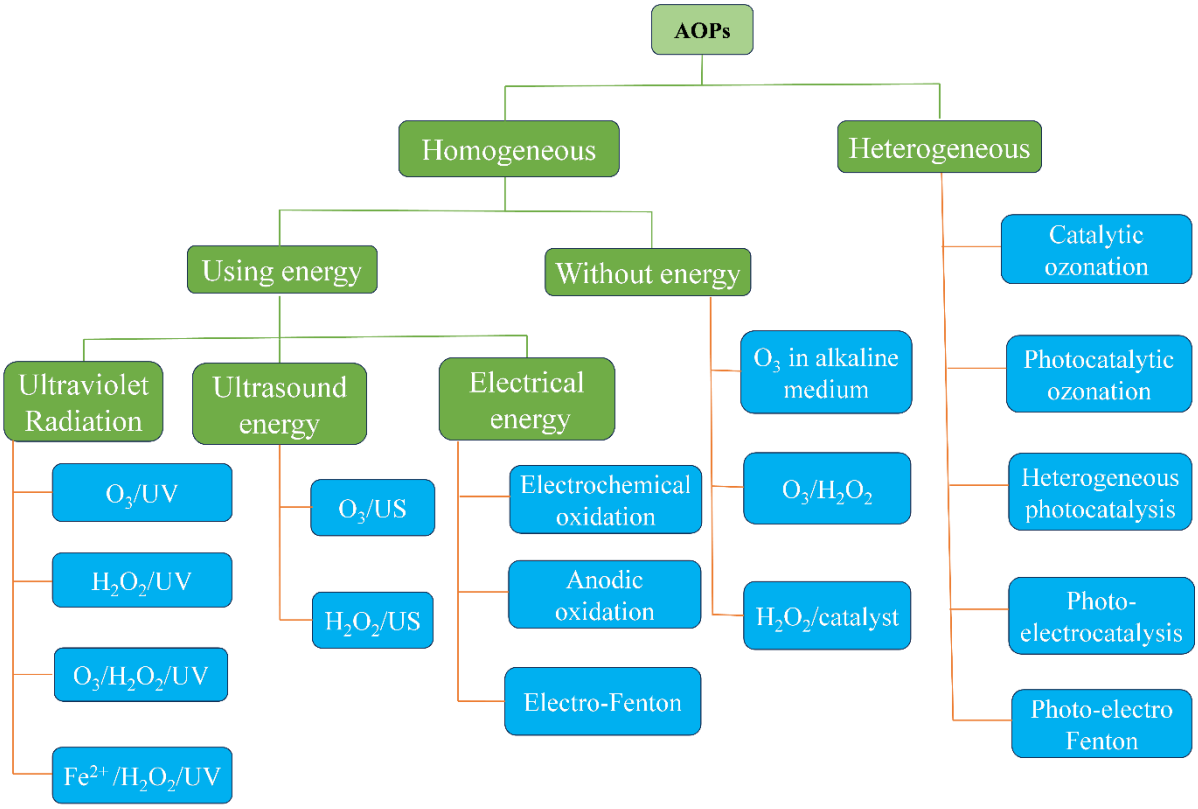

Figure 2.2 Schematic overview of the most used treatments based on AOPs.

2.4 Photocatalytic oxidation processes

In recent years, heterogeneous photocatalysis has gained significant attention as a promising approach to address water pollution. When applied in water treatment plants, this technology can effectively break down persistent organic pollutants into more biodegradable and less toxic compounds. The process relies on the synergistic action of light energy and semiconductor photocatalysts to degrade contaminants. Additionally, photocatalysis is recognised as an efficient, cost-effective, and environmentally friendly method, particularly using visible or solar light. Owing to these advantages, it has become a key technology within advanced oxidation processes (AOPs) for the removal of pharmaceuticals, dyes, pesticides, and other emerging contaminants [13, 32, 67].

2.4.1 Principle

The fundamental mechanism of semiconductor-based heterogeneous photocatalysis begins when the photocatalyst is exposed to light with a wavelength equal to or greater than its band gap, as illustrated in **Figure 2.3.** The absorbed photons excite electrons (e^-) from the valence band to the conduction band, leaving behind positive holes (h^+) in the valence band. These photogenerated holes can oxidise water or hydroxide ions adsorbed on the catalyst surface to

produce highly reactive hydroxyl radicals (•OH). Simultaneously, the excited electrons reduce dissolved oxygen molecules to form superoxide radical ($•O_2^-$). Both •OH radicals and $•O_2^-$ radicals are powerful oxidising agents capable of attacking and breaking down a wide range of organic pollutants present in wastewater, including pharmaceuticals, dyes, and other persistent contaminants.

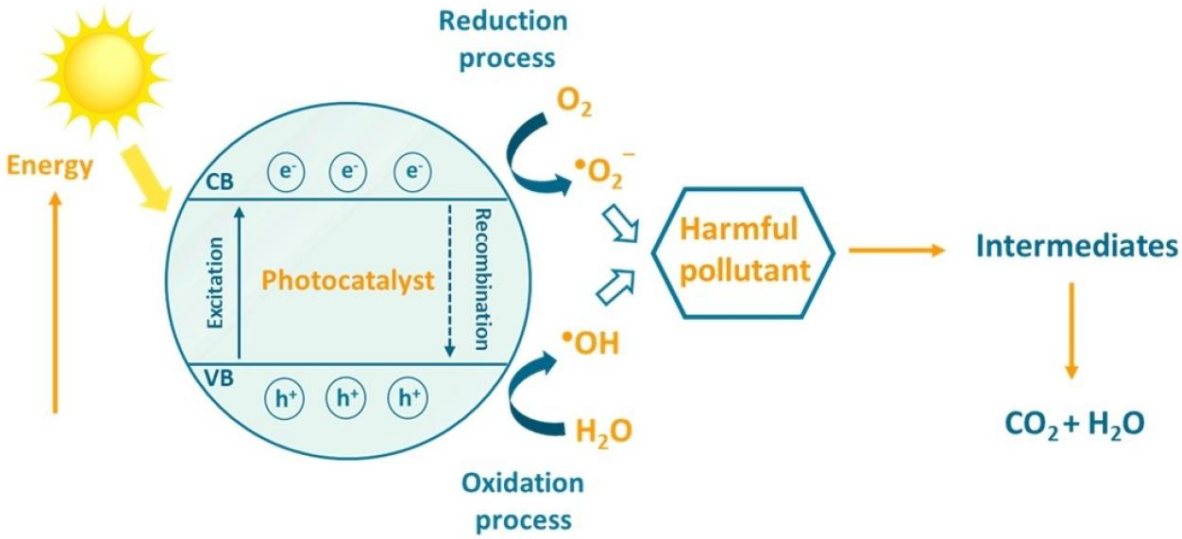

Figure 2.3 The fundamental process through which photocatalysis degrades pollutants [68]

The radicals react with the pollutants by abstracting electrons, breaking chemical bonds, and ultimately converting them into harmless end products such as carbon dioxide (CO_2), water (H_2O), and mineral acids. This sequence of reactions, light absorption, electron-hole generation, radical formation, and pollutant degradation, forms the core of photocatalytic wastewater treatment, making it an effective method for removing recalcitrant and toxic compounds from water [25]. The detailed reactions are typically represented by Eqs (2.5–2.10), which illustrate the specific pathways for radical generation and contaminant mineralisation.

$$\text{Photocatalyst} + hv \rightarrow e^- + h^+ \quad (2.5)$$

$$e^- + O_2 \rightarrow \bullet O_2^- \quad (2.6)$$

$$h^+ + H_2O \rightarrow \bullet OH + H^+ \quad (2.7)$$

$$\bullet O^{2-} + e^- + 2H^+ \rightarrow H_2O_2 \quad (2.8)$$

$$H_2O_2 + e^- \rightarrow \bullet OH + OH^- \quad (2.9)$$

$$\bullet OH + \text{organic pollutant} + \text{intermediates} \rightarrow CO_2 + H_2O \quad (2.10)$$

2.4.2 Parameters affecting the mechanism of photocatalysis

The conditions required to achieve high photocatalytic removal efficiency can vary widely and are influenced by several key factors, including the type of semiconductor used, the pH of the solution, the characteristics of the light source, and the ratio of catalyst to pollutants. Each of these parameters plays a critical role in determining the overall performance of the photocatalytic process [82].

2.4.2.1 Semiconductor

In photocatalytic wastewater treatment, the choice of catalyst material is one of the most critical factors determining the efficiency of contaminant removal. A suitable photocatalyst must have an appropriate band gap that allows it to absorb light energy and generate electron-hole pairs. These photogenerated electrons and holes then react with water and oxygen to produce highly reactive species such as hydroxyl radicals (•OH) and superoxide radicals ($\bullet O_2^-$), which can break down a wide range of organic pollutants, including pharmaceuticals, dyes, and other emerging contaminants [39]. The photocatalyst must also maintain chemical and photochemical stability in aqueous conditions, since wastewater contains various dissolved ions and molecules that can deactivate or degrade the catalyst. Strong adsorption capacity is important because pollutants must first attach to the catalyst surface to be effectively degraded. Additionally, a high quantum yield, the efficiency of converting absorbed light into reactive species, is desirable for faster and more complete degradation [83].

To make the process sustainable and cost-effective, the photocatalyst should absorb as much of the visible light spectrum as possible, since sunlight is an abundant and free energy source. Most traditional catalysts, like pure TiO_2, primarily absorb ultraviolet (UV) light, which makes up less than 5% of sunlight. Modifying the catalyst to extend its light absorption into the visible range can greatly enhance its performance under natural sunlight, reducing the need for artificial light sources and lowering operational costs [84].

In short, an ideal photocatalyst for wastewater treatment should be stable, efficient, capable of pollutant adsorption, and able to utilise sunlight effectively to generate reactive species that degrade contaminants into harmless products.

Titanium dioxide (TiO_2) is a widely used semiconductor for heterogeneous photocatalysis due to its chemical stability, low toxicity, and high oxidation efficiency, enabling the mineralisation of a broad range of organic contaminants, including pharmaceuticals. However, its practical

application under visible light is limited by the rapid recombination of photogenerated electron-hole pairs and its wide band gap of 3.2 eV. TiO_2 primarily absorbs ultraviolet (UV) light, which constitutes less than 5% of the total solar spectrum. Consequently, numerous studies have focused on modifying TiO_2 to suppress electron-hole recombination and extend its light absorption into the visible region, enhancing its photocatalytic performance under sunlight [92].

2.4.2.2 pH

The efficiency of photochemical reactions is strongly influenced by solution pH, which affects both the surface charge and the oxidation potential of the photocatalyst. Additionally, pH affects the formation of •OH radicals through the interaction of photogenerated holes with surface hydroxide ions on titanium dioxide. At acidic conditions, the photogenerated holes serve as the primary oxidising species, whereas at neutral or alkaline pH •OH radicals become the dominant reactive oxygen species [86]. Recent studies have highlighted the significant role of pH in controlling the photocatalytic performance of TiO_2-based systems. The effect of the initial solution pH on the photocatalytic degradation of paracetamol was investigated over a pH range of 2.5–10 using TiO_2 as the photocatalyst. The highest photodegradation was observed at pH 8, which is attributed to the abundance of hydroxyl radicals on the TiO_2 surface. However, the degradation rate decreased at a more alkaline pH of 10. This reduction is due to electrostatic repulsion between paracetamol, which exists predominantly in its anionic form at this pH (pKa = 9.5), and the negatively charged TiO_2 surface, leading to reduced adsorption and lower degradation efficiency [87].

2.4.2.3 Light intensity

The light source plays a crucial role in photocatalytic processes because it drives the generation of electron-hole pairs in the semiconductor. When the semiconductor absorbs light of a suitable wavelength, electrons are excited from the valence band to the conduction band, leaving behind positively charged holes [88]. These photogenerated electrons and holes then react with water and oxygen molecules to produce reactive oxygen species (ROS), such as hydroxyl radicals and superoxide anions, which are responsible for breaking down contaminants. The intensity of the light directly affects the number of electron-hole pairs generated; higher light intensity produces more charge carriers, leading to increased ROS formation and improved degradation of pollutants. Therefore, both the wavelength and intensity of the light are critical parameters for achieving optimal photocatalytic performance [89].

2.4.2.4 Catalyst/ Pollutant ratio

The initial concentration of contaminants significantly influences the removal kinetics, in addition to the optimal catalyst loading. At optimal catalyst dosing and low pollutant concentrations, enough radicals ensure complete mineralisation of organic compounds. However, when the pollutant concentration exceeds the optimal level, the limited availability of •OH radicals leads to incomplete removal. Excess reactant molecules adsorbed on the catalyst surface can hinder light absorption and reduce •OH radical generation, as fewer active sites are available for hydroxyl ion adsorption. Therefore, maintaining an appropriate catalyst-to-pollutant ratio is essential for achieving optimal degradation efficiency [90].

2.4.2.5 Other parameters

The performance of TiO_2-based photocatalysis is influenced by several key factors. For instance, solutions with high ionic strength can reduce photocatalytic efficiency, as the abundance of ions competes with pollutants for active sites on the TiO_2 surface. Similarly, natural organic matter in water can lower efficiency by occupying adsorption sites and, in some cases, acting as scavengers for the reactive species generated during photocatalysis. Conversely, higher temperatures generally enhance photocatalytic activity by increasing molecular kinetic energy and accelerating reaction rates. However, the effect of temperature is context-dependent, varying according to the specific reaction and catalyst type. Extremely high or low temperatures may also compromise the stability of the catalyst, potentially diminishing the overall effectiveness of the process [81].

2.5 Latest development in TiO_{2-x} based photocatalysts for antibiotic degradation

In the last five years, notable advancements have been achieved in engineering and refining TiO_{2-x}-based photocatalysts, spanning from basic doping approaches to sophisticated hierarchical ternary heterojunction designs. Table 2.1 summarises major studies, detailing the targeted antibiotics, photocatalyst formulations, synthesis techniques, and performance indicators, thereby providing a basis for examining current trends and progress in this research area. Various approaches have been explored, either to modify pristine TiO_2 by introducing oxygen vacancies (O_v) or to synthesise TiO_{2-x} directly from raw precursor materials.

The most frequently used techniques for producing TiO_{2-x} include annealing under reducing conditions, chemical reduction, and solvothermal synthesis. Among these, annealing in reducing oxygen-deficient atmospheres, such as N_2, H_2, Ar, or vacuum, is widely employed to introduce oxygen vacancies (Ov) [91]. This method is valued for its ability to yield high-purity

TiO_{2-x} with well-controlled stoichiometry. However, its major drawbacks are high energy requirements and lengthy processing durations, which hinder large-scale applications.

A variety of modification strategies have been applied to TiO_{2-x} to improve its photocatalytic activity. Non-metal and metal doping enhances visible light absorption and charge transport [92], while magnetic and plasmonic doping enable easy recovery and stronger visible light activation. Composite and mineral-based TiO_{2-x} systems provide synergistic improvements in stability and reactivity. Quantum dots increase surface area and accelerate charge transfer, and advance heterojunctions (S-scheme, Z-scheme, type-II, p-n-n), promoting efficient charge separation [93]. Core- shell, hierarchical, graphene–based, and MOF–coupled structures further enhance electron mobility and suppress recombination. Together, these approaches significantly boost the overall photocatalytic efficiency of TiO_{2-x}.

Table 2.1: Overview of antibiotic photocatalytic degradation by TiO_2-x based photocatalysts.

Antibiotic	**Concentration (mg L^{-1})**	**Type of photocatalyst**	**Catalyst loading (mg L^{-1})**	**S_{BET} (m^2 g^{-1})**	**Degradation (%)/time (min)**	**PFO *k* ($min^{-1}x10^{-3}$)**	**Mineralisation (%)/ time (min)**	**Reference**
Ciprofloxacin	10	TiO_{2-x}	30	-	90/90	23.00	-	[94]
Amoxicillin	20	TiO_{2-x}	25	90.21	100/720	6.09	75/280	[95]
Ciprofloxacin	4.5	N-TiO_{2-x}	100	100.56	70/90	13.20	61/90	[96]
Gatifloxacin	10	Au-TiO_{2-x}	-	-	95/150	20.10	66.7/150	[97]
Norfloxacin	30	Ti^{3+}-TiO_{2-x}/Ar-Fe_2O_3	30	103	40/30	33.50	61.15/30	[98]
Sulfamethoxazole	20	TiO_{2-x}/Fe	40	52.22	90/60	36.00	53/120	[99]
Sulfathiazole	10	C-TiO_{2-x}	20	97	70/360	3.89	-/-	[35]
Tetracycline	10	TiO_{2-x}	20	-	66.2/240	4.50	29.6/240	[24]
Tetracycline	10	Ag/La-TiO_{2-x}	10	78.56	98/90	39.00	39/90	[100]
Tetracycline	10	TiO_{2-x}/AgI	30	-	-/40	35.50	52.70/40	[101]
Tetracycline	15	TiO_{2-x}	-	-	91.52/360	6.79	53/360	[102]
Tetracycline	30	(QDs)TiO_{2-x}/$Cu_3Mo_2O_9$	100	193	100/30	11.60	72/30	[103]

- Data not reported or not applicable

S_{BET} Specific surface area.

PFO *k* Pseudo-first-order rate constant.

2.6 Knowledge gap and research opportunities

In municipal wastewater treatment plants (WWTPs), influent characteristics vary widely depending on community lifestyle and fluctuate over time, resulting in non-uniform inputs that complicate plant operation and compliance with stringent effluent standards [104]. Improper operation can cause environmental and public health issues by discharging contaminated water. At Kality WWTP, emerging contaminants remain largely unidentified and unquantified, highlighting a critical knowledge gap. Predictive tools based on operational parameters could improve plant performance and safety.

Despite considerable progress in TiO_2-based advanced oxidation processes (AOPs), several challenges hinder their practical application, particularly in real-world wastewater treatment. A major limitation is the poor visible-light activity of TiO_2 [105]. While modifications such as metal–nonmetal doping, defect engineering, surface sensitisation, and composite formation with carbon-based supports can enhance light absorption, controlling band-gap narrowing without promoting electron–hole recombination or compromising stability remains difficult [106]. Rapid recombination of photogenerated charge carriers reduces quantum yield and slows reaction kinetics, while TiO_2's wide band gap (3.2 eV for anatase) restricts radical generation to UV light, increasing energy consumption [107].

Existing studies on AOPs for emerging contaminant removal often fail to achieve complete degradation in secondary effluents [108]. The efficiency of photocatalytic reactions depends on electron–hole recombination rates and light absorption capacity, and hybrid systems (e.g., TiO_2 + PMS) remain poorly understood in terms of radical generation, selectivity, reaction kinetics, and interactions with pollutants in complex water matrices [109]. Real wastewater adds further challenges, including salts, natural organic matter, and competing species, which can inhibit radical production, cause catalyst fouling, or alter by-product formation as shown in Figure 2.4.

Despite these advances, composite photocatalyst systems, such as KBN-TiO_2 integrated with rGO-activated PMS, have been insufficiently studied, particularly regarding their effects on treated water quality and by-product formation. Moreover, there is a lack of systematic research on operational optimisation, long-term stability, pilot-scale performance, and environmental risk assessment, all of which are essential for translating laboratory advances into real-world applications [110].

Overall, these gaps underscore the need for developing robust, visible-light-responsive TiO_2-based catalysts with controlled doping, defect engineering, and optimised morphology, integrated with carbon-based supports or heterojunctions. Future research should include mechanistic studies of hybrid AOPs, systematic evaluation of operational parameters, long-term stability, catalyst recovery, by-product toxicity, and nanomaterial fate. Pilot-scale studies, techno-economic analyses, and life-cycle assessments are also critical to enable safe, scalable, and sustainable wastewater treatment solutions [68].

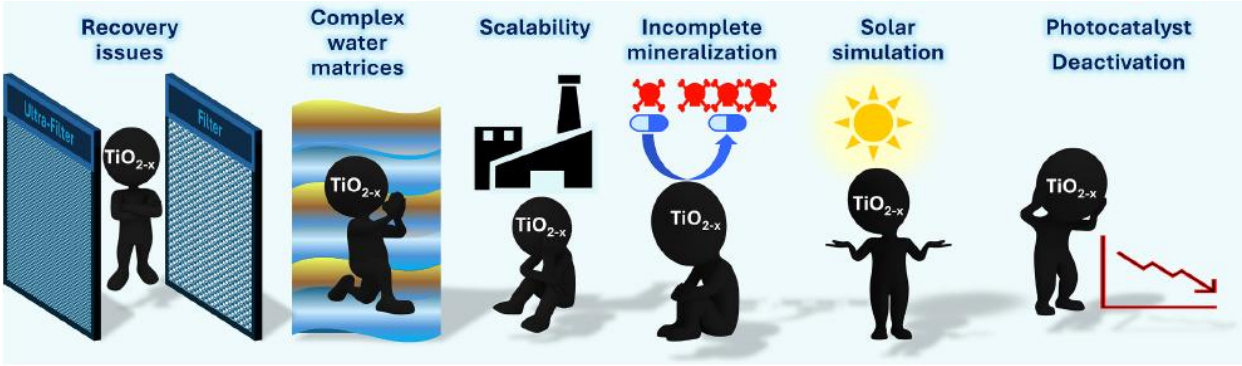

Figure 2.4 Overview of the challenges and research gaps in the photocatalytic degradation of antibiotics [58]

Table 2.2: Research Gaps and Proposed Questions/Hypotheses in Advanced Oxidation Processes Using Modified TiO_2.

No.	Research Question/hypothesis	Underlying rationale, current gaps, and uncertainties	References
1	How do dopant level, dopant type, and synthesis method influence band-gap narrowing, charge-carrier behavior, and radical generation under visible light?	Although doping improves visible-light activity, comparative data on dopant types, concentrations, and their impacts on quantum yield and radical generation remain scarce.	[115]
2	How do interfacial interactions in TiO_2 composites or heterojunctions influence charge separation, adsorption, and radical generation under visible/solar light?	Although hybrids enhance charge separation and light absorption, mechanistic insights under realistic light and water conditions remain limited and charge-transfer pathways are still unclear.	[111]

3	How do TiO_2–PMS/PS AOPs perform under visible/solar light, and what mechanisms control the degradation of real-world micropollutants?	Hybrid PS/PMS photocatalysis produces strong radicals, but their radical profiles, reaction kinetics, and pollutant degradation pathways remain unclear.	[74]
4	How do real wastewater conditions (salts, NOM, pH, competing ions) affect modified TiO_2 AOPs in terms of radical yield, pollutant degradation, by-products, and catalyst fouling?	Most lab studies use clean water, but real wastewater components can suppress radicals, block active sites, or scavenge reactive species, factors rarely examined systematically.	[89]
5	Do modified TiO_2-PS/PMS or hybrid AOPs achieve full mineralisation or only degrade parent compounds, and what intermediates form benign or potentially more toxic?	Many studies target pollutant removal or decolourisation but rarely assess intermediates or TOC, leaving by-product risks largely unexamined.	[112]
6	How do pH, ions, hardness, and NOM affect efficiency and radical formation in modified TiO_2 photocatalysis or AOPs?	Water chemistry impacts radicals, adsorption, and surface charge, but is rarely studied systematically under real conditions.	[86]
7	How do co-existing contaminants affect modified TiO_2 AOP efficiency, synergistically or antagonistically?	Real wastewater contains multiple pollutants, where competition, site blocking, or quenching can alter degradation and by-product formation.	[85]

CHAPTER THREE

Physicochemical Characterisation and Emerging Contaminant Analysis in Wastewater: A Case Study from Kality Treatment Plant, Ethiopia

Abstract

Wastewater treatment plants are increasingly recognised as sources of emerging pollutants due to the limitations of conventional treatment technologies. This study evaluated the physicochemical characteristics of municipal wastewater and the treatment performance of the Kality Municipal Wastewater Treatment Plant (KMWWTP) in Ethiopia, with a focus on emerging contaminants. Influent and effluent samples were analysed for pH, BOD, COD, TSS, VSS, TOC, total nitrogen, total phosphorus, phosphate, ammonium-N, nitrate, and selected pharmaceutical compounds using APHA standard methods. Heavy metals in the effluent, determined by ICP-MS, were Mn (0.63 ± 0.03 mg L^{-1}), Fe (0.72 ± 0.04 mg L^{-1}), Ni (0.02 ± 0.01 mg L^{-1}), Cu (0.12 ± 0.01 mg L^{-1}), Zn (0.17 ± 0.02 mg L^{-1}), Cd (0.004 ± 0.00 mg L^{-1}), Hg (0.030 ± 0.00 mg L^{-1}), Pb (0.073 ± 0.01 mg L^{-1}), As (0.033 ± 0.06 mg L^{-1}), Cr (0.011 ± 0.01 mg L^{-1}), and Se (0.072 ± 0.01 mg L^{-1}). Notably, Ni, Cd, Pb, and As increased after treatment, while removal efficiencies for other metals ranged from 2% to 63%. Pharmaceuticals quantified using LC-MS/MS included amoxicillin (2.54 µg L^{-1}), ciprofloxacin (2.43 µg L^{-1}), carbamazepine (0.82 µg L^{-1}), ibuprofen (8.21 µg L^{-1}), and caffeine (1.24 µg L^{-1}). Overall, KMWWTP only partially complies with the WHO and USEPA effluent standards, particularly showing deficiencies in removing heavy metals, total phosphorus, and total nitrogen.

3.1 Introduction

Water is essential for the survival of all species and sustainable development, yet its availability is increasingly limited. Industrialisation, urbanisation, socioeconomic growth, and other human activities have led to declining water quality and contamination [1, 2]. Population growth and climate change have further reduced freshwater resources, increasing the frequency and severity of droughts over the past three decades. This trend is projected to continue, raising global concern and posing serious environmental and economic challenges [3].

In recent decades, growing attention has focused on contaminants of emerging concern (CECs), such as pharmaceuticals and personal care products (PPCPs), artificial sweeteners (ASs), endocrine-disrupting chemicals (EDCs), flame retardants, fuel additives, and various industrial organic products. This concern arises from their widespread occurrence and potential adverse

health impacts [4]. CECs enter aquatic environments through municipal, hospital, or industrial discharges, sewage leakage, and surface runoff from urban or agricultural areas [4, 5]. Wastewater treatment plants (WWTPs) are major sources, as CECs are detected in both influent and effluent at concentrations ranging from ng L^{-1} to µg L^{-1}[5,9,10]. During treatment or in natural systems, they may transform into by-products that are even more persistent or toxic [10,11]. The limited removal efficiency of CECs in WWTPs poses a significant challenge to the safe and sustainable reuse of wastewater, particularly for irrigation.

Conventional municipal wastewater treatment plants (MWWTPs) are not designed to effectively remove emerging contaminants (ECs). Consequently, these pollutants are released into the environment, exposing all living organisms to various risks such as bacterial resistance, endocrine disruption, feminisation of aquatic organisms, neurotoxicity, and even carcinogenic effects [9]. In Ethiopia, wastewater generation has increased due to rapid population growth, unplanned urbanisation, inadequate sanitation infrastructure, and poorly regulated industrial activities. Moreover, current environmental legislation does not specify permissible limits for most ECs [10]. Consequently, many rivers and streams become highly polluted as they pass through major urban areas and settlements [11].

The Kality WWTP, Ethiopia's only and largest municipal wastewater treatment facility, treats over 34 million m^3 of septic wastewater annually and discharges effluent into the Little Akaki River, which supports downstream irrigation. Despite global concern over emerging contaminants (ECs), little attention has been given to this issue in Ethiopia. To date, no studies have reported on the occurrence of ECs in municipal wastewater entering or leaving the Kality WWTP, and the plant's performance regarding the removal of these contaminants remains unexplored. Therefore, this study aimed (a) to evaluate the treatment performance of the Kality MWWTP using main wastewater quality indicators, (b) to identify and quantify common emerging pharmaceutical organic compounds, and (c) to generate baseline data for evaluating the performance of the municipal wastewater treatment plants.

3.2 Materials and Methods

3.2.1 Study area and description of Kality WWTP

Kality WWTP receives 100,000 m^3/d of MWW, serving only a portion of Addis Ababa city. The facility consists of a grit chamber, UASB, trickling filters, and a secondary settling tank.

A schematic diagram of the facility (treatment plant) and the sampling points is shown in Figure 3.1.

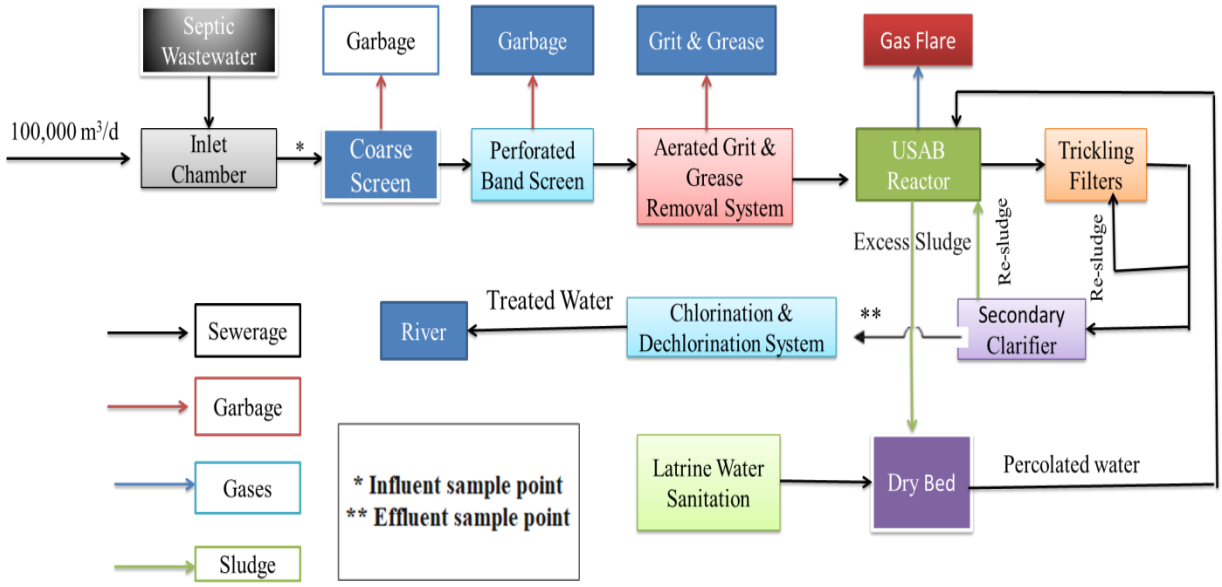

Figure 3.1 Schematic diagram of the Kality municipal WWTP.

3.2.2 Chemicals and Standards

LC-MS grade acetonitrile, methanol, and formic acid 98% were supplied from Merech (Darmstadt, Germany). Glass microfiber 47 mm GF/D (2.7µm) and 0.45µm were purchased from Neway PLC laboratory suppliers in Ethiopia. Caffeine ≥ 99.5 %, pharmaceutical standards such as ciprofloxacin, amoxicillin, carbamazepine, diclofenac, and ibuprofen, purity ≥ 98% were obtained from Ethio pharma Share Company, Ethiopia. Ultrapure water and analytical grade reagents were used. Individual standards 30 mg L^{-1} were prepared in appropriate solvents and diluted to a mixed stock (10 mg L^{-1}) with 1:1 methanol/ water (v/v), stored at +4°C in the dark.

3.2.3 Sample collection and preparation

Four 24-hour composite samples were collected weekly from November 16 to December 9, 2023, at the Kality municipal WWTP from two sampling points: the influent (inlet to the coarse screen) and the effluent (outlet from the secondary clarifier). Figure 3.1. Samples were collected in 1-L glass bottles pre-rinsed with methanol and rinsed with distilled water. All samples were stored at 4 °C until preparation and extraction. Sample preparation and extraction were completed within 24 hours, following established procedures and standards as described elsewhere [113].

3.2.4 Physicochemical analysis

The physicochemical analysis included pH, electrical conductivity (EC), total suspended solids (TSS), volatile suspended solids (VSS), total Kjeldahl nitrogen, total phosphorus, total organic carbon, biological oxygen demand, and chemical oxygen demand (COD). The pH and EC of the wastewater samples were measured on-site using a portable pH and EC digital measuring instrument. Other measurements were conducted using conventional techniques as per APHA 1999. COD levels were determined using a WTW brand spectrophotometer and ready kits [114]. Table 3.1 summaries the methods/ instruments used.

3.2.5 Heavy Metal Analysis

Samples were analysed using a PerkinElmer Optima 800 ICP-OES (PerkinElmer, USA) with radial plasma observation. A Spectro Arcos optical emission spectrometer (32 CCD detectors) measured elements across 130-770 nm. The samples were nebulised into an argon plasma, and emitted intensities were used to determine concentrations from linear calibration curves (R^2 >0.998). Optimal digestion was achieved using 50 mL of water, 4 mL of HNO_3, and 1 mL of HCl at 250 °C for three hours. Limits of detection (LOD) were determined from three digested blanks. Analysed elements included Mn, Fe, Ni, Cu, Zn, Cd, Hg, Pb, As, Cr, and Se, with standard concentrations ranging from 1.4 to 4 mg L^{-1}. Removal efficiency was evaluated using Equation (3.1) [115].

$$\textit{R}\text{emoval Efficiency } (\%) = \frac{C_0 - C_f}{C_O} * 100 \quad (3.1)$$

where C_0 = mean concentration of heavy metal in influent, C_f = mean concentration of heavy metal in effluent.

Table 3.1: Instruments/methods used for the determination of Physicochemical Parameters.

No.	Parameters	Abbreviations	Method of Analysis
1	pH	------	Digital Multi-parameter Analyser
2	Chemical Oxygen Demand	COD	spectrophotometer/open reflux
3	Biological Oxygen Demand	BOD	5-day method/ BOD Sensor
4	Volatile suspended solids	VSS	Gravimetric Method
5	Total Suspended Solids	TSS	Gravimetric Method
6	Electrical Conductivity	EC	Direct measurement by digital benchtop
7	Total Kjeldahl nitrogen	TN	4500-N(Org) C. Semi-Micro-Kjeldahl
8	Total Phosphorous	TP	APHA4500-P.C colorimetric
9	Heavy Metals	HMs	Acid digestion + ICP-OES
10	Total Organic Carbon	TOC	Shimadzu TOC-LCSH analyser (Kyoto, Japan)

3.2.6 Solid Phase Extraction of Emerging Contaminants

Solid phase extraction (SPE) was performed with Oasis hydrophilic-lipophilic balance (HLB) cartridges (6 mL, 200 mg). The four phases of the SPE method were conditioning, loading, washing, and elution. Cartridges were preconditioned with methanol, followed by ultrapure water, and then loaded at a flow rate of approximately 10 mL min^{-1} using an SPE vacuum manifold (Supelco, Bellefonte, PA, USA) and dried in a vacuum for 5 minutes. After drying, the cartridges were cleaned with ultrapure water and further dried under vacuum for 10 minutes before elution. All eluted extracts were evaporated in a stream of nitrogen at 40 °C and reconstituted with 1 mL of H_2O/ACN 80/20 (v/v), followed by filtration through a 0.2 µm cellulose acetate syringe filter before injection into the LC-MS/MS apparatus.

3.2.6.1 LC-MS/MS analysis of selected emerging organic contaminants

Pharmaceuticals were analysed using liquid chromatography coupled with a triple quadrupole mass spectrometer (LC-MS/MS) (Xevo TQS, Acquity H-Class, Waters, and Milford, CT, USA). Chromatographic separation was performed on a CORTECS T3 column (100 mm 2.1 mm, particle size 1.6 mm, Waters). Based on optimised conditions from previous studies [116], the mobile phase consisted of 0.1% formic acid in water (A) and 0.1 % formic acid in acetonitrile

(B). Gradient elution started at 95% A and 5% B, reaching 60% B in 7 min, 50% B in 12 min, and 100% B at 15 min, held for 3 min, then re-equilibrated to initial conditions for 5 min**.** The flow rate of 0.3 mL min^{-1} with a 5 µL injected volume. Most analytes were detected in positive electrospray ionisation (ESI^+) mode. The dissolution temperature was 350 ℃, with desolation gas flow and cone gas flows of 900 and 150 L h^{-1}, respectively. Data acquisition and processing were performed using MassLynx v4.1 [117].

3.2.6.2 Quality assurance

Calibration was performed using five calibration points in MeOH: Milli-Q® water (10:90, v/v) with an Internal standard mixture (ISM) at 0.25 µg L^{-1} across a concentration range of 0.01 -1 ng μL^{-1}. Pharmaceutical recoveries were evaluated by spiking wastewater samples at 4 µg L^{-1} with a mixture of target analytes. Five pharmaceutical internal standards were used for extraction and analytical control, while external calibration provided enhanced responses for specific compounds. The instrumental detection limit (IDL) was defined as the lowest amount of analyte concentration yielding a single - to - noise (S/N) ratio of 3. The method detection limit (MDL) and limit of quantification (LOQ) were determined using spiked wastewater samples (4 µg L^{-1}) corresponding to S/N ratios of 3 and 10, respectively. Method precision was evaluated from the intra-day assays expressed as relative standard deviation (% RSD) based on five replicate injections of 0.1 ng μL^{-1} standards. Matrix effects (ME) were calculated from signal area ratios in spiked wastewater using Equation (2); ME values of 100 %, > 100%, and < 100% indicate no effect, ion enhancement, and ion suppression [118].

$$\mathrm{ME}(\%) = \frac{\mathrm{A}-\mathrm{B}}{\mathrm{C}} * 100 \qquad (3.2)$$

where *A* represents the peak area of each analyte in spiked wastewater samples, *B* represents the peak area of each analyte in non-spiked wastewater, and *C* represents the peak area of each analyte in the standard solution. The calculated matrix effect (ME) values, along with other quality assurance parameters, such as recovery precision, IDL, MDL, and LOQ, are summarised in Table 3.2.

Table 3.2: Quality parameters obtained for six selected pharmaceutical compounds.

Compounds	*Linearity (µg L^{-1})*	*R^2*	*IDL (pg)*	*Intra day Precision (%)*	*% R±RSD (ww)*	*MDL (ngL^{-1})*	*LOQ (ngL^{-1})*	*Matrix Effect (%)*
Amoxicillin	10-1000	0.9982	2.82	12	101±4	8	14	98
Ciprofloxacin	10-1000	0.9985	1.58	12	78±12	15	54	55
Carbamazepine	10-1000	0.9925	0.68	5	118±11	2	9	85
Caffeine	10-1000	0.9924	1.11	11	52 ± 4	9	19	78
Ibuprofen	10-1000	0.9971	2.08	2	100±7	13	48	121
Diclofenac	10-1000	0.9954	2.26	2	73±11	2	4	154

R^2: coefficient of determination, IDL: instrumental detection limit, RSD: relative standard deviation, MDL: method detection limit, ME: matrix effect, LOQ: limit of quantification

3.2.7 Statistical Analysis

All analyses were performed in triplicate, and the mean and standard deviation values were used to calculate the final concentrations of each element. Correlations among EC concentrations were evaluated using linear statistical analysis in Microsoft® Office Excel, expressed as Pearson or Spearman correlation coefficients as appropriate. Graphical illustrations were generated using Microsoft Excel and SPSS software.

3.3 Results and discussion

3.3.1 Investigation of physicochemical variables

3.3.1.1 pH and total suspended solids (TSS)

The pH of wastewater is a critical factor in treatment, as it influences biological activity and treatability [119]. Controlling pH is important to reduce contaminants and ensure effluent safety for the environment and public health [120]. In this study, the average pH of Kality municipal WWTP influent and effluent was 7.6 ± 0.2 and 8.3 ± 0.5, respectively, both within WHO and USEPA permissible limits (Table 3). Similarly, studies in Cape Town, South Africa, and Delhi, India, reported pH values of influent and effluent within recommended discharge limits, ranging from slightly acidic to alkaline conditions, highlighting comparable physicochemical characteristics across different wastewater treatment systems [112, 121].

Total suspended solids represent the dry weight of material retained on a standard filter from a measured water volume, including both organic and inorganic solids, expressed in mg L^{-1}.

Samples are dried at 105 ℃ to remove liquid and absorbed moisture, and the mass difference reflects the suspended solids. In this study, the treatment process reduced TSS from 280 ± 61.3 mg L^{-1} in the influent to 29 ± 5.3 mg L^{-1} in the effluent (Table 3.3 and Figure 3.2), corresponding to an overall removal efficiency of 89.6%.

3.3.1.2 BOD and COD analysis

Biological oxygen demand (BOD) represents the amount of oxygen required by microorganisms to decompose organic matter under aerobic conditions. It is determined by measuring the remaining oxygen dissolved over time [122]. Typically, 95-99% of organic matter is oxidised within 20 days, while approximately 70% is degraded during the first 5 days (BOD_5) [114]. As shown in Table 3. 3 and Figure 3.2**,** the wastewater treatment processes were highly efficient in reducing BOD, from 410 ± 21.6 mg L^{-1}, in influent wastewater to 23.5 ± 6.0 mg L^{-1} in effluent. This meets WHO and US EPA guidelines, which recommend BOD levels below 30 mg L^{-1}. Overall, the BOD removal efficiency was 94.4%.

Chemical oxygen demand (COD) measures the oxygen required to chemically oxidise organic materials in a sample [123]. COD analysis revealed a reduction from 896.5 ± 102.5 mg L^{-1} in influent to 88.3 ± 12.5 mg L^{-1} in effluent, corresponding to a 90.2 % removal efficiency. While COD removed at the Kality municipal WWTP is below the US EPA discharge limit, the treatment effectively reduces most organic pollutants, as shown in Table 3.3 and Figure 3.2

3.3.1.3 Nitrate and Electrical Conductivity

Nitrate is the final product of aerobic nitrogen compound stabilisation and is believed to be the most stable oxygen-containing chemical in water [114]. Surface water nitrate primarily originates from large discharges of sewage and wastewater, which exceed groundwater concentrations [120]. In this study, nitrate levels decreased during treatment Table 3.3, but remained above WHO and US EPA standards, with a removal efficiency of 72.5% at the Kality municipal WWTP. Wastewater conductivity was high in both influent (949.5 ± 52.4 µs cm^{-1}) and effluent (1044 ± 25 µs cm^{-1}), Table 2.3, reflecting elevated ionic concentrations and turbidity. The effluent slightly exceeded the WHO guideline, like higher values reported in Uganda (1021.17 µs cm^{-1}) [123]. High conductivity in treated sewage likely results from residual dissolved ions, indicating limited removal efficiency of inorganic compounds and heavy metals during treatment [124,26].

Table 3.3: Physicochemical characterisation of wastewater sample from Kality MWWTP.

Parameters	Experimental Values			Permissible limits	
	Influent	Effluent	RE (%)	WHO (2006)	USEPA (2012)
pH	7.6 ± 0.2	8.3 ± 0.5	-	6.5-8.5	6-9
COD	896.5 ± 102.5	88.3 ± 13	90.2	-	79
BOD_5	410 ± 21.6	23.5 ± 6.0	94.4	30	30
VSS	244.8 ± 74.7	23.5 ± 5.2	90.6	-	30
TSS	280 ± 61.3	29 ± 5.3	89.6	30	30
EC	949.5 ± 52.4	1044 ± 25	-	-	1000
TN	55.6 ± 01.7	51.3 ± 1.8	7.7	15	10
TP	7.63 ± 0.62	7.23 ± 0.6	5.2	2	1
TOC	430.3 ± 30.7	76.3 ± 18	82.3	30	100
$NH_4^+ - N$	25.06 ± 2.7	36.8 ± 6.5	-	0.5	0.2-4
$NO_3^- - N$	40.21 ± 3.1	11.57 ± 2.5	72.5	9	3-10
$PO_4^{-3} - P$	14.47 ± 2.4	8.5 ± 1.2	42.8	5	2

All values presented mean (n=3) ± SD in mg L^{-1} except electrical conductivity (µs cm^{-1}), n-replicate experiments, RE, Removal Efficiency

3.3.1.4 Analysis of Total Phosphorus, Nitrogen, and Carbon

Phosphorus is a key constituent in wastewater effluents, and its monitoring is essential as discharge limits become increasingly stringent [125]. In this study, the mean total phosphorus (TP) concentration exceeded the permissible limits set by WHO and USEPA (Table 2.3), suggesting that conventional biological treatment at KMWWTP is ineffective, possibly due to the limited phosphorus uptake of microbial biomass [126]. Effluent TP standards depend on site sensitivity; for instance, the EU specifies 2 mg L^{-1} for plants serving 10,000 -100,000 population equivalent (PE) and 1 mg L^{-1} for larger facilities, with at least 80% removal efficiency [125]. Recent studies [127] indicate that such stringent standards are promoting the adoption of advanced phosphorus removal technologies.

Similarly, total nitrogen (TN) concentrations exceeded WHO and USEPA limits, decreasing marginally from 55.6 ± 1.7 mg L^{-1} in influent to 51.3 ± 1.8 mg L^{-1} in effluent, indicating poor nitrogen removal efficiency. Elevated TN, composed of organic, ammonium, and nitrate forms, contributes to eutrophication and water quality degradation[128,31]. Total organic carbon (TOC) results also indicated persistent organic pollution after treatment.

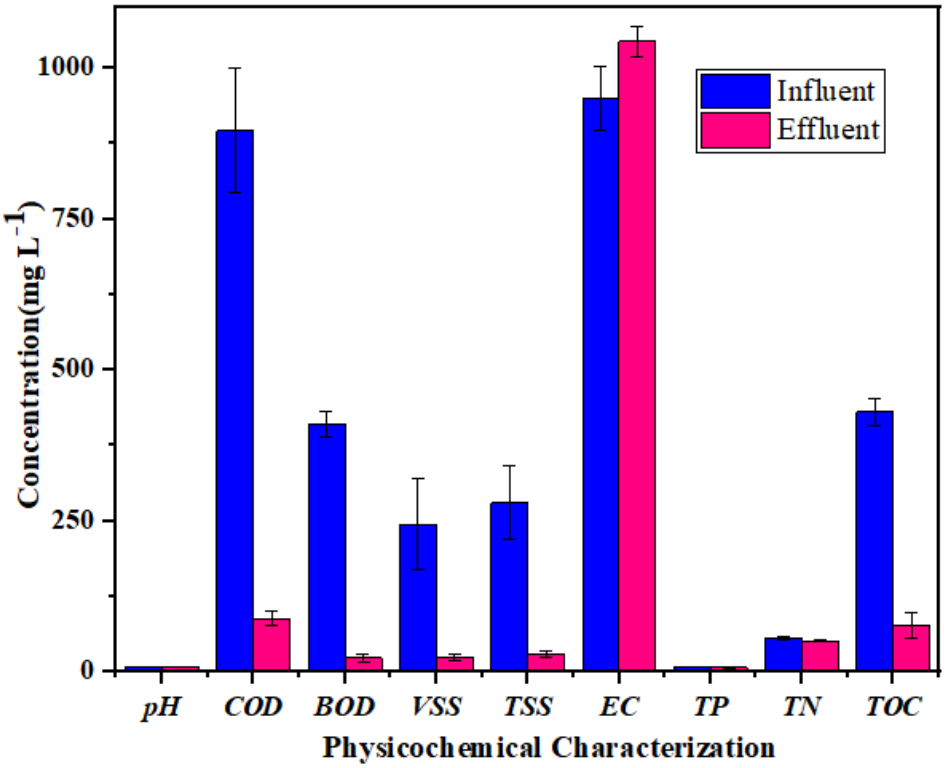

Figure 3.2 Physicochemical characterisation of Kality Municipal WWTP.

3.3.1.5 Heavy Metal Levels in Influent and Effluent Samples

Table 3. 4 and Figure 3. 3 present the concentrations of selected heavy metals (Mn, Fe, Ni, Cu, Zn, Cd, Hg, Pb, As, Cr, and Se) detected in both influent and effluent samples. The average concentrations in influent ranged from 0.002 to 1.95 mg L^{-1}, while effluent values varied between 0.004 to 0.72 mg L^{-1}. Except for iron and zinc, all heavy metals exceeded the maximum permissible limits recommended by the WHO and the USEPA. Although wastewater treatment is designed to reduce metal concentrations, metals such as Ni, Cd, Pb, and As can appear higher in the effluent in the influent. This is primarily due to desorption from sludge particles, transformation into more soluble chemical forms, and corrosion of system components, all of which release additional metals into the water. Such increases do not necessarily indicate treatment failure but reflect the dynamic behavior of metals within the system, highlighting the need to consider both chemical transformations and operational factors when evaluating treatment efficiency. Arsenic, which occurs in both organic and inorganic forms, is particularly difficult to remove and often accumulates in treatment plants [129].

Among the analysed metals, Fe was the most abundant, with mean concentrations of 1.95 mg L^{-1} in influent and 0.72 mg L^{-1} in effluent- below the USEPA effluent limit (1.03 mg L^{-1}), but higher than the surface water guideline (0.07 - 0.3 mg L^{-1}). Similar findings were reported by

Agoro et al. [115] in South Africa and Bahiru [130] in central Ethiopia. Elevated Fe levels may cause soil acidification and nutrient depletion, while excessive human intake can lead to tissue damage, anaemia, and neurological effects [131].

The mean Pb and As concentrations in influent and effluent were 0.065 – 0.073 mg L^{-1} and 0.025 – 0.033 mg L^{-1}, respectively, both exceeding WHO (0.01 mg L^{-1}) and USEPA (0.015 mg L^{-1}) limits. These values were also higher than those reported in Kenya (0.0153 mg L^{-1}) [132]. Lead and arsenic are highly toxic, causing neurological, metabolic, and carcinogenic effects even at trace levels. Other significant metals included Zn and Ni, with influent and effluent concentrations of 0.40 – 0.17 mg L^{-1} and 0.01 – 0.02 mg L^{-1}, respectively. Ni levels exceeded standard limits, whereas Zn remained below threshold values. Nonetheless, both can bioaccumulate and pose ecological and health risks- Ni being linked to dermatitis, organ damage, and cancers, and Zn toxicity affecting aquatic organisms [133,135].

Overall, the results highlight the inefficiency of the treatment system in fully removing heavy metals and underscore the need for strict discharge control, regular monitoring, and improved treatment processes to mitigate potential environmental and health impacts.

Table 3.4: Heavy metal analysis and percentage removal from the Kality Municipal WWTP.

Heavy metals	**Heavy metals Concentration (mg L^{-1}) (n=3)**				
	Influent	**Effluent**	**% RE**	**WHO Limit**[134]	**USEPA** [141]
Mn	0.640 ± 0.08	0.630 ± 0.03	2	0.4	0.05
Fe	1.950 ± 0.02	0.720 ± 0.04	63	2	1.03
Ni	0.010 ± 0.06	0.020 ± 0.01	-	0.02	0.013
Cu	0.130 ± 0.03	0.120 ± 0.01	8	0.25	0.2
Zn	0.400 ± 0.07	0.170 ± 0.02	56	3.00	2.00
Cd	< 0.002	0.004 ± 0.00	-	0.003	0.005
Hg	0.032 ± 0.02	0.030 ± 0.01	6	0.001	0.003
Pb	0.065 ± 0.01	0.073 ± 0.01	-	0.05	0.015
As	0.025 ± 0.02	0.033 ± 0.01	-	-	0.05
Cr	0.019 ± 0.012	0.011 ± 0.01	42	0.05	0.01
Se	0.085 ± 0.06	0.072 ± 0.01	15	0.01	0.02

All values presented mean (n=3) ± SD in mg L^{-1} except removal percentage, n-replicate experiments, RE, Removal Efficiency

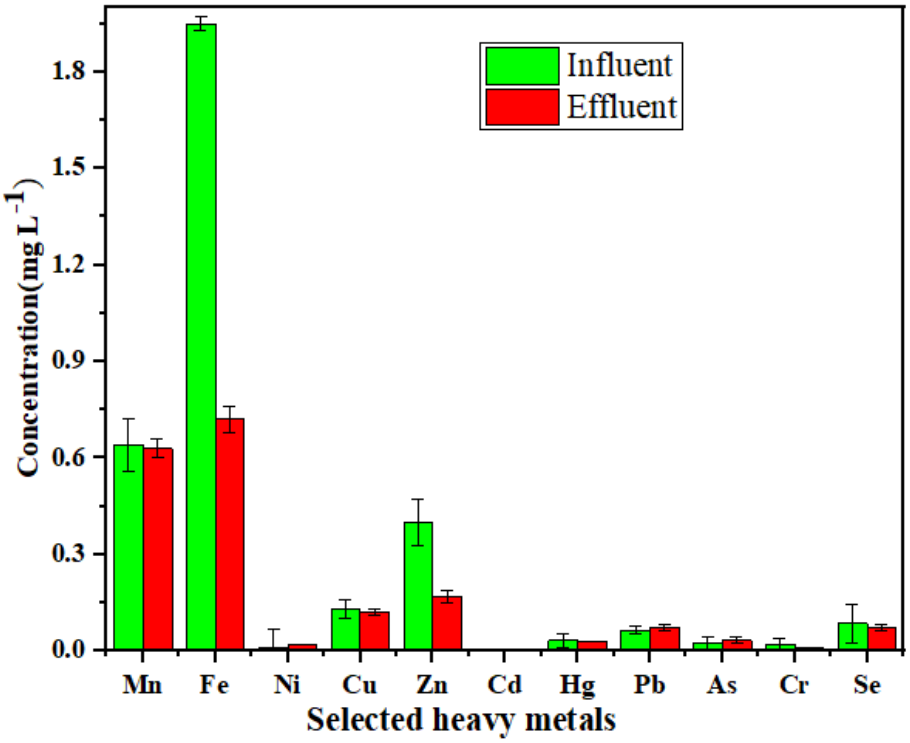

Figure 3.3 Selected heavy metals analysis from Kality MWWTP.

3.3.2 Analysis of Emerging Contaminants

3.3.2.1 Identification of Emerging Contaminants from KMWWTP

Emerging contaminants (ECs) in Kality Municipal WWTP were identified using mass spectrometry (MS) by detecting specific mass – to – charge (m/z) values of targeted compounds: amoxicillin (m/z 377), ciprofloxacin (m/z 33), carbamazepine (m/z 231), caffeine (m/z 149), ibuprofen (m/z 209), diclofenac (m/z 305), and tetracycline (m/z 409) Figure 3.4. The mass spectra of influent and effluent samples were nearly identical Figure 4b,4d; Table S1, figure S3, indicating that the WWTP was largely ineffective at removing ECs, consistent with reports that conventional treatment plants poorly remove persistent pollutants like carbamazepine and ciprofloxacin [137,138]. Other detected compounds included acetaminophen (m/z 117), metoprolol (m/z 158), sulfamethoxazole (m/z 247), phenol (m/z 133), and clozapine (m/z 177), with caffeine (m/z 149) being the most abundant.

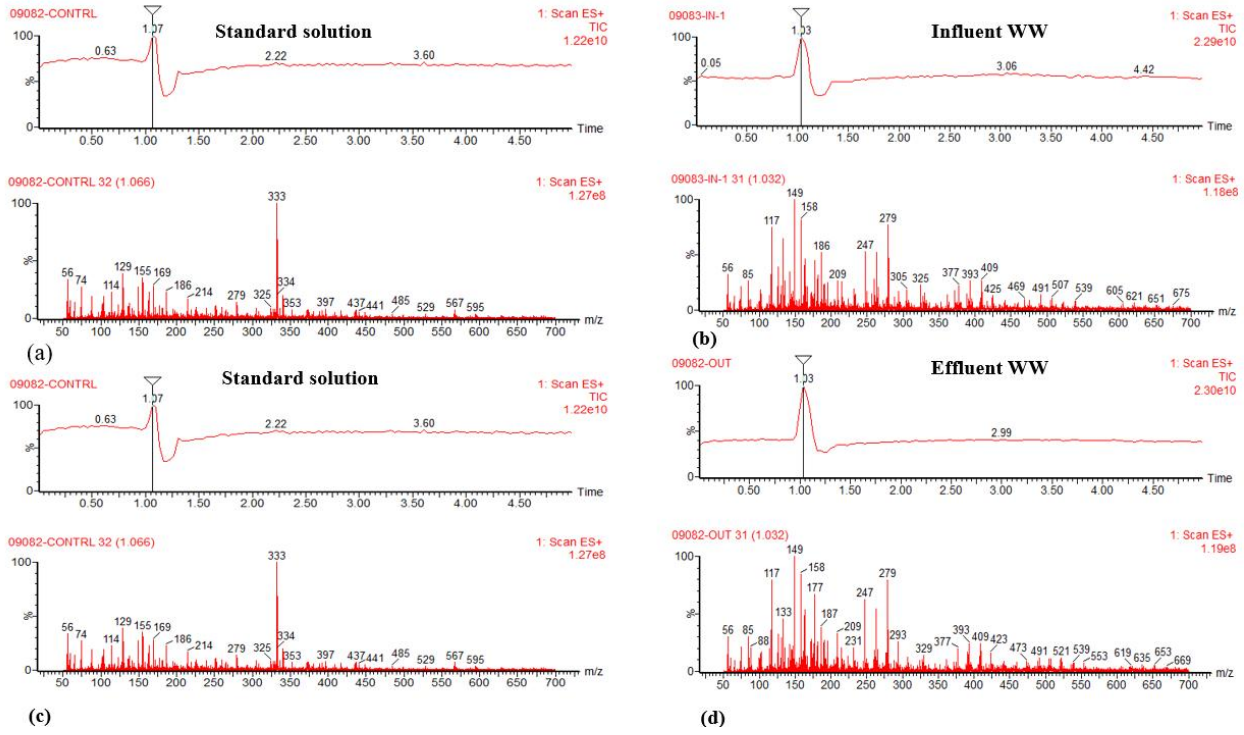

Figure 3.4 LC-MS/MS analysis (a, c) Standard solution of each 10mg L^{-1} amoxicillin, ciprofloxacin, and tetracycline, (b) influent; (d) effluent from Kality municipal wastewater. LC-MS Conditions: ESI (+/-), Source Tem: 150, Capillary voltage: 4 kV, Cone Voltage: 40V, Mass range: 50-500, Column: BEH 2.1(2.7X50mm 1.8um), Column Tem: 40, Flow:0.2mL/min mobile phase: 0.1% formic acid: MeOH (2:8) for amoxicillin, 70% is 1% formic acid 30% of acetonitrile for others.

3.3.2.2 Quantification of Selected Organic Pharmaceutical Compounds

The average concentrations of pharmaceutical compounds in the Kality municipal wastewater effluent are shown in Table 3.5. All targeted pharmaceuticals were detected, with Ibuprofen being the highest (8.21 µg L^{-1}), followed by Amoxicillin (2.54 µg L^{-1}) and Ciprofloxacin (2.43 µg L^{-1}), while Carbamazepine (0.82 µg L^{-1}) and Caffeine (1.24 µg L^{-1}) were lowest. These findings indicate that antibiotic and non-steroidal anti-inflammatory drugs persist at significant levels, reflecting the plant's limited removal efficiency. Seasonal, regional, and socioeconomic factors affect pharmaceutical concentrations, which are typically higher in winter[139,140]; this study was conducted in winter.

Municipal WWTPs, while effective at removing biodegradable carbon, nitrogen, phosphorus, and pathogens, are largely ineffective against persistent micropollutants, resulting in

continuous discharge into aquatic environments [141,142]. Additional treatment processes at KMWWTP are therefore needed to reduce these emerging contaminants Table 3.5.

Table 3.5: Average values of selected pharmaceutical pollutants reported by previous studies.

Pollutants	Present study Kality WWTP	US EPA Recommended Value [134]	WHO recommended value [135]	Previous study [143,136]
Amoxicillin	2.54 ± 0.01	1.0	0.1	1.2
Ciprofloxacin	2.43 ± 0.03	1.0	0.1	0.6
Carbamazepine	0.82 ± 0.01	70.0	10	0.9
Caffeine	1.24 ± 0.06	400.0	70	46.7
Ibuprofen	8.21 ± 0.12	120	10	3.1
Diclofenac	1.86 ± 0.02	1	0.1	0.833

All present work values presented mean (n=3) ± SD in µg L^{-1}, others also describe an average value in µg L^{-1}

Table 3.6: Concentrations and ranges in (µg L^{-1}) of treated effluent from large-scale WWTPs in different areas.

Target ECs	present research	Literature Values			
		Asia	North America	European	References
Amoxicillin	2.54	1.67	0.18	0.19	[7,145]
Ciprofloxacin	2.43	1.52	0.62	1.69	[7,145]
Carbamazepine	0.82	0.90	0.55	0.60	[7,143]
Caffeine	1.24	4.35	5.76	3.90	[37,146]
Ibuprofen	8.21	22.71	11.23	18.6	[7,137]
Diclofenac	1.86	1.14	0.36	0.16	[38,45]

Among the analysed pharmaceutical compounds, ibuprofen, amoxicillin, ciprofloxacin, and diclofenac showed the highest concentrations in the KMWWTP effluent. Compared with wastewater from the USA, Europe, and Asia Table 3.6, Figure 3.5, concentrations in Kality MWWTP were higher [148], likely due to frequent prescriptions in Addis Ababa and differences in treatment technologies. In contrast, caffeine, though not a medicinal, was prevalent due to widespread coffee and soft drink consumption [147]. Pharmaceutical

discharges from WWTPs vary with consumption patterns, treatment design, and operation conditions [48].

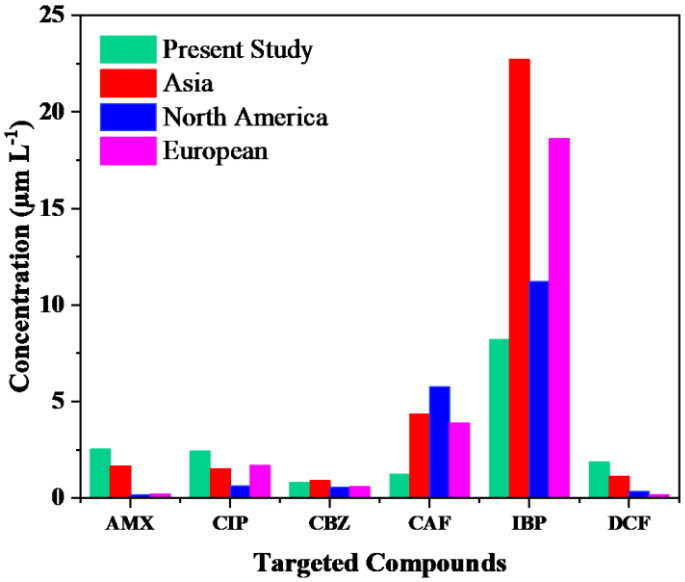

Figure 3.5 Regional comparison of target pollutants in WWTP effluents [144,148].

3.4 Conclusions

This study evaluated the performance of the Kality Municipal Wastewater Treatment Plant (KMWWTP) through a physicochemical assessment of key wastewater quality parameters, including COD, BOD, TSS, TOC, TP, TN, and VSS. Targeted pharmaceutical residues were also identified and quantified in both influent and effluent samples. The results revealed that all investigated pharmaceuticals were detected in the effluent, with concentrations ranging from 0.82-8.21µg L^{-1}. The average concentrations of Mn, Ni, Cu, Cd, Hg, Pb, As, and Se in the wastewater effluent exceeded the permissible limits set by the World Health Organisation (WHO) and the United States Environmental Protection Agency (US EPA). Overall removal efficiencies for nutrients, heavy metals, and emerging pollutants were below 50%. Notably, Ni, Cd, Pb, and As exhibited higher average effluent concentrations than influent levels, indicating inadequate treatment efficiency. These findings suggest that municipal WWTP effluents are a major source of aquatic pollution due to residual heavy metals, nutrients, and pharmaceuticals. Therefore, incorporating an additional tertiary treatment stage is essential. The data generated in this study provides baseline information for future investigations on emerging pollutants and their ecological and toxicological impacts on downstream irrigation and the aquatic system.

CHAPTER FOUR

Response Surface Methodology-Based Optimisation of Triple KBN-Doped TiO_2 Synthesis Parameters for Ciprofloxacin Degradation

Abstract

The Box–Behnken design (BBD), a type of response surface methodology, was employed to determine the optimal parameters for synthesising active visible light-modified doped KBN-TiO_2 via the sol-gel process. The boron-to-titanium molar ratio, calcination temperature, and calcination time were considered as the synthesis parameters, with the doping molar ratios of potassium and nitrogen held constant. The crystalline structure, specific surface area, morphology, and optical properties of the synthesised photocatalyst were examined using X-ray diffraction, Brunauer–Emmett–Teller analysis, scanning electron microscopy, ultraviolet-visible spectroscopy, and Fourier-transform infrared spectroscopy. The performance of the synthesised photocatalyst was evaluated through ciprofloxacin degradation. A test of 15 samples showed varying photoactivity performance under visible light conditions. Furthermore, analysis of variance was applied to investigate the influence of the synthesis parameters on the surface area and ciprofloxacin degradation efficiency. The calcination temperature and boron concentration strongly influenced the surface area, photoactivity, and crystal phase composition of the synthesised photocatalysts. Regression analysis and model adequacy tests revealed that the quadratic model equations provided an excellent fit with the findings. Strong agreement was observed between the model predictions and actual experimental results, with surface area and ciprofloxacin degradation showing variability of 98.60% and 99.44%, respectively. The optimal BBD-based experimental values were 66.476 $m^2\ g^{-1}$ surface area and 84.3% ciprofloxacin degradation under a B/Ti of 5%, a calcination temperature of 500°C, and a calcination time of 2.5 h. Finally, TiO_2 and modified TiO_2 were synthesised under optimal conditions, and their physical and chemical characteristics were evaluated.

4.1 Introduction

Response surface methodology (RSM) is a statistical approach used to explore the correlations between multiple explanatory variables (factors) and one or more response variables [148, 149]. It combines experimental design, regression analysis, and optimisation techniques to enhance or optimise the performance of a process or product [150]. By enabling a detailed understanding of how various factors affect the response variable, including the interaction effects at different levels, RSM provides a robust framework for process optimisation [150]. It is an effective strategy for optimising complex processes more conveniently, significantly reducing costs, labour, and time[151]. One specific type of RSM, the Box–Behnken design (BBD), is used to develop second-order response models and highly effective response surface designs, providing insights into the impact of experimental variables and associated errors in the fewest possible runs [162]. BBD combines efficiency, practicality, and accuracy, making it a valuable choice for response surface optimisation studies. Furthermore, unlike other statistical methods such as central composite design (CCD) and full factorial design analysis, BBD requires fewer experimental runs and eliminates extreme combinations (e.g., highest and lowest values), which can lead to unreliable results [4,152].

Among photocatalytic semiconductors, titanium dioxide (TiO_2) is a promising material widely used as a heterogeneous photocatalyst [153]. Its main applications include organic and inorganic pollutant degradation [154], microorganism inactivation in water, wastewater [155], and air, and dye degradation [156]. TiO_2, an n-type semiconductor, is commonly used as a photocatalyst due to its high oxidising activity, low cost, non-toxicity, availability, biological safety, photostability, and flat band potential [148-158]. The rutile and anatase polymorphs of TiO_2 are reported to have band gap values of 3.0 eV and 3.2 eV, respectively [158], with anatase TiO_2 exhibiting superior photocatalytic activity. Despite rutile TiO_2 having a narrower band gap, the anatase phase is preferred for its lower recombination of photogenerated electron–hole pairs and higher reduction potential. Most significantly, its catalytic capability enables frequent application over time [11,158]. However, a fundamental limitation of TiO_2 is that it can only be stimulated by UV light, which accounts for just 3–5% of the solar energy reaching the Earth's surface due to its high energy band gap (3.2 eV) [106]. Furthermore, the high recombination rate of radicals has been identified as another factor limiting its practical application in industrial settings. Modifying the TiO_2 photocatalyst structure with foreign

elements could reduce its band gap energy and expand the visible region's absorption, potentially enhancing photocatalytic efficiency [159].

Doping the TiO_2 lattice with metal and non-metal atoms reduces the electron–hole recombination and narrows the energy band gap, thereby enhancing its reactivity to sunlight [160,161]. Numerous studies have demonstrated that doping TiO_2 with metal and non-metal elements, such as Fe [162], N [170], B [163], C[164], and K [165] can extend its absorption spectrum into the visible light region. Furthermore, co-doping with multiple metal and non-metal elements, such as N and C [164], N and B [165,166], Cu and K [167], and KBN [168 ,169] has been shown to improve photocatalytic performance by reducing carrier charge recombination. The ionic radius of N atoms closely matches that of O atoms in the TiO_2 lattice, causing the N2p orbital to merge with the O2p states [169]. This alters the electron configuration of the valence band, enabling easier charge carrier transfer. Additionally, B atoms, similar to N atoms, can replace O atoms in the TiO_2 lattice, reducing the band gap. Xinyu et al. [170] found that the surface was changed by a K^+ layer of passivation that partially crystallised TiO_2, increasing the photocatalytic degradation efficiency for methylene blue under both visible and UV light. More recently, Dapeng et al. [171] developed a Titania photocatalyst capable of functioning under visible light through co-doping with boron and nitrogen. The photocatalyst activity was evaluated via phenol degradation, revealing that co-doping with boron and nitrogen significantly reduced the band gap and enhanced photocatalytic performance. Similarly, Zhang et al. [172] reported that TiO_2 co-doped with boron and nitrogen exhibited superior photocatalytic activity compared to undoped TiO_2 under visible and UV light. This enhancement was attributed to its narrower band gap, which effectively suppressed photo-generated electron–hole recombination.

Metal- and non-metal-doped TiO_2 can be synthesised using various techniques, including implantation, sputtering, ball milling, hydrothermal, and sol-gel methods [173]. The sol-gel process is often considered more advantageous than other alternatives [174], owing to its low-temperature requirements, cost-effectiveness, and ease of controlling dopant levels and crystal size without the need for specialised equipment [157]. The doping of non-metals during the sol-gel process is influenced by several synthesis factors, including the type and amount of dopant, solvent, solution pH, calcination temperature, and calcination time [166]. These parameters significantly affect dopant incorporation and properties of the final nanoparticle. Previous studies have focused on the impact of sol-gel synthesis parameters on KBN-doped

TiO_2 preparation, typically employing a one-factor-at-a-time method [176]. Despite being widely accepted, this method has a drawback in evaluating the effect of interaction components and lacks predictive potential. While TiO_2 photocatalysts have been extensively studied for air and water purification, less attention has been dedicated to their use in removing emerging pollutants from municipal wastewater [177]. Recently, some researchers investigated metal and non-metal doping for transforming emerging pollutants into less harmful compounds [178].

In light of this, the current study focused on the following objectives: a) the synthesis and characterisation of modified KBN-TiO_2 photocatalysts; b) evaluation of the effectiveness of the synthesised KBN-TiO_2 for ciprofloxacin (CIP) degradation; c) optimisation of the operating conditions for synthesising the modified KBN-TiO_2 nanomaterials; and d) assessment of modified TiO_2's effectiveness in degrading CIP in different water matrices. The study considered the boron-to-titanium (B/Ti) molar ratio, calcination time, and calcination temperature as operating parameters for synthesising modified KBN-TiO_2, while specific surface area (S_{BET}) and CIP degradation efficiency under visible light were selected as response variables. This study highlights the potential of modified KBN-TiO_2 as a sustainable solution for emerging organic contaminants, offering new opportunities for addressing environmental challenges.

4.2 Experimental

All chemicals used in the experiments were of reagent grade and did not require further purification. KBN triple-doped TiO_2 nanoparticles were synthesised using potassium nitrate (KNO_3, 99%), boric acid (H_3BO_3, 99.5%), ammonia (NH_3, 28%), titanium tetra-isopropoxide ($C_{12}H_{28}O_4Ti$, 97%), absolute ethanol (C_2H_5OH, 99%), and ciprofloxacin ($C_{17}H_{18}FN_3O_3$, 99 %). All chemicals were purchased from Sigma-Aldrich (Greece and the Republic of Korea).

4.2.1 Synthesised catalyst

The BBD approach was adapted to synthesise KBN-TiO_2 using the sol-gel method, with specific amounts of boric acid (H_3BO_3) (2wt.%, 5wt.%, and 8wt.%: B-Ti) and potassium nitrate (KNO_3) (2wt.% % K-Ti). The required quantities of potassium nitrate and boric acid were dissolved separately in a mixture of 10 mL of absolute ethanol and 3 mL of water, and sonicated in an ultrasonic bath for 30 min to form Solutions 1 and 2, respectively. Subsequently, 17 mL of titanium (IV) isopropoxide was slowly added to 47 mL of anhydrous ethanol, followed by 14 mL of ultrapure water (UPW), under vigorous stirring to form Solution 3. Solutions 1 and

2 were then slowly added dropwise to Solution 3, and the required amount of ammonia (NH_3) was gradually introduced into Solution 3 (5wt.% N-Ti). After being aged for 24 h at room temperature to promote hydrolysis, the mixture was dried in an oven set at 50 ℃ to remove the solvents. The resulting product was ground and calcined in a muffle furnace with air heating at a rate of 5 ℃ per minute. Three calcination times (2, 3, and 4 h) and three calcination temperatures (300, 400, and 500 ℃ were used. A total of 15 experimental runs were performed using BBD. After optimisation, both doped and undoped samples were synthesised using the optimised parameters. In this case, x, y, and z represent the B-Ti molar ratio, calcination temperature, and calcination time, respectively, and the KBN-doped and undoped TiO_2 were labelled as x%B (TiO_2) yz.

4.2.2 Characterisation of synthesised catalyst

The characteristics of the photocatalysts were determined using the following methods: (a) The specific surface area (SSA) was measured via nitrogen physisorption at 77 K on a Micromeritics Gemini III (2375, Norcross, GA, USA) using the Brunauer–Emmett–Teller (BET) method. Before measurement, the sample was outgassed for 2 h at 250 ℃ under a dynamic vacuum. (b) The crystalline structure was analysed through X-ray diffraction (XRD). Powder XRD patterns were obtained using a Brucker D8 Advance (Billerica, MA, USA) equipped with a 40 kV, 40 mA Cu Kα source. Data were collected over a 2θ range of 2º to 85º with step intervals of 0.015º and a scan rate of 0.05º s^{-1}. The phases were identified using JCPDS reference cards. (c) Scanning electron microscopy (SEM) images were captured, and an energy dispersive spectrometer (EDS) integrated with a JEOL 6300 scanning electron microscope (Peabody, MA, USA) was used to examine the materials' elemental distribution and chemical composition. (d) UV-Vis diffuse reflectance spectroscopy (DRS) was employed to evaluate the optical characteristics of the materials. Diffuse reflectance spectra were obtained using a UV-Vis spectrophotometer (Varian Cary 3, 3E Palo Alto, CA, USA) equipped with an integrating sphere and $BaSO_4$ as a reference. Spectra in the 200–800 nm wavelength range were recorded at room temperature after the catalyst powder was placed into a quartz cell. The Kubelka–Munk function was applied to diffuse reflectance, which measures the reflection of light scattered in multiple directions, converting it into equivalent absorption coefficients [179].

$$F = (R_\infty) = \frac{K(\lambda)}{S(\lambda)} = \frac{(1-R_\infty)^2}{2R_\infty} \tag{4.1}$$

where F represents the Kubelka–Munk function, R_∞ indicates the diffuse reflectance of an infinitely thick sample layer, K and S denote the absorption and scattering coefficients, respectively, and λ represents the wavelength of light. The optical band gaps of the semiconductors were determined using the following formula[180]:

$$(\alpha h\nu)^{\frac{1}{n}} = K(h\nu - E_{bg}) \tag{4.2}$$

where α (cm^{-1}) is the absorption coefficient, $h\nu$ (eV) is the incident photon energy, E_{bg} (eV) is the energy of the band gap, K is a variable that depends on the type of optical transition associated with photon absorption, and n is a constant related to the effective masses of charge carriers in the valence and conduction bands. The energy of the band gap (absorption threshold) was determined based on the assumption that the synthesised materials are indirect semiconductors and that $F(R)$ (reflectance to the absorption and scattering coefficients of the material) values are proportional to the optical absorption coefficients, with $n = 2$. The band gap energy values were obtained by plotting $[F(R)\ h\nu]^{1/2}$ against $h\nu$ (Tauc plot) in the region of high absorption and extrapolating the linear region to the horizontal axis at zero $F(R)$. The average crystallite size (designated as D) was determined using Debye–Scherrer's formula, stated as follows [180]:

$$D = \frac{0.9\lambda}{\beta \cos\theta} \tag{4.3}$$

where D denotes the average size of crystallites, λ represents the wavelength of the X-rays used, β indicates the full width at half maximum (FWHM) of the diffraction peak, and θ denotes the diffraction angle. Erlangshen CCD Camera (Gatan Model 782 ES500 W, Pleasanton, California, USA).

4.2.3 An adsorption–photocatalytic degradation experiment

The adsorption and photocatalytic activities of modified KBN@TiO_2 nanomaterials were investigated using CIP as a model antibiotic pollutant in batch adsorption and photodegradation under visible light irradiation, respectively. Typically, 0.25 g L^{-1} of photocatalyst was added to 150 mL of UPW containing 10 mg L^{-1} of CIP. The mixture was then agitated for 15 min in the dark until it attained adsorption–desorption equilibrium. Photodegradation experiments were conducted using an Oriel solar simulator (LCS-100 model), with a 100 W Xenon ozone-free lamp as the light source, producing an incidence intensity of 1.3×10^{-4} Einstein m^{-2} s^{-1}. At predefined intervals, 3 mL samples were collected and filtered using a PVDF Whatman uniflow syringe filter with a polypropylene over-mould housing (0.2 µm, Whatman, UK). CIP

concentration was measured using a Hach DR 5000 portable spectrometer, which measures absorbance at a wavelength of 278 nm. Detailed procedures and additional information are provided in the supplementary material, Fig. S1. The CIP degradation efficiency (R) was calculated using the following equation [153]:

$$R(\%) = \frac{C_0 - C_f}{C_0} \times 100 \quad (4.4)$$

where C_0 and C_f represent the concentrations of CIP before and after adsorption and degradation under visible light irradiation.

4.2.3.1 Box–Behnken experimental design

Experiments were conducted using the BBD approach, with the three primary sol-gel synthesis parameters previously defined. The response parameters were optimised by analysing the effects of individual parameters and their interactions. The factors and their levels are provided in Table 4.1. The variables, namely the B-Ti molar ratio, calcination temperature, and calcination time, were designated as x_1, x_2, and x_3, respectively.

Table 4.0-1: Experimental variables and levels were determined for BBD based on an initial investigation.

Factor Abbreviation	Name of Variables	Units	Factor levels		
			-1 (Low)	0 (Medium)	1 (High)
x_1	x%B/Ti (5%N and 2%K)	Molar ratio	2	5	8
x_2	Calcination Temp	℃	300	400	500
x_3	Calcination Time	h	2	3	4

Based on the BBD method, the total number of experiments (N) can be estimated as follows:

$$N = K^2 + K + CR \quad (4.5)$$

where K represents the number of factors, and CR indicates the central replication point [165]. The 15 experimental runs, arranged according to BBD, are presented in Table 4.2.

Table 4.2: Actual and predicted BBD values for specific area (S_{BET}) and CIP degradation efficiency (R%)

Run	x_1	x_2	x_3	S_{BET} (m^2 g^{-1})		R (%)	
				Actual	Predicted	Actual	Predicted
1	2(-1)	300(-1)	3(0)	69.67	69.76	85.76	84.71
2	8(1)	300(-1)	3(0)	46.01	47.59	54.45	54.43
3	2(-1)	500(1)	3(0)	55.76	54.18	51.23	51.25
4	8(1)	500(1)	3(0)	42.74	42.65	68.32	69.40
5	2(-1)	400(0)	2(-1)	67.77	67.89	82.89	83.45
6	8(1)	400(0)	2(-1)	48.89	47.51	80.55	80.05
7	2(-1)	400(0)	4(1)	58.45	59.83	74.74	75.24
8	8 (1)	400(0)	4(1)	46.63	46.51	77.02	77.55
9	5(0)	300(-1)	2(-1)	65.19	64.98	84.12	84.64
10	5(0)	500(1)	2(-1)	51.35	52.82	88.92	88.34
11	5(0)	300(-1)	4(1)	60.01	58.58	86.12	86.70
12	5(0)	500(1)	4(1)	49.98	50.19	65.02	64.50
13	5(0)	400(0)	3(0)	48.24	48.29	79.45	77.57
14	5(0)	400(0)	3(0)	47.62	48.29	77.02	77.57
15	5(0)	400(0)	3(0)	49.02	48.29	76.24	77.57

x_1: Molar ratio (B to Ti)
x_2: Temperature of calcination (°C)
x_3: Time of calcination (h)

The relationship between the independent variables and the outcome was determined using a second-order polynomial equation. The equation for the three factors is expressed as follows:

$$Y_i = \beta_0 + \beta_1 x_1 + \beta_2 x_2 + \beta_3 x_3 + \beta_{12} x_1 x_2 + \beta_{13} x_1 x_3 + \beta_{23} x_2 x_3 + \beta_{11} x_1^2 + \beta_{22} x_3^2 + \beta_{33} x_3^2 + \varepsilon \quad (4.6)$$

where Y_i (i =1, 2, and 3) represents the responses (S_{BET} (m^2 g^{-1}) and R (%)), β_0 is a constant, x_1, x_2, and x_3, are the independent variables, β_is indicates linear interaction, β_{ii}s represents cross-product interaction, β_{ij}s refers to quadratic interaction, and ε denotes random error. Regression

analysis and coefficient estimation were performed using Design-Expert® version 13.0 (Stat-Ease, Inc.).

4.3 Results and Discussions

4.3.1 Best synthesis conditions for modified KBN@TiO_2 catalyst.

Fifteen experimental runs were performed to evaluate the process's stability and inherent variability based on the BBD. The relationships outlined in Table 4.1 were applied during these experimental runs. The experimental responses were derived from the BET characterisation results and R values listed in Table 4.2. Model analysis revealed high significance for the responses, with F-values of 39.00 for S_{BET} and 98.51 for R, both exhibiting p-values < 0.0001. Additional details, including comprehensive ANOVA results for both selected responses, are provided in Tables S4.1 and S4.2.

The model's adequacy was further investigated by examining the coefficient of determination (R^2) values for the two responses (S_{BET} and R). The R^2 values for surface area (S_{BET}) and CIP degradation efficiency (R) were calculated as 0.9860 and 0.9944, as shown in Tables S4.3 and S4.4, respectively. These results indicate that the models accurately forecast the response parameters within the experimental range, with variability of 98.60% and 99.44%, respectively. Table 4.2 and Figure S4.2 highlight a strong agreement between the predicted and measured values. The predicted R^2 values indicate that the S_{BET} and R model equations provide accurate forecasts, with variability of 76.79% and 95.30%, respectively. Furthermore, the adjusted R^2 values for S_{BET} (96.07%) and R (98.43%) demonstrated satisfactory agreement with the predicted R^2 values, as detailed in Table S3. This level of reliability and accuracy can be attributed to the low coefficient of variation (CV) values, 6.52 for S_{BET} and 1.92 for R. Moreover, the reasonable precision values for the responses were calculated as 19.69 for S_{BET} and 31.71 for R. When considering the statistically significant terms (refer to Tables S4.1 and S4.2 of the supplementary information), all aforementioned values can be altered. Furthermore, 'Prob > F' values of less than 0.05 indicate that the model terms are significant.

The significant variables identified by regression analysis can be considered when developing the quadratic model equations for the two responses, S_{BET} and R, based on actual values, as expressed as follows:

$$S_{BET}(mg\ g^{-1}) = 48.29 - 8.42x_1 - 5.13x_2 - 2.27x_3 + 2.66x_1x_2 + 3.22x_2^2 + 5.11x_3^2 \quad (4.7)$$

$$R(\%) = 77.57 - 3.03x_1 - 4.62x_2 - 5.44x_3 + 12.11x_1x_2 - 6.48x_2x_3 - 8.68x_1^2 - 3.94x_2^2 + 7.42x_3^2 \quad (4.8)$$

The experimental performance of the synthesised photocatalyst was evaluated using a catalyst dose of 0.25 g L^{-1}, an unadjusted pH of 5.65, and a CIP concentration of 10 mg L^{-1}, as shown in Table 4.2. Furthermore, as illustrated in Figure 4.8b, the performance assessment with various operational parameters revealed that the modified KBN-TiO_2 photocatalyst achieved a 99.59% removal efficiency under optimum conditions.

4.3.2 Crystal phase composition

The XRD patterns of the KBN-doped TiO_2 samples, synthesised with varying boron-to-titanium molar ratios (2%, 5%, and 8%) under constant calcination temperature, potassium and nitrogen dopant concentrations, and calcination times, are displayed in Figure 4.1. The crystal phases were effectively characterised using reference card (JCPDS) No. 21-1272 for anatase and No. 96-201-6173 for boron oxide. Notably, the rutile phase does not occur at calcination temperatures below 500 ℃ [148-156]. None of the XRD patterns showed peaks corresponding to nitrogen and potassium. This absence of peaks could be attributed to the uniform distribution of the dopant within the TiO_2 crystal structure, occupying either interstitial or substitution sites. Additionally, the anatase peak became sharper and more intense as the calcination temperature increased from 300 ℃ to 500 ℃, as shown in Figure 4.1. The average crystal size of all samples increased with rising calcination temperature due to enhanced crystallite aggregation at higher temperatures [181]. Compared to the effect of calcination temperature, dopant (boron) concentration significantly influenced the crystal structure and particle size of all samples. However, the findings indicate that calcination time had no noticeable effect on modified TiO_2 for CIP degradation efficiency.

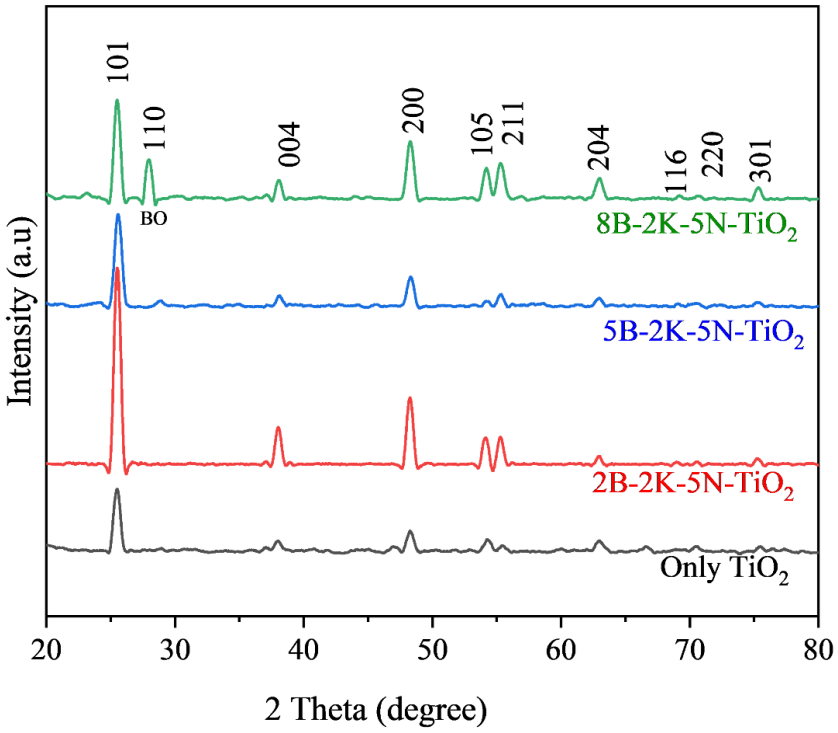

Figure 4.1 XRD patterns of KBN-doped TiO_2 samples calcined at 500℃ for 3 h under a fixed concentration of 5 mol% N and 2 mol% K, with varying B - Ti molar ratio of 2mol%B, 5mol%B, and 8mol%B.

4.3.3 Specific surface area

Figure 4.2 displays the adsorption and desorption isotherms for KBN-doped and undoped TiO_2 under optimal conditions. In general, the S_{BET} of all KBN-doped TiO_2 samples was greater at lower calcination temperatures and smaller at higher calcination temperatures. This trend can be attributed to the expansion of mesopores and the formation of larger pores with increasing calcination temperature and time, as reported by He et al. [182]. Furthermore, as illustrated in Figure 4.2(a), the specific surface area of the synthesised TiO_2 decreased when the boron dopant concentration increased from 2% to 8%, compared to the 2%B dopant concentration. Similarly, Figure 4.2(b) shows a decline in specific surface area with increasing calcination temperature and time.

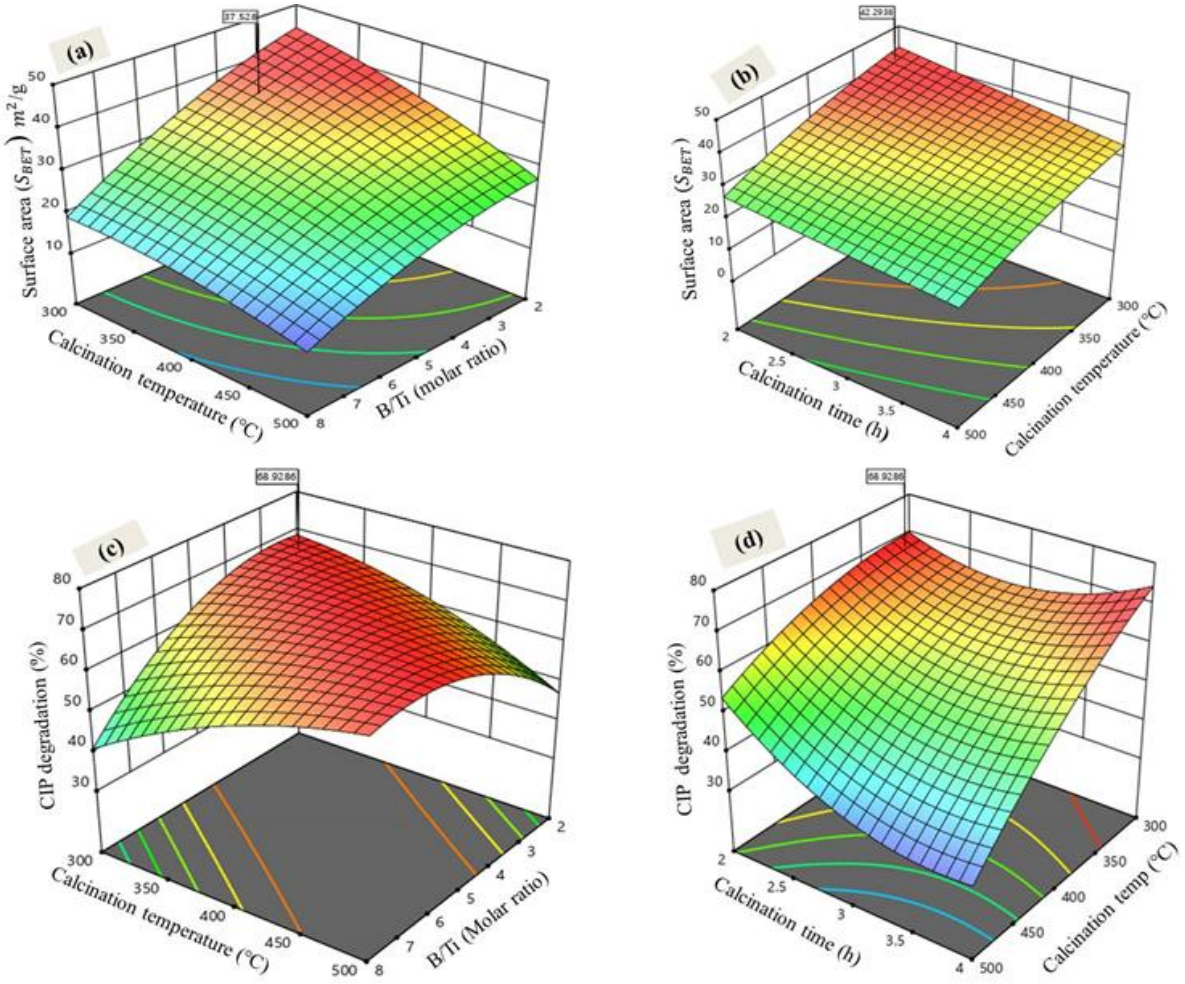

Figure 4.2 Three-dimensional interaction plots showing the effects of (a) calcination temperature and B/Ti molar ratio on surface area, (b) calcination temperature and calcination time on surface area, (c) calcination temperature and B/Ti molar ratio on CIP degradation efficiency, and (d) calcination temperature and calcination time on CIP degradation efficiency for the KBN@TiO_2 system.

4.3.4 Adsorption and photocatalytic degradation tests

All synthesised KBN-doped TiO_2 samples were evaluated for photocatalytic performance under visible light ($\lambda > 400$ nm) in degrading or removing CIP from a synthetic solution. To identify the most effective catalyst among those synthesised under various conditions (calcination temperature, calcination time, and dopant concentration), adsorption and photocatalysis investigations were conducted concurrently, with the results presented in Figure 4 3. The optimal catalyst was determined based on its strong photocatalytic contribution to CIP degradation and minimal adsorption effect.

Figure 4.3a illustrates the adsorption of CIP, achieving a removal efficiency of 75.6% using 2% B-TiO_2 synthesised at 300 ℃ for 3 h, with a high absorbance removal ratio C(t)/C_0 compared to 5%B and 8%B-TiO_2. Additionally, Figure 4.3b shows the significant degradation effectiveness of 2% B-TiO_2, attributed to the combined effects of adsorption and photocatalytic degradation. The adsorption and photocatalytic activity of CIP at 400 ℃ and 500 ℃, respectively, are depicted in Figure 4.3(c–f). As the temperature increases, the photocatalytic degradation of CIP improves. This is likely due to the temperature-induced changes in the crystalline structure and particle size, which enhance photocatalytic activity [182]. However, at temperatures exceeding 500 ℃, a phase shift from anatase to rutile occurs in the KBN-doped TiO_2, which is unfavourable for photocatalysis [183]. As shown in Figure 4. 4a and 4.4b, there was also a slight variation in the calcination times (2, 3, and 4 h) in the CIP photocatalytic degradation experiments (81.4%, 78.8%, and 72.6%, respectively). The primary factors contributing to enhanced photoactivity in this study were the calcination temperature and the amount of boron dopant. Charge recombination, associated with lower crystallinity and extremely small particle sizes, may result in lower photoactivity [184]. The optimal photocatalytic activity of the KBN-doped TiO_2 sample can be attributed to its large specific surface area, boron content (with constant K and N dopants), and enhanced anatase crystallinity.

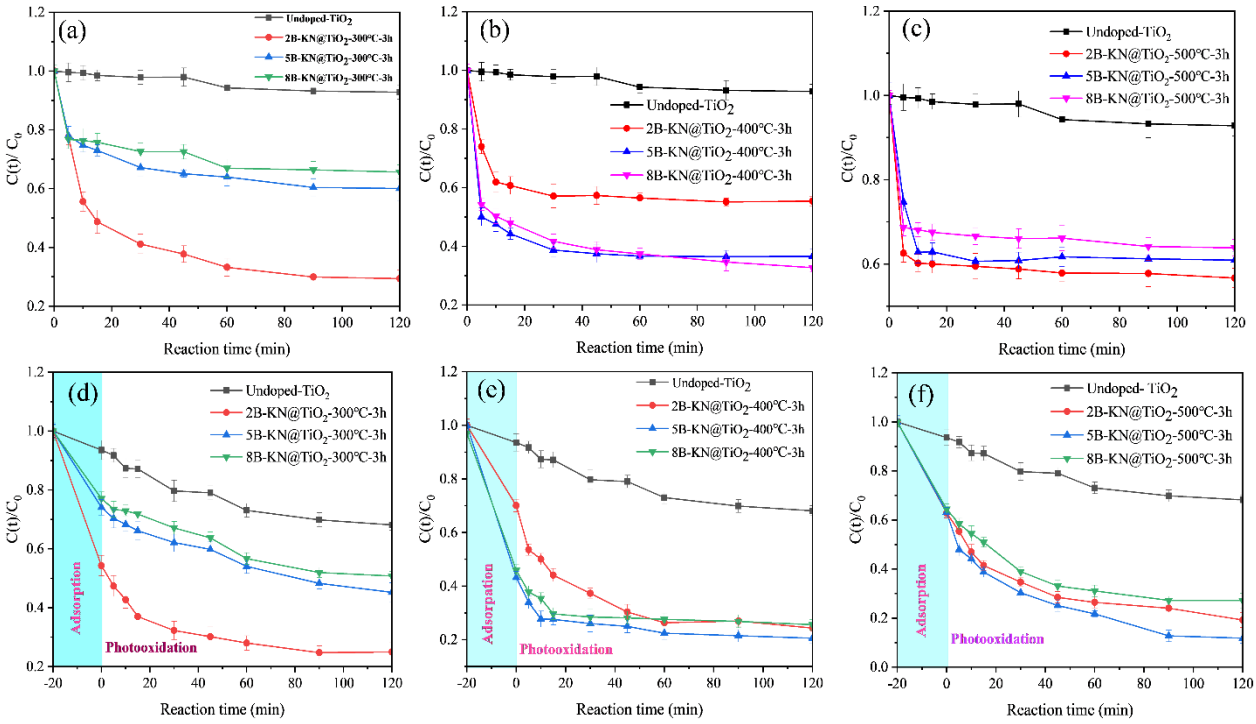

Figure 4-3 Catalyst performance was evaluated through adsorption and photocatalysis at various dopant concentrations and calcination temperatures. Adsorption performance (a, b, and

c) and photocatalytic oxidation performance (d, e, and f) were compared under identical conditions. (Experimental conditions: catalyst dosage = 0.25 g L^{-1}, Initial pH 5.56 (unadjusted), and [CIP] =10 mg L^{-1}).

The 5%B-TiO_2 sample, synthesised at a calcination temperature of 500 ℃ for 2 h, demonstrated the best photocatalytic properties among samples with a constant composition of 2% K-5 % N-TiO_2. This sample was selected for further investigation due to its high CIP degradation efficiency.

4.3.4.1 Effect of B doping on the KN-doped TiO_2

Figure 4.3f illustrates the photocatalytic degradation of CIP solutions under visible light by TiO_2 catalysts with varying boron dopant concentrations. The experiment used 150 mL of a 10 mg L^{-1} CIP solution and a catalyst concentration of 0.5 g L^{-1}. The results indicate that KBN-doped TiO_2 exhibits higher photocatalytic efficiency than undoped TiO_2. The first-order degradation rate constants for 2%B-TiO_2, 5%B-TiO_2, and 8%B-TiO_2 are 0.03885, 0.07813, and 0.06326 min^{-1}, respectively, at a calcination temperature of 500 ℃ and a calcination time of 3h.

Zhang et al. [36,37] reported that under UV light irradiation, the photocatalytic activity of 4% B-doped TiO_2 is 2.87 times greater than that of undoped TiO_2. In the current study, boron doping at a concentration of (5%B-TiO_2) increased the degradation rate from 57.9% to 78.8%, reaching an optimum point before declining to 65.0%. Therefore, 5% boron doping has been identified as the optimal concentration for enhancing the photocatalytic performance of TiO_2. Both synthesis cost and catalyst degradation efficiency were considered while using 5%B-TiO_2 in photocatalytic investigations. Compared to undoped TiO_2, the improved performance of 5%B-TiO_2 can be attributed to its narrower band gap, higher specific surface area, and smaller particle size, as confirmed by XRD, BET, and UV-Vis characterisation. However, some adsorption activity was observed, as illustrated in Figure 4.4a, with the adsorption process reaching saturation after 15–20 min. This finding suggests that the synthesised material primarily functions as a photocatalyst, with CIP degradation or removal predominantly driven by the photocatalytic process rather than adsorption.

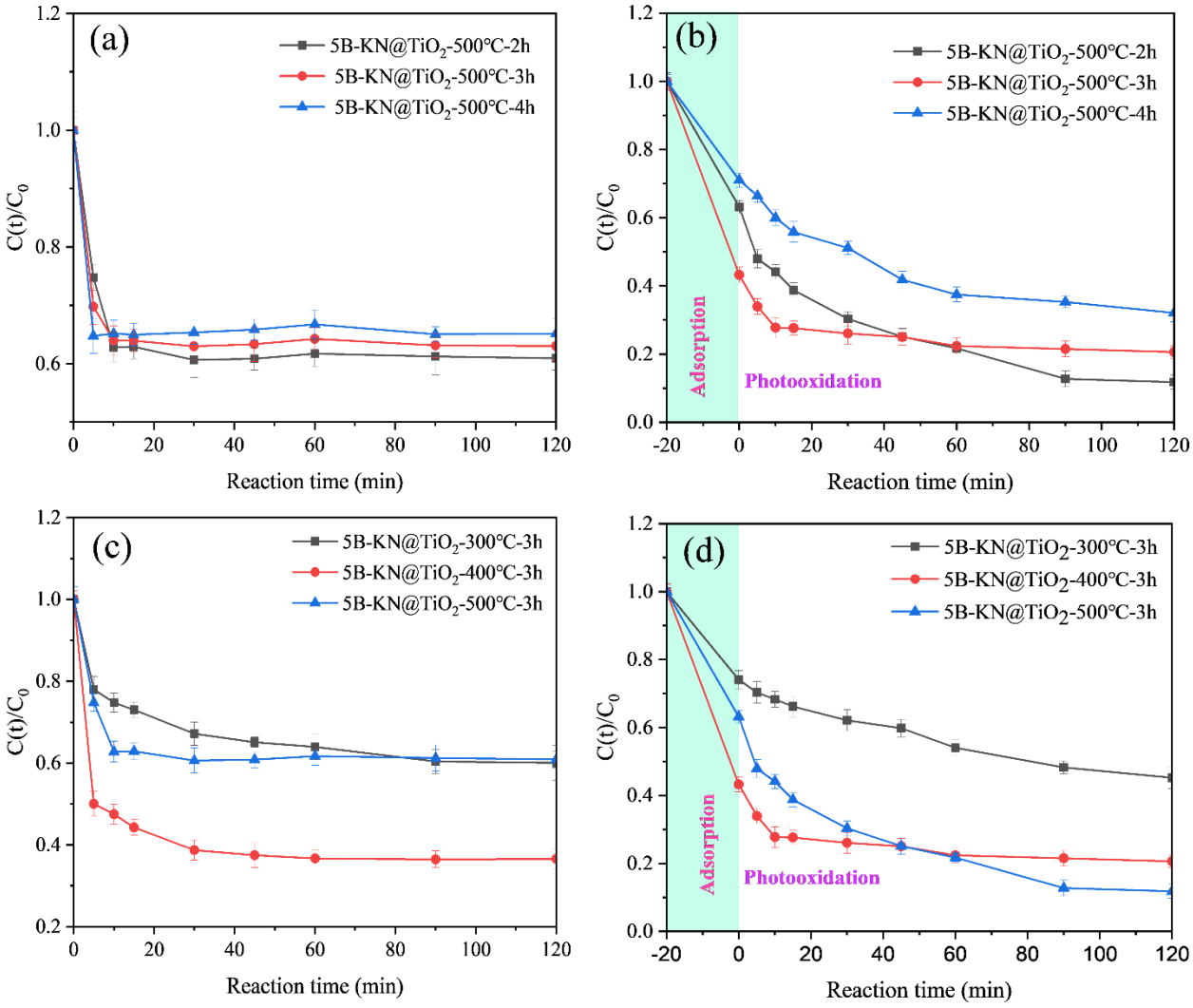

Figure 4.4 Effect of calcination time on (a) adsorption and (b) photocatalytic activity, and Effect of calcination temperature on (c) adsorption and (d) photocatalytic activity of 5%B-doped KN@TiO_2 nanocomposite. (Experimental Condition: $[CIP]_0$ = 10 mg L^{-1}, Catalyst dosage = 0.5g L^{-1}, and pH =5.65 (Unadjusted)).

4.3.4.2 Effect of calcination time and temperature

Figure 4.4b shows photocatalytic activity at different calcination times. However, the calcination time variation does not affect the CIP degradation, and the fitting curves are closely associated. Once calcination is performed at 500 °C, extending the calcination time from 2 to 4 h has no significant effect on degradation. Consequently, a calcination time of 3 h was chosen as the empirical data value. Thus, the 5%B-TiO_2 catalyst, prepared with constant K-N doping by calcination at 500 °C for 2.5 h, was selected for the subsequent experiments. These values

were chosen based on the optimal values of specific surface area and CIP removal efficiency Figure 4. S2.

As shown in Figure 4.4d, the CIP degradation efficiency for the 5%B-TiO_2 photocatalyst reaches 84.8% at a calcination temperature of 500 ℃, demonstrating the highest degradation performance**.** However, when the temperature exceeds 500 ℃, the rutile phase begins to appear, leading to a decline in catalytic efficacy. The experimental results and XRD characterisation confirm the formation of high-activity anatase at 500 ℃. The initial investigation revealed that the degradation rate significantly decreases at 200 ℃ and 700 ℃. At 200 ℃, a brookite phase forms, while at 700 ℃, a rutile phase is formed. Notably, both excessively low and high temperatures negatively impact the photocatalytic activity of 5%B-TiO_2 with constant 2% K and 5% N doping. Specifically, particle sintering occurs at excessively high calcination temperatures [12,22,17].

4.3.5 Model verification and optimisation

The intended set of variables for the sol-gel synthesis was determined by optimising the outcomes of the two quadratic models using the desirability function of the Derringer technique for multiple outcome processes (Eqs. 7 and 8). Consequently, a 0.987 desirability value to anticipate a 100% anatase weight fraction, a 65.276 $m^2\ g^{-1}$ BET surface area, and 84% CIP degradation efficiency led to the selection of a B-Ti molar ratio of 5, a calcination temperature of 500 ℃, and a calcination time of 2.5 h (5BT52.5). The predicted values were likewise confirmed on a sample prepared under optimal conditions Table 4.3. The findings indicate that the fitted model equations for each response can be employed to forecast sol-gel synthesis parameters in similar preparation procedures. Figure S4.3 provides detailed information for model diagnostics.

Table 4.3: Doped and undoped TiO_2 model validation results were established under optimal conditions.

Sample	Crystal phase composition (%)	Crystal size (nm)	S_{BET} ($m^2\ g^{-1}$)	UV-Vis (eV)	R (%)
KBN-TiO_2	100 (WA)	19.0	65.27	2.42	84.3 ± 1.02
Only-TiO_2	86.2 (WA)	17.4	50.34	3.21	14.7 ± 0.8

Note: WA: anatase weight percentage, S_{BET}: BET specific surface area, R: ciprofloxacin degradation efficiency, UV-Vis: optical property (band gap energy), experimental conditions [CIP] = 10 mg L^{-1}, catalyst dose = 0.25 g L^{-1}, natural pH = 5.65, and reaction time = 120 min.

4.3.6 Characterisation of the synthesised catalyst under optimum conditions.

4.3.6.1 XRD Analysis

Figure 4.5a displays the XRD patterns of the synthesised photocatalysts, KBN-TiO_2 and BN-TiO_2. According to the American Society for Testing and Materials (ASTM) 21-1272 anatase card, there was little difference between the modified sample and anatase TiO_2. Trace amounts of the rutile phase were observed in the undoped TiO_2 samples. However, doping with N, K, and B inhibited rutile formation. The XRD patterns of the boron-doped TiO_2 samples revealed a single, weak peak at approximately 27.8˚, corresponding to the presence of B_2O_3 on the TiO_2 surface [197]. Compared to the undoped condition and other doping ratios, the most noticeable <101> peak of anatase appeared broader in the KBN-TiO_2 samples, suggesting a reduction in particle size. At a boron weight percentage of 8%, the B_2O_3 phase begins to form, consistent with the XRD results shown in Figure 4.1. This indicates that the doped boron ions separate and form a layer of B_2O_3 outside of the anatase structure.

The XRD patterns of KBN-TiO_2 and BN-TiO_2 samples are displayed in Figure 4.5a. The anatase phase of TiO_2 is characterised by a strong peak at approximately 25°, designated as (101). Other peaks, including (004), (200), (105), (204), (211), (116), and (312), are indicative of a well-crystallised anatase structure in KBN-TiO_2, with prominent and sharp peaks suggesting high crystallinity. The BN-TiO_2 sample exhibits similar peaks, although at lower intensities, which suggests that potassium may enhance the KBN-TiO_2 sample's crystallinity or more effectively sustain the anatase phase. Compared to the BN-TiO_2 sample, the (103) and (112) peaks in the KBN-TiO_2 sample are sharper and more intense, indicating fewer defects, larger crystallite sizes, and higher crystallinity in KBN-TiO_2 [170]. The improvement is most likely due to the presence of potassium in KBN-TiO_2, which enhances the stability of the anatase phase and promotes crystal growth [44]. Overall, the higher peak intensities in KBN-TiO_2 indicate larger crystallite sizes or improved crystallinity. The anatase phase of TiO_2 is represented by peaks in both samples, although KBN-TiO_2 seems to be more crystalline. Both KBN-TiO_2 and BN-TiO_2 primarily exhibit the anatase phase, as indicated by the XRD patterns in Figure 4.5a, with no noticeable peaks suggesting the presence of rutile or brookite phases. Supplementary data for undoped TiO_2 and doped KBN@TiO_2 are also provided in Tables S4.5 and S4.6.

4.3.6.2 FT-IR Analysis

Fourier-transform infrared (FT-IR) spectra of undoped and KBN-TiO_2 samples are presented in Figure 4.5b. Peaks around 3425 and 1632 cm^{-1} correspond to the bending and stretching modes of the catalyst's surface hydroxyl groups and adsorbed water, respectively [182]. A strong band between 400 and 500 cm^{-1}, particularly at 427 cm^{-1}, is attributed to the Ti–O–Ti stretching vibration. This peak, consistent across all samples, shows the basic TiO_2 structure [164]. Other functional groups identified in Figure 4.5b include Ti–O stretching or O–Ti–O bending vibrations, O–H, and C≡N at 811, 1632, and 2158 $cm^{-1,}$ respectively. Notably, the BN- and KBN-doped TiO_2 samples exhibit a new peak at 1395 cm^{-1}, attributed to the introduction of B-N atoms into the TiO_2 lattice structure, which is absent in pure TiO_2 [185]. The Brunauer–Emmett–Teller (BET) surface area measurements Figure 4.5c showed that pure TiO_2 possessed a specific surface area of 50.34 $m^2\ g^{-1}$**,** whereas the KBN@TiO_2 composite synthesised under optimised conditions exhibited an increased surface area of 65.27 $m^2\ g^{-1}$**,** reflecting the beneficial effect of KBN triple-doping on pore development and particle dispersion.

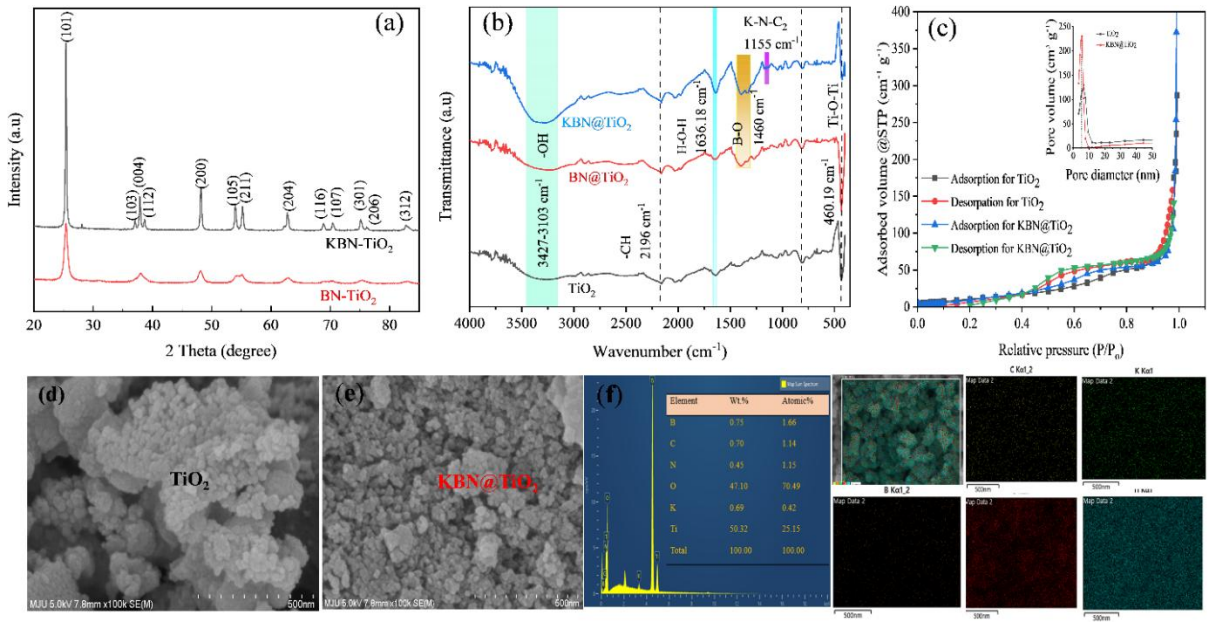

Figure 4.5 Characterisation of the optimised synthesised samples: (a) X-ray diffraction (XRD) patterns of BN-TiO_2 and KBN-TiO_2, (b) FT-IR spectra of TiO_2, BN@TiO_2 and KBN@TiO_2, (c) N2 adsorption-desorption isotherms (BET), (d) SEM image of Only TiO_2, (e) SEM image of KBN@TiO_2, and (f) SEM-EDX elemental mapping of KBN@TiO_2.

4.3.6.3 SEM Analysis

Figure 4.5d and Figure 4.5e display the SEM images and elemental mapping of undoped TiO_2 and KBN-TiO_2, respectively. The SEM micrographs reveal that the prepared photocatalysts consist of agglomerated particles. The elemental composition of the 2% K-5 % B-5 % N-TiO_2 sample, as determined by EDX analysis, is presented in Table S4.8. The EDX results indicate that the undoped TiO_2 microstructure consists entirely of TiO_2, with Ti and O comprising 35.31 wt.% and 64.69 wt.%, respectively. For the KBN-doped TiO_2 sample, the analysis revealed elemental compositions of 50.32 wt.% Ti, 47.10 wt.% O, 0.75 wt.% B, 0.45 wt.% N, and 0.69 wt.% K, as shown in Table S4.8. Images of elemental mapping on KBN-TiO_2 nano-catalyst are displayed in Figure 4.5f. The consistent dispersion of Ti, O, K, B, and N elements throughout the sample is evident from these images, suggesting that the KBN nano-catalyst is well dispersed throughout the TiO_2 nano-catalyst. Based on these findings, the sol-gel method proved effective for synthesising the KBN-TiO_2-modified Nano-catalyst. A trace amount of carbon was detected, which might have originated from the calcination process.

4.3.6.4 Modified KBN@TiO_2 analysis using XPS

The overall XPS scan survey spectrum displayed in Figure 4.6a shows individual peaks corresponding to Ti 2p (458.19 eV), O1s (529.70 eV), C 1s (284.31 eV), K 2p (295.16 eV), B 1s (191.55 eV), and N 1s (401.1 eV). These peaks provide some preliminary details about the material composition of the composites by indicating the existence of Ti, O, K, B, N, and C elements. The Ti 2p configuration of Ti^{4+} $2p^{3/2}$ and Ti^{4+} $2p^{1/2}$ double peaks at 458.19 eV and 463.89 eV are revealed by the appropriate spikes in Figure 4.6b, which offer information on the coordination environments and chemical states of titanium inside the nanocomposites [204]. A double peak at 531.49 eV and 529.7 eV in the O 1s spectra Figure 4.6c indicates the existence of oxygen in different chemical conditions. These peaks' locations and forms provide details regarding the kinds of oxygen species that contribute to the surface chemistry of the nanocomposites, including metal oxides and functional groups. The C 1s + K 2p spectrum revealed in Figure 4.6d had recognizable peaks at 284.31 eV, confirming the existence of Sp3 carbon (C=C) and K 2p3/2 (292.41 eV), K 2P1/2 (295.16 eV), respectively, confirming the presence of carbon during calcination time, K from potassium doping and also displays O relating units over the surface [186]. These characteristics influence the electrical structure and surface reactivity of nanoparticles. The B 1s spectra in Figure 4.6e show a single spike at 191.55 eV (B–O–N), suggesting the presence of boron and its functional groups and influencing the chemistry at the surface by reducing the band gap energy of modified TiO_2

[206]. The last N 1s spectra in Figure 4.6f shows two spikes at 400.08 eV and 401.1 eV, indicating the presence of distinct nitrogen functions. These peaks reveal details about the species that contain nitrogen, including amino groups and graphitic nitrogen, which affect the electrical structure and catalytic capabilities of the nanomodified TiO_2.

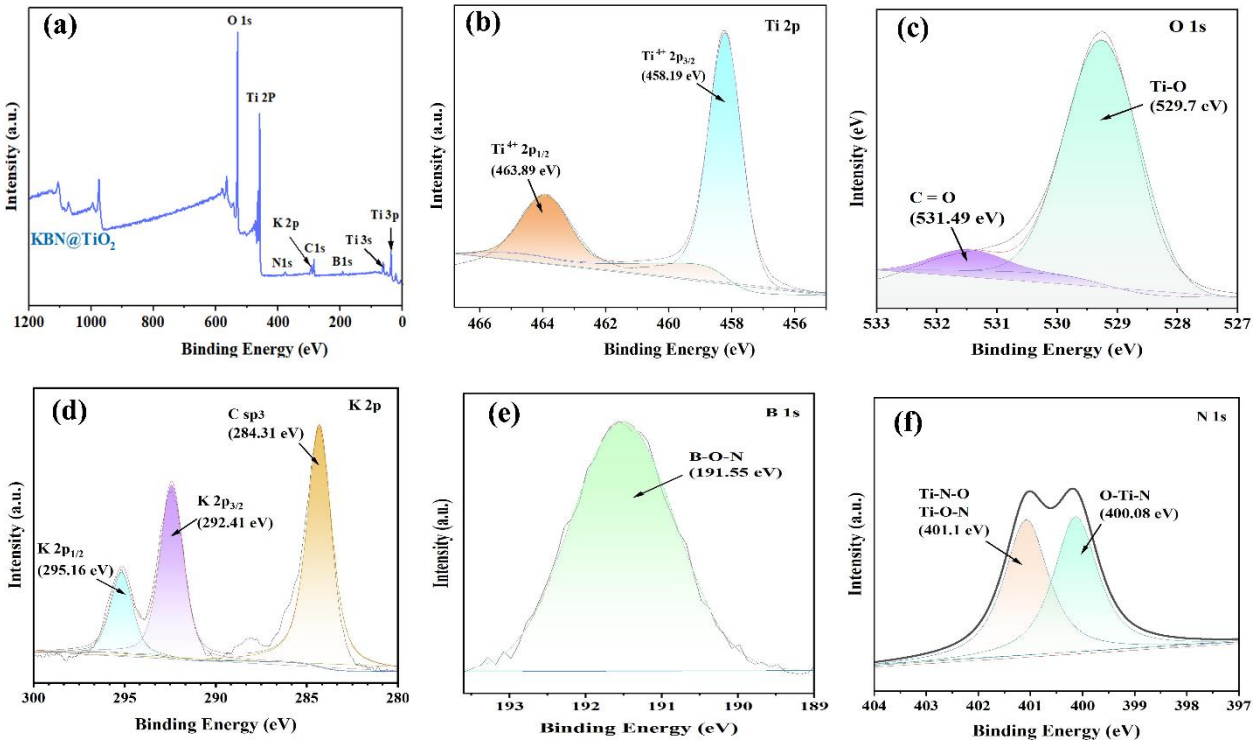

Figure 4.6 XPS analysis of KBN@TiO_2 nanoparticles (a) Overall survey, (b) Ti 2p, (c) O 1s, (d) C 1s + K 2p, (e) B 1s, and (f) N 1s.

4.3.6.5 Band structures and optical properties

The diffuse reflectance spectra of TiO_2 and 5%B-2%K-5%N-TiO_2 are displayed in Figure 4.7. The light absorption edge of TiO_2 is approximately 395 nm, indicating its limited catalytic activity under visible light. As shown in Figure 4.7a, the light absorption edge, represented by a blue line, shifts to the dual visible light regions at 435 nm and 686 nm due to KBN doping in the TiO_2 lattice structure. This redshift in the light absorption band, particularly around the coarse crystal substance, can be attributed to changes in the band structure and reduced energy level spacing caused by increased internal particle stress[115].

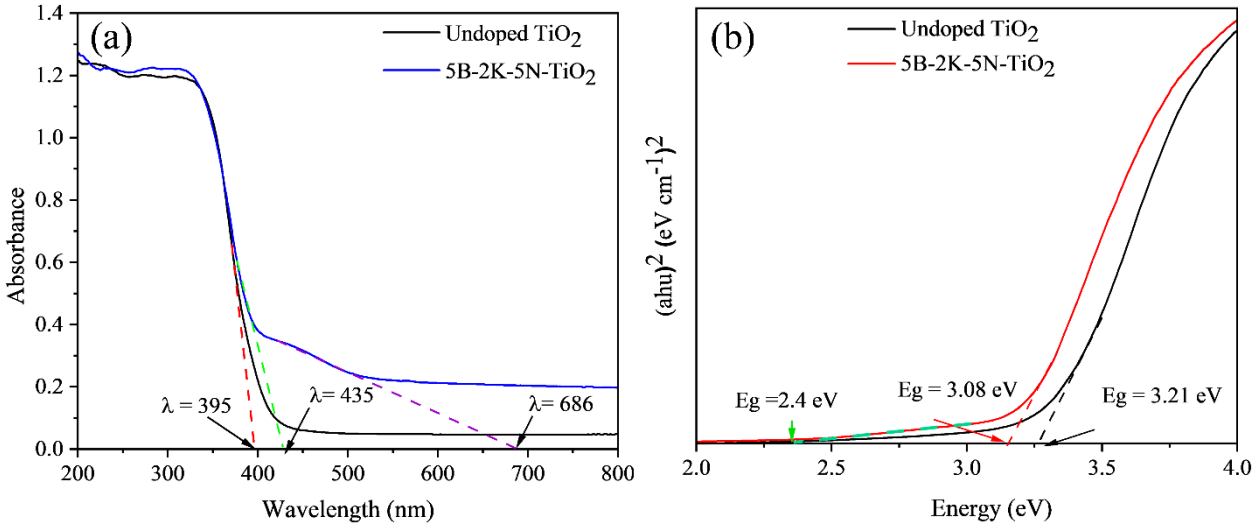

Figure 4.7 (a) UV–Vis DRS and (b) Tauc-plot of undoped TiO_2 and 5%B- 2%K-5%N-TiO_2.

Figure 4.7b illustrates the graphs of hν against $(\alpha h\nu)^2$ for TiO_2 and KBN-TiO_2, with the band gap energies of semiconductors calculated using the Tauc-plot method. In this case, the hν-$(\alpha h\nu)^2$ schematic corresponds to the direct band gap of anatase-phase TiO_2. The intersection of the abscissa axis and the line starting from the linear region of the graph indicates the absorption onset. TiO_2 exhibits a wide band gap of 3.21 eV, which is reduced to 2.35 eV after KBN doping. detail results for all synthesised materials are presented in Table S4.7. The Tauc curve analysis and UV-Vis spectroscopy revealed that KBN-doped TiO_2 exhibits enhanced visible light absorption. Moreover, the band gap of 5% B-2 % K-5 % N-TiO_2 is reduced, broadening the range of TiO_2's light absorption to include visible light [187]. This characteristic enables the catalyst to absorb sunlight at long wavelengths efficiently, enhancing its photoconversion effectiveness [188].

4.3.7 Effects of operational parameters on CIP degradation

Catalyst loading and pollutant concentration at the initial stage have a strong mutual dependence. A higher catalyst dose, as previously mentioned, provides many active sites for adsorption and facilitates the formation of free radicals, thereby enhancing the degradation rate. However, this is only true up to a specific optimal level [189]. Beyond this point, the experimental solution becomes more turbid, hindering uniform light irradiation [119]. Figure 4.8a illustrates the effects of different catalyst loadings on CIP degradation. The highest removal efficiency, 89.32%, was achieved using 0.75 g L^{-1} after 120 min of reaction time, closely followed by 88.24%, 85.18%, and 27.9% for 0.5 g L^{-1}, 1 g L^{-1}, and 0.1 g L^{-1}, respectively.

In this study, more rapid degradation occurred as the initial concentration decreased. This can be attributed to the higher availability of reactive radicals relative to organic molecules in the solution [50]. For a given catalyst loading, the formation of radicals is inhibited by the increased adsorption of contaminants on the active sites as concentration rises. Therefore, it is important to optimise the pollutant concentration of the available surface area and active sites [51]. With a natural pH of 5.65 (unadjusted), the initial CIP concentration varied between 5 mg L^{-1} and 20 mg L^{-1}, and the results are shown in Figure 4.8b. An increase in the initial CIP concentration at a specific catalyst loading leads to a decrease in removal efficiency. After 120 min, 99.59% removal was observed for an initial CIP concentration of 5 mg L^{-1}. However, as the concentration increased from 5 mg L^{-1} to 20 mg L^{-1}, the degradation rate decreased from 99.59% to 62.83%.

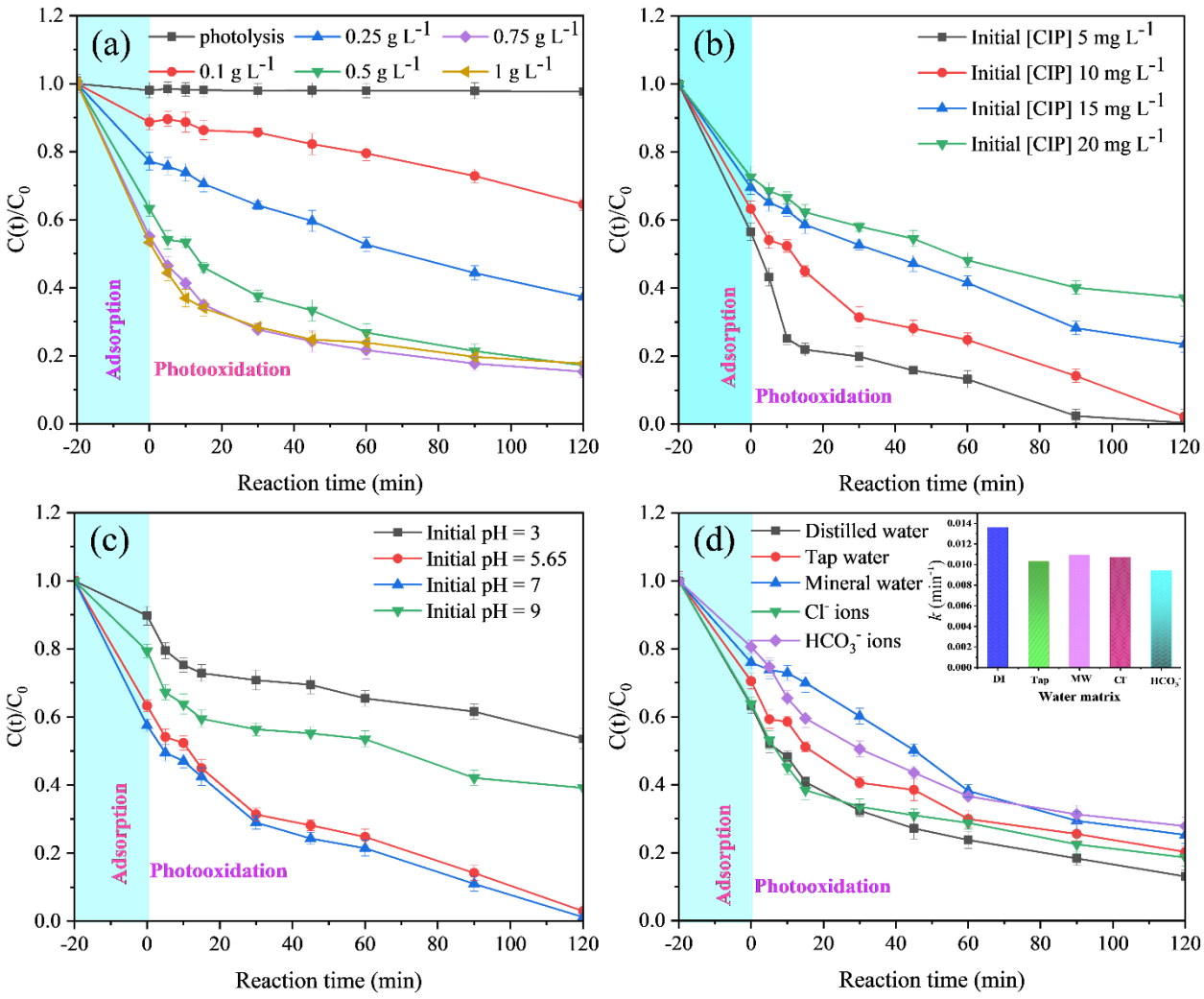

Figure 4.8 Effects of (a) catalyst dosage, (b) initial [CIP], (c) initial pH, and (d) water matrices via photocatalytic degradation of CIP on the KBN@TiO_2 system.

Factors such as surface charge and agglomeration tendencies are influenced by the pH of the solution [190]. Additionally, pH level controls the quantity of hydroxyl radicals produced in the reaction. Neutral pH conditions are favourable for CIP degradation. According to Kumar et al.[191], the optimal surface charge of TiO_2 particles at natural pH values facilitates the adsorption of contaminants onto the catalyst surface, enabling more efficient degradation. Figure 4.8c demonstrates the effect of pH on CIP degradation. For pH values of 3, 5.65 (unadjusted), 7, and 9, the reduction of 10 mg L^{-1} CIP was approximately 46.40%, 97.02%, 98.78%, and 60.84% after 120 min, respectively. Finally, a different water matrix was tested, as shown in Figure 4.8d, and neither chloride nor bicarbonate ions significantly affected the CIP degradation. This suggests that KBN@TiO_2 exhibits good performance in the presence of co-existing ions and substances.

4.3.8 Reusability and degradation of other antibiotics

To investigate the reusability and stability of KBN@TiO_2, the modified photocatalyst was recycled five times under the same conditions. The photocatalytic performance results are displayed in Figure 4.9a and Figure 4.9b. After five cycles, the degradation efficiency was only decreased by 8.12%, which indicates that the KBN@TiO_2 catalyst has excellent stability and reusability.

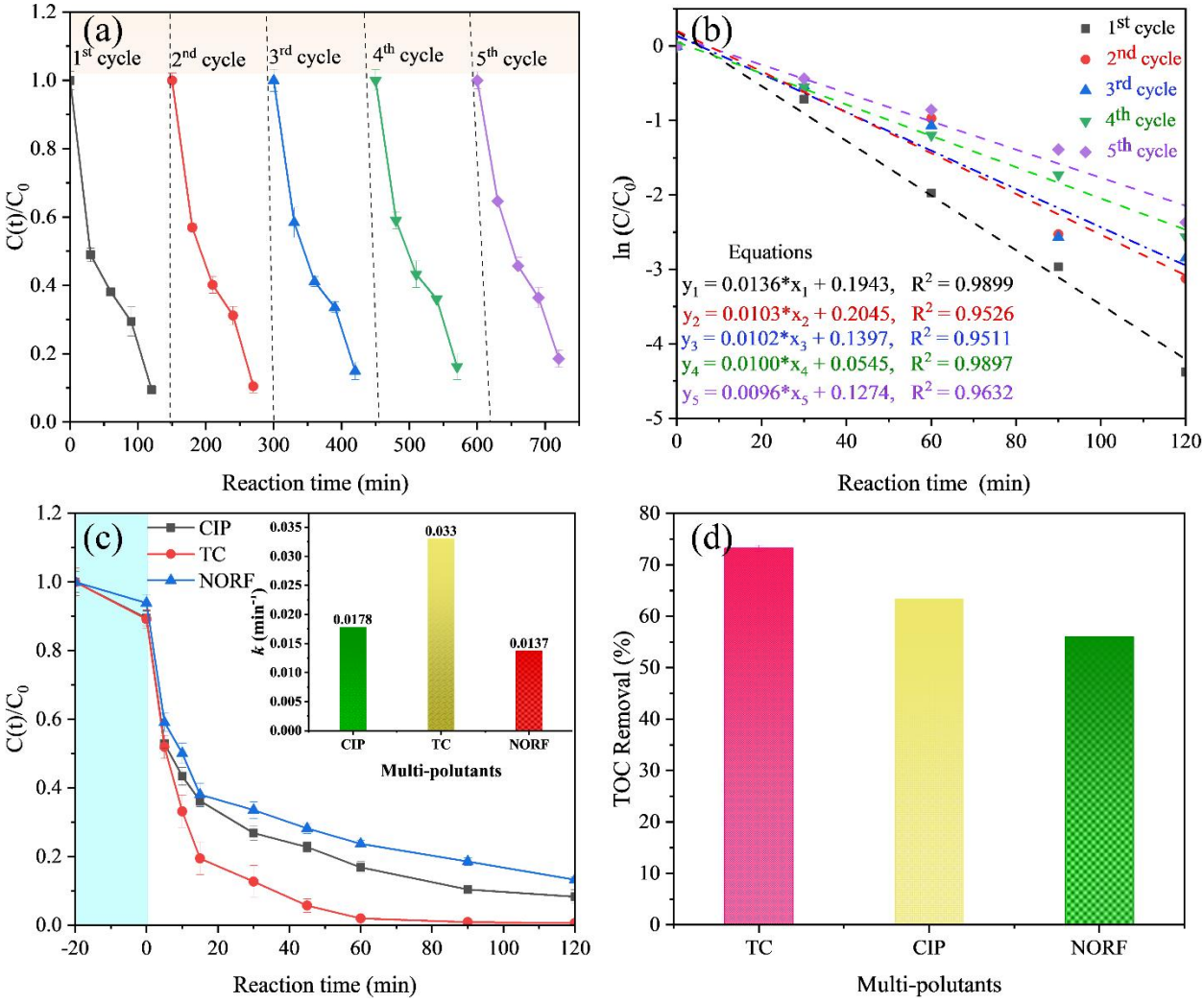

Figure 4.9 (a) reusability of KBN@TiO_2, (b) reaction rate constants, (c) degradation of different antibiotics, and (d) TOC removal by the KBN@TiO_2 system. (Experimental conditions: CIP = TC = NORF = 10 mg L^{-1}, catalyst dose = 0.5 g L^{-1}, pH = 5.65 (unadjusted)).

The performance of KBN@TiO_2 was further evaluated for the degradation of a couple of antibiotics, i.e., norfloxacin (NORF) and tetracycline (TC). They are among the most prevalent antibiotics and cause a variety of concerns to different aquatic life forms, such as fish, bacteria, algae, plants, and crustaceans [176]. The removal percentage for TC was the fastest, followed by CIP and NORF Figure 4. 9c. The k value was 0.1336, 0.0344, and 0.0339 min^{-1}, while the removal at 120 min was 100%, 90.18%, and 86.83% for TC, CIP, and NORF, respectively. Moreover, the TOC removal % of TC, CIP, and NORF were 73.26%, 63.39%, and 56.00%, respectively, Figure 4. 9d. These results strengthen the modified KBN@TiO_2 catalyst's ability to degrade different antibiotics apart from CIP. Finally, a comparison of the synthesised

KBN@TiO_2 nanoparticles' photocatalytic effectiveness with reported research was presented in a detailed Table S4.9.

4.3.9 CIP degradation mechanism

Figure 4.10 presents a schematic illustration of the CIP adsorption–photodegradation mechanism under visible light irradiation. When adsorption occurs, as shown in Figure 4.10, the pollutants (in this case, CIP) adhere to the surface of the KBN-TiO_2 catalyst. This is a surface phenomenon where the pollutant is present on the catalyst [97]. However, in photocatalytic studies, entirely different conditions occur. When incident photons with sufficient energy are absorbed by 5%B-5%N-2%K-TiO_2, they cross the photocatalyst's band gap energy and excite e^- from the valence band to the conduction band [175]. Concurrently, h^+ is generated in the semiconductor's valence band. One mechanism by which the strong reducing capacity of e^- in the conduction band is utilised involves the reduction of the physically adsorbed O_2 to form superoxide radicals ($^{\bullet}O_2^-$). These radicals can further combine with H^+ to yield H_2O_2 and O_2. Subsequently, H_2O_2 can be broken down into $^{\bullet}OH$ and OH^-. Additionally, h^+ in the catalyst can react with H_2O or OH^- to produce $^{\bullet}OH$, which exhibits a strong oxidising effect [187]. The reactive radical species formed during the reaction process can degrade organic contaminants (in this case, CIP) and facilitate their mineralisation to CO_2, H_2O, and more stable inorganic molecules. The formation of these radicals improves the lifetime of charge carriers, efficiently blocks electron–hole pair recombination, and facilitates the carriers' efficient migration to the catalyst surface. This improved photo-generated charge carrier separation ability results in higher degradation efficiency[192]. A detailed description of the reaction mechanisms of the modified KBN-TiO_2 photocatalyst for CIP degradation is provided in the supplementary information, Text S4.2.

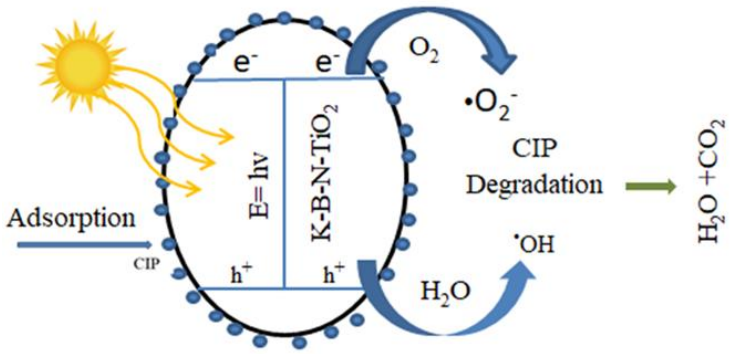

Figure 4.10 Schematic diagram of the CIP removal mechanism (adsorption–photocatalysis) by triple-doped KBN-TiO_2.

4.4 Conclusions

This study aimed to optimise the conditions of the sol-gel synthesis for preparing modified KBN triple-doped TiO_2 employing the BBD RSM. The results demonstrate that this experimental approach is effective in evaluating the interaction effects between different sol-gel preparation conditions. The optimum synthesis conditions for modified KNB-TiO_2 using the sol-gel method were determined to be a 5%B/Ti molar ratio, with constant 2%K and 5%N doping, a calcination temperature of 500 ℃ and a calcination time of 2.5 h. Moreover, additional experiments could provide further insights into the synthesis technique. Compared to undoped TiO_2 (15%) and BN-doped TiO_2 (44%), the triple-doped KBN-TiO_2 exhibited a significant enhancement in photocatalytic activity, reaching 84.3%. The crystal structure of the anatase phase was observed in the XRD patterns, and the composite 2%K, 5%B, and 5%N-TiO_2 showed an improvement of grain size from 17.4 nm to 19.0 nm compared to the undoped TiO_2 nano-catalyst. The SEM image revealed that the addition of potassium, boron, and nitrogen resulted in uniform doping or composite formation, which can enhance TiO_2 properties. Under optimal processing conditions, the system achieved 84.3% CIP degradation efficiency, a 100% anatase crystalline phase, and a specific surface area of 66.476 $m^2\ g^{-1}$. Each characterisation method employed in this work confirmed the effective synthesis of active visible light KBN-doped TiO_2, with increased S_{BET}, smaller crystal size, larger pore space, improved crystallinity, and a dominant anatase phase. The modified KBN-TiO_2 photocatalyst successfully degraded the antibiotic organic pollutants, suggesting that modified TiO_2 is an effective and environmentally friendly technology for degrading recalcitrant emerging pollutants in wastewater.

CHAPTER FIVE

Highly efficient KBN@TiO_2@rGO composite for photodegradation of antibiotics under visible light irradiation

Abstract

Antibiotic pollution in surface and groundwater systems raises significant concerns for both ecological and human health, necessitating the development of efficient remediation strategies. To address this challenge, a novel composite material, KBN@TiO_2@rGO, was synthesised through a two-step procedure: i) the sol–gel method was employed to prepare KBN-doped TiO_2 nanoparticles, and ii) these particles were subsequently dispersed onto reduced graphene oxide (rGO) via hydrothermal treatment for ciprofloxacin (CIP) photooxidation applications. The synthesised nanomaterials and photocatalytic composites were characterised using diverse analytical techniques, including X-ray photoelectron spectroscopy, scanning electron microscopy with energy-dispersive X-ray spectroscopy, optical spectroscopy, and photoluminescence. The KBN@TiO_2@rGO composite exhibited outstanding photocatalytic activity, achieving 99.21% degradation of CIP and a 75.09% reduction in total organic carbon during illumination (950 W m^{-2}). Notably, this corresponds to a 3.3-fold increase in the CIP removal efficiency compared to simple TiO_2, highlighting the synergistic effect of ternary atom (B, N, and K) doping and rGO integration. Divalent cations, including Mg^{2+} and Ca^{2+}, slightly inhibited the CIP removal. In contrast, anions such as Cl^-, NO_3^-, and HCO_3^- enhanced CIP degradation, while SO_4^{2-}, PO_4^{3-}, and humic acid exerted inhibitory effects. Furthermore, the degradation performance of the prepared photocatalyst was investigated across different water matrices, showing slightly lower efficiency due to the presence of natural radical quenchers and organic materials. The formation of reactive oxygen species, including $^{\bullet}OH$, $O_2^{\bullet-}$, and $^1O_2$, was verified through electron spin resonance spectroscopy and chemical scavenger experiments. Finally, possible CIP degradation pathways were elucidated using UPLC-MS/MS analysis. These findings highlight the promising potential of the KBN@TiO_2@rGO photocatalytic system for CIP degradation in various water matrices.

5.1 Introduction

Pharmaceuticals and personal care products (PPCPs) are frequently detected in aquatic environments and have emerged as a global environmental concern [193]. In 2024, global pharmaceutical consumption was estimated at 3.8 trillion daily doses [194]. Since the discovery of penicillin by Alexander Fleming in 1928, antibiotics have been extensively used to treat bacterial infections [195]. Due to the substantial rise in global antibiotic consumption in recent years, these compounds have been detected in natural water bodies and raw sewage at concentrations ranging from nanograms per litre (ng L^{-1}) to micrograms per litre (μg L^{-1}), and even milligrams per litre (mg L^{-1}) in some pharmaceutical wastewaters [196]. The proliferation of antibiotics and their metabolites has been associated with the emergence of antibiotic-resistant genes and antibiotic-resistant bacteria. Moreover, the presence of PPCPs and antibiotics in wastewater can disrupt the natural microbial communities and the ecosystem.

Ciprofloxacin (CIP) is a widely used antibiotic belonging to the broad-spectrum fluoroquinolone class. It is frequently detected in wastewater treatment plants at concentrations ranging from 0.013–104.2 μg L^{-1} [195] and even at high-level concentrations of mg L^{-1} in effluents from pharmaceutical companies [197]. CIP is commonly used to treat both human and animal bacterial infections. Due to its high chemical stability and low biodegradability, approximately 70% of administered CIP remains unmetabolized and is excreted via the renal system in both humans and animals [198]. Physicochemical treatment techniques, including membrane filtration, adsorption, and electrocoagulation, are expensive, energy-intensive, and generate undesirable by-products (such as sludge and organic intermediates), which limit their widespread application in the degradation of antibiotics. Additionally, conventional biological treatment processes are often ineffective in eliminating emerging organic contaminants, such as antibiotics, which may persist in treatment effluents as refractory residues and pose risks to human health, animal life, and aquatic ecosystems [199,8]. Therefore, developing cost-effective, environmentally friendly, and highly efficient remediation strategies is imperative. Photocatalysis has emerged as a promising technique for the degradation of antibiotics, owing to its outstanding redox performance, zero-sludge output, and solar energy utilisation capabilities [200].

Advanced oxidation processes, such as heterogeneous photocatalysis, are considered effective treatment methods, especially for recalcitrant organic pollutants [10,112]. Among these, titanium dioxide (TiO_2)-based photocatalysis is the most widely employed method due to its

operational simplicity, significant chemical stability, affordability, relative availability, and eco-friendliness. This approach offers several distinct advantages: (1) tailored morphologies provide abundant active sites for various applications; (2) the ionic radius of Ti^{4+} closely matches that of many metal cations, facilitating the incorporation of heteroatom dopants; (3) the flexible energy band structure promotes efficient storage of free electrons in the conduction band; and (4) defect engineering, such as the introduction of oxygen vacancies, creates a new-fangled band gap in the prohibited band, thereby improving the absorption of visible light [14]. Therefore, TiO_2-based photocatalysis shows strong potential for the efficient degradation of recalcitrant organic pollutants and other substances resistant to conventional biological treatment methods [13,14]. Nevertheless, several critical limitations hinder the practical application of TiO_2 in commercial settings [13]. First, due to its high band gap energy (3.20 eV), TiO_2 must be exposed to Ultraviolet A radiation (UVA) to become photoactivated. However, its solar utility is severely limited, as UVA constitutes only approximately 5% of the solar spectrum [16]. Additionally, the rapid recombination of photogenerated electron–hole pairs and the low adsorption capacity for hydrophobic pollutants lead to reduced photonic efficiency when TiO_2 photocatalysts are applied for water treatment. In recent years, extensive research has focused on overcoming these limitations to enhance the photocatalytic performance of TiO_2 [17]. Strategies such as metal and non-metal doping, formation of composites with other photocatalysts, and the development of heterojunction photocatalysts have been explored to address these limitations [18].

Doping TiO_2 with metal and non-metal to enhance its photocatalytic efficacy has been the subject of extensive research [201]. The incorporation of dopants can modify the electronic structure of TiO_2, thereby improving its visible light irradiation efficiency. Metal-doped photocatalysts, such as those modified with silver (Ag) [20], iron (Fe) [21], potassium (K) [22], and boron (B) [23], exhibit superior photocatalytic performance due to the localised surface plasmon resonance (LSPR) and the electron-accepting capabilities of the metal dopants. These dopants capture electrons due to the altered Fermi level in the metallic oxide, facilitating the separation of photogenerated electron–hole pairs [24]. Furthermore, metal doping-induced LSPR can lower the bandgap and introduce new energy levels between the valence and conduction bands, thereby enabling photocatalytic activation under visible light. Similarly, non-metal doping involves the introduction of heteroatoms, such as nitrogen (N) [25], carbon (C) [26], and phosphorus (P) [27], into the metal oxide lattice by partially replacing oxygen

atoms. The incorporation of non-metal dopants enhances charge carrier separation, creates non-metallic energy levels, and facilitates electron capture, thereby lowering the bandgap. Moreover, co-doping with multiple heteroatoms (C/N) [28] and (B/N) [29] can suppress the recombination of charge carriers by leveraging the electron-accepting properties of non-metals, further reducing the bandgap of bare TiO_2 by creating new energy levels. Additionally, ternary doping (KHB) [14] can significantly enhance photocatalytic activity, particularly for the degradation of antibiotics.

It has been widely reported that combining TiO_2 with graphitic materials, characterised by a higher specific surface area and superior charge carrier mobility compared to pristine TiO_2, is among the most effective approaches for enhancing its photocatalytic activity. Specifically, reduced graphene oxide (rGO) and graphene oxide (GO) have recently been used as substrates for loading TiO_2 particles due to their enhanced mechanical, electrical, and chemical properties, as well as their high surface conductivity and outstanding absorptivity [18,19]. The adsorption of organic contaminants onto rGO is facilitated by the presence of carboxylic acid (–COOH) at the edges and hydroxyl (–OH) and epoxide (C–O–C) groups on the basal plane [202].

To the best of our knowledge, sol–gel-assisted hydrothermal synthesis of KBN@TiO_2@rGO for single and multi-antibiotic degradation under solar simulator irradiation has not yet been reported in the literature. Accordingly, the novelty and objectives of the present study include: (a) fabrication of KBN@TiO_2@rGO composite using a sol–gel method followed by hydrothermal treatment and characterise its physicochemical and structural properties; (b) to evaluate the adsorption capacity and photocatalytic degradation efficiency of the KBN@TiO_2@rGO system for CIP; (c) to systematically examine the effects of key variables, including initial CIP concentration, catalyst loading, and solution pH, on the photocatalytic mechanism and overall performance; (d) to investigate the generation of reactive oxygen species (ROS) and elucidate the mechanisms underlying photocatalytic activity in the KBN@TiO_2@rGO system; and (e) to assess the reusability of the KBN@TiO_2@rGO photocatalyst and examine its performance across different water matrices (river water, groundwater, and municipal water) to determine its practical applicability.

5.2 Materials and Methods

5.2.1 Materials

The details of chemical reagents and instruments used for characterisation are provided in Text S5.1 and Text S5.2 in Supplementary Information, respectively.

5.2.2 Synthesis of KBN@TiO_2

A KBN@TiO_2 photocatalyst was synthesised using a simple and effective sol–gel method, incorporating specific amounts of boric acid (H_3BO_3) (5 wt.% B-Ti) and potassium nitrate (KNO_3) (2 wt.% K-Ti) [14]. To prepare the dopant solutions, the required quantities of potassium nitrate and boric acid were dissolved separately in a mixture of 10 mL of absolute ethanol and 3 mL of water, followed by sonication in an ultrasonic bath for 30 min to form solutions 1 and 2, respectively. Subsequently, 17 mL of titanium (IV) isopropoxide was slowly added to 47 mL of anhydrous ethanol, after which 14 mL of double-distilled deionised (DDI) water was added under vigorous stirring to form Solution 3. Solutions 1 and 2 were then added dropwise to Solution 3. Thereafter, ammonia (NH_3) was gradually introduced (5 wt.% N-Ti), and the mixture was stirred continuously for 4 h. The resulting solution was aged at room temperature for 24 h to promote hydrolysis, then dried in an oven at 50 ℃ to remove residual solvents. The dried product was subsequently ground, placed in a silica boat, and calcined in a tubular furnace at 500 ℃ for 2 h, with a heating rate of 5 ℃ min^{-1} in air. BN@TiO_2 and undoped TiO_2 were synthesised using a similar method.

5.2.3 Synthesis of GO and rGO

Graphite powder was converted into GO using a modified Hummers' approach at low temperatures [203]. Initially, 2 g of graphite, 1 g of $NaNO_3$, and 50 mL of H_2SO_4 were mixed in an ice bath for 1 h using a magnetic stirrer. Subsequently, 6 g of $KMnO_4$ was gradually added over 1 h at 40 ℃ under continuous stirring. Next, 250 mL of DDI water was added to the solution, followed by the dropwise addition of 30% H_2O_2 (12.5 mL) until the solution turned yellow-brown. The resultant GO powder was washed five times with DDI water, then treated with 10 mL of 0.1 M HCl and left to settle overnight. After repeatedly washing the suspension until a neutral pH was achieved, the GO powder was isolated through centrifugation. Finally, the powder was dried overnight at 60 ℃ in a vacuum oven.

Using ultrasonication, a 2.8 g GO aqueous suspension was prepared in 100 mL of DDI water for subsequent reduction via the ascorbic acid method. Following this, 1.0 g of ascorbic acid was added, and the mixture was stirred for 30 min. To improve colloidal stability through electrostatic repulsion, 0.5 g of NaOH was introduced to adjust the solution pH to a basic range. After further agitation, the reaction mixture was heated at 90 ℃ for 1 h. Upon completion, the resulting reduced black product was separated by centrifugation and thoroughly washed with water to remove any residual unreacted components. Finally, the synthesised rGO was

dried overnight at 50 ℃, followed by an additional 4 h at 60 ℃ in a vacuum oven, yielding 2.15 g of rGO.

5.2.4 Synthesis of KBN@TiO_2@rGO composite

The KBN@TiO_2@rGO composite photocatalyst was synthesised through dispersion and thermal treatment techniques. Specifically, 0.9 g of modified KBN@TiO_2 and 0.1 g of rGO were dispersed in 100 mL of DDI water and stirred for 2 h. The resulting suspension was then transferred to a Teflon-lined autoclave and subjected to hydrothermal treatment at 150 °C for 3 h. After cooling, the mixture was washed three times with DDI water to remove impurities, centrifuged at 3000 rpm, and dried overnight at 50 ℃ to obtain the KBN@TiO_2@rGO nanocomposite. The BN@TiO_2@rGO and TiO_2@rGO composites were synthesised using the same method. Figure 5.1 illustrates the procedure used to synthesise the composite photocatalyst.

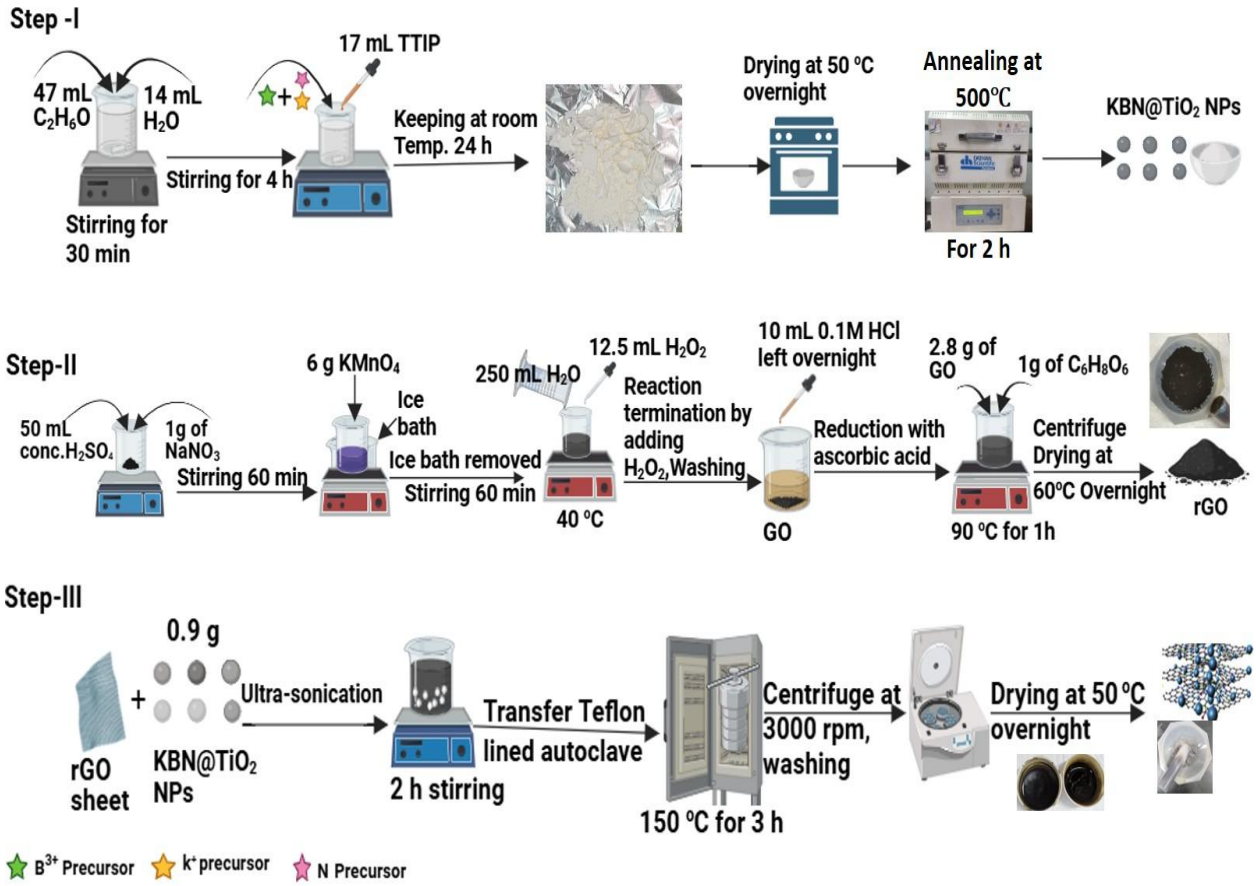

Figure 5.1 Schematic illustration of the synthesis process for the KBN@TiO_2@rGO nanocomposite.

5.2.5 Photocatalytic degradation experiments

The photocatalytic degradation tests were conducted in batch mode using a cylindrical quartz photocatalytic reactor (open at the top) with a total volume of 250 mL (radius: 5 cm; height: 10 cm). A 500 W Xenon lamp, positioned 20 cm above the upper edge of the reactor, served as the UV–visible light irradiation source (wavelength range: 400–780 nm). In each degradation experiment, a sample amount of the photocatalyst was dispersed in 100 mL of CIP solution and stirred in the dark for 20 min until absorption–desorption equilibrium was achieved before exposing it to UV-visible light. The photocatalytic degradation performance of KBN@TiO_2@rGO was evaluated in comparison to that of synthetic TiO_2, BN@TiO_2, and BN@TiO_2@rGO. Additionally, the effects of initial pH (3–11), catalyst dosage (0.025–0.25 g), and initial CIP concentration (1–10 mg L^{-1}) on the photocatalytic degradation efficiency were examined through a series of experiments. After each experiment, a 3 mL aliquot of the reaction solution was collected and filtered through a 0.2 μm syringe filter (Whatman, cellulose nitrate membrane, ø = 25 mm) before analysis. To identify the ROS involved in the photocatalytic process, scavenger experiments were conducted, followed by real water matrix experiments to evaluate the practical applicability of the catalyst. The concentration of CIP was quantified using high-performance liquid chromatography (HPLC; Agilent Technologies, 1200 series, USA) at a detection wavelength of 277 nm (Table S5.1). The reusability of the photocatalyst was assessed by repeating the experiment five times. Detailed analytical procedures are provided in Text S5.3. All experiments were conducted at least in duplicate under ambient temperature and atmospheric pressure.

The CIP removal efficiency (%) was calculated using Eq. (5.1):

$$Removal\ efficiency\ (\%) = \frac{C_0 - C_t}{C_0} \times 100 \quad (5.1)$$

The first-order kinetic rate constant (k_x, min^{-1}) was defined by Eq. (5.2) [225].

$$\ln \frac{C_t}{C_0} = -k_x t \quad (5.2)$$

where C_0 and C_t represent the initial and time-dependent concentrations of the antibiotic (mg L^{-1}), respectively; t is the reaction time (min); and k_x denotes the rate constant (min^{-1}) for adsorption (k_{ads}) or photocatalytic degradation (k_{deg}).

5.3 Results and Discussions

5.3.1 Characterisation of synthesised KBN@TiO_2@rGO

5.3.1.1 XRD and FTIR analysis of synthesised composites

XRD analysis was employed to determine the crystal structures of TiO_2, KBN@TiO_2, KBN@TiO_2@rGO, and recycled KBN@TiO_2@rGO. The TiO_2 nanoparticles exhibited an anatase crystalline phase. Characteristic diffraction peaks are observed in Figure 5. 2a at 2θ angles 25.69°, 38.40°, 48.80°, 54.78°, 55.94°, 63.74°, 69.95°, 71.48°, and 75.38°, corresponding to the (101), (004), (200), (105), (211), (204), (116), (220), and (107) planes of TiO_2, respectively (JCPDS 21–1272) [35, 36]. As can be observed, the KBN@TiO_2 nanocomposite displayed 2θ values corresponding to the (101), (004), (200), (105), (211), (204), (116), (220), and (107) crystal planes, respectively, of 25.69°, 38.40°, 48.80°, 54.78°, 55.94°, 63.73°, 69.95°, 71.48°, and 75.38° (JCPDS 21–1272). Additionally, a few rutile phases were detected in the undoped TiO_2 sample (JCPDS 21–1276) [204]. Compared to pure TiO_2, doping with potassium (K), boron (B), and nitrogen (N) expanded the most intense (101) peak of the anatase. The KBN@TiO_2@rGO nanocomposite presented spikes at 2θ angles of 24.77°, 37.38°, 46.89°, 53.13°, 53.74°, 61.44°, 67.69°, 68.48°, and 73.02°, corresponding to the (101), (004), (200), (105, (211), (204), (116), (220), and (107) planes, respectively. The average crystallite size of the nanoparticle was 19.04 nm. The absence of additional diffraction peaks confirms the successful synthesis of KBN@TiO_2@rGO nanocomposites. However, the XRD spectra of the KBN@TiO_2@rGO nanocomposite do not show any clear peaks for B_2O_3 or rGO, which is attributed to their trace concentrations. First, the composite's peaks may be too weak to be seen or distinguished over the background noise because boron doping and rGO were utilised at their optimal levels (5% B and 10% rGO). Moreover, the characteristic peaks of rGO and TiO_2 may overlap, making it challenging to distinguish them in the XRD spectra; therefore, peak overlay cannot be ruled out [205].

Figure 5. 2b presents the FT-IR spectra of TiO_2, KBN@TiO_2, KBN@TiO_2@rGO, and the used KBN@TiO_2@rGO (Figure S5.1) nanocomposite photocatalysts. In the TiO_2 spectrum, a broad band between 3427 and 3102 cm^{-1} corresponds to the O–H stretching vibrations of surface hydroxyl groups and adsorbed water molecules. This is further supported by the band observed at 1636.18 cm^{-1}, which is attributed to the bending vibrations of molecular water and Ti–OH groups [19]. This band also reflects the vibrational modes of aromatic rings in the rGO structure within the composites. The reduced intensity of the band at 1720 cm^{-1} suggests that the

composites primarily include hydroxyl groups instead of ketone or carboxylic groups [206]. Furthermore, the weakened signal at 1239 cm^{-1} in the FT-IR spectra indicates the presence of C–O functional. The bands observed at 809.32 and 460.19 cm^{-1} in the spectra of both TiO_2 and the composites are ascribed to the vibration of Ti–O–Ti linkages in TiO_2. In the composite, the chemical interaction of TiO_2 with rGO usually produces broad absorption bands below 1000 cm^{-1}, indicating a combination of Ti–O–C and Ti–O–Ti vibrations. When hydrothermally treated, Ti–O–C connections demonstrate how rGO, which possesses residual carboxyl groups, interacts effectively with the surface hydroxyl groups of TiO_2 nanoparticles to form chemical bonds in the composites [207]. The significant reduction or disappearance of absorption peaks corresponding to oxygenated functional groups, such as C=O (1636.18 cm^{-1}), –OH (1353.35 cm^{-1}), and C–O–C (1035.23 cm^{-1}), in the nanocomposites further confirms the strong binding of TiO_2 to rGO at these reactive sites [208].

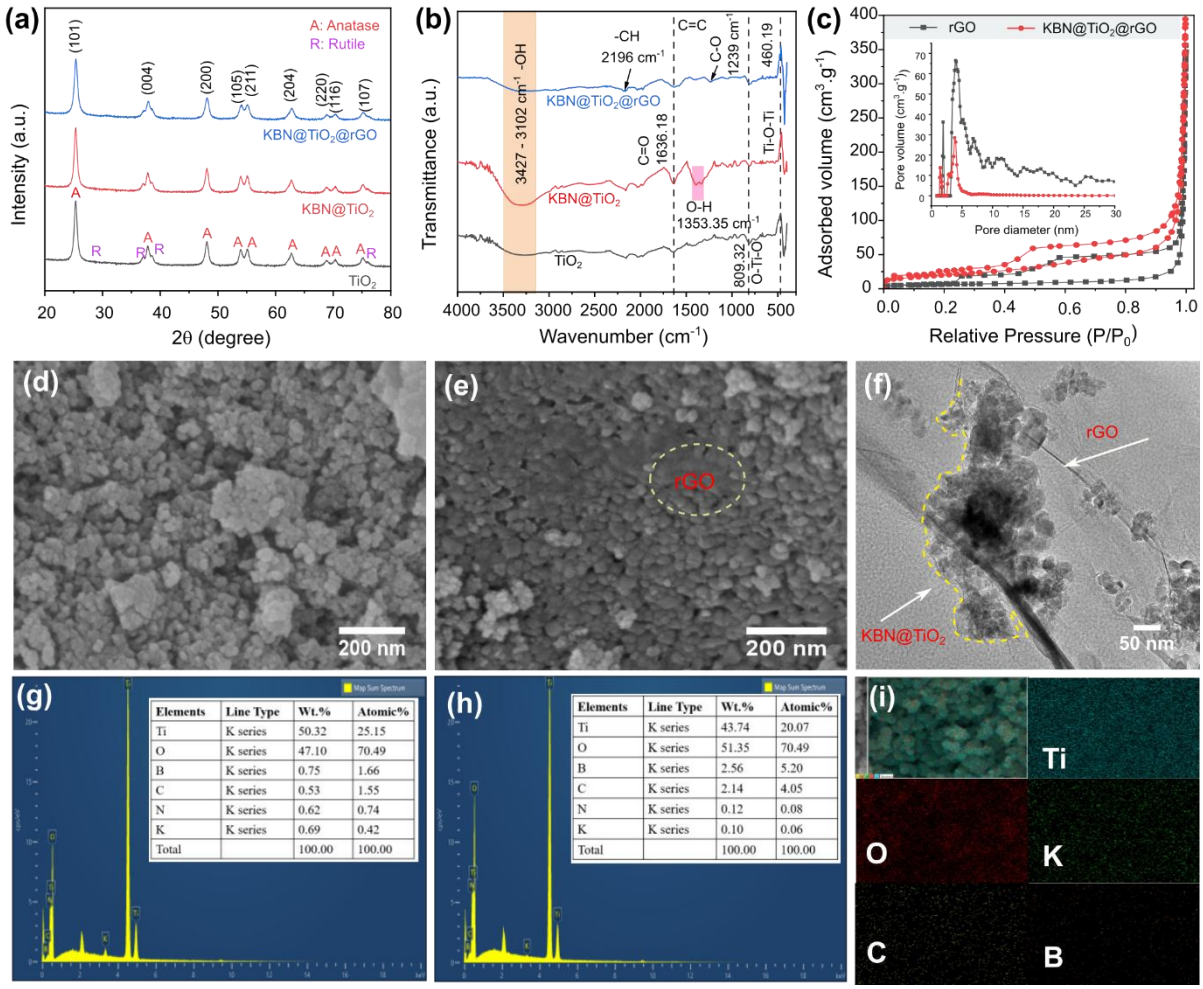

Figure 5.2 Characterization of the synthesized materials: (a) XRD patterns; (b) FTIR spectra; (c) N_2 adsorption-desorption isotherms; FE-SEM images of (d) KBN@TiO_2 and (e) KBN@TiO_2@rGO; (f) TEM image of KBN@TiO2@rGO composite; EDX spectra of (g) KBN@TiO_2 and (h) KBN@TiO_2@rGO;and (i) elemental mapping of KBN@TiO_2@rGO.

5.3.1.2 BET and SEM analysis

As shown in Table 5.1, nitrogen adsorption–desorption isotherms were employed to estimate the BET surface areas of the synthesised rGO, as well as the fresh and used KBN@TiO_2@rGO samples. Compared to pristine TiO_2 and KBN@TiO_2, KBN@TiO_2@rGO displayed a significantly high specific surface area of 71.35 m^2 g^{-1}, which is attributed to the successful incorporation of rGO into the KBN@TiO_2 [229]. This high surface area is expected to facilitate adsorption and electron transfer capability of the KBN@TiO_2@rGO composite [227]. Although the surface area of the used KBN@TiO_2@rGO decreased from 71.35 m^2 g^{-1} to 50.91 m^2 g^{-1}, this reduction did not result in a marked decline in photocatalytic activity. The pore size distributions of the three materials, based on the nitrogen adsorption–desorption method, are presented in Figure 5.2c and S5.2. The rGO sample (black squares) exhibited strong mesopores, characterised by a broad pore size distribution ranging from 2 nm to 30 nm and a very high pore volume, with a sharp peak near 4 nm. This porosity is typically attributed to the ragged and wrinkled sheet-like morphology of rGO [19]. The fresh KBN@TiO_2@rGO (red circles) displayed a narrower pore size distribution, primarily centred around 3–5 nm, and exhibited a greater total pore volume.

Table 5. 1: Surface area and pore size distribution of prepared samples.

Samples	**Surface area (m^2 g^{-1})**	**Average pore size (nm)**	**Pore volume (cm^3 g^{-1})**
rGO	60.615	3.407	0.060
KBN@TiO_2@rGO fresh	71.354	4.301	0.117
KBN@TiO_2@rGO used	50.911	3.054	0.134

The SEM images in Figures 5.2d and 5.2e reveal the morphological properties of KBN@TiO_2 and KBN@TiO_2@rGO, respectively. As shown in Figure 5.2d**,** the KBN@TiO_2 structure is larger, rougher, and irregularly shaped. In contrast, Figure 5.2e shows that the particles in

KBN@TiO_2@rGO appear smaller and more evenly distributed. A smoother, layered region observed beneath or surrounding the nanoparticles is attributed to rGO. The aggregation of rGO sheets was invisible as a result of the chemical interaction between KBN@TiO_2 and rGO. Furthermore, the TEM image of KBN@TiO_2@rGO in Figure 5.2f indicates that the incorporation of rGO provides a conductive platform for the photoactive material, enabling these particles to be more uniformly distributed. The chemical functionalities in rGO improve interfacial adhesion and prevent the aggregation of KBN@TiO_2, which is beneficial for surface catalytic reactions.

The elemental composition of the KBN@TiO_2@rGO photocatalysts was determined using EDX, as presented in Figures 5.2g and 5.2h. The quantitative data, summarised in the inset tables of these figures, indicate that the photocatalysts were primarily composed of boron (B), carbon (C), nitrogen (N), oxygen (O), potassium (K), and titanium (Ti). As shown in the inset table of Figure 5.2g, the elemental composition of the KBN@TiO_2 sample was 97.42% Ti and O, with small amounts of B (0.75%), C (0.53%), N (0.62%), and K (0.69%). In contrast, the composite sample comprised 43.74% Ti, 51.35% O, 2.56% B, 2.14% C, 0.12% N, and 0.10% K, as shown in Figure 5.2h. Overall, KBN@TiO_2@rGO exhibited a much more sophisticated structure that combined the positive properties of rGO (conductivity and dispersion) with the active site generation provided by KBN doping on TiO_2 (Figure 5.2i). Compared to KBN@TiO_2, the observed structural and elemental changes suggest that KBN@TiO_2@rGO possesses superior photocatalytic, electronic, and adsorption capabilities.

5.3.1.3 Analysis of synthesised composites using XPS

The XPS survey spectrum displayed in Figure 5.3a reveals distinct peaks corresponding to Ti 2p (458.19 eV), O 1s (529.48 eV), C 1s (283.90 eV), K 2p (292.40 eV), B 1s (191.60 eV), and N 1s (402.23 eV). These peaks provide preliminary details about the elemental composition of the composites, confirming the presence of Ti, O, K, B, N, and C. As shown in Figure 5.3b**,** the Ti 2p spectrum displays distinct peaks at 458.19 eV and 463.89 eV, corresponding to the Ti^{4+} $2p_{3/2}$ and Ti^{4+} $2p_{1/2}$ states, respectively. These features offer information on the coordination environments and chemical states of titanium inside the nanocomposites [186]. Additionally, the O 1s spectrum in Figure 5.3c displays two peaks at binding energies 529.48 and 531.45 eV, indicating the presence of oxygen in different chemical coordination. The combined C 1s and K 2p spectrum shown in Figure 5.3d displays distinct peaks at 283.9, 286.1, 286.6, 288.1, and 292.4 eV. These are attributed to sp^2 carbon (C=C), C–N/C–OH, C–O–C, C=O, and K $2p_{3/2}$,

respectively, confirming the presence of rGO and K, as well as oxygen-containing functional groups distributed across the nanocomposite surface [209]. These characteristics influence the electrical structure and surface reactivity of the nanocomposites. On comparison, the binding energies of Ti^{4+} $2p_{3/2}$ and $2p_{1/2}$ in KBN@TiO_2@rGO are slightly shifted to higher values relative to those in KBN@TiO_2 (Figure S5.2), indicating strong interactions between Ti species and the oxygen-containing functional groups of rGO. The B 1s spectrum in Figure 5.3e exhibits a distinct peak at 191.1 eV, attributed to B–O–Ti, which indicates the presence of interstitial boron [210]. This bonding configuration is known to influence the surface chemistry by reducing the band gap energy of modified TiO_2 [14]. The peak at 191.9 eV stem from B_2O_3 surface species. The N 1s spectrum in Figure 5.3f shows two prominent peaks at 399.76 eV and 400.8 eV, corresponding to different nitrogen functionalities. These peaks provide information about nitrogen-containing species, such as amino groups and graphitic nitrogen. The identification of K, B, and N elements by XPS affirms their successful incorporation in the prepared composite. The co-doping of B and N has been widely reported to synergistically enhance the visible light activation ability of TiO_2 by modulating its electronic structure and suppressing charge recombination compared to B or N doping [210]. Whereas the K doping that was observed in Figure 5.3d primarily contributes to the improvement of the TiO_2 crystalline structure stability and strengthens the catalytic properties of the nanocomposites, which is more evident from the high photodegradation ability of KBN@TiO_2@rGO than BN@TiO_2@rGO, which is described in section 3.2.

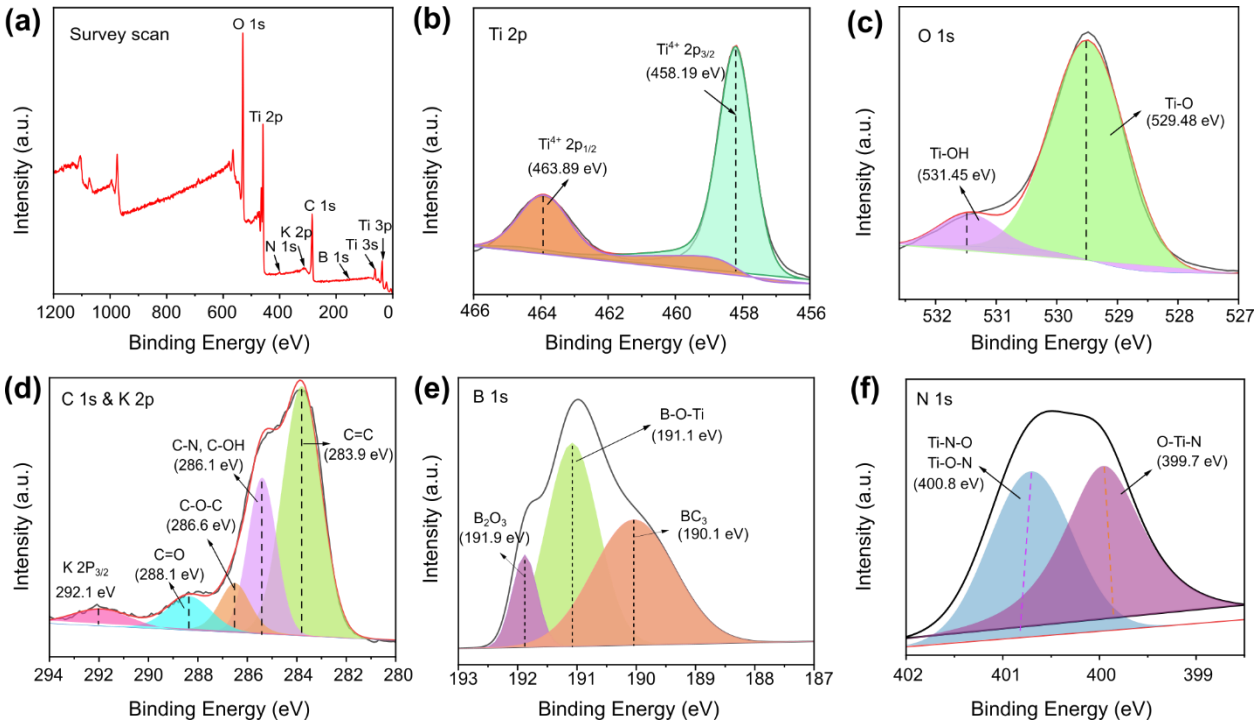

Figure 5.3 XPS analysis of KBN@TiO_2@rGO NCs: (a) Overall survey, (b) Ti 2p, (c) O 1s, (d) C 1s + K 2p, (e) B 1s, and (f) N 1s.

5.3.1.4 Evaluation of optical, photoluminescence and electrochemical properties

DRS can be used to determine the band gap energy (E_g) of materials by analysing their light absorption performance and applying relevant transformation equations. As illustrated in Figure S5.3, the absorption edge of TiO_2 is limited to wavelengths below 400 nm. However, the absorption edges of KBN@TiO_2 and KBN@TiO_2@rGO demonstrate a significant redshift, as shown in Figure 5.4a. This enhancement is likely attributed to KBN doping within the TiO_2 lattice and the interfacial interaction between rGO and TiO_2 following hydrothermal treatment [79]. The introduction of rGO into KBN@TiO_2 further increases light absorption in both the visible and ultraviolet regions, suggesting that KBN@TiO_2@rGO can absorb more visible light. The band gap energy (E_g) values for TiO_2, rGO, KBN@TiO_2, and KBN@TiO_2@rGO were calculated using Tauc's equation (Eq. 5.3):

$$(\alpha h\nu)^{1/n} = A(h\nu - E_g) \tag{5.3}$$

where A is a constant, while h, α, ν, and E_g denote the Planck constant (eV·s), absorption coefficient (cm^{-1}), photon's frequency (s^{-1}), and band gap energy (eV), respectively. The transition characteristics of the semiconductor establish n (TiO_2, $n = 4$) [211]. The calculated

band gap energies (E_g) for TiO_2, rGO, KBN@TiO_2, and KBN@TiO_2@rGO were 3.21, 0.76, 2.87, and 2.11 eV, respectively, as shown in Figures S5.3 and 5.4b. Compared with TiO_2 and KBN@TiO_2, the KBN@TiO_2@rGO composite exhibits the lowest bandgap energy, indicating its enhanced capability to harvest solar light for photocatalytic applications.

PL spectra of the modified TiO_2 (KBN@TiO_2) and KBN@TiO_2@rGO photocatalysts are presented in Figure 5.4c. The PL spectrum's peak intensity reflects the recombination rate of photo-generated electron–hole pairs [24]. A lower PL intensity corresponds to a reduced recombination rate, enabling more efficient charge separation and transport. The highest intensity was observed at an excitation wavelength of 458 nm, with a prominent emission peak in the 380–480 nm range. Notably, the PL intensity of KBN@TiO_2@rGO was significantly lower than that of KBN@TiO_2, indicating that the incorporation of KBN dopants and rGO suppresses the recombination of photo-induced holes and electrons, thereby improving the photocatalytic activity of the nanocomposite.

Electrochemical impedance spectroscopy (EIS) analysis was performed for TiO_2, KBN@TiO_2, and KBN@TiO_2@rGO samples at open circuit potentials under dark conditions (Figure 5.4d). The Nyquist plot results display no semi-circle region at high frequencies for all three tested materials, which indicates the charge transfer kinetics at these interfaces are extremely fast. Similarly, the Warburg impedance at the low-frequency region showed a straight line and their angles were > 45°, >60°, and >70° for TiO_2, KBN@TiO_2, and KBN@TiO_2@rGO, respectively. These features represent that ion diffusion becomes limited upon doping and exhibited a finite-length diffusion for KBN@TiO_2@rGO due to the more porous nature of rGO. Mott-Schottky (M-S) analysis for TiO_2, KBN@TiO_2, and KBN@TiO_2@rGO modified electrodes was conducted at an applied frequency of 1000 Hz (Figure 5.6e) to understand the nature of the semiconductor. Only TiO_2 exhibited the n-type semiconductor characteristics in the tested potential window. Whereas, KBN@TiO_2, and KBN@TiO_2@rGO reveal both n-type and p-type semiconductor features upon doping [238]. These unique M-S features suggest that the crystal structure of the TiO_2 contains these doped elements. Furthermore, the intercept of these positive slopes shifted to smaller values for KBN@TiO_2 and KBN@TiO_2@rGO compared to TiO_2. The negative shift observed in the flat band potential (E_{fb}) of these materials indicates that these materials exhibit higher donor density, which is associated with the defects created by the B, N, and K atoms in the TiO_2.

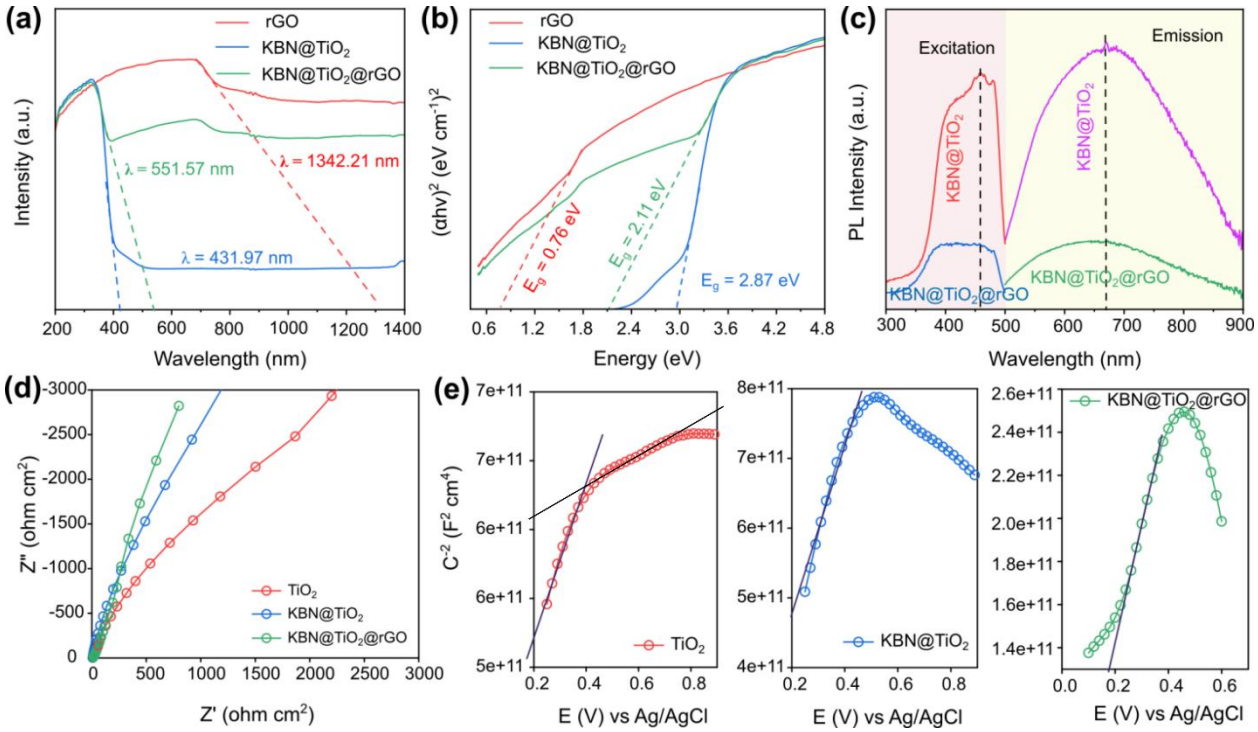

Figure 5.4 UV-Vis diffuse reflectance spectra of (a) rGO, KBN@TiO_2, and KBN@TiO_2@rGO, (b) Tauc plots of rGO, KBN@TiO_2, and KBN@TiO_2@rGO, and (c) PL spectra of KBN@TiO_2 and KBN@TiO_2@rGO. (d) EIS Nyquist plot and (e) Mott-Schottky plot for different materials.

5.3.2 Effect of rGO content and photocatalytic activity of the composite

A high surface area in the TiO_2@rGO nanocomposite primarily depends on the weight percentage of rGO [226]. As shown in Figure S5.4a-b, increasing the weight ratio of rGO from 5% to 15% led to a rise in adsorption efficiency from 12.10% to 34.32%, primarily due to the increased surface area. However, the photocatalytic performance decreased slightly from 94.29% to 91.15% (Figure S5.4c), accompanied by a reduction in the reaction rate constant from 0.0206 to 0.0167 min^{-1} (Figure S5.4d). This can be explained by the possibility that a high rGO loading (wt.%) can inhibit the active sites of KBN@TiO_2 [230]. The 10% rGO loading in KBN@TiO_2 provides an effective compromise between maintaining active sites and boosting photocatalytic activity. This composition achieved a notably high degradation efficiency under visible light irradiation. A 5% decrease in the rGO level leads to a slight increase in photocatalytic activity. Thus, 10% rGO was identified as the optimum mass ratio for compositing with modified KBN@TiO_2, achieving the maximum photocatalytic performance for antibiotic degradation.

5.3.2.1 Catalyst selection

CIP adsorption performance was evaluated using both undoped and doped TiO_2 under dark

conditions for 60 min until adsorption–desorption reached equilibrium. As shown in Figure 5.5a, the rGO modified KBN@TiO_2 composite exhibited improved CIP adsorption efficiency except for TiO_2@rGO. A lower adsorption capacity often suggests enhanced photocatalytic performance, as more active sites remain available for photodegradation reactions [234]. In contrast, KBN@TiO_2@rGO achieved a CIP degradation efficiency of 99.21% within 120 min (Figure 5.5c), with a corresponding degradation rate constant (k_{deg}) of 0.0337 min^{-1} (Figure 5.5d). These findings confirm that the KBN-doped TiO_2@rGO photocatalyst exhibited excellent CIP degradation efficiency compared to both undoped TiO_2@rGO and BN-doped TiO_2@rGO.

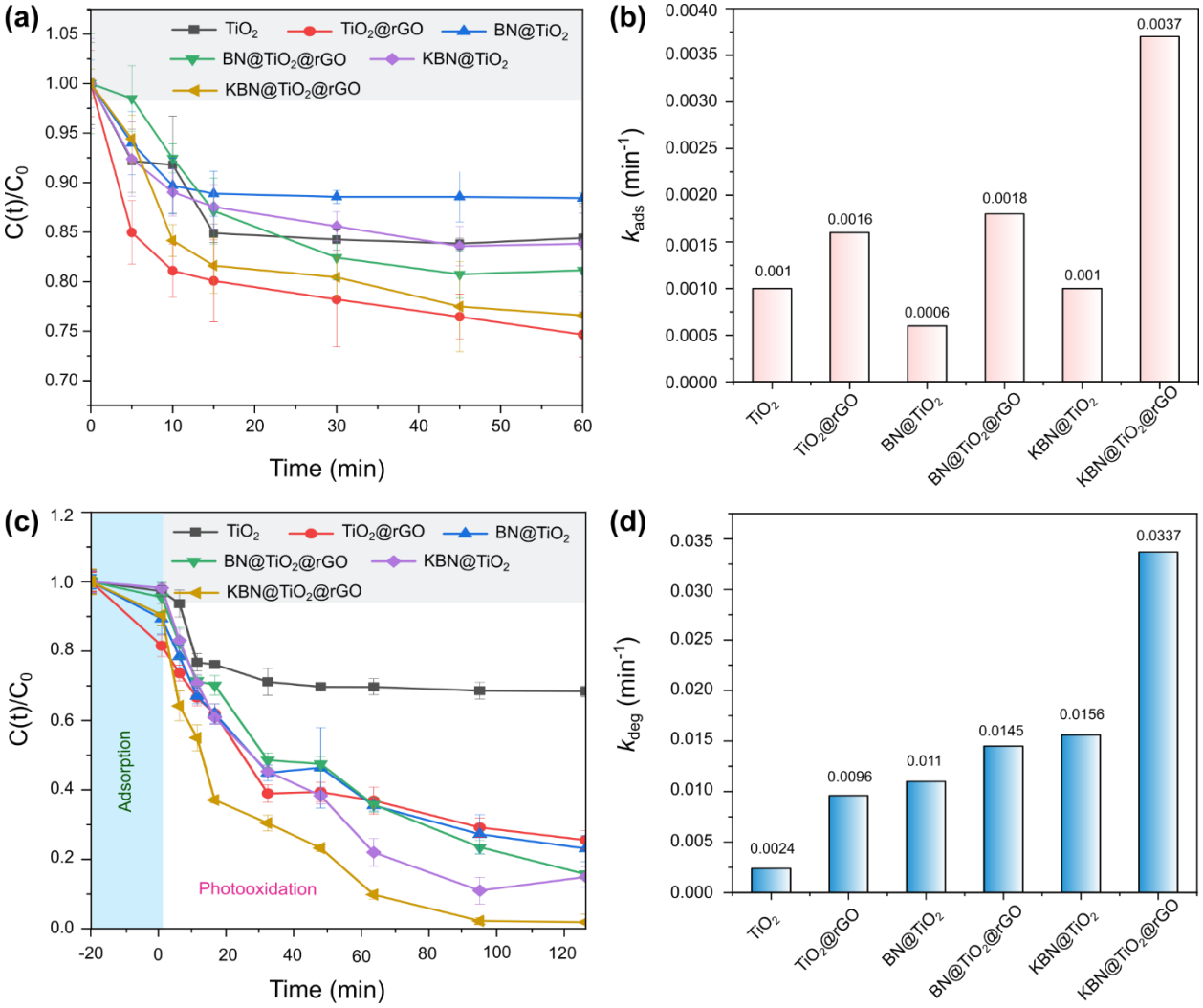

Figure 5.5 Evaluation of catalyst performance (a) adsorption, (b) pseudo-first-order rate constants for adsorption, (c) photocatalytic degradation, and (d) pseudo-first-order rate constants for photocatalytic degradation system. (Experimental conditions: $[CIP]_0$ = 10 mg L^{-1}, catalyst dose = 0.2 g L^{-1}, unadjusted pH = 5.23, at controlled temperature = 23°C).

The first-order kinetic model further supported the reaction rate analysis. As shown in Figures 5.5b and 5.5d, the first-order rate constant for the adsorption process (k_{ads}) was 3.7×10^{-3} min^{-1} for KBN@TiO_2@rGO, while for degradation, the k_{deg} value was 3.37×10^{-2} min^{-1} **(**Tables 5.2 and 5.3**)**. Furthermore, BET analysis confirmed that KBN@TiO_2@rGO possesses a higher number of active sites (Figure 5.2c). This photocatalyst also exhibited a narrow band gap energy (Figure 5.4b) that enables more ROS generation that readily oxidise antibiotics [202]. As shown in Tables S5.2a and S5.2b**,** the CIP removal performance of KBN@TiO_2@rGO surpasses that of many reported TiO_2 derivatives and metal oxide systems (e.g., MoS_2, ZnO, WO_3, Bi-O). The composite achieves a CIP removal of 99.21% at lower catalyst dosage and within shorter irradiation times, reflecting its superior catalytic efficiency. This improvement is mainly attributed to ternary B/N/K doping, which enhances visible-light utilisation and charge separation, together with rGO providing an efficient electron transport pathway.

Table 5.2: Effect of adsorption on CIP removal by the synthesised catalysts.

Catalyst type	**Removal (%)**	k_{ads} **(min^{-1})**	$t_{1/2}$ **(min^{-1})**	R^2
TiO_2	15.59 ± 0.032	0.0010	693.00	0.5909
TiO_2/rGO	25.34 ± 0.022	0.0016	433.13	0.6199
BN@TiO_2	11.57 ± 0.053	0.0006	1155.00	0.4598
BN@TiO_2/rGO	18.85 ± 0.008	0.0018	385.00	0.8090
KBN@TiO_2	16.16 ± 0.030	0.0010	693.00	0.7267
KBN@TiO_2/ rGO	23.41 ± 0.011	0.0037	187.30	0.9135

k_{ads} = Adsorption pseudo-first-order kinetic rate constant (min^{-1}), $t_{1/2}$ = Half-life of the reaction (min^{-1}).

Table 5.3: Effect of photocatalysis on CIP degradation by the synthesised catalysts.

Catalyst type	**Removal (%)**	k_{deg} **(min^{-1})**	$t_{1/2}$ **(min^{-1})**	R^2
TiO_2	31.57 ± 0.016	0.0024	288.75	0.5307
TiO_2/rGO	74.46 ± 0.027	0.0096	72.19	0.8813
BN@TiO_2	76.92 ± 0.037	0.0110	63.00	0.9422
BN@TiO_2/rGO	84.30 ± 0.020	0.0145	47.80	0.9874
KBN@TiO_2	85.04 ± 0.029	0.0156	44.42	0.9338
KBN@TiO_2/rGO	98.10 ± 0.023	0.0337	20.56	0.9627

k_{deg} = Pseudo-first-order degradation rate constant (min^{-1}), $t_{1/2}$ = Half-life of the reaction (min^{-1}).

5.3.2.2 Effect of catalyst dosage

Figure 5.6a and Table S5.3 present the effect of KBN@TiO_2@rGO concentration on CIP degradation efficiency. When the catalyst dosage was increased from 25 mg L^{-1} to 200 mg L^{-1}, the KBN@TiO_2@rGO system exhibited a significant enhancement in the photodegradation efficiency of CIP, with the removal percentage rising from 76.23% to 99.59% within 120 min. Correspondingly, the k_{deg} value increased from 0.0113 min^{-1} to 0.0325 min^{-1}, as shown in Table S5.3. This can be attributed to the continuous increase in the active radical's generation with KBN@TiO_2@rGO dosage. However, when the photocatalyst dosage was further increased to 250 mg L^{-1}, the degradation efficiency decreased slightly to 97.33%, and the corresponding k_{deg} value decreased to 0.0275 min^{-1}. This reduction in performance is attributed to the obstruction of light caused by the increase in photocatalyst dosage [212]. Therefore, a catalyst dosage of 200 mg L^{-1} was identified as optimal KBN@TiO_2@rGO concentration for further studies.

5.3.2.3 Effect of initial CIP concentration

Figure 5.6b illustrates the impact of varying initial CIP concentrations (1−10 mg L^{-1}) on the photocatalytic degradation efficiency of the KBN@TiO_2@rGO system. As the initial CIP concentration increased, a gradual decline in CIP degradation efficiency, with removal rates of 100%, 100%, 99.09%, 98.84%, and 96.08% corresponding to initial concentrations of 1, 3, 5, 7, and 10 mg L^{-1}, respectively. These findings indicate that KBN@TiO_2@rGO maintains a high level of photocatalytic activity even at elevated CIP concentrations (10 mg L^{-1}). Furthermore, as presented in Table S5.3, the k_{deg} value decreased from 0.1807 to 0.0337 min^{-1} as the initial CIP concentration increased from 1 to 10 mg L^{-1}, respectively. The plausible reasons for this phenomenon are outlined as follows: (1) Higher concentrations of CIP may result in a photon-shielding effect between the molecules, reducing the number of photons that reach the catalyst surface [213]; (2) the increased antibiotic concentration leads to extensive coverage of the catalyst surface by CIP molecules, hindering the generation of free radicals and electron–hole pairs due to limited available active sites [214].

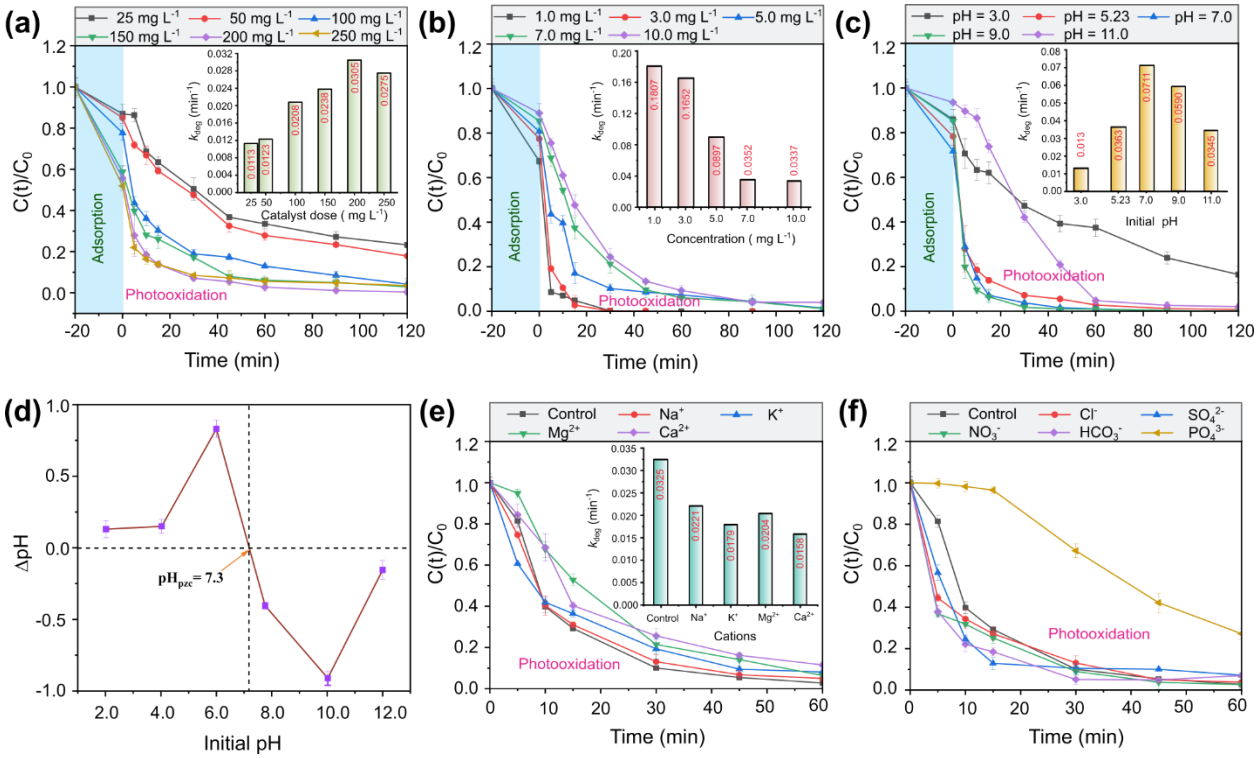

Figure 5-6 Effects of (a) catalyst dose, (b) initial CIP concentration, (c) initial pH, (d) point of zero charge (pHpcz) for KBN@TiO_2@rGO, (e) cation effects, and (f) anion effects on photocatalytic degradation of CIP using the KBN@TiO_2@rGO system. (Experimental conditions: $[CIP]_0$ = 10 mg L^{-1}, catalyst dose = 0.2 g L^{-1}, $[cations]_0$ = $[anions]_0$ = 200 mg L^{-1}, unadjusted pH = 5.23, at controlled temperature = 23°C).

5.3.2.4 Effect of initial pH values

The initial solution pH highly influences photodegradation, as it directly alters the catalyst's surface charge characteristics. Therefore, the photodegradation efficiency of KBN@TiO_2@rGO was evaluated at pH values of 3, 5.23 (unadjusted), 7, 9, and 11. As shown in Figure 5. 6c**,** the initial pH was varied while other operational parameters were held constant. When the initial solution pH was adjusted to 3, 5.23, 7, 9, and 11 before the reaction, the corresponding photocatalytic degradation efficiencies were 83.60%, 99.21%, 99.99%, 99.94%, and 97.96%, respectively, within 120 min, as shown in Figure S5.5c. The k_{deg} at these pH values was 0.0130, 0.0363, 0.0711, 0.0590, and 0.0345 min^{-1}, respectively (Table S5.4**)**. The photodegradation efficiency was notably lower at pH 3, primarily due to the strong acidity of the solution. The excess H^+ ions likely consumed the generated •OH radicals, thereby hindering their reaction with CIP and slightly suppressing the overall photodegradation efficiency. Furthermore, CIP possesses pKa values of 5.9 and 8.9, which indicate that it exists as a cation

below pH 5.9, a zwitterion between pH 5.9 and 8.9, and an anion above pH 8.9 [89]. As illustrated in Figure 5.6d**,** the pH_{pzc} of the KBN@TiO_2@rGO nanocomposite was determined to be 7.3. Accordingly, the catalyst surface becomes negatively charged at pH values above 7.3, favouring the adsorption of cationic species (CIP^+), while it remains positively charged at pH values below this threshold, promoting the attraction of anionic species (CIP^-) to the surface. Photodegradation activity increased progressively as the pH was raised from 3 to 7, with 99.99% photodegradation achieved within 120 min at pH 7. However, in the high pH conditions, the photodegradation efficiency declined only slightly. This reduction is primarily attributed to electrostatic repulsion occurring above pH 8.9, where CIP exists predominantly as an anion, and the surface of KBN@TiO_2@rGO was also negatively charged (Figure 5.6d). This like-charge interaction hinders the adsorption of CIP onto the photocatalyst surface. Despite this, a significant CIP degradation was observed at pH 11 after 1 h. These results demonstrate that the KBN@TiO_2@rGO nanocomposite exhibits robust photocatalytic performance across a broad pH range (3–11), highlighting its strong potential for environmental remediation applications.

5.3.2.5 Effects of cations, anions and Humic Acid

The treatment of real wastewater is often complicated by the presence of inorganic ions, which compete with target pollutants for ROS [55]. Figure 5.6e illustrates the effects of various inorganic cations on the photodegradation efficiency of CIP using the KBN@TiO_2@rGO system. The presence of Na^+, K^+, Mg^{2+}, and Ca^{2+} slightly inhibited photodegradation activity, resulting in efficiencies of 94.96%, 91.88%, 93.59%, and 88.47%, respectively, compared to 97.24% in the control (Table S5.5). All measurements were taken after 120 min of irradiation. Both wastewater and natural water contain inorganic salts that affect the photocatalytic activity of photocatalysts. Therefore, the effects of various inorganic anions such as Cl^-, SO_4^{2-}, NO_3^-, HCO_3^-, and PO_4^{3-} on the photodegradation effectiveness of CIP were examined. As shown in Figure 5.6f, the introduction of 200 mg L^{-1} of each anion exhibits different inhibitory effects on CIP photocatalytic efficiency, following the order: $PO_4^{3-} > SO_4^{2-} > HCO_3^- > Cl^- > NO_3^-$ (Figure S5.5). After 120 min of exposure to PO_4^{3-}, only 72.81% of CIP was degraded, and the k_{deg} significantly decreased from 0.0325 min^{-1} to 0.01 min^{-1}, as shown in Table S5.5. This reduction in photocatalytic efficiency can be attributed to: (1) phosphate ions (PO_4^{3-}) inhibit radical formation that adsorb onto the surface of photocatalysts such as TiO_2 [243]. As a result, fewer active sites are available for photocatalytic processes; (2) the efficacy of the photocatalytic process may be diminished by the potential of phosphate ions to promote the

recombination of photogenerated electron–hole pairs.

The degradation efficiency of CIP also slightly decreased in the presence of HCO_3^-, dropping from 97.24% to 92.97%, while k_{deg} declined from 0.0325 to 0.0183 min^{-1}, indicating a slight inhibitory effect of HCO_3^- (Table S5.5). In addition, the carbonate ion scavenges h^+ and $^\bullet OH$ to generate $CO_3^{\bullet-}$, which reduces the oxidation potential **(**Eqs. (5.7) and (5.8)). The addition of HCO_3^- to the CIP solution increases the pH to 12, leading to stronger electrostatic repulsion between the negatively charged KBN@TiO_2@rGO nanoparticles and the anionic form of CIP. This repulsion inhibits adsorption onto the catalyst surface, thereby reducing degradation efficiency compared to the KBN@TiO_2@rGO system alone [216].

$$Cl^- + {}^\bullet OH \rightarrow {}^\bullet Cl + OH^- \quad (5.4)$$

$$Cl^- + h^+ \rightarrow {}^\bullet Cl \quad (5.5)$$

$${}^\bullet Cl + Cl^- \rightarrow {}^\bullet Cl_2^- \quad (5.6)$$

$$CO_3^{2-} + {}^\bullet OH \rightarrow CO_3^{\bullet-} + OH^- \quad (5.7)$$

$$CO_3^{2-} + h^+ \rightarrow CO_3^{\bullet-} \quad (5.8)$$

$$SO_4^{2-} + {}^\bullet OH \rightarrow SO_4^{\bullet-} + OH^- \quad (5.9)$$

$$SO_4^{2-} + h^+ \rightarrow SO_4^{\bullet-} \quad (5.10)$$

$$NO_3^- + H_2O + hv \rightarrow NO_2^{\bullet} + OH^- + {}^\bullet OH \quad (5.11)$$

$$NO_3^- + h^+ \rightarrow NO_3^{\bullet} \quad (5.12)$$

Interestingly, the presence of Cl^- and SO_4^{2-} did not significantly impede the photocatalytic degradation of CIP. The degradation efficiencies were 96.20% and 92.82%, with corresponding k_{deg} values of 0.0226 and 0.0164 min^{-1}, respectively. The minor inhibitory effect of these anions on CIP photodegradation with the KBN@TiO_2@rGO system is primarily attributed to the formation of less reactive species ($^\bullet Cl$ and $^\bullet Cl_2^-$) compared to $^\bullet OH$, as shown in Eqs. (5)– (10). Additionally, the influence of NO_3^- ions on the photocatalytic degradation of CIP was examined. The introduction of nitrate ions had a negligible effect on the degradation efficiency, which remained essentially unchanged, increasing only slightly from 97.24% to 97.40%. This marginal increase may be attributed to the generation of additional reactive radicals (Eqs. 11 and 12), despite a decrease in k_{deg} from 0.0325 to 0.0251 min^{-1}. Nitrate ions can also act as electron acceptors, which lowers the recombination of photogenerated electron–hole pairs, promotes synergistic effects of active radicals (see Eqs. 5.11 and 5.12) and enhances photocatalytic efficiency. Thus, in the KBN@TiO_2@rGO system, cations and anions did not

significantly inhibit CIP photodegradation, except for phosphate ions.

Considering that humic acid (HA) is a major constituent of natural organic matter (NOM) commonly present in both groundwater and surface water, it was selected as the model organic compound to investigate the effects of NOM on CIP degradation. As shown in Figure 5.7a**,** the photodegradation of CIP decreased markedly from 97.24% to 87.57%, 73.07%, 68.24%, and 20.13% as the HA concentration increased from 0 mg L^{-1} to 25, 50, 100, and 200 mg L^{-1}, respectively. The k_{deg} value also decreased from 0.0325 min^{-1} to 0.0112, 0.0081, and 0.0016 min^{-1}, respectively, as shown in Figure 5.7b. This reduction can be attributed to the interaction between HA and •OH [216]. Moreover, TiO_2 can also interact with humic substances, including HA, through adsorption to produce surface complexes. The functional groups present in HA, such as carboxyl (–COOH) and hydroxyl (–OH) groups, commonly bind to the surface of TiO_2 particles to form these complexes [217].

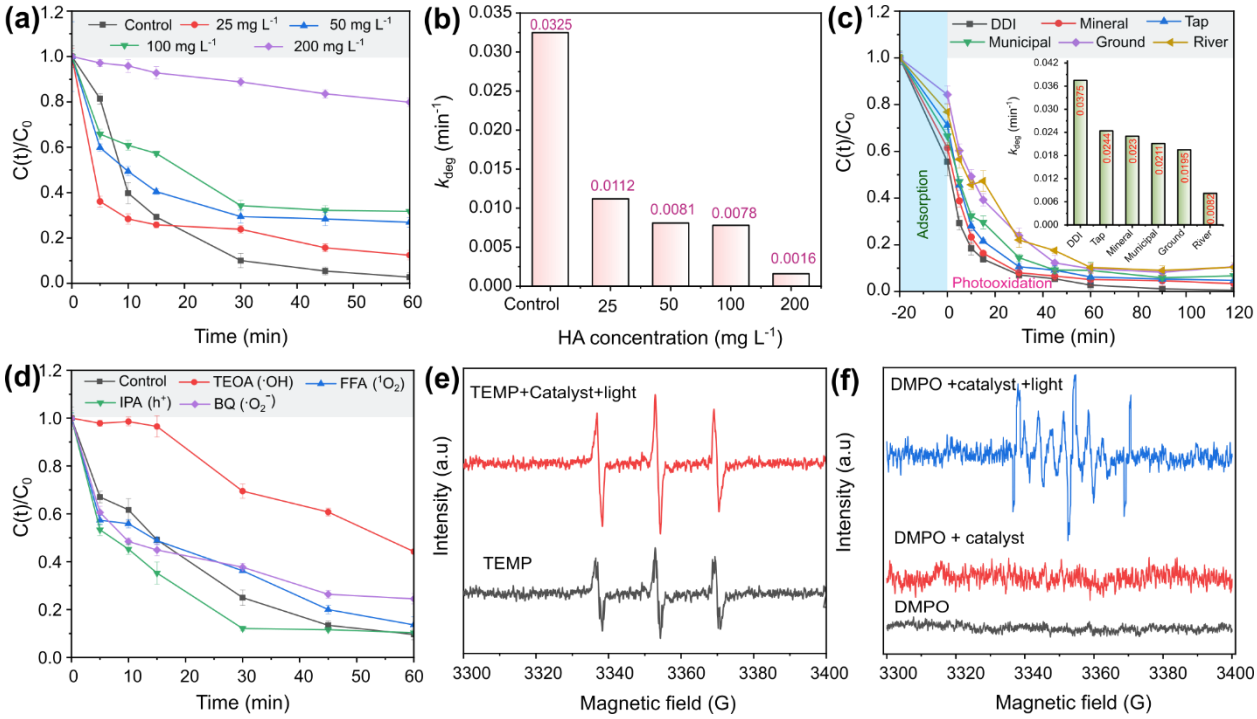

Figure 5.7 Effects of (a) humic acid, (b) rate constants at different concentrations of HA, (c) effects of water matrix, (inset) corresponding rate constant values, (d) quenching experiments, ESR spectra using (e) TEMP and (f) DMPO spin-trapping agents. (Experimental conditions: $[CIP]_0$ = 10 mg L^{-1}, catalyst dose = 0.2 g L^{-1}, $[scavenger]_0$ = 5 mM, and unadjusted pH = 5.23, at controlled temperature = 23 °C).

5.3.2.6 Effect of water matrix

The photocatalytic performance of the synthesised KBN@TiO_2@rGO composite for CIP degradation was further evaluated in various water matrices, such as mineral water, tap water, municipal wastewater, ground water, and river waters. As shown in Figure 5.7c**,** the CIP degradation efficiency varied across these matrices with KBN@TiO_2@rGO. The order of degradation efficiency was as follows: DDI water > mineral water (MW) > tap water (TW) > municipal wastewater (MWW) > river water (RW) > groundwater (GW), with corresponding values of 99.46%, 96.66%, 95.22%, 93.28%, 89.59%, and 89.37%, respectively, (Figure S5.5). The respective k_{deg} values were 0.0375, 0.0244, 0.023, 0.0211, 0.0195 min^{-1}, and 0.0082 min^{-1} as presented in Figure 5.7c and Table S5.6**.** Notably, the overall degradation efficiency of KBN@TiO_2@rGO in all water samples decreased by approximately 10.09% compared to the control (DDI water). This finding indicates that the KBN@TiO_2@rGO composite nanomaterial exhibited robust photocatalytic performance across different water matrices, consistent with the observed influence of anions. The reduced photodegradation efficiency of CIP in groundwater is attributed to the high concentrations of dissolved chloride (Cl^-), sulfate (SO_4^{2-}), and bicarbonate (HCO_3^-) ions, which can act as scavengers for ROS [227]. This explanation is further supported by the experimental results presented in Table S5.7.

$$^{\bullet}OH + CO_3^{2-} \rightarrow OH^- + O_3^{\bullet-},\ k = 3.9\times10^8\, M^{-1}s^{-1} \quad (5.13)$$

$$^{\bullet}OH + SO_4^{2-} \rightarrow OH^- + SO_4^{\bullet-},\ k = 3.5\times10^5\, M^{-1}s^{-1} \quad (5.14)$$

$$^{\bullet}OH + Cl^- \rightarrow ClOH^{\bullet-} + Cl_2^{\bullet-},\ k = 4.31\times10^9\, M^{-1}s^{-1} \quad (5.15)$$

5.3.2.7 Identification of ROS KBN@TiO_2@rGO system

Quenching experiments were performed to identify the ROS ($^{\bullet}OH$, $^1O_2$, and $O_2^{\bullet-}$) generation in the KBN@TiO_2@rGO system (Figure 5.7d). Totally four reagents, triethanolamine (TEOA; for • $^{\bullet}OH$), furfuryl alcohol (FFA; for $^1O_2$), isopropyl alcohol (IPA; for h^+), and benzoquinone (BQ; for $O_2^{\bullet-}$) were used as radical and non-radical trapping agents [218]. The addition of each scavenger showed a varying degree of inhibition for CIP degradation. Among these, $^{\bullet}OH$ exhibited the strongest inhibitory effect, followed by $O_2^{\bullet-}$, $^1O_2$, and h^+. In the presence of TEOA, only 55.76% (6.12×10^{-3} min^{-1}) of CIP was degraded, highlighting the pivotal role of $^{\bullet}OH$ in the KBN@TiO_2@rGO-mediated degradation process. Interestingly, non-radical, singlet oxygen ($^1O_2$) also contributed to CIP degradation. The CIP removal efficiency decreased from 99.21% to 86.38%, and the corresponding *k* value declined from 0.0363 to 0.0130 min^{-1} when

FFA was added as a scavenger. This result indicates that the CIP/KBN@TiO_2@rGO system under visible light irradiation generates non-radical $^1O_2$. The ROS generation rates (Eq. S5) of $^{\bullet}OH$, $^1O_2$, h^+, and $O_2^{\bullet-}$, were found to be 2.76 × 10^{-2} mg min^{-1}, 2.07 × 10^{-2} mg min^{-1}, 1.82 × 10^{-2} mg min^{-1}, and 2.50 mg min^{-1} in the KBN@TiO_2@rGO system, respectively (Text S5.7, Table S5.8). These findings confirm that the hydroxyl radical ($^{\bullet}OH$) played a dominant role in the photocatalytic degradation of CIP within the KBN@TiO_2@rGO system.

$$H_2O \rightarrow {}^{\bullet}OH + H^+ \quad (5.16)$$

$$O_2 + e^- \rightarrow {}^{\bullet}O_2^- \quad (5.17)$$

$$h^+ + OH^- \rightarrow {}^{\bullet}OH \quad (5.18)$$

$$^{\bullet}O_2^- + 2H_2O \rightarrow {}^1O_2 + H_2O_2 + 2OH^- \quad (5.19)$$

$$^{\bullet}O_2^- + {}^{\bullet}OH + 2H^+ \rightarrow {}^1O_2 + OH^- \quad (5.20)$$

$$\text{Radicals} + CIP + KBN@TiO_2@rGO \rightarrow \text{products } (CO_2 + H_2O) + \text{intermidates} \quad (5.21)$$

The role of ROS in CIP degradation by the KBN@TiO_2@rGO system was further validated by ESR analysis, as presented in Figures 5.7e and 5.7f. 5,5-Dimethyl-1-pyrroline N-oxide (DMPO) was employed as a spin-trapping agent for the radical species ($^{\bullet}OH$ and $O_2^{\bullet-}$), while 2,2,6,6-tetramethylpiperidine (TEMP) was used for the non-radical $^1O_2$. As shown in Figure 5.7f, weak ESR signals corresponding to $^{\bullet}OH$ and comparatively stronger signals for $O_2^{\bullet-}$ were observed. Additionally, $^{\bullet}OH$ can react with $O_2^{\bullet-}$ to form $^1O_2$ (Eq. 20). Although hydroxyl radicals ($^{\bullet}OH$) were identified as the most actively generated radicals and played a dominant role by scavenger experiments, the ESR analysis revealed only weak $^{\bullet}OH$ signals. This is attributed to the extremely short lifespan of $^{\bullet}OH$, which makes it difficult to capture its formation at a specific reaction time during the photocatalytic process. A triplet signal with a 1:1:1 spin-splitting pattern was observed when TEMP was used as a spin-trapping agent in the KBN@TiO_2@rGO system, indicating the formation of $^1O_2$, as shown in Figure 5.7e. Singlet oxygen ($^1O_2$) is a non-ionic, non-radical species generated from the lowest excited state of $O_2^{\bullet-}$ [21]. The ESR signal intensity for the TEMP + catalyst + light combination was higher than that of TEMP alone, further confirming the involvement of $^1O_2$ in CIP degradation.

5.3.3 Adsorption kinetics and isotherms

To examine the adsorption characteristics and mechanism of KBN@TiO_2@rGO for CIP removal, the impact of adsorption time on removal efficacy was investigated using pseudo-first-order (PFO) and pseudo-second-order (PSO) adsorption kinetic models (Figure S5.6a,

Figure S5.6b, and Table 5.4). The equations for the PSO and PFO models are provided in Text S5.6 (Eqs. S5.1 and S5.2). The PFO model (k_1 = 0.2626 min^{-1}) suggested a moderate initial adsorption rate; however, the calculated adsorption capacity ($q_{e(cal)}$) significantly exceeded the experimental value, implying poor model accuracy. Moreover, the low correlation coefficient (R^2 =0.8063) further confirmed that the PFO model did not adequately describe the adsorption process. In contrast, the PSO model (k_2 = 0.0285 g mg^{-1} min^{-1}) demonstrated a better fit, as evidenced by a higher correlation coefficient (R^2 = 0.9988), indicating that the adsorption process followed chemisorption and was more accurately described by the PSO model. Furthermore, the equilibrium adsorption capacity calculated from the PSO model ($q_{e(cal)}$ = 25.77 mg g^{-1}) closely matched the experimental value ($q_{e(exp)}$ = 25.06 mg g^{-1}), indicating strong agreement. Based on the overall evaluation, the PSO kinetic model provided a more accurate representation of the CIP adsorption process on KBN@TiO_2@rGO than the PFO model. This suggests that the adsorption mechanism is chemisorption, which primarily involves the sharing or exchange of electrons between the adsorbent and the adsorbate [215].

Table 5.4: The fitting constant of adsorption kinetics for CIP removal on KBN@TiO_2@rGO.

$q_{e(exp)}$ (mg g^{-1})	Pseudo-first order	Pseudo-second order
25.06	k_1 (min^{-1}) = 0.2626	k_2 (g mg^{-1} min^{-1}) = 0.0285
	$q_{e(cal)}$ (mg g^{-1}) = 48.53	$q_{e(cal)}$ (mg g^{-1}) = 25.77
	R^2 = 0.8063	R^2 = 0.9988

q_e(exp): Equilibrium adsorption capacity was directly calculated using experimental data, $q_{e(cal)}$: Equilibrium adsorption capacity was directly calculated using fitted model, k_1: Pseudo-first-order rate constant, k_2: Pseudo-second-order rate constant, R^2: Coefficient of determination.

The adsorption characteristics of KNB@TiO_2@rGO towards the antibiotic CIP were examined in the study at various initial concentrations, ranging from 1 to 20 mg L^{-1}. The two most common models, Langmuir and Freundlich, were used to fit the experimentally generated data (Figures S5.6c and S5.6d)**,** and applicable parameters are presented in Table 5.5. The Langmuir adsorption isotherm model appears to represent the adsorption process better, as evidenced by its relatively high coefficient of determination, R^2 = 0.9876, based on the fitting parameters. The maximum adsorption capacity of 29.56 mg g^{-1} indicates that the adsorption of CIP onto KBN@TiO_2@rGO material occurs via a monolayer adsorption process [247]. The predicted

(1/*n*) values (0.4239) of the Freundlich model are less than 1, indicating that CIP may absorb favourably onto KBN@TiO_2@rGO [215].

Table 5.5: The isothermal adsorption parameters for CIP on KBN@TiO_2@rGO.

Langmuir	Freundlich
q_m = 29.5596 (mg g^{-1})	1/*n* = 0.4239
K_L = 1.4203 (L mg^{-1})	K_F = 13.5119
R^2 = 0.9876	R^2 = 0.8972

q_m: Maximum adsorption capacity, K_L: Langmuir constant,1/*n*: non-uniform factor, K_F: Freundlich constant, and R^2: Coefficient of determination.

5.3.4 CIP degradation mechanisms and pathways

CIP degradation by photocatalysis is a complex process that produces several intermediates [220]. The main photodegradation by-products of CIP were discovered using UPLC-MS/MS in both detector types, ESI (–) and ESI (+), to investigate possible degradation mechanisms and intermediates. The relevant mass spectra in (a) ESI (–) and (b) ESI (+) are shown in Fig. S5.7. During the CIP photodegradation process, at least 22 intermediates were produced. After 60 min of irradiation, various degradation intermediates were present, and CIP was completely degraded after 120 min. Based on experimental data and previous studies [221,58], five potential degradation pathways were proposed, as illustrated in Figure 5. 8. The primary hydroxylation of the quinolone ring takes place initially in the degradation pathway (1). The structural formula for CIP (P1) $^{\bullet}OH$ targets the C2 site's hydroxylation, converting it to P2 (m/z 377.10). The piperazinyl moiety is initially oxidised by $O_2^{\bullet-}$, leading to the formation of intermediates P3 and P4. Subsequent oxidation of P4 results in the removal of alkylamine or aniline, yielding product P5. Further defluorination and cleavage of the piperazinyl structure led to the formation of P6. In pathways (2) and (3),$^{\bullet}OH$ and h^+ oxidatively eliminate the piperazine ring of CIP, producing intermediates P7/P12 (m/z 361.11) [250]. Through piperazine ring splitting and decarboxylation in the aniline or alkylamine's N14 site, pathway (2) produces P8 (m/z 333.11) from P7 [222]. Simultaneously, in pathway (3), P12 undergoes direct oxidation by photogenerated holes (h^+) to produce P13 [21]. After the hydroxylation process, P10 is formed, while P13 or P8 lose the formaldehyde group (P9) as a result of further oxidation by h^+ and $O_2^{\bullet-}$. Defluorination of P10 results in P11 [59, 20]. Furthermore, h^+ directly oxidises P10 to eliminate the carbonyl (C=O) group, producing P14. P19 is also generated through defluorination. In pathway (5), P18 (m/z 315.12) is produced via oxidation of the piperazine

ring, accompanied by the elimination of carbonyl groups and F atoms. After that, P18 undergoes N-dealkylation and decarboxylation to transform into P19 [223]. In pathway (4), P20 (m/z 347.13) was initially obtained through a different piperazine ring hydroxylation mechanism. By adding OH^- to the amine group after photocatalytic oxidation, P20 was further degraded to P21 [224]. During oxidation, a carbonyl group and P22 (m/z 345.11) are added to the piperazine ring [221]. Finally, the intermediates described above may undergo mineralisation into small inorganic molecules such as CO_2, H_2O, and F^-.

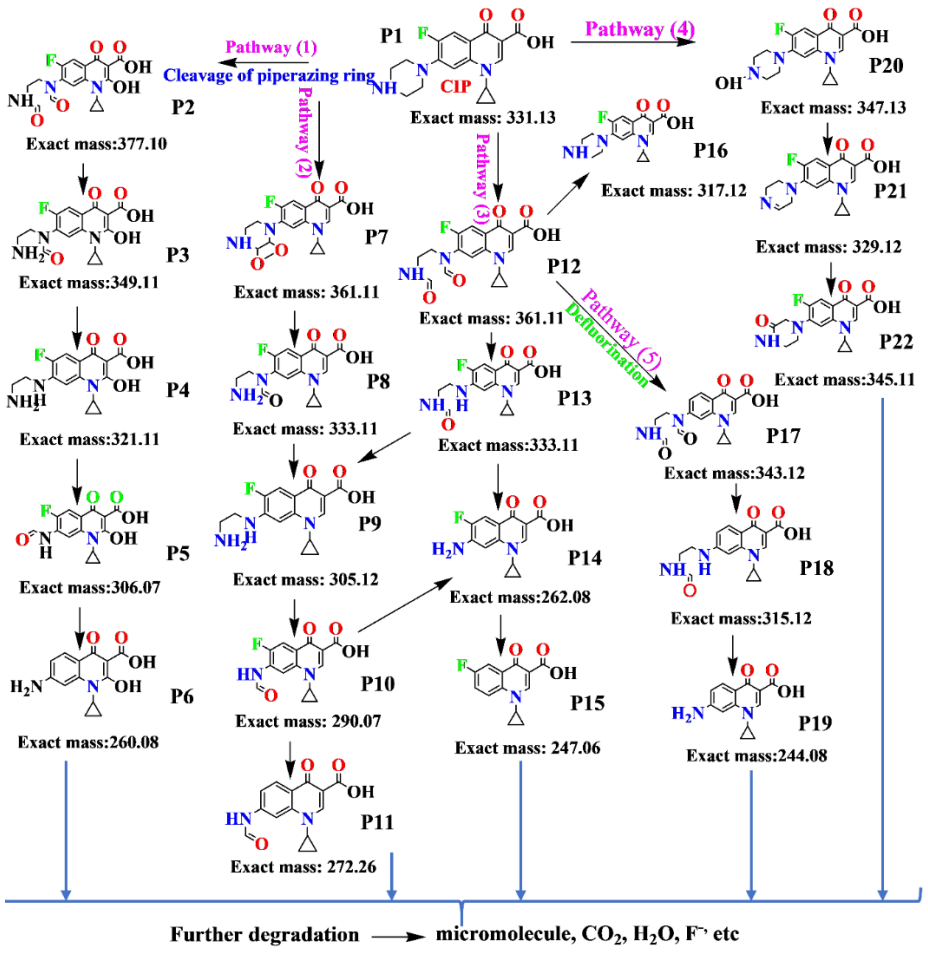

Figure 5-8 Possible degradation pathways of CIP in photocatalytic oxidation over the KBN@TiO_2@rGO system.

It is evident from the by-product analysis that the oxidative attack occurs predominantly at the substituent sites, however, the quinolone moiety of CIP is mostly unaffected. Since the system achieves only 75 % of total organic carbon (TOC) removal, the environmental toxicities of these by-products were assessed using ECOSAR toxicity analysis (Table S5.9). The acute toxicity caused by these CIP-degraded by-products on Fish, Daphnid, and green algae falls in

the not-harmful category. In contrast, the chronic toxicity analysis revealed that only the P15 and P21 species are harmful to Daphnid and fish, and green algae, respectively. The corresponding toxicity values are 87.2 mg L^{-1} (Daphnid) for P15 and 32.8 (Fish), 24.0 (Daphnid), 68.3 (green algae) mg L^{-1} for P21. Since the initial concentration of CIP (10 mg L^{-1}) employed in our study were well below these toxicity limits, the impact will be negligible in the reported system.

5.3.5 Reusability and stability of the KBN@TiO_2@rGO system

To fully assess the effectiveness of photocatalysts for practical applications, evaluating their reusability is essential. After use, the KBN@TiO_2@rGO was recycled by vacuum filtration, thoroughly washed with DDI water, dried at 50 ℃, and then quickly added to a new CIP solution to evaluate its reusability. As illustrated in Figure 5.9a, the KBN@TiO_2@rGO nanocomposite exhibited a satisfactory reusability performance, with the CIP photodegradation efficiency decreasing slightly from 99.21% to 90.81% after five consecutive cycles. Correspondingly, the k_{deg} value declined from 0.0337 min^{-1} to 0.0126 min^{-1}, as shown in Figure 5.9b. This decrease may be attributed to the accumulation of intermediate products during photocatalysis and residual CIP molecules, which can block the active sites of the KBN@TiO_2@rGO nanocomposite.

Finally, instrumental analysis was conducted to investigate the stability of the KBN@TiO_2@rGO photocatalyst. During CIP degradation, the photocatalyst maintained its initial photodegradation performance over five consecutive cycles (Figure 5.9a). The recycled material was examined using XRD (Figure S5.1a), FTIR (Figure S5.1b), BET (Figure S5.1c), and XPS (Figure S5.8 and Table S5.10). After five cycles, the physicochemical properties remained largely unchanged except for the BET surface area and BJH pore size distribution, suggesting that KBN@TiO_2@rGO has decent stability. The loss in BET surface area from 71.35 to 50.91 m^2 g^{-1} after the reusability test and the decrease in differential pore volume between 0 and 150 nm after the reaction were attributed to pore blocking after continuous reaction, as evident from the BJH pore distribution curves (Figure S5.1d). In the case of XPS, the slight changes in composition and binding energy provided hints regarding surface interactions in the catalyst. These findings indicate that the KBN@TiO_2@rGO nanocomposite remained stable even after five reuse cycles.

5.3.6 Other antibiotic degradation and TOC removal

The photocatalytic performance of KBN@TiO_2@rGO towards other antibiotics, i.e.,

norfloxacin (NORF) and tetracycline (TC), was further evaluated (See Table S5.11) for their physicochemical properties. These antibiotics are among the most widely used and pose significant threats to various aquatic life forms, such as bacterial resistance, algae growth inhibition, harm to fish, crustaceans, and plant toxicity [225]. As presented in Figure 5. 9c and Table S5.12**,** the removal efficiency of these antibiotics followed the order: TC (100%) > CIP (99.46%) > NORF (95.56%), with corresponding k_{deg} values of 0.0636 min^{-1}, 0.0379 min^{-1}, and 0.0221 min^{-1}, respectively. In addition to single-antibiotic systems, a binary-antibiotic system (CIP/NORF) was investigated to evaluate the synergistic effect of multiple antibiotics on KBN@TiO_2@rGO performance. The k_{deg} values were 0.0292 min^{-1} and 0.0257 $min^{-1,}$ while the photocatalytic degradation removal efficiencies at 120 min were 98.80% and 97.50% for CIP and NORF, respectively. Furthermore, single and binary antibiotic systems showed 75.09%, 73.31%, and 81.82% TOC removal (%) for CIP, NORF, and TC, respectively (Figure 5.9d). According to these results, the synthesised KBN@TiO_2@rGO photocatalyst has a high mineralisation performance, produces ROS, and degrades a variety of antibiotics across classes other than CIP alone.

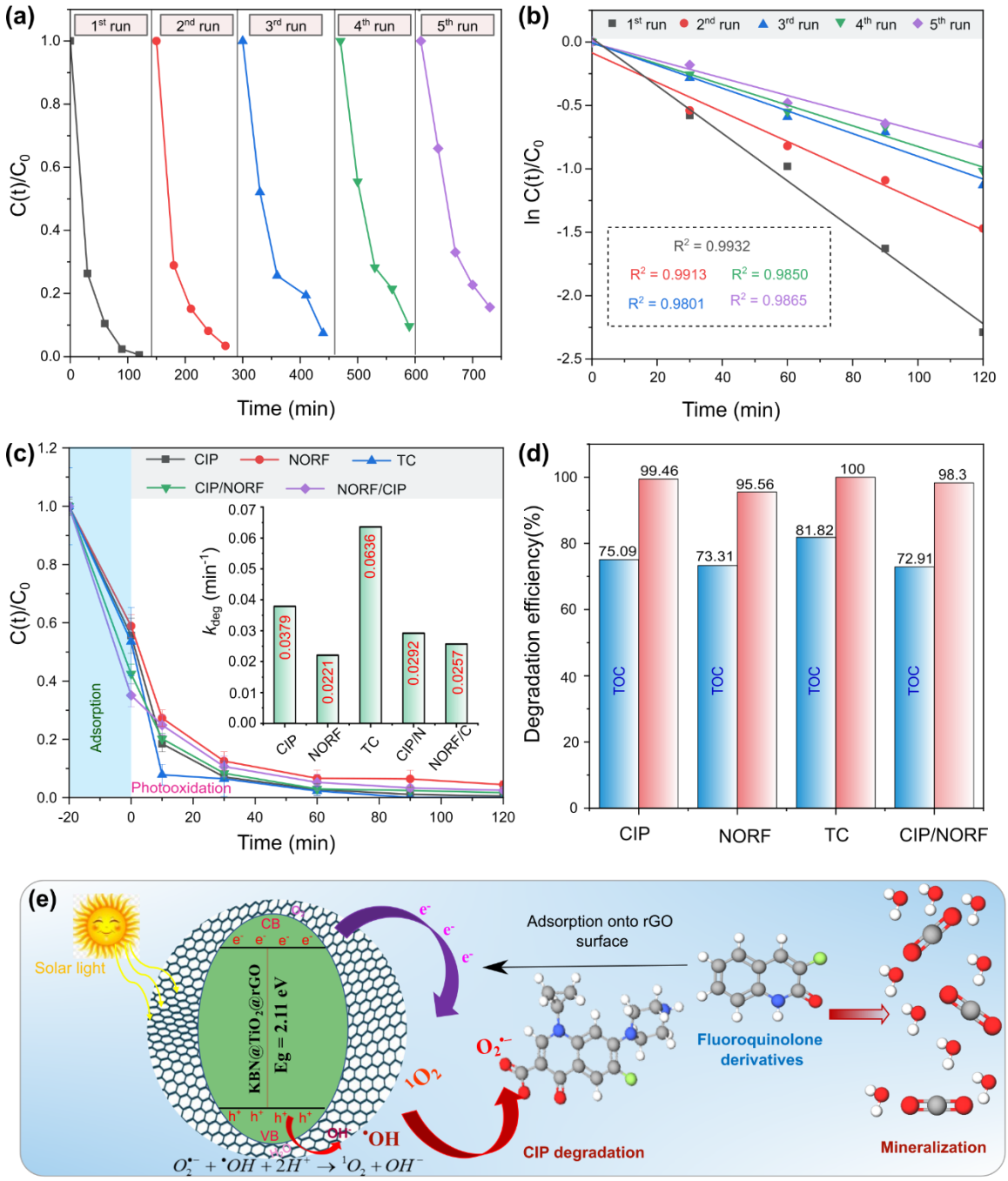

Figure 5-9 (a) Reusability and stability, (b) rate constants of five cycles, (c) the effect of multi-antibiotics, and (d) multi-antibiotics and TOC removal efficiency, degradation on the KBN@TiO_2@rGO system, and (e) schematic illustration of the photocatalytic degradation of the CIP process. (Experimental conditions: $[CIP]_0$ = $[NORF]_0$ = $[TC]_0$ = 10 mg L^{-1}, $[CIP/NORF]_0$ = 5 mg L^{-1} for each, catalyst dose = 0.2 g L^{-1}, and unadjusted pH = 5.23, at controlled temperature = 23℃).

5.3.7 Photocatalytic process in KBN@TiO_2@rGO

The photocatalytic mechanism of the KBN@TiO_2@rGO composite was proposed based on the radical scavenging experiments illustrated in (Figure 5.9e). Upon light exposure, an electron transfer occurs from the O 2p orbital to the Ti 3d orbital, generating holes in the O 2p orbital with a very high redox potential [226]. These photogenerated holes can immediately react with air and water molecules to generate hydroxyl radicals. Simultaneously, photogenerated electrons are transferred from the conduction band of TiO_2 to rGO due to its lower work function (–4.4 eV) compared to that of the conduction band (–4.2 eV) [226]. It efficiently suppresses electron–hole recombination and separates the charge carriers. The planar π-conjugated two-dimensional rGO structure offers excellent electrical conductivity, and it may also serve as an electron acceptor and transporter [227], absorbing photogenerated electrons emitted on the TiO_2 surface and reacting with O_2 to produce $O_2^{\bullet-}$, close to the conduction band (CB). Compared with bare TiO_2, the incorporation of metal and non-metal dopants, along with rGO, allows contaminant particles to accumulate near the photocatalyst surface. The CIP molecules adsorbed on the photocatalyst can be directly oxidised to fluoroquinolone derivatives and eventually be mineralised into smaller molecules such as CO_2 and H_2O through the action of strong oxidising radicals, including $^{\bullet}OH$ and $O_2^{\bullet-}$, and non-radical singlet oxygen ($^1O_2$). Furthermore, the formation of new chemical bonds (Ti–O–C), facilitated by the rGO coating on the outer surface of KBN@TiO_2, offers a new channel for the flow of electrons and improves the material's carrier migration rate.

5.4 Conclusions

In summary, a novel binary composite photocatalyst, KBN@TiO_2@rGO, was successfully prepared using the sol-gel-assisted hydrothermal method. The synthesis of the KBN-doped TiO_2 nanoparticles and their integration with rGO nanosheets were characterised by XPS, XRD, UV-DRS, FT-IR, SEM-EDX, PL, and BET techniques. The reported KBN@TiO_2@rGO composite exhibited excellent physicochemical properties, such as low band gap energy (2.11 eV), high surface area (71.35 $m^2\ g^{-1}$), and average pore size (4.3 nm) compared to simple TiO_2. Additionally, the composite demonstrated superior photocatalytic performance compared with TiO_2, TiO_2@rGO, BN@TiO_2, BN@TiO_2@rGO, and KBN@TiO_2. The removal efficiencies of CIP, NORF, and TC reached 99.21%, 95.56%, and 100%, respectively. Notably, the photodegradation efficiency of CIP using KBN@TiO_2@rGO was approximately twice that of KBN@TiO_2 and 14 times greater than that of bare TiO_2. The enhanced photocatalytic

performance of the KBN@TiO_2@rGO composite can be attributed to the synergistic interactions among TiO_2, co-doping with metal and nonmetal (KBN), and the incorporation of rGO. Doping TiO_2 and integrating rGO significantly enhanced the photocatalytic removal efficiency of the composites. Furthermore, the effectiveness of KBN@TiO_2@rGO was examined in the actual wastewater matrix, demonstrating over 70% mineralisation of TOC and over 80% degradation efficiency for CIP. These results, along with their decent photocatalytic activity, stability, and reusability, suggest that KBN@TiO_2@rGO nanocomposites hold strong potential for practical applications in photocatalysis and wastewater remediation.

CHAPTER SIX

Peroxymonosulfate Activation by KBN-Doped TiO_2@rGO: Multi-Site Radical and Non-Radical Degradation of Antibiotics

Abstract

The effective synthesis of advanced composite photocatalysts for wastewater treatment remains a major challenge in attaining sustainability goals. In this study, a KBN-doped TiO_2@rGO composite was developed to activate proxymonosulfate (PMS) for enhanced photocatalytic degradation of emerging pollutants. The KBN@TiO_2@rGO/PMS system achieved complete ciprofloxacin (CIP) degradation (100%) and 74.23% total organic carbon (TOC) removal under optimal conditions (CIP: 10 mg L^{-1}, catalyst: 0.1 g L^{-1}, PMS: 0.5 mM, 90 min, and 950 W m^{-2}), outperforming TiO_2/PMS (45.53%). The superior performance was attributed to enhanced electron transfer and generation of both radical (•OH, O_2•$^-$, and SO_4•$^-$) and non-radical ($^1O_2$) reactive oxygen species, facilitated by structural defects, O–C=O groups, and Ti-oxide sites. CIP degradation efficiency increased 6.6- and 2.1-fold compared with pristine TiO_2 and KBN@TiO_2@rGO, respectively, indicating strong synergistic effects of ternary (K, B, N) doping, rGO integration, and PMS activation. Co-existing substances such as HPO_4^{2-} and HCO_3^- enhanced CIP degradation, while Cl^- and SO_4^{2-} had negligible influence; conversely, SO_4^{2-}, PO_4^{3-}, and high humic acid levels inhibited performance. The photocatalyst maintained high performance across various water matrices, with only a slight reduction due to natural quenchers. ESR and scavenging experiments confirmed reactive species formation, while UPLC-MS/MS revealed degradation pathways. Response Surface Methodology (RSM) optimisation identified optimal conditions (pH 8.17, time 101.2 min, photocatalyst 0.13 g L^{-1}, and [CIP] 9.99 mg L^{-1}), achieving predicted 100% CIP degradation and 75.91% TOC removal with 100% desirability. This system shows strong potential for sustainable removal of pharmaceuticals from water.

6.1 Introduction

6.2 Materials and methods

6.2.1 Materials

The details of the materials and chemicals are provided in the supporting information, Text S6.1. The chemical and physical characteristics of ciprofloxacin (CIP) are summarised in our previous work [44]. The analytical methods and the characterisation of KBN@TiO_2@rGO are described in Texts S6.2 and S6.3.

6.2.2 Design and preparation of the KBN@TiO_2@rGO composite nanoparticle

The KBN@TiO_2@rGO nanocomposite photocatalyst was prepared via dispersion and hydrothermal treatment. Briefly, 0.9 g of modified KBN@TiO_2 and 0.1 g of rGO were dispersed in 100 mL of double-deionised (DDI) water and stirred for 2 h. The suspension was then transferred to a Teflon-lined autoclave and subjected to hydrothermal treatment at 150 ℃ for 3 h. After cooling to room temperature, the product was washed three times with DDI water, centrifuged at 3000 rpm, and dried overnight at 50 ℃ to yield the KBN@TiO_2@rGO nanocomposite. The detailed synthesis procedure is described in our previous work [44].

6.2.3. Characterisation of the KBN@TiO_2@rGO nanocomposite

The synthesised materials were comprehensively characterised using X-ray diffraction (XRD), Fourier-transform infrared spectroscopy (FT-IR), Brunauer-Emmet-Teller (BET) surface area analysis, scanning electron microscopy (SEM) equipped with energy-dispersive spectroscopy (EDX), X-ray photoelectron spectroscopy (XPS), UV-visible diffuse reflectance spectroscopy (DRS), and photoluminescence (PL) spectroscopy. The PL spectra were recorded on a FluoroMax-4 spectrofluorometer (Horiba, Japan) with an excitation wavelength of 320 nm. Detailed characterisation methodologies are provided in Text S6.2.

6.2.4. Photocatalytic degradation experiments

Photocatalytic degradation was conducted in batch mode within an open-top cylindrical quartz reactor (250 mL total volume; radius: 5 cm; height: 10 cm). Simulated visible light was supplied by a 500 W xenon lamp positioned 20 cm above the reactor, emitting in the UV-visible range (400-700 nm). Selected process parameters, including solution pH, reaction time, photocatalyst loading, and initial pollutant concentration, were systematically varied using the Box-Behnken Design (BBD) experimental methodology, as displayed in Table 6.1. In the CIP photocatalytic degradation test, 0.1g L^{-1} of catalyst was suspended in a 100 mL quartz glass

reactor. This was followed by the simultaneous addition of 10 mL of CIP and 1 mL of PMS solution (0.5 mM), along with exposure to simulated visible light. For the photocatalytic degradation experiments, a freshly synthesised PMS stock concentration was used in the KBN@TiO_2@rGO system. At a predetermined time interval, 2 mL samples were collected and immediately treated by adding 2 mL of 20 mM sodium thiosulfate to stop the reaction. The samples were then filtered through a 0.2 µm syringe filter (ø = 13 mm, Whatman, USA) and subsequently analysed using HPLC, as detailed in Table S6.1**.** Furthermore, TOC analysis was conducted to evaluate the extent of CIP mineralisation Text S6.3. The CIP photocatalytic removal results were analysed based on the pseudo-first-order kinetic model **(**Eq.6.1**)**, and the photodegradation (%) was calculated from **(**Eq.6.2**)**

$$In\left(\frac{C(t)}{C_0}\right) = -kt \tag{6.1}$$

$$Photo\,\text{deg}\,rdation(\%) = \left(\frac{C_0 - C(t)}{C_0}\right) \times 100 \tag{6.2}$$

where C_0 and C(t) represent the CIP concentration (mg L^{-1}) at the initial time and at reaction time t (min), respectively, while *k* denotes the pseudo-first-order rate constant (min^{-1}).

Table 6.1: Experimental key study factors and levels.

Factors	Name	Unit	Study range	
			Minimum	Maximum
A	Solution pH	-	3	11
B	Irradiation time	min	30	150
C	Catalyst loading	g L^{-1}	0.05	0.15
D	Initial contaminant concentration	mg L^{-1}	5	15

6.2.5 Experimental design via response surface methodology (RSM)

RSM is a combined statistical and mathematical modelling approach employed to elucidate the relationships between dependent and independent variables [206]. RSM maximises information extraction from limited experimental data, offers predictive capability through a sequential experimentation framework, facilitating the development and optimisation of

empirical models. As summarised, experiments listed in Table 6.2 were conducted using a fully randomised design that involved four main factors: solution pH, reaction time, photocatalyst loading, and initial pollutant concentration, with each factor tested at three levels and measuring two responses: CIP photodegradation and TOC removal efficiency

Table 6.2: Experimental design matrix generated using BBD-RSM.

Runs	**Factors**				**Responses**	
	A: Solution pH	B: Irradiation time (min)	C: Catalyst loading (g L^{-1})	D: Initial CIP concentration (mg L^{-1})	CIP degradation efficiency (%)	TOC removal efficiency (%)
1	7	90	0.15	5	94.29	74.41
2	7	30	0.15	10	89.47	69.57
3	3	150	0.1	10	99.82	68.75
4	11	30	0.1	10	89.28	66.45
5	11	90	0.1	15	97.1	75
6	7	90	0.1	10	99.1	72.05
7	3	30	0.1	10	82.3	58
8	7	90	0.1	10	99.96	71.41
9	7	150	0.1	5	100	75.51
10	7	150	0.05	10	100	71.12
11	3	90	0.05	10	88.14	59.9
12	7	30	0.1	15	82.66	67.92
13	11	90	0.05	10	96.18	66.65
14	7	150	0.1	15	97.9	68.23
15	7	30	0.1	5	82.66	57.63
16	7	90	0.15	15	97.93	74.25
17	7	30	0.05	10	77.89	57.87
18	3	90	0.15	10	97.13	69.84
19	3	90	0.1	15	90.27	62.36
20	11	150	0.1	10	100	71.7
21	7	90	0.1	10	100	70.74
22	7	90	0.1	10	100	72.09
23	7	90	0.05	15	85.47	65.77
24	7	150	0.15	10	100	75.78
25	11	90	0.15	10	96.82	74.23
26	7	90	0.05	5	93.56	63.42
27	11	90	0.1	5	94.5	65.63
28	7	90	0.1	10	100	71.9
29	3	90	0.1	5	94.23	66.54

A second-order polynomial model was used to represent the relationship between independent variables and the response. For the four selected key experimental factors, the general equation is given by:

$$Y = \beta_0 + \sum_{i=1}^{k} \beta_i X_i + \sum_{i=1}^{k} \beta_{ii} X_i^2 + \sum_{1 \le i \le j} \sum \beta_{ij} X_i X_j + \varepsilon \quad (6.3)$$

where $Y$is the experimental response, with $X_i$and $X_j$represent the experimental variables, β_0 denotes a constant value, β_i, β_{ii}, and β_{ij} are the regression coefficients corresponding to the linear, quadratic, and interaction (cross-product) effects, respectively, and ε represents the random error. The regression analysis and estimation of these coefficients were performed using the Design-Expert version 13.0.1.0 (Stat-Ease, Inc.) was used for statistical modelling, and ANOVA was applied to evaluate the adequacy of the model equations. The quality of fit and statistical significance of the model was assessed using the F-test, the coefficient of determination (R^2)**,** adjusted R^2 (adj-R^2)**,** predicted R^2 (Pred R^2)**,** and the coefficient of variation (CV)**.**

6.3 Results and discussion

6.3.1 Characterisation of prepared photocatalyst

6.3.1.1 Structural and functional characterisation of the prepared nanocomposite

X-ray diffraction (XRD) was employed to identify the crystalline phases and examine the photocatalytic behavior of KBN@TiO_2@rGO and KBN@TiO_2. As can be observed in Fig.1a, the XRD pattern of the KBN@TiO_2 displayed diffraction peaks at 2θ values of 25.69°, 38.40°, 48.80°, 54.78°, 55.94°, 63.73°, 69.95°, 71.48°, and 75.38°, which can be attributed to the (101), (004), (200), (105), (211), (204), (116), (220), and (107) crystal planes of anatase TiO_2 (JCPDS No. 21-1272). Moreover, a few rutile phase peaks were observed in the undoped TiO_2 sample (JCPDS No.21-1276). Compared with pure TiO_2, doping with potassium (K), boron (B), and nitrogen (N) resulted in a slight expansion and broadening of the most intense anatase (101) peak, indicating lattice distortion due to dopant incorporation. The KBN@TiO_2@rGO displayed diffraction peaks at 2θ values of 24.77°, 37.38°, 46.89°, 53.13°, 53.74°, 61.44°, 67.69°, 68.48°, and 73.02°, corresponding to the (101), (004), (200), (105), (211), (204), (116), (220), and (107) crystal planes, respectively. The average particle crystallite size of the nanoparticles was calculated to be approximately 19.04 nm. The KBN@TiO_2@rGO showed a slight decrease in diffraction peak intensity due to the incorporation of rGO sheets, which reduced the crystallinity of TiO_2. The lack of a distinct rGO peak in the range of 24-26º further indicates that the graphene oxide layers were effectively exfoliated and homogeneously distributed within the TiO_2 framework. In addition, the rGO phase is likely to exist in an

amorphous form, which typically does not produce sharp diffraction peaks but appears as a broad hump or remains undetectable under certain conditions. Furthermore, the characteristic peaks of rGO may overlap with those of TiO_2, making it difficult to distinguish them in the XRD spectra clearly. Thus, the possibility of peak overlap cannot be excluded [237].

FT-IR spectroscopy exploits the molecular vibrations associated with each absorption band to provide information regarding the chemical composition and structural characteristics of compounds. The FT-IR spectra of KBN@TiO_2 and KBN@TiO_2@rGO nanocomposite photocatalysts are depicted in Figure 6.1b, highlighting the characteristic vibrational bands of their functional groups. The TiO_2 FT-IR spectrum exhibits a wide absorption band at 3375 – 3219 cm^{-1}, associated with the O – H stretching vibrations of hydroxyl groups on the surface and physically adsorbed water molecules, as depicted in Figure 6.1b. Further evidence is provided as indicated by the band at 1356 cm^{-1}, which was attributed to the bending vibration of water molecular and Ti – OH groups [238]. This band corresponds to the aromatic ring vibrations in the rGO structure within the composites. The reduced intensity of the band at 1629 cm^{-1} suggests that hydroxyl groups, rather than ketone or carboxylic groups, predominantly exist in the composites [239]. Additionally, a weakened signal at 1238 cm^{-1} indicates the presence of functional groups that are oxygenated, like C-O. The band observed at 815 cm^{-1} in the composite spectra is attributed to O–Ti–O vibrations. In the composites, chemical interactions between TiO_2 and rGO typically generate a wide absorption band under 1000 cm^{-1}, reflecting a combination of Ti–O–Ti and Ti–O–C vibrations. Upon hydrothermal treatment, Ti–O–C linkages illustrate how rGO, containing residual carboxyl groups, interacts with the surface hydroxyl groups of TiO_2 nanoparticles to form chemical bonds within the composites. The significant reduction or absorption peak disappearance associated with functional groups that are oxygenated, like C=O (1240 cm^{-1}), –OH (1356 cm^{-1}), and C–O–C (1035 cm^{-1}), further confirms strong binding of TiO_2 to rGO at the reactive sites [240, 25].

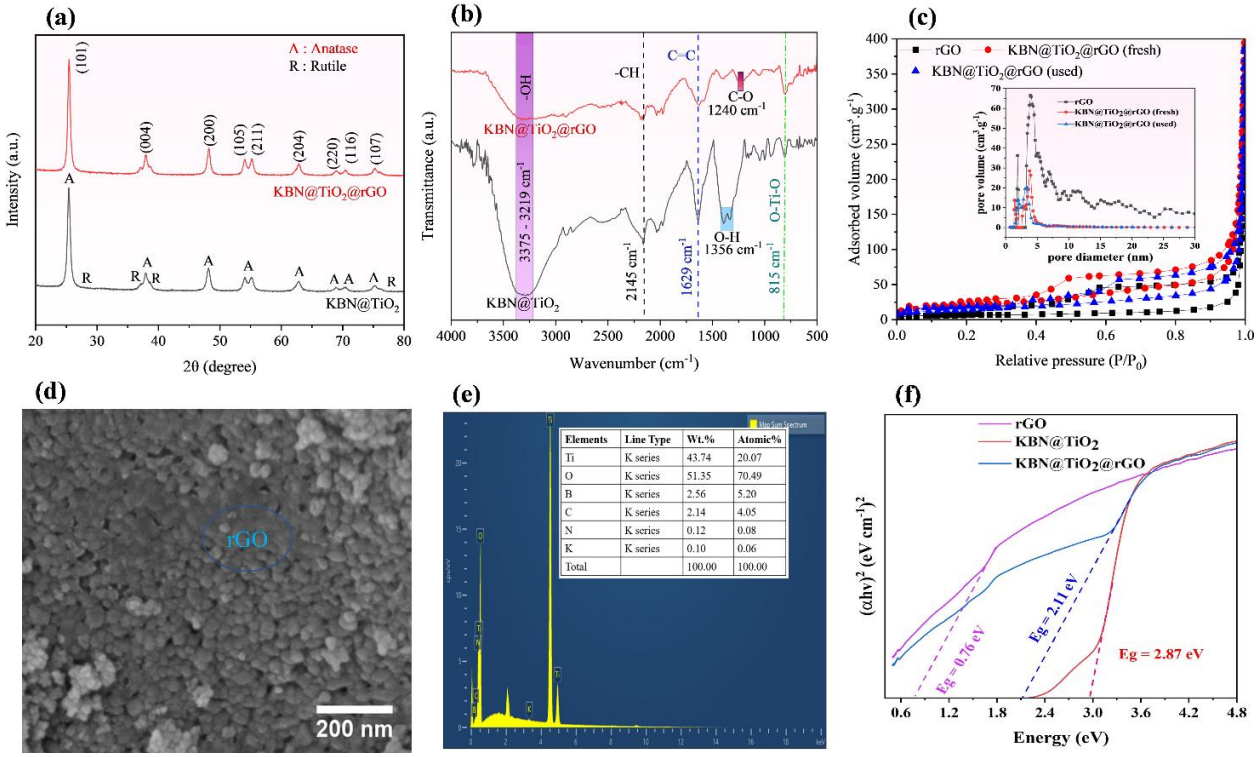

Figure 6-1 XRD patterns of the synthesised (a) KBN@TiO_2 and KBN@TiO_2@rGO, (b) FTIR spectra of KBN@TiO_2 and KBN@TiO_2@rGO, (c) N2 adsorption-desorption isotherms of rGO, fresh KBN@TiO_2@rGO and used KBN@TiO_2@rGO, (c) pore size distribution curves for rGO, fresh KBN@TiO_2@rGO, and used KBN@TiO_2@rGO, (d)FE-SEM images of the synthesised KBN@TiO_2@rGO composite, (e) EDX spectra of KBN@TiO_2@rGO, and (f) Tauc plots of rGO, KBN@TiO_2@rGO, and KBN@TiO_2@rGO

6.3.1.2. Investigation of surface area and porosity using BET analysis

As revealed in Table 6.3, the BET analysis of the samples shows that the synthesised rGO has the surface area of 65.615 $m^2\ g^{-1}$, an average pore size of 3.207 nm, and a pore volume of 0.050 cm^3/g, indicating that it is primarily mesoporous and provides moderate surface area and pore volume for interaction with TiO_2 nanoparticles. Upon forming the KBN@TiO_2@rGO nanocomposite, the surface area increases to 73.354 m^2/g, the average pore size rises to 4.201 nm, and the pore volume reaches 0.116 cm^3/g, suggesting that the incorporation of rGO prevents aggregation of TiO_2 nanoparticles and introduces additional mesopores, thereby enhancing the accessibility of active sites. After use, the surface area slightly decreases to 67.911 m^2/g and the average pore size reduces to 3.034 nm, while the pore volume slightly increases to 0.124 cm^3/g, as shown in Figure 6.1c; these changes may be attributed to partial pore blockage, agglomeration, or deposition of reaction by-products, along with minor

structural rearrangements, yet the material retains significant mesoporosity favorable for adsorption and catalytic performance. This enhancement is ascribed to the effective integration of rGO into the KBN@TiO_2 matrix, which prevents nanoparticle aggregation and introduces additional mesopores [44]. The enhanced surface area and adsorption capacity of the KBN@TiO_2@rGO composite are expected to promote more efficient electron transfer, leading to improved photocatalytic performance [44].

Table 6.3: Investigation of surface area and pore size distribution in synthesised samples.

Samples	Surface area ($m^2\ g^{-1}$)	Average pore size (nm)	Pore volume ($cm^3\ g^{-1}$)
rGO	65.615	3.207	0.050
KBN@TiO_2@rGO fresh	73.354	4.201	0.116
KBN@TiO_2@rGO used	67.911	3.034	0.124

6.3.1.3. Investigation of surface structure and morphology

The SEM image of KBN@TiO_2@rGO Figure 6.1d shows that incorporating 10 wt.% rGO significantly alters the morphology of KBN@TiO_2. The nanoparticles appear smaller and more uniformly distributed, with smoother, layered regions ascribed to the rGO sheets. The absence of visible rGO aggregation indicates strong interfacial interactions between rGO and KBN@TiO_2. This modification enhances the dispersion of TiO_2 nanoparticles, increases the specific surface area, and prevents particle agglomeration. Consequently, the KBN@TiO_2@rGO composite with 10 wt.% rGO exhibits improved porosity and surface uniformity, which are beneficial for catalytic and surface-related applications.

Energy-dispersive X-ray spectroscopy (EDX) was used to analyse the elemental composition of the KBN@TiO2@rGO photocatalyst, as revealed in Figure 6.1e. The quantitative results, summarized in the inset table, reveal that the photocatalyst primarily consists of nitrogen (N), boron (B), potassium (K), carbon (C), oxygen (O), and titanium (Ti). The detection of these elements confirms the successful incorporation of rGO and dopant elements into the KBN@TiO_2 framework, validating the formation of the intended composite structure. The nanocomposite sample comprised 51.35% O, 43.74% Ti, 2.56% B, C, 0.12%, 2.14% N, and 0.10% K, as displayed in Figure 6.1e. These results confirm the successful incorporation of boron, nitrogen, and potassium dopants, along with rGO, into the TiO_2 framework. Overall, the

KBN@ TiO_2@rGO composite exhibits a more sophisticated and integrated structure that combines the high electrical conductivity and excellent dispersion characteristics of rGO with the enhanced active site generation provided by KBN doping in TiO_2.

6.3.1.4. Examination of photoluminescence and optical characteristics

Diffuse Reflectance Spectroscopy (DRS) is widely used to determine the band gap energy (Eg) of materials by analysing their light absorption behavior and applying suitable transformation equations. As illustrated in Figure S6.2, the absorption edge of TiO_2 is confined to wavelengths below 400 nm. However, the absorption edges of KBN@TiO_2 and KBN@ TiO_2@rGO exhibit a pronounced redshift, as shown in Figure 6.1f. The improvement is likely attributed to KBN doping within the TiO_2 lattice and the strong interfacial coupling between rGO and TiO_2 formed during the hydrothermal treatment [95]. The incorporation of rGO into KBN@TiO_2 further enhances absorption of light in the visible and ultraviolet spectrums, indicating that KBN@TiO_2@rGO can utilise a greater portion of the visible spectrum. To determine the values of the band gap energy (Eg) of KBN@TiO_2@rGO, KBN@TiO_2, and rGO, Tauc's equation was employed (Eq. 6.4):

$$(\alpha h\nu)^{1/n} = A(h\nu - E_g) \tag{6.4}$$

where A is a constant, and α, h, ν, and E_g represent the absorption coefficient (cm^{-1}), Planck constant (eV·s), photon's frequency (s^{-1}), and band gap energy (eV), respectively. The semiconductor transition characteristics determine the value of n(for TiO_2, $n = 4$) [241], and the calculated band gap energies for KBN@TiO_2@rGO, KBN@TiO_2, and rGO were 2.11 eV, 2.87, 0.76, and, respectively, Figures 6.1f and S6.2a. Notably, the modified KBN@TiO_2@rGO exhibits the lowest band gap energy, confirming its superior ability to absorb solar light compared with KBN@TiO_2.

The KBN@TiO_2 and KBN@TiO_2@rGO PL spectra in Figure S6.2b show that the lower peak intensity corresponds to reduced electron–hole recombination and improved charge separation [44]. A prominent emission was observed at 380–480 nm, and KBN@TiO_2@rGO exhibited significantly lower intensity than KBN@TiO_2, indicating that KBN doping and rGO incorporation effectively enhance photocatalytic performance.

6.3.1.5. XPS study of synthesised nanocomposites

As shown in Figure 6.2a, the XPS survey spectrum displays well-defined peaks assigned to Ti 2p (458.19 eV), O 1s (529.48 eV), C 1s (283.5 eV), K 2p (291.9 eV), B 1s (191.0 eV), and N

1s (400.6 eV), confirming the presence of these elements in the composite. These peaks confirm the presence of O, Ti, N, B, K, and C elements in the composite, indicating successful formation of the designed nanomaterial. As illustrated in Figure 6.2b, the Ti 2p spectrum displays two characteristic peaks at 458.19 eV and 463.98 eV, corresponding to the Ti^{4+} $2p_{3/2}$ and Ti^{4+} $2p_{1/2}$ states, respectively. These features provide insights into the coordination environment and oxidation state of titanium within the nanocomposite [95]. The O 1s spectrum, as shown in Figure 6.2c, exhibits two distinct peaks at 529.48 eV and 531.45 eV, indicating the presence of oxygen in different chemical environments. These are typically associated with lattice oxygen in Ti–O bonds and surface hydroxyl or adsorbed oxygen species, reflecting the complexity of the surface chemistry. As shown in Figure 6.2d, the B 1s peak at 191.6 eV is attributed to B–O–N bonding, confirming the incorporation of boron and its related functional groups into the structure. The N 1s spectrum, as depicted in Figure 6.2e**,** presents two main peaks at 399.7 eV and 400.6 eV, corresponding to graphitic nitrogen and amino-type nitrogen species, respectively, which play a significant role in tuning the electronic and catalytic properties of the nanocomposites. As shown in Figure 6.2f, the combined C 1s and K 2p spectrum displays peaks at 283.5, 286.2, 286.6, 288.5, and 291.9 eV, assigned to sp^2 carbon (C=C), C–N/C–OH, C–O–C, C=O, and K $2p_{3/2}$, respectively, confirming the presence of rGO, potassium, and oxygen-containing functional groups uniformly distributed across the nanocomposite [33, 34]. Such bonding configurations are known to modulate the surface chemistry and electronic structure, thereby reducing the band gap energy and enhancing the photocatalytic activity of the modified TiO_2 [243, 30]. Furthermore, Table S6.7 presents the XPS peak fitting results for fresh and used KBN@TiO_2@rGO catalysts.

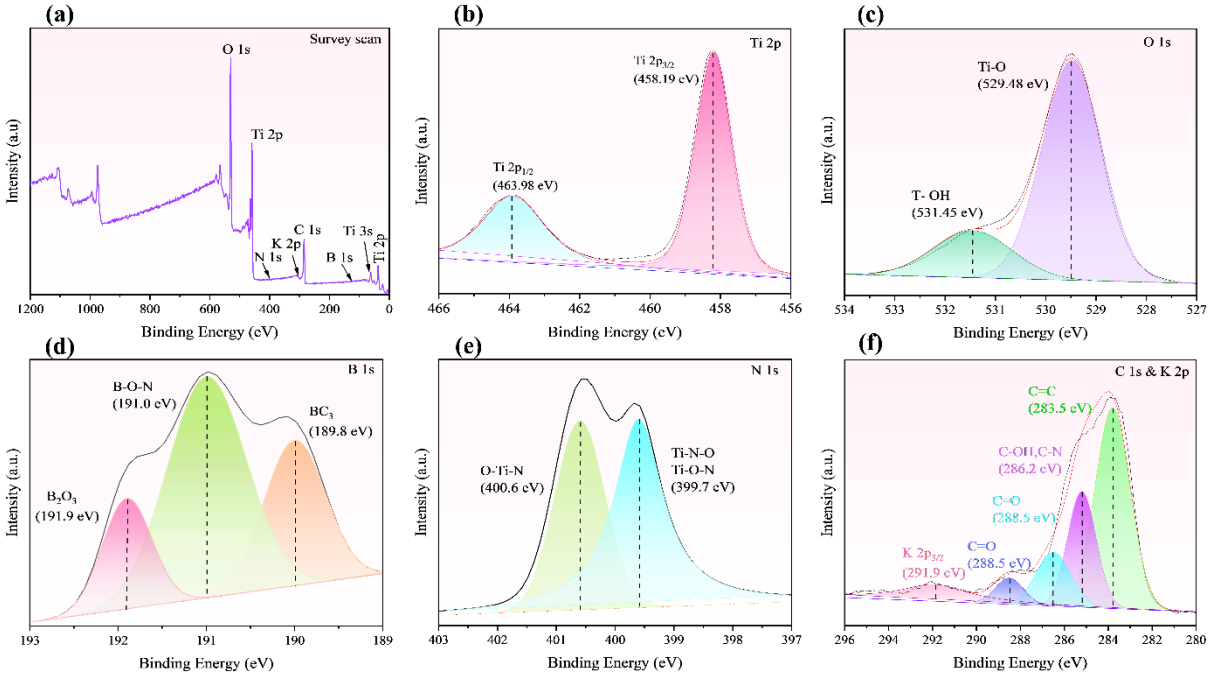

Figure 6-2 XPS analysis of KBN@TiO_2@rGO Nanocomposite: (a) Overall survey, (b) Ti 2p, (c) O 1s, (d) B 1s, (e) N 1s, and (f) C 1s + K 2p.

6.3.3 Evaluation of PMS activation performance and photocatalytic oxidation

6.3.3.1 Selection of the best photocatalyst

The CIP in the wastewater contamination was selected as the target antibiotic contaminants to investigate the photocatalytic performance of the KBN@TiO_2@rGO for PMS activation. CIP adsorption and photocatalytic degradation performance were evaluated with and without metal-nonmetal, a modified TiO_2, as displayed in Figure S6.3 and Figure 6.3a. In the control system, without light, oxidant and photocatalyst, the degradation of CIP was < 15% over 120 min. As revealed in Figure 6.3b, the percentages of self-decomposition and PMS consumption progressively rose to 87.07% and 48.2%, respectively, over 120 min. Nearly 45.2% and 100% of CIP photocatalytic degradation were achieved in the TiO_2 and KBN@TiO_2@rGO with PMS, respectively, as seen in Figure 6.3a within 90 min. The degradation kinetics were found to conform to the pseudo-first-order kinetic model (PFOKM), as shown in Figure S6.4a and Figure S6.4. For KBN@TiO_2@rGO/PMS, the PFOKM k reaction rate constant (66.25 x 10^{-3} min^{-1}), was 11.83-fold higher than that of TiO_2/PMS (5.6 x 10^{-3} min^{-1}) with oxidant, Figure S6.4a. It shows that KBN@TiO_2@rGO/PMS's more colloidal nature had more active sites, which readily interacted with PMS and produced ROS [117]. Therefore, KBN@TiO_2@rGO was selected as the photocatalyst for the degradation of antibiotics in the wastewater.

6.3.3.2 PMS concentration's effect

The effect of oxidant concentration was investigated using KBN@TiO_2@rGO with PMS concentrations ranging from 0.125 to 1 mM. As shown in Figure 6.3b, only ~13.5% of CIP removal was achieved by adsorption (KBN@TiO_2@rGO in the absence of light), while photocatalytic degradation accounted for ~43.9% of CIP removal. The degradation efficiency of CIP was significantly enhanced by the addition of PMS in the presence of KBN@TiO_2@rGO. In the KBN@TiO_2@rGO/PMS system under visible light, the photocatalytic degradation efficiency of CIP increased markedly from 13.5% to 100% as the PMS concentration rose from 0.125 to 0.5 mM. However, the photodegradation efficiency slightly decreased to 96.4% when the PMS concentration was increased to 1 mM. The *k* value of the PFOKM increased from 3.16×10^{-2} min^{-1} to 4.74×10^{-2} min^{-1} as the PMS concentration increased from 0.0125 to 1 mM. At a higher PMS concentration (1 mM), however, the *k* value of the PFOKM decreased again to 3.01×10^{-2} min^{-1}**,** as revealed in Figure S6.4b. This indicates that a self-quenching reaction occurred when the PMS concentration increased in the KBN@TiO_2@rGO/PMS system (Eqs. (6.5) – (6.10)). A similar observation was reported by Al Masud et al.[244] who found that CIP degradation efficiency decreased at excessive PMS concentrations in the seaweed kelp biochar (KBCBM)/PMS system. Consequently, 0.5 mM PMS was determined as the optimum oxidant concentration for CIP photodegradation in this study.

$$KBN@TiO_2@rGO-surface + HSO_5^- \rightarrow HO^- + SO_4^{\bullet-} + KBN@TiO_2@rGO-surface^+ \quad (6.5)$$

$$KBN@TiO_2@rGO-surface + HSO_5^- \rightarrow HO\bullet + SO_4^{2-} + KBN@TiO_2@rGO-surface^+ \quad (6.6)$$

$$HSO_5^- + SO_4^{\bullet-} \rightarrow HSO_4^- + SO_5^{\bullet-} \ (SO_5^{\bullet-} \text{ less reactive toward CIP}) \quad (6.7)$$

$$HSO_5^- + HO\bullet \rightarrow H_2O + SO_5^{\bullet-} \ (HO\bullet \text{ quenched}) \quad (6.8)$$

$$SO_4^{\bullet-} + SO_4^{\bullet-} \rightarrow S_2O_8^{2-} \text{ (radical -radical recombination)} \quad (6.9)$$

$$2SO_5^{\bullet-} \rightarrow S_2O_8^{2-} + O_2 \quad (6.10)$$

6.3.3.3 Effect of KBN@TiO_2@rGO concentration

The CIP photodegradation efficiencies were approximately 95.67 %, 100 %, 98.39 % and 97.09 % at photocatalyst dosages of 0.05, 0.1, 0.15, and 0.2 g L^{-1}, respectively, within 120 min of the photooxidation, as presented in Figure 6.3c, in the KBN@TiO_2@rGO/PMS system. The photodegradation rate constants (*k*) were 2.73×10^{-2} min^{-1}, 4.90×10^{-2} min^{-1}, 3.71×10^{-2} min^{-1}, and 3.01×10^{-2} min^{-1}, respectively, Figure 6.3c inset. There are several possible reasons for the slight decrease in CIP photodegradation efficiency observed at higher catalyst dosages. Excessive

photocatalyst loading raises the suspension's turbidity, which limits photon penetration to the catalyst surface due to shielding and light scattering effects [245]. Moreover, a high concentration of photocatalyst particles can promote aggregation, reduce the available active surface area and facilitate the recombination of photogenerated electron-hole pairs or reactive radicals [93]. Once the optimal photocatalyst dosage is exceeded, the number of active sites surpasses the available pollutant molecules, resulting in either no further improvement or a slight decline in photodegradation efficiency [37, 38]. Considering both performance and economic efficiency, a photocatalyst dosage of 0.1 g L^{-1} KBN@TiO_2@rGO was identified as the optimal condition, achieving complete (100 %) photodegradation of CIP in the KBN@TiO_2@rGO/PMS. Consequently, this dosage was adopted for all subsequent photocatalytic experiments. Compared to other documented PMS-based photocatalytic systems in the literature Table S6.2, the KBN@TiO_2@rGO/PMS system revealed markedly enhanced photodegradation performance, achieving higher removal efficiency of both CIP and TOC at relatively low catalyst dosage and irradiation time.

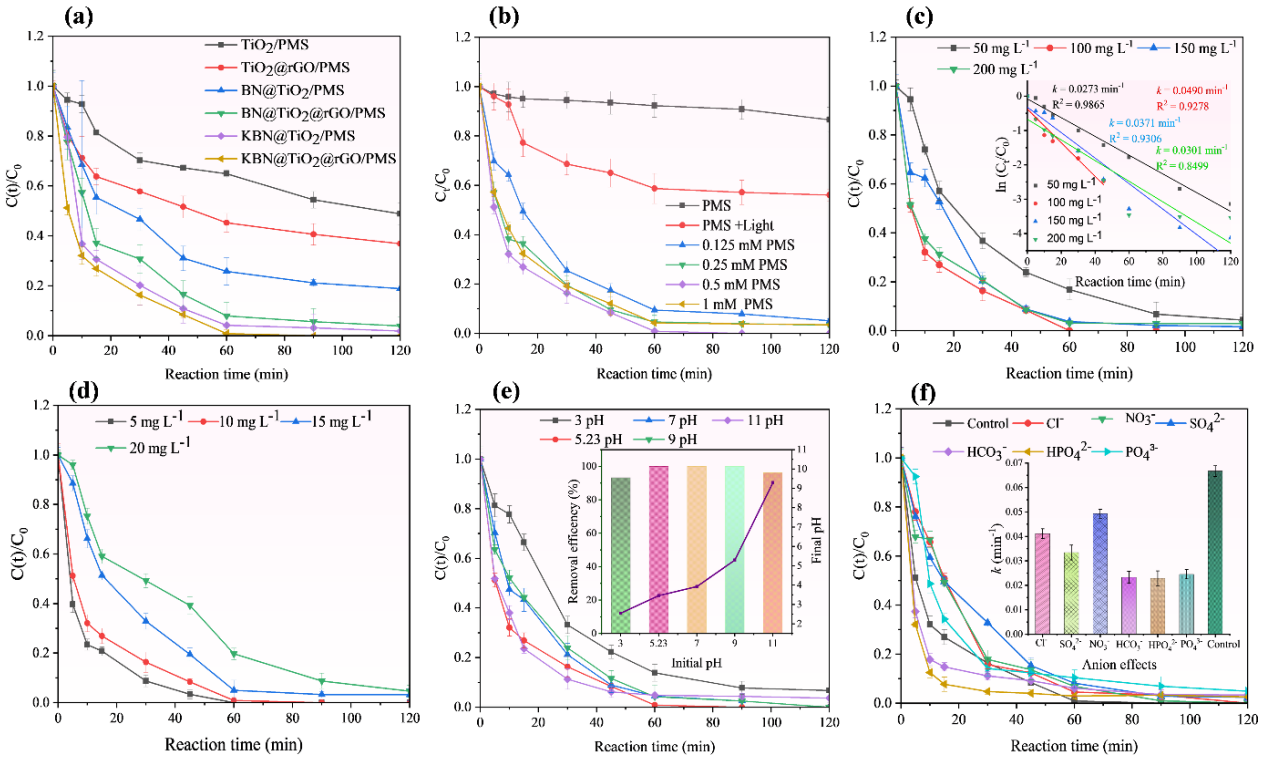

Figure 6.3 Effects of (a) catalyst type, (b) PMS dose, (c) catalyst dose, (inset) corresponding rate constant values, (d) initial CIP concentration, (e) initial pH, (inset) corresponding final pH values and (f) anion effects on photocatalytic degradation of CIP using the KBN@TiO_2@rGO/PMS system. (Experimental conditions: $[CIP]_0$ = 10 mg L^{-1}, $[PMS]_0$

=0.5mM, catalyst dose = 0.1 g L^{-1}, $[anions]_0$ = 200 mg L^{-1}, unadjusted pH = 5.23, at controlled temperature = 23℃).

6.3.3.4 Effect of initial CIP concentration

As illustrated in Figure 6.3d**,** increasing the initial CIP concentration from 5 to 20 mg L^{-1} led to a gradual decrease in removal efficiency from 100 % to 95.39 %**.** This decline may be attributed to the higher pollutant loading, which requires more reactive species for complete degradation. Nevertheless, these findings indicate that the KBN@TiO_2@rGO/PMS system retains a high degree of photocatalytic activity even when CIP concentrations were high (20 mg L^{-1}). However, as shown in Table S6.4, the apparent photodegradation rate constant ***k*** decreased from 0.0676 to 0.0265 min^{-1} as the starting concentration of CIP rose from 5 to 20 mg L^{-1}, respectively. The reduction in rate constant can be ascribed to the limited availability of reactive species relative to the higher number of pollutant molecules at increased concentrations, as well as possible light attenuation effects that reduce photon absorption by the catalyst. The following is a summary of the likely causes of this occurrence. (1) At higher CIP concentrations, a photon-shielding effect may occur due to the increased number of pollutant molecules in the solution, thereby reducing the number of photons that can reach the catalyst surface [246]. (2) The higher antibiotic concentration can also lead to extensive adsorption of CIP molecules on the catalyst surface, which limits the availability of active sites and subsequently hinders the generation of reactive radicals and photogenerated electron–hole pairs [247]. Consequently, as the initial CIP concentration increases, both photodegradation efficiency and the apparent rate constant decrease, indicating that photocatalytic activity was more effective at lower pollutant loading.

6.3.3.5 Effect of pH

As shown in Figure 6.3e, the influence of the starting pH 3.0 to 11.0 on CIP photodegradation was investigated in the KBN@TiO_2@rGO/PMS system. The photodegradation efficiency increased from 93.27 to 100 % as the starting pH rose from 3.0 to 9.0, and then slightly declined to 96.29 % when the pH increased to 11.0. The apparent rate constant (k, min^{-1}) for CIP degradation in the KBN@TiO_2@rGO/PMS obeyed the order: pH 5.23 (0.0490) > pH 7.0 (0.0425) > pH 9.0 (0.0421) > pH 11.0 (0.0259) > pH 3.0 (0.0245) (Table S6.5). This trend indicates that near-neutral and slightly alkaline conditions are more favourable for CIP photodegradation in the KBN@TiO_2@rGO/PMS system. As shown in Figure 6.3e (inset), as the initial pH increased from 3.0 to 9.0, the final pH showed a slight increase from 3.0 to 3.8

and further rose to 9.3 when the initial pH was 11. The decrease (as compared to the initial pHs) in the final pHs observed after the reactions can be attributed to the generation of H^+ ions during the hydrolysis of PMS [74]. The decreased CIP photodegradation efficiency in an acidic environment (Eqs. 6.12**)** can be attributed to the generation of H^+ ions. Initially, the presence of H^+ promotes hydrogen bonding with the oxygen atoms of HSO_5^-, thereby stabilising HSO_5^- by introducing a positive charge [248]. This stabilisation effect suppresses the activation of PMS and the subsequent formation of sulfate radicals. Secondly, the generation of reactive species that are surface-bound (i.e., PMS* [34]) on KBN@TiO_2@rGO may be hindered due to the lowered contact between PMS and the catalyst surface under acidic conditions. As a result, the interaction between HSO_5^- and KBN@TiO_2@rGO is weakened, leading to lower photocatalytic efficiency. As well, the interaction between KBN@TiO_2@rGO and CIP can also be decreased because CIP is primarily found as CIP^+ at pH values lower than its pKa1 (5.90), Figure S6.5. Thirdly, reactive species could scavenge by H^+, i.e., $HO\bullet$ and $SO_4^{\bullet-}$ (Eqs. (6.11**),** (6.12**)** [81].

$$\bullet OH + H^+ + e^- \rightarrow H_2O \tag{6.11}$$

$$SO_4^{\bullet-} + H^+ + e^- \rightarrow HSO_4^{\bullet-} \tag{6.12}$$

$$2HSO_5^- + 2OH^- \rightarrow 2SO_4^{2-} + O_2 + H_2O \tag{6.13}$$

In contrast, CIP photodegradation was slightly suppressed at pH 11.0. In pH values below and over the pKa2 of 8.89, PMS is present as both a divalent ion (SO_5^{2-}) and a monovalent ion (HSO_5^-), respectively [249]. At high pH (> 8.89), PMS exists predominantly as SO_5^{2-}**,** which has lower photooxidation capacity than HSO_5^- [249]. Furthermore, PMS's the self-decomposition into O_2 and SO_4^{2-} is accelerated under high OH^- concentrations (Eq. 6.13). Consequently, CIP degradation is slightly inhibited at pH 11.0, and the inhibition is more pronounced than under acidic conditions, indicating that the speciation of PMS has a greater impact on catalyst activation than the reduced contact between PMS/CIP and KBN@TiO_2@rGO under low pH. Overall, these findings show that the KBN@TiO_2@rGO/PMS system's CIP photodegradation was best suited for near-neutral to slightly alkaline conditions, which balance photocatalyst–pollutant interactions, PMS activation, and radical production.

6.3.4 Feasibility of practical application

6.3.4.1 Effect of anions and HA

In the KBN@TiO_2@rGO/PMS system, the degradation of CIP may be inhibited by the presence of anions and organic matter (such as humic acid, or HA) in municipal wastewater. The impact of these compounds on the performance of the KBN@TiO_2@rGO/PMS system was thus assessed. The impacts of anions are shown in Figure 6.3f. The presence of Cl^-, NO_3^- had a negligible impact on CIP removal compared with the control, whereas SO_4^{2-} and PO_4^{3-} caused a slight inhibition. Because the $SO_4^{\bullet-}$ / SO_4^{2-} redox pair has a lower oxidation-reduction potential at high SO_4^{2-} concentrations, PMS activation may be inhibited [109]. Interestingly, the presence of HCO_3^- and HPO_4^{2-} slightly promoted CIP photodegradation of synthetic wastewater within the CIP/KBN@TiO_2@rGO/PMS system.

Humic acid (HA) was used as a model organic chemical to examine the impact of organic matter in nature on CIP degradation because it is a significant component of NOM, which is frequently present in both surface and groundwater. The HA concentration was increased from 0 to 25, 50, 100, and 200 mg L^{-1}, respectively, the photodegradation efficiency of CIP dramatically dropped from 100% to 98.94%, 79.72%, 72.85%, and 30.53%, as illustrated in Figure 6.4a. Accordingly, as Figure 6.4b illustrates, the degradation rate constant (k_{deg}) dropped from 0.0490 min^{-1} to 0.0256, 0.0099, and 0.0021 min^{-1}. The interaction between HA and hydroxyl radicals(•OH) is responsible for this decrease [250]. Furthermore, TiO_2 can create surface complexes by interacting through adsorption with humic compounds, such as HA. These complexes are created when the hydroxyl (-OH) and carboxyl (-COOH) functional groups found in HA easily attach to the TiO_2 particle surface [251]. The coexistence of anions had no significant effect on the photodegradation efficiency of CIP in the CIP/KBN@TiO_2@rGO/PMS system, suggesting that singlet oxygen ($^1O_2$) generation and electron transfer reactions were involved in the reaction pathways [252].

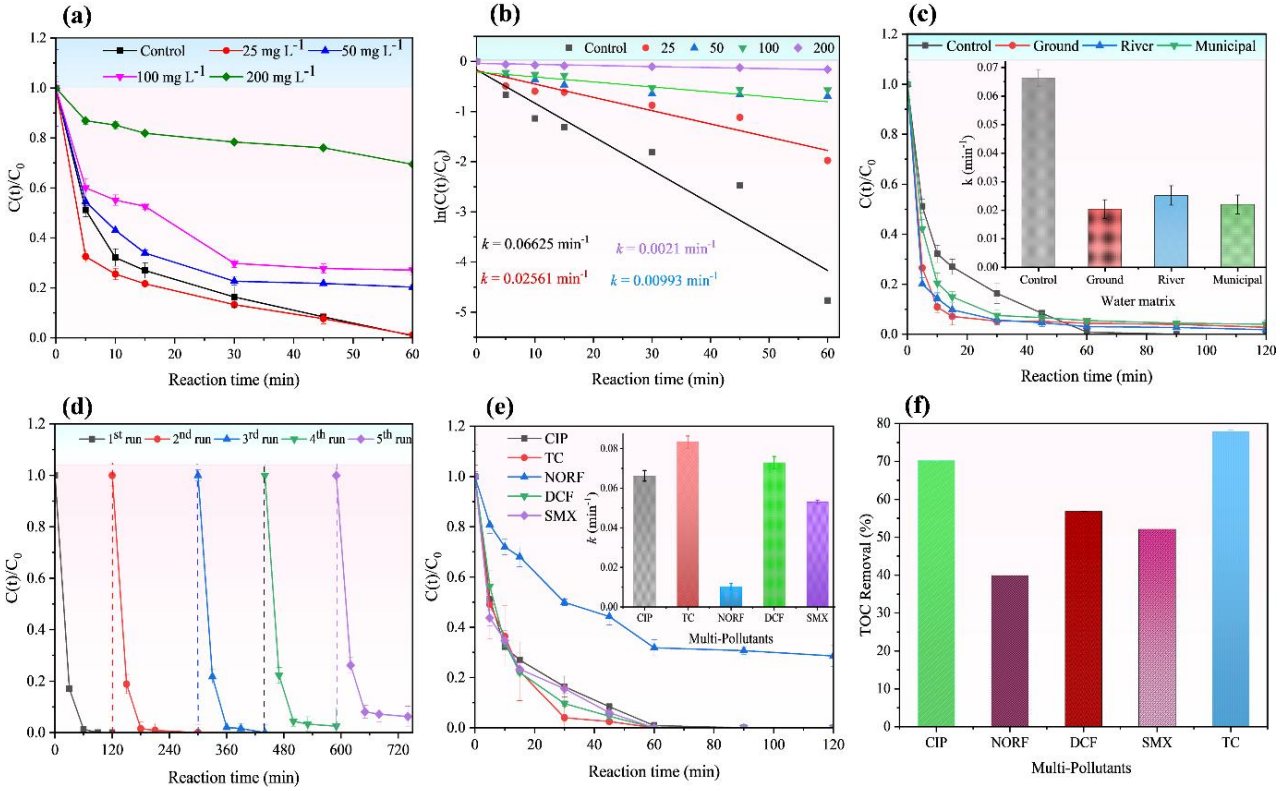

Figure 6.4 Effects of (a) humic acid, (b) rate constants at different concentrations of HA, (c) effects of water matrix, (inset) corresponding rate constant values, (d) reusability and stability on the degradation of ciprofloxacin, (e) different pollutants, (inset) corresponding rate constant values, and (f) TOC removal from different pollutants on the KBN@TiO_2@rGO/PMS system. (Experimental conditions: $[CIP]_0$ = 10 mg L^{-1}, $[PMS]_0$ =0.5mM, catalyst dose = 0.1 g L^{-1}, and unadjusted pH = 5.23, at controlled temperature = 23 °C).

6.3.4.2 Application and reusability of KBN@TiO_2@rGO/PMS

The CIP degradation performance of the KBN@TiO_2@rGO/PMS system was further evaluated in groundwater, river water, and municipal wastewater collected from a local site in Daegu, Republic of Korea. The water quality parameters for these samples were reported in our previous study [44]. The CIP degradation efficiencies of the KBN@TiO_2@rGO/PMS system were 100% in deionised water (DIW) and 97.22%, 98.15%, and 96.03% in groundwater, river water, and municipal wastewater, respectively, as shown in Figure 6.4c. These results demonstrate the versatility and potential applicability of KBN@TiO_2@rGO composites in various water treatment scenarios. In particular, the composites show significant promise for the remediation of contaminated wastewater.

Investigating the reusability of photocatalysts is essential for evaluating their overall performance in practical applications, particularly from an economic perspective. To assess reusability, KBN@TiO_2@rGO was recovered after each cycle by filtration, washed thoroughly with deionised water, and then reused in a fresh CIP/PMS solution. As shown in Figure 6.4d, the CIP removal efficiency gradually decreased with successive cycles. The CIP removal efficiency in the fifth cycle remained as high as 93.75%. These results indicate that the synthesised KBN@TiO_2@rGO composite exhibits excellent reusability and stability, demonstrating its potential for multiple uses in practical wastewater remediation applications.

6.3.4.3 Degradation of other pharmaceutical pollutants

The KBN@TiO_2@rGO/PMS system's performance was further assessed for the degradation of other pharmaceuticals, such as sulfamethoxazole (SMX), CIP, tetracycline (TC), norfloxacin (NORF), and diclofenac (DCF), as revealed in Figure 6.4e. Among the most widely used antibiotics and anti-inflammatory medications, these substances can harm aquatic life, including bacteria, algae, fish, crabs, and plants [47, 48]. According to Figure 6.4e, the highest removal efficiency was observed for TC, followed by DCF, SMX, CIP, and NORF. After 60 minutes of irradiation reaction, the removal efficiencies for TC, DCF, SMX, CIP, and NORF were 100%, 99.68%, 98.99%, 97.98%, and 68.13%, respectively, with corresponding kinetic rate constants (k) of 0.0729, 0.0833, 0.0530, 0.06625, and 0.0103 min^{-1}. In addition, the TOC removal efficiencies for TC, DCF, SMX, CIP, and NORF were 77.79%, 56.78%, 52.07%, 70.29%, and 39.88%, respectively, Figure 6.4f**.** These results demonstrate the strong potential of the synthesised KBN@TiO_2@rGO photocatalyst in activating PMS for the efficient degradation of diverse antibiotics and anti-inflammatory drugs beyond CIP.

6.3.5 Mechanisms of photocatalytic degradation in KBN@TiO_2@rGO/PMS

6.3.5.1 Quenching experiments

The CIP removal in the KBN@TiO_2@rGO/PMS system was examined with different reactive species quenchers employed, since the activation of PMS can generate both radical species, as $SO_4^{\bullet-}$, •OH, and $O_2^{\bullet-}$, and non-radical species, like $^1O_2$ [117]. In this study, t-butyl alcohol (TBA), methanol (MeOH), furfuryl alcohol (FFA), 1,4-benzoquinone (p-BQ), and isopropanol (IPA) were employed as agents that quench •OH, •OH + $SO_4^{\bullet-}$, $^1O_2$, $O_2^{\bullet-}$, and the transfer electron, respectively [253]. The photodegradation of CIP was most significantly inhibited by MeOH, moderately suppressed by TBA, FFA, and p-BQ, and slightly affected by IPA as, shown in Figure 6.5(a–b). Since MeOH and TBA are known scavengers of sulfate ($SO_4^{\bullet-}$) and

hydroxyl (•OH) radicals, these results suggest that both species were the primary reactive oxidants responsible for CIP degradation. The noticeable inhibition observed with FFA and p-BQ further indicates that singlet oxygen ($^1O_2$) and superoxide radicals ($O_2•^-$) also contributed to the photodegradation process, although to a lesser extent. The degree of inhibition was inversely related to the rate at which each ROS is produced when scavengers are present, as calculated using Eq. (S6.1) (Text S6.6) [244]. Upon the addition of MeOH, TBA, p-BQ, FFA, and IPA, the corresponding ROS generation rates were 5.77 x 10^{-2}, 5.23 x 10^{-2}, 5.54 x 10^{-2}, 5.56 x 10^{-2}, and 4.44 x 10^{-2} mg. min^{-1}, respectively, Table S6.6.

The KBN@TiO_2@rGO/PMS system CIP photodegradation was facilitated by both •OH and $SO_4•^-$ radicals, with $SO_4•^-$ having the most significant contribution, as indicated by the inhibition observed with MeOH and TBA. The strong suppression by FFA further confirms the production of $^1O_2$ in the system. The interactions of $O_2•^-$ with •OH or H_2O, which are created through PMS activation (Eqs. (6.14) and (6.15)), can produce singlet oxygen ($^1O_2$). A sequence of reactions involving HSO_5^-, •OH, H_2O_2, and $HO_2•^-$ yields $O_2•^-$ itself (Eqs. (6.16) – (6.19)) [109]. The recombination of $SO_5•^-$ (Eq. (6.20)), the reaction of $SO_5•^-$ with H_2O (Eq. (6.21) and the self-decomposition of PMS (Eq. (6.22) can also produce $^1O_2$ [94]. However, the inhibition from quenching $^1O_2$ (using FFA) was somewhat stronger than that from scavenging $O_2•^-$ (using p-BQ), indicating that $O_2•^-$ is the primary source of $^1O_2$ in the KBN@TiO_2@rGO/PMS system. Due to its strong electron-donating ability and negative redox potential (- 0.81 V), $O_2•^-$ serves as a precursor for the potent non-radical oxidant $^1O_2$ (E_0 = 2.2 V) in catalytic oxidation systems [94]. Consequently, scavenging $O_2•^-$ leads to a decrease in $^1O_2$-mediated oxidation, as observed in this study, which is displayed in Figure 6. 5(a and b). Moreover, the significant reduction in CIP removal upon addition of IPA suggests the presence of electron-transfer routes between CIP and PMS, which were potentially facilitated by TiO_2@rGO and/or the doped KBN species [36, 56].

$$O_2^{\bullet -} + \bullet OH \rightarrow OH^- + {}^1O_2 \quad (6.14)$$

$$2O_2^{\bullet -} + 2H_2O \rightarrow 2OH^- + {}^1O_2 \quad (6.15)$$

$$HSO_5^- + H_2O \rightarrow HSO_4^- + H_2O_2 \quad (6.16)$$

$$\bullet OH + \bullet OH \rightarrow H_2O_2 \quad (6.17)$$

$$H_2O_2 + \bullet OH \rightarrow HO_2^{\bullet} + H_2O \quad (6.18)$$

$$HO_2^{\bullet} \rightarrow O_2^{\bullet -} + H^+ \quad (6.19)$$

$$HSO_5^- + SO_5^{2-} \rightarrow HSO_4^- + SO_4^{2-} + {}^1O_2 \quad (6.20)$$

$$2SO_5^- + H_2O \rightarrow 2HSO_4^- + SO_4^{2-} + 1.5{}^1O_2 \quad (6.21)$$

$$SO_5^{\bullet -} + SO_5^{\bullet -} \rightarrow S_2O_8^{2-} + {}^1O_2 \quad (6.22)$$

6.3.5.2 Electron Spin Resonance (ESR) study

The presence of ROS in the CIP/KBN@TiO_2@rGO/PMS system was further verified using electron spin resonance analysis, and the corresponding results are presented in Figure 6.5(c and d). For radical species (•OH and SO_4•$^-$) and non-radical species ($^1O_2$), respectively, DMPO and TEMP were used as spin-trapping agents. In the presence of DMPO, a distinctive septet spin-splitting pattern was seen within the CIP/KBN@TiO_2@rGO/PMS system Figure 6.5c, confirming the generation of both •OH and SO_4•$^-$ radicals during the oxidation process [81]. The spin-splitting pattern with an intensity ratio of 1:2:1: 2:1:2:1 corresponds to the DMPO–X adduct. The signal intensity of DMPO–x slowly decreased over time, indicating the transient nature of the radical species. In addition, a strong triplet (1:1:1) spin-splitting signal was seen when TEMP was exploited as a spin-trapping agent Figure 6.5d, confirming the generation of singlet oxygen ($^1O_2$) in the KBN@TiO_2@rGO/PMS system. The combined findings from the chemical scavenger experiments, ROS generation rate analysis, and ESR measurements revealed that radicals (•OH, SO_4•$^-$, and O_2•$^-$) and singlet oxygen ($^1O_2$) were the dominant reactive oxygen species in the CIP/KBN@TiO_2@rGO/PMS system.

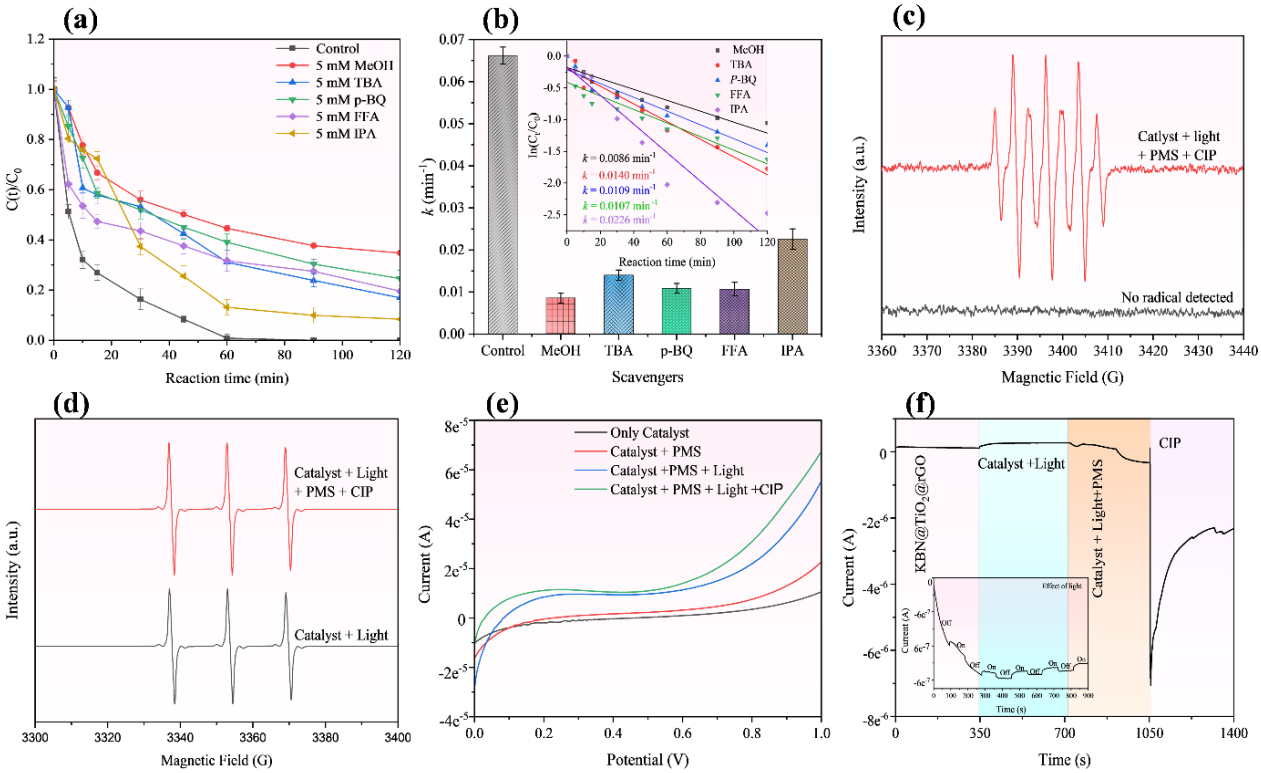

Figure 6.5 Effects of (a) CIP degradation with the addition of various scavengers, (b) First-rate constants of in the CIP@ KBN@TiO_2@rGO/PMS system, (c) DMPO as a spin-trapping agent, (d) ESR spectra using TEMP, (e) LSV analysis, and (f) i-t curve experiment for Light/ KBN@TiO_2@rGO/PMS system. (Experimental conditions: $[CIP]_0$ = 10 mg L^{-1}, $[PMS]_0$ =0.5 mM, catalyst dose = 0.1 g L^{-1}, $[scavenger]_0$ = 5 mM, and unadjusted pH = 5.23, at controlled temperature = 23 °C).

6.3.5.3 Electrochemical studies

The exchange of charges between PMS molecules and the KBN@TiO_2@rGO photocatalyst was examined through an electrochemical study. An electrode system coated with KBN@TiO_2@rGO was used to perform linear sweep voltammetry (LSV) measurements, Figure 6.5e. Notable variations in the present responses from LSV measurements were observed among the systems containing only the catalyst, KBN@TiO_2@rGO/PMS, KBN@TiO_2@rGO/PMS/light, and KBN@TiO_2@rGO/PMS/ light /CIP in Figure 6.5e. The increased current response in the KBN@TiO_2@rGO/PMS/light/CIP system suggests that efficient electron transfer occurred between the photocatalyst and the reactive species. Furthermore, the i–t curve experiment provided additional evidence of electron transfer in the KBN@TiO_2@rGO/PMS/light/CIP system. As presented in Figure 6.5f, the current response

was steady at first. Upon turning on the light at 350 s, a slight increase in current was observed, indicating the formation of metastable (light–KBN@TiO_2@rGO*) complexes. Following the addition of CIP/PMS at 700 s, the response of current increased further, suggesting electron flow from CIP to the metastable complexes of the system [74]. Finally, when catalyst/light/CIP was introduced at 1050 s, a sharp increase in current was observed, confirming enhanced electron transfer from CIP to the metastable complexes. Overall, the electrochemical investigations demonstrated that electron transfer took place between KBN@TiO_2@rGO, light, PMS, and the CIP aqueous system.

6.3.5.4 Reaction mechanisms

The KBN@TiO_2@rGO/PMS system's suggested reaction mechanism for ciprofloxacin (CIP) photodegradation combines the advantages of advanced oxidation and photocatalysis. The KBN@TiO_2@rGO nanocomposite improves the efficiency of TiO_2 by lowering electron-hole recombination and boosting visible light absorption, while PMS acts as an extra activator to produce more potent ROS. The degradation of CIP in the KBN@TiO_2@rGO/PMS system occurs via a synergistic combination of photocatalysis and advanced oxidation, as presented in Figure 6.6**.** Under light irradiation, TiO_2 is excited, generating electron–hole pairs (e^- / h^+), while KBN enhances visible-light absorption and rGO facilitates electron transfer, suppressing recombination. Electrons and holes, along with PMS, produce reactive oxygen species ($\bullet OH$, $SO_4^{\bullet-}$, $O_2^{\bullet-}$, and $^1O_2$) which attack CIP at electron-rich sites such as the piperazine ring, cyclopropyl group, and carboxylic acid group [284]. This leads to defluorination, ring-opening, and dealkylation, forming various intermediates that are further oxidised and ultimately mineralised into CO_2, H_2O, NH_4^+, and F^- [92]. The combined action of light, KBN@TiO_2@rGO, and PMS thus drives efficient CIP degradation through multiple oxidative pathways.

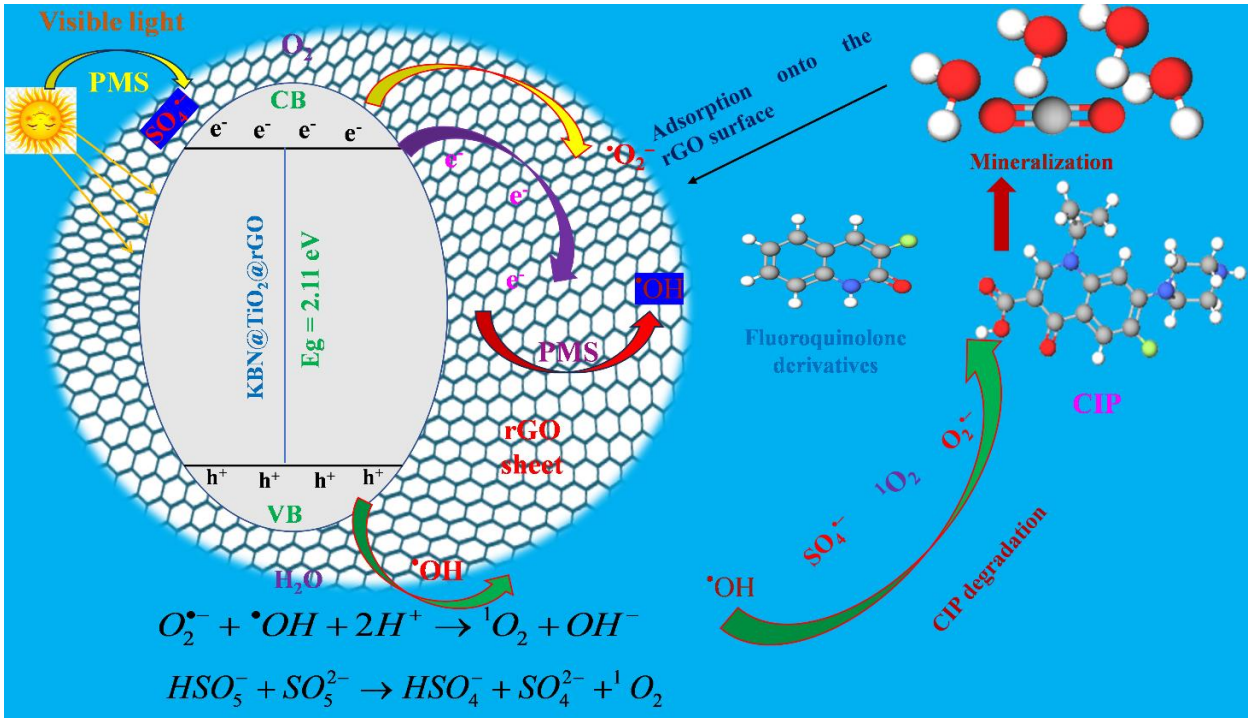

Figure 6-6 Schematic illustration of the proposed reaction mechanism for ciprofloxacin (CIP) photodegradation over the KBN@TiO2@rGO/PMS catalyst under solar light irradiation.

6.3.5.5 Analysis of intermediate and proposed mineralisation pathways

To better understand the mechanism of CIP degradation in the KBN@TiO2@rGO/PMS system, the photodegradation intermediates of CIP were found using UPLC-MS/MS. Twelve various main intermediates were seen after 120 min of oxidation and were correspondingly labelled P1 - P12, as revealed in Figure 6.7. The protonated CIP was the predominant species in the mass spectrum, with a ratio of mass to charge (m/z) 332, Figure S6.6a. Several intermediates were detected in the CIP/KBN@TiO2@rGO/PMS system, including m/z values of 401, 377, 288, 263, 219, 179, 175, 150, 113, and 62, which have been reported in previous studies [53, 54, 55] as shown in Figure S6.6b. The proposed mechanism for the photocatalytic removal of CIP is demonstrated in Figure 6.7. In general, •OH and $SO_4^{•-}$ radicals can degrade CIP through three main pathways: defluorination, piperazine ring oxidation, or quinolone ring opening [255]. In pathway 1, CIP's electrophilic sites reacted with •OH radicals to produce a mono-hydroxylated result, causing the formation of m/z = 348 (P2) [256]. Subsequent piperazine ring cleavage and dihydroxylation led to the development of P4 (m/z = 291) [254]. In pathway 2, •OH and $SO_4^{•-}$ radicals attack the CIP molecule, producing intermediate products P5 (m/z = 331) and P6 (m/z = 288) through defluorination [91]. Additionally, the intermediate P7 (m/z = 219), P8 (m/z

=150), and P9 (m/z =62) are generated via quinolone ring-opening and decarboxylation processes [84]. In pathway 3, P10 (m/z = 377), P11 (m/z=263), and P12 9m/z =179) are formed because of decarboxylation at the P1 quinolone group [256]. Further oxidation transforms P4, P9, and P12 into minor organic intermediates. Fluoride (F^-) ions released in the effluent after CIP degradation were detected by ion chromatography (IC), with a measured concentration of 0.39 mg L^{-1}. In the following processes, the CIP intermediates may mineralise into CO_2, H_2O, NH_4^+, NO_3^-, and F^- or undergo additional degradation into tiny molecules.

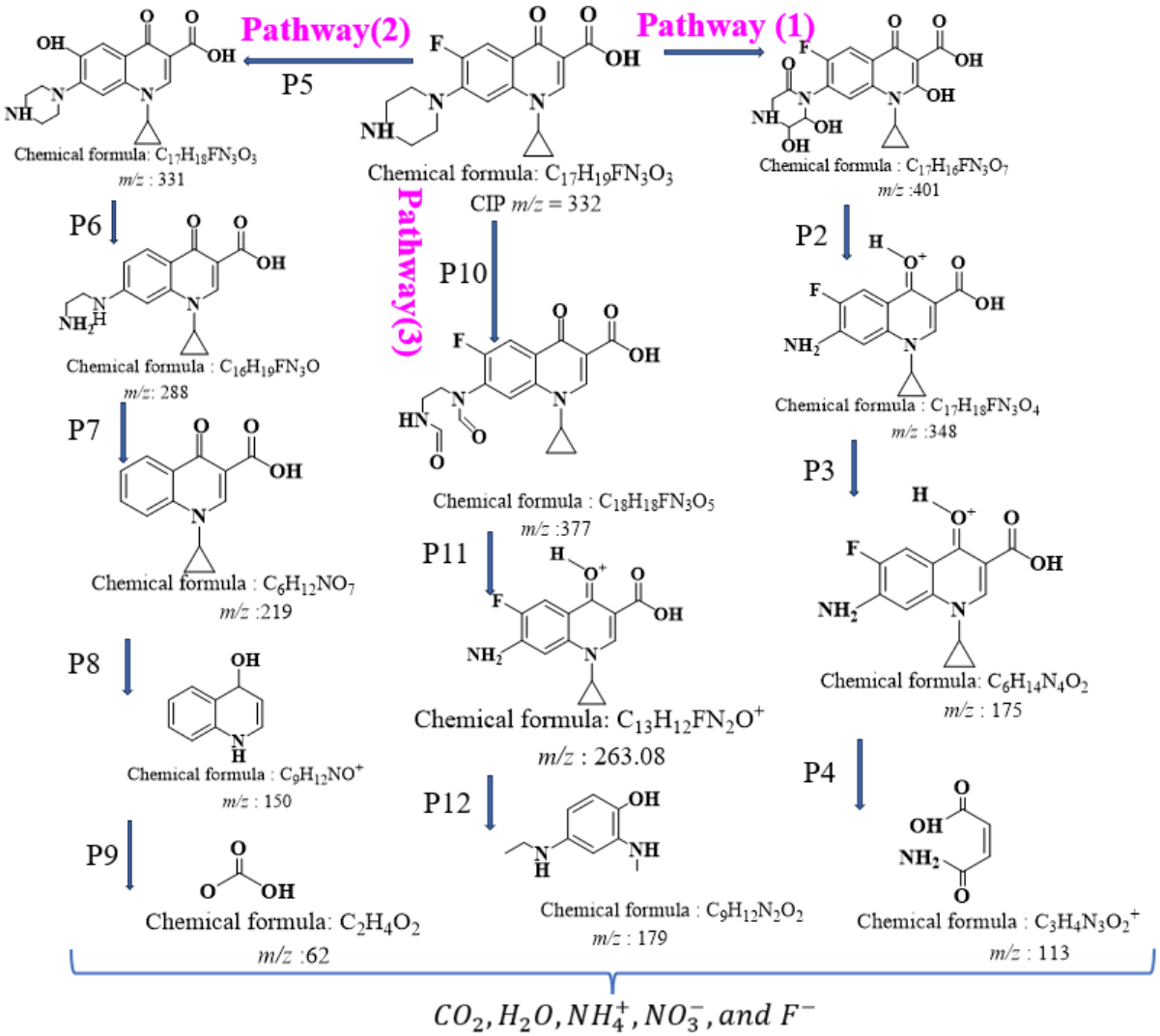

Figure 6.7 Proposed photodegradation pathway of CIP in aqueous solution using the KBN@TiO_2@rGO/PMS system.

6.3.6 Statistical analysis using RSM

Tables 6. 4 and 6.5 show the results of the analysis of variance (ANOVA) for TOC removal and CIP photodegradation. The models are very significant for both CIP photodegradation and

TOC removal efficiency, as shown by the model F-values of 171.49 and 108.17, respectively. P-values below 0.05 indicate the significance of the relevant model terms in both ANOVA tables. Accordingly, the significant model terms for CIP photodegradation and TOC removal were identified as A, B, C, D, AB, AC, AD, BC, CD, A^2, B^2, C^2, and D^2 for CIP, and A, B, C, D, AB, AD, BC, A^2, B^2, C^2, and D^2 for TOC removal. In contrast, terms with p-values above 0.05 were considered insignificant, specifically, BD for CIP photodegradation and AC and CD for TOC removal in this study

Table 6.4: ANOVA of the response surface model for CIP photodegradation.

Source	Sum of Squares	df	Mean Square	F- value	P-value	
Model	1213.21	14	86.66	171.49	<0.0001	Significant
A-pH	38.56	1	38.56	76.30	<0.0001	
B-Time	727.74	1	727.74	1440.15	<0.0001	
C-Cat. dose	97.07	1	97.07	192.10	<0.0001	
D- Initial [CIP]	4.26	1	4.26	8.43	0.0116	
AB	11.56	1	11.56	22.88	0.0003	
AC	17.43	1	17.43	34.49	<0.0001	
AD	9.55	1	9.55	18.89	0.0007	
BC	33.52	1	33.52	66.34	<0.0001	
BD	1.11	1	1.11	2.20	0.1599	
CD	32.83	1	32.83	64.97	<0.0001	
A^2	25.47	1	25.47	50.40	<0.0001	
B^2	162.25	1	162.25	321.09	<0.0001	
C^2	62.59	1	62.59	123.87	<0.0001	
D^2	95.97	1	95.97	189.91	<0.0001	
Residual	7.07	14	0.5053			
Lack of fit	6.44	10	0.644	4.06	0.0947	Not significant
Pure Error	0.6349	4	0.1587			
Cor Total	1220.29	28				

The lack-of-fit test evaluates how accurately the model describes the experimental data at points excluded from the regression analysis [257]. As presented in Tables 6.4 and 6.5, the lack of fit F- and *p*-values were 4.04 and 0.0947 for CIP photodegradation and 1.63 and 0.3385 for TOC removal, respectively. The lack of fit was not significant because the p-values were higher than 0.05, suggesting that both responses within the examined range are sufficiently described and predicted by the model equations. The regression models of CIP photodegradation and TOC removal had coefficients of determination (R^2) of 0.9942 and 0.9908, respectively, based on the RSM results. These results show that the models accounted for 99.42% and 99.08% of the total variability within the experimental range, as summarised in Table S8. Moreover, the

predicted R^2 values of 0.9688 and 0.9548 confirm that the model equations can reliably forecast the responses (CIP degradation and TOC removal) even outside the tested conditions. Overall, in a well-fitted model, both R^2 and predicted R^2 values should approach 1, indicating a high level of agreement between the experimental results and the model's predictions. Equations (6.23) and (6.24**)** show the model equations that correlate the responses with the process variables stated in terms of actual values and eliminating the insignificant term

Table 6.5: ANOVA of the response surface model for TOC removal.

Source	Sum of Squares	df	Mean Square	F- value	P-value	
Model	811.94	14	58.00	108.17	< 0.0001	Significant
A-pH	97.87	1	97.87	182.53	< 0.0001	
B-Time	248.98	1	248.98	464.36	< 0.0001	
C-Cat. dose	234.79	1	234.79	437.90	< 0.0001	
D- Initial [CIP]	7.79	1	7.79	14.53	0.0019	
AB	7.56	1	7.56	14.10	0.0021	
AC	1.39	1	1.39	2.60	0.1294	
AD	45.90	1	45.90	85.61	< 0.0001	
BC	12.39	1	12.39	23.11	0.0003	
BD	68.56	1	68.56	127.87	< 0.0001	
CD	1.25	1	1.25	2.34	0.1484	
A^2	53.81	1	53.81	100.37	< 0.0001	
B^2	42.81	1	42.81	79.85	< 0.0001	
C^2	3.12	1	3.12	5.83	0.0300	
D^2	16.30	1	16.30	30.41	< 0.0001	
Residual	7.51	14	0.5362			
Lack of fit	6.02	10	0.6024	1.63	0.3385	Not significant
Pure Error	1.48	4	0.3706			
Cor Total	819.45	28				

CIP Photodegradation Efficiency (%) $= 30.20 + 3.09\,\mathrm{A} + 0.54\mathrm{B} + 350.71\mathrm{C} - 1.43\mathrm{D} - 0.01 \times \mathrm{A} \times \mathrm{B} - 10.44 \times \mathrm{A} \times \mathrm{C} + 0.08 \times \mathrm{A} \times \mathrm{D} - 0.97 \times \mathrm{B} \times \mathrm{C} + 11.46 \times \mathrm{C} \times \mathrm{D} - 0.12\mathrm{A}\text{^}2 - 0.001\mathrm{B}\text{^}2 - 1242.57\mathrm{C}\text{^}2 - 0.15\mathrm{D}\text{^}2$ (6.23)

TOC Removal Efficiency (%) $= 11.83 + 2.35A + 0.44B + 239.84C + 1.71D - 0.01 \times A \times B + 0.17 \times A \times D - 0.59 \times B \times C - 0.01 \times B \times D - 0.18A\text{^}2 - 0.001B\text{^}2 - 277.6C\text{^}2 - 0.06D\text{^}2$ (6.24)

6.3.6.2 Effects of process variable interactions on CIP degradation

Figures 6.8a–e illustrate the interactive impacts of the operational variables on CIP photodegradation as functions of solution pH, reaction time, photocatalyst dosage, and initial pollutant concentration. As shown in Figure 6.8a, the removal efficacy increased with longer irradiation times and peaked in moderately acidic to neutral conditions (pH 6-7). Conversely, highly acidic and alkaline environments reduced performance due to variations in CIP speciation and a reduction in reactive oxygen species (ROS) generation. Increasing the catalyst dosage enhanced CIP degradation because there were more active sites and more ROS generated, as depicted in Figure 6.8b, with the optimum once again being observed around neutral pH. The combined impacts of catalyst dose and irradiation time demonstrated a synergistic effect, as revealed in Figure 6.8c, where both longer irradiation times and larger catalyst loading boosted photocatalytic efficiency. As seen in Figure 6.8d, near-neutral pH circumstances encouraged higher performance, whereas raising the initial CIP concentration resulted in decreased degradation efficiency, perhaps because there were fewer active sites and oxidising radicals available in comparison to pollutant molecules. Similarly, Fig. 8e shows that CIP removal efficiency increased with increasing catalyst dosage but decreased at higher pollutant concentrations, indicating that high contaminant levels impede catalytic activity. In conclusion, the response surface plots show that near-neutral pH, longer irradiation times, moderate-to-high catalyst dosages, and lower initial pollutant concentrations resulted in optimal CIP degradation, confirming the significant interactive and nonlinear effects among the parameters under investigation.

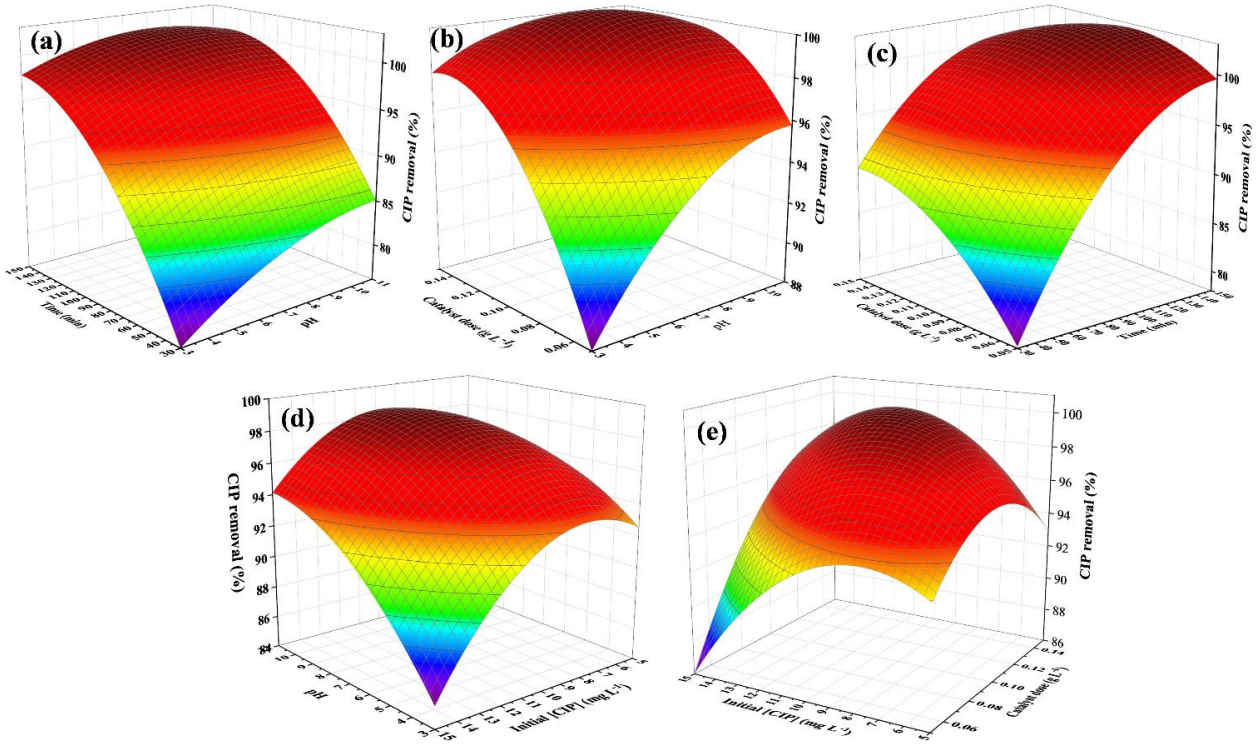

Figure 6.8 3D surface plot of CIP photodegradation efficiency as a function of (a) Solution pH and reaction time, (b) Solution pH and catalyst dosage, (c) reaction time and catalyst dosage, (d) Initial CIP concentration and pH, and (e) catalyst dosage and Initial concentration of CIP in the KBN@TiO_2@rGO/PMS system.

6.3.6.3 Interaction effects of process parameters on TOC removal

The effects of operational parameter interactions on TOC removal are shown in Figure 6.9 (a–d). As seen in Figure 6.9a, TOC removal increased with reaction time until it reached an optimum, after which it somewhat decreased. Near-neutral pH (approximately 6–7) was found to have the maximum effectiveness. Extreme pH conditions adversely affected the removal efficiency of TOC, likely resulting from decreased PMS activation and catalyst instability. According to Figure 6.9b, TOC removal declined as the starting pollutant content increased, with intermediate pH values producing the best results. Catalyst dose and reaction time showed a synergistic effect in Figure 6.9c, with longer reaction times and larger catalyst loading increasing TOC removal. However, using more catalyst than the optimal amount, approximately 0.15 g L^{-1}, only slightly decreased TOC removal, possibly due to particle agglomeration and light scattering. Figure 6.9d shows that while longer reaction times enhanced TOC removal, higher initial concentrations led to lower efficiency, indicating that reactive oxygen species were insufficient at elevated pollutant loads. Overall, the highest TOC

removal occurred under moderate pH and initial concentration, together with increased photocatalyst dosage and extended reaction time, demonstrating synergistic and inhibitory effects among the variables.

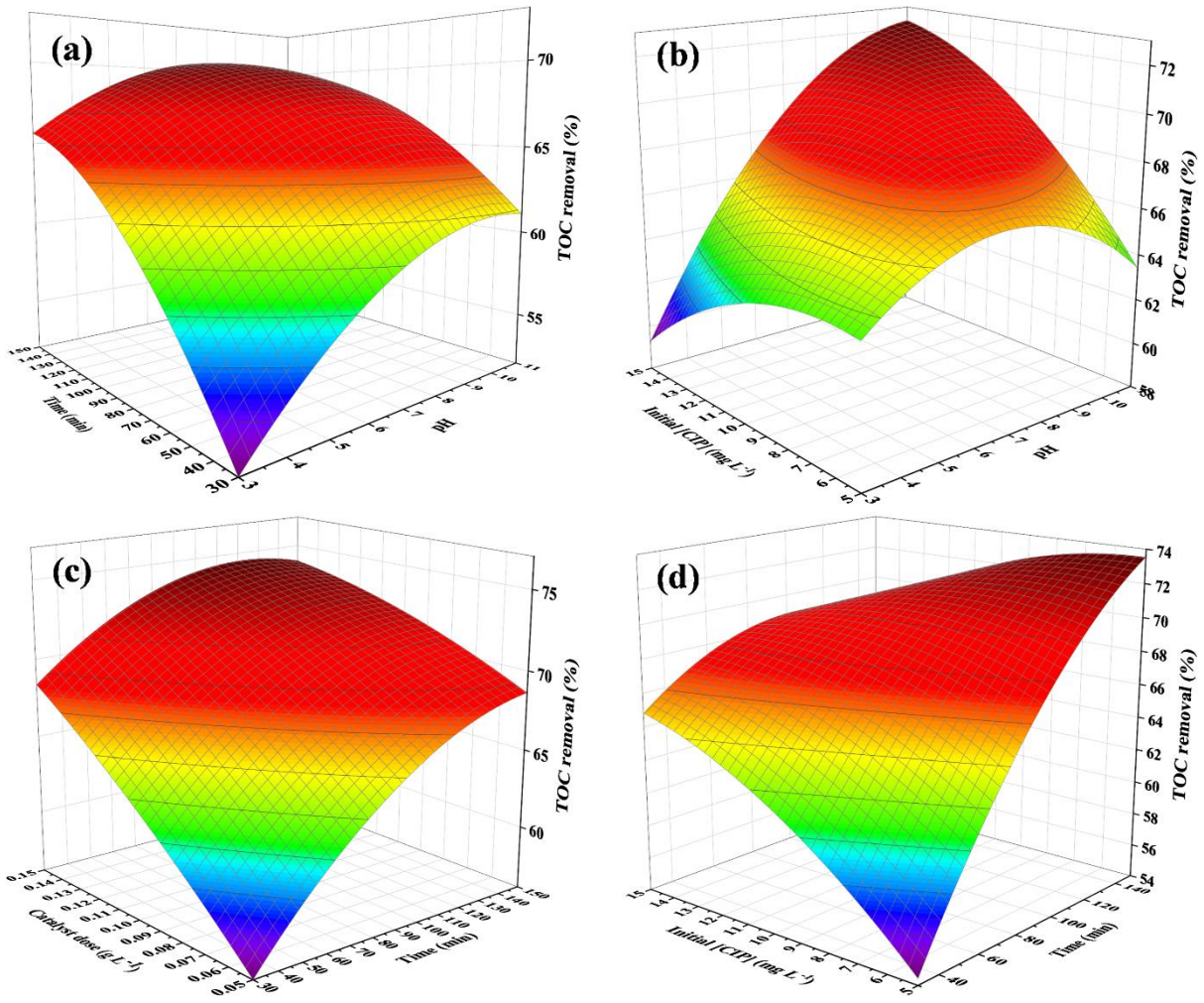

Figure 6.9 3D surface plot of TOC removal as a function of (a) solution pH and reaction time, (b) solution pH and Initial concentration of CIP, (c) reaction time and catalyst dosage, and (d) reaction time and Initial concentration of CIP in the KBN@TiO_2@rGO/ PMS system.

6.3.6.3 Model optimisation and verification

The optimum process conditions for photocatalytic degradation were determined using a numerical optimisation approach based on Box–Behnken Design (BBD)-RSM. The main objective was to maximise ciprofloxacin photocatalytic degradation and total organic carbon removal efficiencies. Derringer's desirability function, which has a range of 0 to 1, was used to evaluate the optimal conditions predicted by BBD-RSM in order to determine how effectively the selected conditions achieved the desired results. The initial pollutant concentration was set

at 10 mg L^{-1}, and the solution pH, reaction time, and catalyst dose were limited within the study range of 3–11, 30–150 min, and 0.05–0.15g L^{-1}, respectively, to maximise CIP degradation and TOC removal.

The optimisation forecasted a CIP photodegradation efficiency of 100% and a TOC removal efficiency of 75.91% at an optimum solution pH of 8.17, a reaction time of 101.15 min, a catalyst dose of 0.13 g L^{-1}, and an initial contaminant concentration of 9.99 mg L^{-1}, with a desirability of 1. To validate the predicted optimum, experiments were conducted in triplicate under the corresponding conditions. The observed CIP photodegradation and TOC removal efficiencies were 99.98 ± 1.23% and 74.68 ± 1.04 %, respectively, exhibiting a high degree of agreement with the predicted values.

6.4 Conclusions

The ability of the PMS-modified KBN@TiO_2@rGO photocatalyst to degrade antibiotics in wastewater was successfully demonstrated. The KBN@TiO_2@rGO/PMS system showed excellent photodegradation performance toward the degradation of antibiotics (TC, CIP, NORF, and SMX) as well as non-steroidal anti-inflammatory drugs (DCF). Under optimal conditions-catalyst dose of 0.1 g L^{-1}, PMS concentration of 0.5 mM, and solution pH of 5.23, complete degradation (100%) of CIP was achieved within 90 min. Chemical quenching and ESR experiments confirmed the generation of ROS under exposure to visible light in the KBN@TiO_2@rGO/PMS system. The photocatalytic degradation of pharmaceutical pollutants was mainly governed by radical species, while electron-transfer mechanisms and non-radical pathways also played supportive roles in the overall degradation process. In addition, intermediate degradation products were determined, and tentative photodegradation pathways were proposed. Overall, the findings demonstrate that KBN@TiO_2@rGO is a novel and highly efficient photocatalyst in combination with PMS for the photodegradation of emerging pollutants in contaminated wastewater. RSM optimisation identified the optimal conditions (pH = 8.17, irradiation time =101.2 min, catalyst dose = 0.13 g L^{-1}, and Initial [CIP] = 9.99 mg L^{-1}), achieving predicted 100% CIP degradation and 75.91% TOC removal with 100% desirability. The RSM model demonstrated excellent predictive accuracy, as evidenced by high correlation coefficients between the experimental and predicted values.

CHAPTER SEVEN
CONCLUSIONS AND RECOMMENDATIONS

7.1 Conclusions

This study provides a holistic evaluation of existing municipal wastewater treatment performance and the development of advanced photocatalytic technologies to address emerging contaminants. The assessment of the Kality Municipal Wastewater Treatment Plant (KMWWTP) revealed that the current treatment system is inadequate for effectively removing nutrients, heavy metals, and widespread pharmaceutical pollutants, as evidenced by low (< 50%) removal efficiencies and effluent concentrations of several contaminants- such as Ni, Cd, Pb, and As exceeding effluent concentrations and surpassing WHO and USEPA permissible limits. These results highlight the urgent need for incorporating a robust tertiary treatment stage to protect downstream aquatic ecosystems and agricultural systems reliant on treated effluent.

To address this challenge, the study successfully synthesised and optimised advanced photocatalytic materials using sol-gel and hydrothermal treatment methods. The triple-doped KBN-TiO_2 photocatalyst, optimised through Box-Behnken response surface methodology (BBD-RSM), exhibited significantly improved photocatalytic activity compared with undoped and binary-doped TiO_2, achieving 84.3% CIP photodegradation efficiency and enhanced structural characteristics such as increased surface area, refined crystal size, and a dominant anatase phase. Building on this, the composite KNB@TiO2@rGO nanomaterial demonstrated even greater improvements in optical, structural, and surface properties, including a low band gap (2.11 eV), high surface area (71.35 m^2 g-1), and superior photocatalytic degradation of CIP, NORF, and TC, achieving up to 100% removal. Its enhanced performance stems from synergistic interactions between KBN doping, TiO_2, and rGO, which collectively promote visible light activity, charge separation, and ROS generation.

Further enhancement was achieved by integrating proxymonosulfate (PMS), resulting in the KBN@TiO_2@rGO/PMS system, which exhibited rapid and complete photodegradation of antibiotics, including CIP, NORF, SMX, and TC, as well as non-steroidal anti-inflammatory drugs like DCF. ESR and quenching experiments confirmed that the radical pathways dominated the photodegradation mechanism, with additional contributions from electron-transfer and non-radical species. RSM optimisation of operational parameters further

demonstrated excellent predictive reliability, achieving 100% CIP photodegradation and 75.91% TOC removal under optimised conditions.

Overall, the findings clearly demonstrate that while conventional wastewater treatment systems remain insufficient for removing persistent emerging pollutants, the engineered KBN-based photocatalytic materials, particularly KBN@TiO_2@rGO and its PMS-activated variant, offer highly efficient, stable, and environmentally friendly alternatives to remediation. These advanced composite photocatalysts show strong potential for practical application in aquatic and agricultural environments.

7.2 Recommendations and Future Outlooks

Based on the overall results of this study, some recommendations and future directions are proposed to advance the development of wastewater treatment technologies, enhance environmental protection, and guide future scientific research.

- **Public Awareness and Pharmaceutical Waste Management:** Coordinated efforts are needed to reduce pharmaceutical contamination. In order to reduce pollutant loading at the source, technological and policy initiatives should be accompanied by public awareness campaigns about the appropriate disposal of unwanted medications, decreased antibiotic overuse, and ecologically responsible consumer patterns.
- **Catalyst immobilisation and Recovery Strategies:** Research should look into immobilisation techniques, including coating photocatalysts on inert substrates (glass, ceramics, membranes), fixed-bed reactors, or magnetic support materials to reduce operating costs and improve catalyst reusability. These tactics will permit recurrent use and enhance catalyst removal from treated effluents.
- **Economic Feasibility and Sustainability Evaluation:** Comprehensive cost-benefit analysis, energy assessments, and life-cycle evaluations should be carried out to facilitate large-scale adoption. These investigations will aid in determining the suggested photocatalytic technologies' long-term operational feasibility, environmental sustainability, and economic feasibility.
- **Comprehensiveness, Toxicity and Environmental Safety Assessment:** Pharmaceuticals are efficiently degraded by photocatalysis, but long-term environmental effects, possible nanoparticle leaching, and the ecotoxicity of

intermediates are still major issues. To ensure safe implementation, future research should incorporate environmental risk studies, life-cycle assessments, and toxicity tests.

- **Mechanistic Insight and Radical Pathway Clarification:** Using methods like LC–MS/MS, EPR spectroscopy, and transient photoluminescence analysis, more investigation of photocatalytic reaction pathways is advised to determine dominating ROS, electron-transfer processes, and degradation intermediates. These investigations will enhance comprehension and facilitate catalyst optimisation.
- **Strengthening Monitoring and Policy Frameworks:** Authorities should implement regular monitoring programs for heavy metals, antibiotics, and developing pharmaceuticals in influent and effluent streams due to the insufficient removal effectiveness of traditional WWTPs. Regulatory bodies ought to think about encouraging the use of cutting-edge treatment technology and revising discharge limitations.
- **Pilot-Scale and Full-Scale Application:** While the KBN-doped TiO_2 and KBN@TiO_2@rGO photocatalyst exhibited excellent performance at laboratory scale, future studies should focus on pilot-scale, continuous-flow, and real wastewater environments to evaluate long-term performance, operational stability, and scalability for practical applications in municipal and industrial wastewater treatment plants.

References

[1] J. A. Garrido-Cardenas, B. Esteban-García, A. Agüera, J. A. Sánchez-Pérez, and F. Manzano-Agugliaro, "Wastewater treatment by advanced oxidation process and their worldwide research trends," *Int J Environ Res Public Health*, vol. 17, no. 1, 2020, doi: 10.3390/ijerph17010170.

[2] P. N. Nyashanu, F. S. Shafodino, and L. M. Mwapagha, "Determining the potential human health risks posed by heavy metals present in municipal sewage sludge from a wastewater treatment plant," *Sci Afr*, vol. 20, 2023, doi: 10.1016/j.sciaf. 2023.e01735.

[3] S. Arzate, S. Pfister, C. Oberschelp, and J. A. Sánchez-Pérez, "Environmental impacts of an advanced oxidation process as tertiary treatment in a wastewater treatment plant," *Science of the Total Environment*, vol. 694, 2019, doi: 10.1016/j.scitotenv.2019.07.378.

[4] M. Sheydaei, H. Reza, K. Shiadeh, B. Ayoubi-feiz, and R. Ezzati, "Preparation of nano N-TiO_2 / graphene oxide / titan grid sheets for visible light assisted photocatalytic ozonation of cefixime," *Chemical Engineering Journal*, vol. 353, no. July, pp. 138–146, 2018, doi: 10.1016/j.cej.2018.07.089.

[5] N. H. Tran, M. Reinhard, and K. Y. H. Gin, "Occurrence and fate of emerging contaminants in municipal wastewater treatment plants from different geographical regions-a review," *Water Res*, vol. 133, no. December, pp. 182–207, 2018, doi: 10.1016/j.watres.2017.12.029.

[6] A. Foglia *et al.*, "Transforming wastewater treatment plants into reclaimed water facilities in water-unbalanced regions. An overview of possibilities and recommendations focusing on the Italian case," *J Clean Prod*, vol. 410, no. November 2022, 2023, doi: 10.1016/j.jclepro.2023.137264.

[7] M. Coccia and E. Bontempi, "New trajectories of technologies for the removal of pollutants and emerging contaminants in the environment," *Environ Res*, vol. 229, no. February, p. 115938, 2023, doi: 10.1016/j.envres.2023.115938.

[8] B. A. Mohamed, H. Hamid, C. V. Montoya-Bautista, and L. Y. Li, "Circular economy in wastewater treatment plants: Treatment of contaminants of emerging concerns (CECs) in effluent using sludge-based activated carbon," *J Clean Prod*, vol. 389, no. October 2021, p. 136095, 2023, doi: 10.1016/j.jclepro.2023.136095.

[9] D. P. Mohapatra and D. M. Kirpalani, "Advancement in treatment of wastewater: Fate of emerging contaminants," *Canadian Journal of Chemical Engineering*, vol. 97, no. 10, pp. 2621–2631, 2019, doi: 10.1002/cjce.23533.

[10] A. Rubio-clemente, “Wastewater Treatment: Research Trends,” vol. 13, 2021, doi: 10.3390/w13172445.

[11] K. Alemu, B. Assefa, D. Kifle, and H. Kloos, “Removal of Organic Pollutants from Municipal Wastewater by Applying High-Rate Algal Pond in Addis Ababa, Ethiopia,” *Earth Systems and Environment*, vol. 2, no. 2, pp. 377–386, 2018, doi: 10.1007/s41748-018-0050-1.

[12] Z. Lu *et al.*, “A multifunctional membrane based on TiO_2/PCN-224 heterojunction with synergistic photocatalytic-photothermal activity under visible-light irradiation,” *Appl Catal B*, vol. 342, no. September 2023, p. 123374, 2024, doi: 10.1016/j.apcatb.2023.123374.

[13] H. Zhou *et al.*, “Photocatalytic degradation by TiO_2-conjugated/coordination polymer heterojunction: Preparation, mechanisms, and prospects,” *Appl Catal B*, vol. 344, no. September 2023, p. 123605, 2024, doi: 10.1016/j.apcatb.2023.123605.

[14] X. Xiao, X. Wang, Y. Li, Y. Li, G. Sun, and Y. Han, “A two-electron migration mechanism co-constructed by K^+ passivation and defect engineering for efficient TiO_2 photocatalytic hydrogen evolution,” *Appl Surf Sci*, vol. 631, no. April, p. 157577, 2023, doi: 10.1016/j.apsusc.2023.157577.

[15] M. Andreozzi *et al.*, “Treatment of saline produced water through photocatalysis using rGO-TiO_2 nanocomposites,” *Catal Today*, vol. 315, no. February, pp. 194–204, 2018, doi: 10.1016/j.cattod.2018.04.048.

[16] O. Samuel *et al.*, “Visible light-driven TiO_2-WO_3@GO photocatalyst with catalytic memory for round-the-clock photocatalytic degradation of oilfield-produced water,” *Ceram Int*, vol. 50, no. 11, pp. 18205–18219, 2024, doi: 10.1016/j.ceramint.2024.02.305.

[17] J. Yu, J. Zou, P. Xu, and Q. He, “Three-dimensional photoelectrocatalytic degradation of the opaque dye acid fuchsin by Pr and Co co-doped TiO_2 particle electrodes,” *J Clean Prod*, vol. 251, p. 119744, 2020, doi: 10.1016/j.jclepro.2019.119744.

[18] S. Rajappa, P. G. Shivarathri, M. H. Rajappa, M. C. Devendrachari, and H. M. N. Kotresh, “Energy-efficient low-power LED-mediated effective photodegradation of cationic and anionic dyes by phthalocyanine-based COF sensitized ZnO photoactive material,” *Polyhedron*, vol. 252, no. October 2023, p. 116881, 2024, doi: 10.1016/j.poly.2024.116881.

[19] G. Sofia, C. Koventhan, S. Kanmani, and A. Y. Lo, “Green synthesized rGO/TiO_2/g-C_3N_4 nanocomposites via Plectranthus ambitious extract for efficient photocatalytic

degradation of methylene blue: RSM optimization, antimicrobial and phytotoxicity assessment," *J Environ Chem Eng*, vol. 13, no. 1, 2025, doi: 10.1016/j.jece.2024.115267.

[20] J. Kuang, Z. Xing, J. Yin, Z. Li, Q. Zhu, and W. Zhou, "Surface plasma Ag-decorated single-crystalline TiO_{2-x}(B) nanorod/defect-rich g-C_3N_4 nanosheet ternary superstructure 3D heterojunctions as enhanced visible-light-driven photocatalyst," *J Colloid Interface Sci*, vol. 542, pp. 63–72, 2019, doi: 10.1016/j.jcis.2019.01.124.

[21] J. Yuan, Y. Zhang, X. Zhang, L. Zhao, H. Shen, and S. Zhang, "Template-free synthesis of core—shell Fe_3O_4@MoS_2@mesoporous TiO_2 magnetic photocatalyst for wastewater treatment," *International Journal of Minerals, Metallurgy and Materials*, vol. 30, no. 1, pp. 177–191, 2023, doi: 10.1007/s12613-022-2473-9.

[22] S. Zhao *et al.*, "Photocatalytic efficiency of K-TiO_2 for air pollutant treatment: Synergistic effect of NO and acetaldehyde by K incorporation," *Appl Surf Sci*, vol. 667, no. May, p. 160374, 2024, doi: 10.1016/j.apsusc.2024.160374.

[23] C. Xiao, X. Chen, X. Tao, X. Liu, X. Wang, and L. Zhu, "In situ generation of hydroxyl radicals by B-doped TiO_2 for efficient photocatalytic degradation of acetaminophen in wastewater," *Environmental Science and Pollution Research*, vol. 30, no. 16, pp. 46997–47011, 2023, doi: 10.1007/s11356-023-25390-1.

[24] R. E. Nimshi, J. J. Vijaya, L. J. Kennedy, P. S. Selvamani, M. Bououdina, and P. J. Sophia, "Effective microwave assisted synthesis of $CoFe_2O_4$@TiO_2@rGO ternary nanocomposites for the synergic Sono photocatalytic degradation of tetracycline and antibiotics," *Ceram Int*, vol. 49, no. 9, pp. 13762–13773, 2023, doi: 10.1016/j.ceramint.2022.12.254.

[25] E. Assayehegn *et al.*, "Effective catalysts for wastewater treatment under sunlight: Gas dependent preparation of mesoporous biphasic N-doped TiO_2 nanoparticles," *Mater Today Commun*, vol. 37, no. November, p. 107447, 2023, doi: 10.1016/j.mtcomm.2023.107447.

[26] M. B. M. Roshtkhari and M. H. Entezari, "Graphite/carbon-doped TiO_2 nanocomposite synthesized by ultrasound for the degradation of diclofenac," *Environmental Science and Pollution Research*, vol. 31, no. 10, pp. 15105–15125, 2024, doi: 10.1007/s11356-024-32182-8.

[27] Z. Cheng, X. Yu, S. Cao, C. Li, Q. Wang, and L. Piao, "A self-supported P-TiO_2(B)/Ni_2P hybrid achieves efficient sunlight-driven seawater splitting," *Sci China Chem*, vol. 2, 2024, doi: 10.1007/s11426-024-2335-y.

[28] G. Wang, Y. Li, J. Dai, and N. Deng, “Highly efficient photocatalytic oxidation of antibiotic ciprofloxacin using TiO_2@g-C_3N_4@biochar composite,” *Environmental Science and Pollution Research*, vol. 29, no. 32, pp. 48522–48538, 2022, doi: 10.1007/s11356-022-19269-w.

[29] R. Nandee, M. A. Chowdhury, M. M. Rana, N. Hossain, and S. K. Nondy, “Bandgap design of fabricated BN/ZnO/Al_2O_3/TiO_2 doped graphene using XPS approach,” *Applications in Engineering Science*, vol. 17, no. December 2023, p. 100166, 2024, doi: 10.1016/j.apples.2023.100166.

[30] A. B. Migdadi, Q. M. Al-Bataineh, A. A. Ahmad, H. M. Al-Khateeb, and A. Telfah, “Titanium dioxide/reduced graphene oxide nanocomposites as effective photocatalytic for hazardous 4-nitrophenol,” *J Alloys Compd*, vol. 971, no. October 2023, p. 172794, 2024, doi: 10.1016/j.jallcom.2023.172794.

[31] R. Kaveh, H. Alijani, E. Falletta, C. L. Bianchi, M. Mokhtarifar, and D. C. Boffito, “Advancements in superhydrophilic titanium dioxide/graphene oxide composites coatings for self-cleaning applications on glass substrates: A comprehensive review,” *Prog Org Coat*, vol. 190, no. February, p. 108347, 2024, doi: 10.1016/j.porgcoat.2024.108347.

[32] B. M. Jun *et al.*, “Photocatalytic and electrocatalytic degradation of bisphenol A in the presence of graphene/graphene oxide-based nanocatalysts: A review,” *Chemosphere*, vol. 356, no. April, p. 141941, 2024, doi: 10.1016/j.chemosphere.2024.141941.

[33] Y. H. Fan, Y. Q. Li, F. Hayat, C. Liu, J. Li, and M. Chen, “Multi-targeted removal of coexisted antibiotics in water by the synergies of radical and non-radical pathways in PMS activation,” *Sep Purif Technol*, vol. 305, p. 122475, Jan. 2023, doi: 10.1016/J.SEPPUR.2022.122475.

[34] M. Cao *et al.*, “A water stable cobalt-bipyridine based hydrogen bonding double layered network for catalytic degradation of tetracycline,” *J Mol Struct*, vol. 1321, p. 140003, Feb. 2025, doi: 10.1016/J.MOLSTRUC.2024.140003.

[35] Y. Wu *et al.*, “Utilizing the enhanced Fenton-like catalytic reactivity and superior photothermal conversion capacity of cobalt doped nickel phosphide for efficient peroxymonosulfate activation and antibiotics degradation,” *J Environ Chem Eng*, vol. 13, no. 3, p. 116797, Jun. 2025, doi: 10.1016/J.JECE.2025.116797.

[36] D. Manos and I. Konstantinou, “Recent Advances in Transition Metal Selenide-Based Catalysts for Organic Pollutant Degradation by Advanced Oxidation Processes,” *Catalysts*, vol. 15, no. 10, p. 938, 2025, doi: 10.3390/catal15100938.

[37] H. Zhang, C. Xie, L. Chen, J. Duan, F. Li, and W. Liu, “Different reaction mechanisms of $SO_4^{\bullet-}$ and •OH with organic compound interpreted at molecular orbital level in Co(II)/peroxymonosulfate catalytic activation system,” *Water Res*, vol. 229, p. 119392, Feb. 2023, doi: 10.1016/J.WATRES.2022.119392.

[38] Y. Dong *et al.*, “Sulfamethazine degradation and copper transformation in Cu(II)/PMS system: In-depth investigation of the interaction between intermediates and copper,” *Journal of Water Process Engineering*, vol. 58, p. 104929, Feb. 2024, doi: 10.1016/J.JWPE.2024.104929.

[39] S. Ye *et al.*, “Nitrogen-doped biochar fiber with graphitization from Boehmeria nivea for promoted peroxymonosulfate activation and non-radical degradation pathways with enhancing electron transfer,” *Appl Catal B*, vol. 269, p. 118850, Jul. 2020, doi: 10.1016/J.APCATB.2020.118850.

[40] K. Zhu *et al.*, “Non-radical pathway dominated degradation of organic pollutants by nitrogen-doped microtube porous graphitic carbon derived from biomass for activating peroxymonosulfate: Performance, mechanism and environmental application,” *J Colloid Interface Sci*, vol. 625, pp. 890–902, Nov. 2022, doi: 10.1016/J.JCIS.2022.06.078.

[41] Z. Wang *et al.*, “Peroxymonosulfate Activation by Bi-Fe Oxide Co-Doped Graphitic Carbon Nitride for Degradation of Sulfamethoxazole: Performance and Mechanism,” *Applied Sciences (Switzerland)*, vol. 14, no. 8, 2024, doi: 10.3390/app14083181.

[42] X. Xiao, X. Wang, Y. Li, Y. Li, G. Sun, and Y. Han, “A two-electron migration mechanism co-constructed by K^+ passivation and defect engineering for efficient TiO_2 photocatalytic hydrogen evolution,” *Appl Surf Sci*, vol. 631, no. May, p. 157577, 2023, doi: 10.1016/j.apsusc.2023.157577.

[43] M. Samy, S. Tang, Y. Zhang, and D. Y. C. Leung, “Understanding the variations in degradation pathways and generated by-products of antibiotics in modified TiO_2 and ZnO photodegradation systems: A comprehensive review,” *J Environ Manage*, vol. 370, no. August, p. 122402, 2024, doi: 10.1016/j.jenvman.2024.122402.

[44] M. E. Hailu *et al.*, "Highly efficient KBN@TiO_2@rGO composite for photodegradation of antibiotics under visible light irradiation," *Sep Purif Technol*, p. 135352, Sep. 2025, doi: 10.1016/J.SEPPUR.2025.135352.

[45] B. C. Y. Lee, F. Y. Lim, W. H. Loh, S. L. Ong, and J. Hu, "Emerging contaminants: An overview of recent trends for their treatment and management using light-driven processes," *Water (Switzerland)*, vol. 13, no. 17, 2021, doi: 10.3390/w13172340.

[46] C. Products, T. Plant, O. Al-mashaqbeh, D. Alsafadi, S. Dalahmeh, and S. Bartelt-hunt, "Removal of Selected Pharmaceuticals and Personal," *Water (Basel)*, vol. 11, pp. 1–13, 2019.

[47] J. Margot, L. Rossi, D. A. Barry, and C. Holliger, "A review of the fate of micropollutants in wastewater treatment plants," *WIREs Water*, vol. 2, no. 5, pp. 457–487, 2015, doi: 10.1002/wat2.1090.

[48] A. Tufail, W. E. Price, and F. I. Hai, "A critical review on advanced oxidation processes for the removal of trace organic contaminants: A voyage from individual to integrated processes," *Chemosphere*, vol. 260, 2020, doi: 10.1016/j.chemosphere.2020.127460.

[49] A. Fraiese *et al.*, "Removal of emerging contaminants in wastewater by sonolysis, photocatalysis and ozonation," *Global Nest Journal*, vol. 21, no. 2, pp. 98–105, 2019, doi: 10.30955/gnj.002625.

[50] J. K. Bwapwa and A. T. Jaiyeola, "Emerging Contaminants in Drinking Water and Wastewater, Effects on Environment and Remediation," *International Journal of Applied Engineering Research*, vol. 14, no. 2, pp. 539–546, 2019.

[51] A. G. Capodaglio, "Critical perspective on advanced treatment processes for water and wastewater: AOPs, ARPs, and AORPs," *Applied Sciences (Switzerland)*, vol. 10, no. 13, 2020, doi: 10.3390/app10134549.

[52] V. Naddeo, M. F. N. Secondes, L. Borea, S. W. Hasan, F. Ballesteros, and V. Belgiorno, "Removal of contaminants of emerging concern from real wastewater by an innovative hybrid membrane process – Ultrasound, Adsorption, and Membrane ultrafiltration (USAMe®)," *Ultrason Sonochem*, vol. 68, no. June, p. 105237, 2020, doi: 10.1016/j.ultsonch.2020.105237.

[53] V. Naddeo, M. F. N. Secondes, L. Borea, S. W. Hasan, F. Ballesteros, and V. Belgiorno, "Removal of contaminants of emerging concern from real wastewater by an innovative hybrid membrane process – Ultrasound, Adsorption, and Membrane ultrafiltration

(USAMe®)," *Ultrason Sonochem*, vol. 68, no. June, p. 105237, 2020, doi: 10.1016/j.ultsonch.2020.105237.

[54] A. Egea-Corbacho, S. Gutiérrez Ruiz, and J. M. Quiroga Alonso, "Removal of emerging contaminants from wastewater using nanofiltration for its subsequent reuse: Full–scale pilot plant," *J Clean Prod*, vol. 214, pp. 514–523, 2019, doi: 10.1016/j.jclepro.2018.12.297.

[55] Y. Li *et al.*, "Efficient adsorption performance and mechanism of fluoroquinolone antibiotic onto the acid wash-assisted Co NPs/N-C adsorbent," *Sep Purif Technol*, vol. 353, no. PB, p. 128457, 2025, doi: 10.1016/j.seppur.2024.128457.

[56] F. de J. Silerio-Vázquez, L. A. González-Burciaga, C. Antileo, C. M. Núñez-Núñez, and J. B. Proal-Nájera, "Photocatalytic degradation of antibiotics in water via TiO2-x: Research needs for technological advancements," *Journal of Hazardous Materials Advances*, vol. 16, no. October, 2024, doi: 10.1016/j.hazadv.2024.100506.

[57] M. Petrović, S. Gonzalez, and D. Barceló, "Analysis and removal of emerging contaminants in wastewater and drinking water," *TrAC - Trends in Analytical Chemistry*, vol. 22, no. 10, pp. 685–696, 2003, doi: 10.1016/S0165-9936(03)01105-1.

[58] N. Miranda-garcía, S. Suárez, B. Sánchez, J. M. Coronado, S. Malato, and M. I. Maldonado, "Applied Catalysis B: Environmental Photocatalytic degradation of emerging contaminants in municipal wastewater treatment plant effluents using immobilized TiO_2 in a solar pilot plant," vol. 103, pp. 294–301, 2011, doi: 10.1016/j.apcatb.2011.01.030.

[59] A. O. Oluwole, E. O. Omotola, and O. S. Olatunji, "Pharmaceuticals and personal care products in water and wastewater: a review of treatment processes and use of photocatalyst immobilized on functionalized carbon in AOP degradation," *BMC Chem*, pp. 1–29, 2020, doi: 10.1186/s13065-020-00714-1.

[60] N. C. Huynh, T. T. T. Nguyen, D. T. C. Nguyen, and T. Van Tran, "Occurrence, toxicity, impact and removal of selected non-steroidal anti-inflammatory drugs (NSAIDs): A review," *Science of The Total Environment*, vol. 898, p. 165317, Nov. 2023, doi: 10.1016/J.SCITOTENV.2023.165317.

[61] S. Mohapatra, C. H. Huang, S. Mukherji, and L. P. Padhye, "Occurrence and fate of pharmaceuticals in WWTPs in India and comparison with a similar study in the United States," *Chemosphere*, vol. 159, pp. 526–535, 2016, doi: 10.1016/j.chemosphere.2016.06.047.

[62] K. K. Kesari, R. Soni, Q. Mohammad, and S. Jamal, “Wastewater Treatment and Reuse : a Review of its Applications and Health Implications,” 2021, doi: 10.1007/s11270-021-05154-8.

[63] S. Zahmatkesh *et al.*, “A comprehensive review of various approaches for treatment of tertiary wastewater with emerging contaminants: what do we know?” *Environ Monit Assess*, vol. 194, no. 12, 2022, doi: 10.1007/s10661-022-10503-z.

[64] O. Gimeno, J. F. García-Araya, F. J. Beltrán, F. J. Rivas, and A. Espejo, “Removal of emerging contaminants from a primary effluent of municipal wastewater by means of sequential biological degradation-solar photocatalytic oxidation processes,” *Chemical Engineering Journal*, vol. 290, pp. 12–20, 2016, doi: 10.1016/j.cej.2016.01.022.

[65] F. Tanos, A. Razzouk, G. Lesage, M. Cretin, and M. Bechelany, “A Comprehensive Review on Modification of Titanium Dioxide-Based Catalysts in Advanced Oxidation Processes for Water Treatment,” *ChemSusChem*, vol. 17, no. 6, 2024, doi: 10.1002/cssc.202301139.

[66] M. C. Maria, R. P. de Mendonça Neto, G. F. F. Pires, P. B. Vilela, and C. C. Amorim, “Combat of antimicrobial resistance in municipal wastewater treatment plant effluent via solar advanced oxidation processes: Achievements and perspectives,” *Science of the Total Environment*, vol. 786, p. 147448, 2021, doi: 10.1016/j.scitotenv.2021.147448.

[67] S. Guerra-Rodríguez *et al.*, “Pilot-scale sulfate radical-based advanced oxidation for wastewater reuse: simultaneous disinfection, removal of contaminants of emerging concern, and antibiotic resistance genes,” *Chemical Engineering Journal*, vol. 477, no. October, 2023, doi: 10.1016/j.cej.2023.146916.

[68] P. Kaur *et al.*, “Photoelectrocatalytic treatment of municipal wastewater with emerging concern pollutants using modified multi-layer catalytic anode,” *Chemosphere*, vol. 339, no. July, 2023, doi: 10.1016/j.chemosphere.2023.139575.

[69] Y. Jin *et al.*, “Spent Coffee Grounds Derived Carbon Loading C, N Doped TiO_2 for Photocatalytic Degradation of Organic Dyes,” *Materials*, vol. 16, no. 14, pp. 1–14, 2023, doi: 10.3390/ma16145137.

[70] Q. Yuan *et al.*, “Synthesis of a novel TiO_2/HA/RGO composite material with photocatalytic activity for dye degradation,” *Mater Chem Phys*, vol. 304, no. March, p. 127847, 2023, doi: 10.1016/j.matchemphys.2023.127847.

[71] D. Paredes *et al.*, “PMS activation via carbon-based-iron catalysts: Ion interactions and predictive modeling in fenton-like systems,” *Chem Eng Sci*, vol. 320, p. 122496, Jan. 2026, doi: 10.1016/J.CES.2025.122496.

[72] P. Pal, Z. F. Lin, and R. A. Doong, “Synergistic adsorption and photocatalytic degradation of ciprofloxacin in aqueous medium using advanced g-C_3N_4/MoS_2 heterostructures,” *Chemical Engineering Journal*, vol. 502, no. July, p. 157884, 2024, doi: 10.1016/j.cej.2024.157884.

[73] S. Zhu, W. Wang, Y. Xu, Z. Zhu, Z. Liu, and F. Cui, “Iron sludge-derived magnetic FeO/Fe_3C catalyst for oxidation of ciprofloxacin via peroxymonosulfate activation,” *Chemical Engineering Journal*, vol. 365, pp. 99–110, Jun. 2019, doi: 10.1016/J.CEJ.2019.02.011.

[74] Y. Lu *et al.*, “Highly efficient photodegradation of ciprofloxacin by dual Z-scheme Bi_2MoO_6/GQDs/TiO_2 heterojunction photocatalysts: mechanism analysis and pathway exploration,” *J Alloys Compd*, vol. 924, p. 166533, 2022, doi: 10.1016/j.jallcom.2022.166533.

[75] X. Hu *et al.*, “Mechanisms underlying the photocatalytic degradation pathway of ciprofloxacin with heterogeneous TiO_2,” *Chemical Engineering Journal*, vol. 380, no. July 2019, 2020, doi: 10.1016/j.cej.2019.122366.

[76] Z. He, M. Zhang, H. Yu, Z. Li, B. Deng, and H. Ren, “Multifunctional $BiPO_4$/TiO_2/rGO composite for enhancement removal of malachite green and levofloxacin via adsorption and visible-light photocatalysis synergy,” *Mater Sci Semicond Process*, vol. 169, no. October 2023, p. 107891, 2024, doi: 10.1016/j.mssp.2023.107891.

[77] E. Seliverstova, T. Serikov, A. Sadykova, N. Ibrayev, and N. Nuraje, “Enhanced photocatalytic properties of TiO_2/rGO nanocomposites Doped with CdS,” *Mater Lett*, vol. 379, no. October 2024, p. 137660, 2025, doi: 10.1016/j.matlet.2024.137660.

[78] M. A. Masud, W. S. Shin, and D. Kim, “Fe-doped kelp biochar-assisted peroxymonosulfate activation for ciprofloxacin degradation: Multiple active site-triggered radical and non-radical mechanisms,” *Chemical Engineering Journal*, vol. 471, p. 144519, Sep. 2023, doi: 10.1016/j.cej.2023.144519.

[79] Q. Khan, M. Sayed, and I. Gul, “Titania/reduced graphene oxide nanocomposites (TiO_2/rGO) as an efficient photocatalyst for the effective degradation of brilliant green in aqueous media: effect of peroxymonosulfate and operational parameters,”

Environmental Science and Pollution Research, vol. 30, no. 27, pp. 71025–71047, 2023, doi: 10.1007/s11356-023-27316-3.

[80] G. Wang, J. Wang, T. Yu, X. Guo, and Y. Chen, "Efficient removal of humic acid in water using a novel TiO_2 composite with biochar doping," *RSC Adv*, vol. 12, no. 49, pp. 31966–31975, 2022, doi: 10.1039/d2ra05358f.

[81] E. Gaggero, A. Giovagnoni, A. Zollo, P. Calza, and M. C. Paganini, "Photocatalytic Degradation of Emerging Contaminants with N-Doped TiO_2 Using Simulated Sunlight in Real Water Matrices," *Inorganics (Basel)*, vol. 11, no. 11, 2023, doi: 10.3390/inorganics11110439.

[82] Y. Tu *et al.*, "Degradation of pharmaceuticals and personal care products (PPCPs) in municipal wastewater by white rot fungi: Neutral environment exploitation and degradation mechanisms," *Chemical Engineering Journal*, vol. 507, no. December 2024, p. 160794, 2025, doi: 10.1016/j.cej.2025.160794.

[83] G. Wang, Y. Li, J. Dai, and N. Deng, "Highly efficient photocatalytic oxidation of antibiotic ciprofloxacin using TiO_2@g-C_3N_4@biochar composite," *Environmental Science and Pollution Research*, vol. 29, no. 32, pp. 48522–48538, 2022, doi: 10.1007/s11356-022-19269-w.

[84] M. Samy, S. Tang, Y. Zhang, and D. Y. C. Leung, "Understanding the variations in degradation pathways and generated by-products of antibiotics in modified TiO_2 and ZnO photodegradation systems: A comprehensive review," *J Environ Manage*, vol. 370, no. August, p. 122402, 2024, doi: 10.1016/j.jenvman.2024.122402.

[85] W. Longfei *et al.*, "Activation of peroxymonosulfate for ciprofloxacin degradation by a novel oxygen-deficient $CoTiO_3$/TiO_2NTs/Ti composite catalytic membrane: Electron transfer pathway and underlying mechanism," *Sep Purif Technol*, vol. 330, p. 125511, Feb. 2024, doi: 10.1016/J.SEPPUR.2023.125511.

[86] Y. Liu, M. Kamali, X. Chen, B. Rossi, L. Appels, and R. Dewil, "Photocatalytic defluorination of ciprofloxacin by nitrogen-defected g-C_3N_4 under simulated sunlight: Mechanistic insight and pathway analysis," *Chemical Engineering Journal*, vol. 493, p. 151950, Aug. 2024, doi: 10.1016/J.CEJ.2024.151950.

[87] J. Carbajo, A. Tolosana-Moranchel, J. A. Casas, M. Faraldos, and A. Bahamonde, "Analysis of photo efficiency in TiO_2 aqueous suspensions: Effect of titania hydrodynamic particle size and catalyst loading on their optical properties," *Appl Catal B*, vol. 221, pp. 1–8, Feb. 2018, doi: 10.1016/J.APCATB.2017.08.032.

[88] C. Sui *et al.*, "Singlet oxygen-dominated peroxymonosulfate activation by layered crednerite for organic pollutants degradation in high salinity wastewater," *Journal of Environmental Sciences*, vol. 135, pp. 86–96, Jan. 2024, doi: 10.1016/J.JES.2023.01.010.

[89] V. Vinesh, A. R. M. Shaheer, and B. Neppolian, "Reduced graphene oxide (rGO) supported electron deficient B-doped TiO_2(Au/B-TiO_2/rGO) nanocomposite: An efficient visible light Sono photocatalyst for the degradation of Tetracycline (TC)," *UltrasonSonochem*, vol. 50, pp. 302–310, Jan. 2019, doi: 10.1016/J.ULTSONCH.2018.09.030.

[90] Y. Yin *et al.*, "Strengthened carbamazepine degradation via producing $^1O_2$ with Ru-doped hollow tubular MoS_2 under peroxymonosulfate activation," *J Environ Chem Eng*, vol. 13, no. 1, p. 115328, 2025, doi: 10.1016/j.jece.2025.115328.

[91] M. A. Gatou, A. Syrrakou, N. Lagopati, and E. A. Pavlatou, "Photocatalytic TiO_2-Based Nanostructures as a Promising Material for Diverse Environmental Applications: A Review," Mar. 01, 2024, *Multidisciplinary Digital Publishing Institute (MDPI)*. doi: 10.3390/reactions5010007.

[92] S. Liu *et al.*, "2D/2D {001}TiO_{2-x}/Ti_3C_2Tx composite with ultra-high sensing performance for NO2 at room temperature," *Sens Actuators B Chem*, vol. 404, p. 135258, Apr. 2024, doi: 10.1016/J.SNB.2023.135258.

[93] M. Jiang, W. Zhang, and J. Xiong, "1D-2D N@TiO_{2-x} nanoassembly with regulating oxygen vacancy for photocatalytic antibiotic remediation," *Molecular Catalysis*, vol. 564, p. 114355, Jul. 2024, doi: 10.1016/J.MCAT.2024.114355.

[94] A. Habibi-Yangjeh, Z. Salmanzadeh-Jamadi, Z. Ahmadi, P. Yekan Motlagh, and A. Khataee, "Modification of S-doped g-C_3N_4 with CDs and brown TiO_{2-x}: Impressive S-scheme photocatalysts with QDs sizes for degradation of pollutants and disinfection of bacteria," *J Taiwan Inst Chem Eng*, vol. 159, p. 105474, Jun. 2024, doi: 10.1016/J.JTICE.2024.105474.

[95] N. Bazzanella, O. P. Bajpai, M. Fendrich, G. Guella, A. Miotello, and M. Orlandi, "Ciprofloxacin degradation with a defective TiO_{2-x} nanomaterial under sunlight," *MRS Commun*, vol. 13, no. 6, pp. 1252–1259, 2023, doi: 10.1557/s43579-023-00440-4.

[96] L. Andronic, D. Ghica, M. Stefan, C. G. Mihalcea, A. M. Vlaicu, and S. Karazhanov, "Visible-Light-Active Black TiO_2 Nanoparticles with Efficient Photocatalytic Performance for Degradation of Pharmaceuticals," *Nanomaterials*, vol. 12, no. 15, 2022, doi: 10.3390/nano12152563.

[97] M. Sarafraz, M. Sadeghi, A. Yazdanbakhsh, M. M. Amini, M. Sadani, and A. Eslami, "Enhanced photocatalytic degradation of ciprofloxacin by black Ti^{3+}/N-TiO_2 under visible LED light irradiation: Kinetic, energy consumption, degradation pathway, and toxicity assessment," *Process Safety and Environmental Protection*, vol. 137, pp. 261–272, May 2020, doi: 10.1016/J.PSEP.2020.02.030.

[98] J. Guo, W. Gan, R. Chen, M. Zhang, and Z. Sun, "Au nanoparticle sensitized blue TiO_2 nanorod arrays for efficient Gatifloxacin photodegradation," *RSC Adv*, vol. 13, no. 40, pp. 28299–28306, 2023, doi: 10.1039/d3ra05552c.

[99] M. Jia *et al.*, "Magnetic heterojunction of oxygen-deficient Ti^{3+}-TiO_2 and Ar-Fe_2O_3 derived from metal-organic frameworks for efficient peroxydisulfate (PDS) photo-activation," *Appl Catal B*, vol. 298, p. 120513, Dec. 2021, doi: 10.1016/J.APCATB.2021.120513.

[100] M. Hou *et al.*, "Ultrathin carbon-coated Fe-TiO_{2-x} nanostructures for enhanced photocatalysis under visible-light irradiation," *Mater Res Bull*, vol. 160, p. 112143, Apr. 2023, doi: 10.1016/J.MATERRESBULL.2022.112143.

[101] C. Li *et al.*, "Fabrication of ternary Ag/La-black TiO_{2-x} photocatalyst with enhanced visible-light photocatalytic activity for tetracycline degradation," *J Alloys Compd*, vol. 891, p. 161960, Jan. 2022, doi: 10.1016/J.JALLCOM.2021.161960.

[102] J. Li *et al.*, "Direct Z-scheme TiO_{2-x}/AgI heterojunctions for highly efficient photocatalytic degradation of organic contaminants and inactivation of pathogens," *Sep Purif Technol*, vol. 261, p. 118306, Apr. 2021, doi: 10.1016/J.SEPPUR.2021.118306.

[103] R. Hosseini, A. Fattah-alhosseini, M. Karbasi, and S. Giannakis, "Tailoring surface defects in Plasma Electrolytic Oxidation (PEO) treated 2-D black TiO_2: Post-treatment role, and intensification by peroxymonosulfate activation in visible light-driven photocatalysis," *Appl Catal B*, vol. 340, p. 123197, Jan. 2024, doi: 10.1016/J.APCATB.2023.123197.

[104] A. Saadati, A. Habibi-Yangjeh, and A. Khataee, "Activation of persulfate ions by QDs-sized Z-scheme TiO_{2-x}/Cu_3Mo_2O9 photocatalysts in visible-light detoxification of organic contaminants," *J Alloys Compd*, vol. 969, p. 172322, Dec. 2023, doi: 10.1016/J.JALLCOM.2023.172322.

[105] G. S. Olabode, O. F. Olorundare, and V. S. Somerset, "Physicochemical properties of wastewater effluent from two selected wastewater treatment plants (Cape Town) for

water quality improvement," *International Journal of Environmental Science and Technology*, vol. 17, no. 12, pp. 4745–4758, 2020, doi: 10.1007/s13762-020-02788-9.

[106] C. Lim *et al.*, "Highly visible-light-responsive nanoporous nitrogen-doped TiO_2(N-TiO_2) photocatalysts produced by underwater plasma technology for environmental and biomedical applications," *Appl Surf Sci*, vol. 638, no. May, p. 158123, 2023, doi: 10.1016/j.apsusc.2023.158123.

[107] I. Rapti, C. Kosma, T. Albanis, and I. Konstantinou, "Solar photocatalytic degradation of inherent pharmaceutical residues in real hospital WWTP effluents using titanium dioxide on a CPC pilot scale reactor," *Catal Today*, vol. 423, no. March 2022, p. 113884, 2023, doi: 10.1016/j.cattod.2022.08.026.

[108] N. A. Sukrey, A. R. Bushroa, and M. Rizwan, "Dopant incorporation into TiO_2 semiconductor materials for optical, electronic, and physical property enhancement: doping strategy and trend analysis," *Journal of the Australian Ceramic Society*, 2023, doi: 10.1007/s41779-023-00958-9.

[109] Z. He, M. Zhang, H. Yu, Z. Li, B. Deng, and H. Ren, "Multifunctional $BiPO_4$/TiO_2/rGO composite for enhancement removal of malachite green and levofloxacin via adsorption and visible-light photocatalysis synergy," *Mater Sci Semicond Process*, vol. 169, no. August 2023, p. 107891, 2024, doi: 10.1016/j.mssp.2023.107891.

[110] H. Y. Yoo, M. S. Kim, H. Shin, and J. Lim, "Peroxymonosulfate activation by black TiO_2 nanotube arrays under solar light: Switching the activation mechanism and enhancing catalytic activity and stability," *J Hazard Mater*, vol. 433, p. 128796, Jul. 2022, doi: 10.1016/J.JHAZMAT.2022.128796.

[111] G. Sofia, C. Koventhan, S. Kanmani, and A. Y. Lo, "Green synthesized rGO/TiO_2/g-C_3N_4 nanocomposites via Plectranthus amboinicus extract for efficient photocatalytic degradation of methylene blue: RSM optimization, antimicrobial and phytotoxicity assessment," *J Environ Chem Eng*, vol. 13, no. 1, 2025, doi: 10.1016/j.jece.2024.115267.

[112] A. Ebanezar John, D. Mishra, S. Thankaraj Salammal, and M. Akram Khan, "Factors that enhance the efficiency of TiO2 based heterogeneous photocatalyst for its application in waste water treatment containing organic dye," *Sustain Water Resour Manag*, vol. 10, no. 3, Jun. 2024, doi: 10.1007/s40899-024-01074-7.

[113] J. Tong *et al.*, "Atomic hydrogen induced single-electron activation of peroxydisulfate on silver-doped MoS_2-x/TiO_2-y for efficient photoelectrocatalytic decontamination," *Appl Catal B*, vol. 366, no. January, pp. 1–11, 2025, doi: 10.1016/j.apcatb.2025.125072.

[114] S. Guerra-Rodríguez *et al.*, "Pilot-scale sulfate radical-based advanced oxidation for wastewater reuse: simultaneous disinfection, removal of contaminants of emerging concern, and antibiotic resistance genes," *Chemical Engineering Journal*, vol. 477, no. October, 2023, doi: 10.1016/j.cej.2023.146916.

[115] S. Daouk, S. Fleury-Souverain, and Y. Daali, "Development of an LC-MS/MS method for the assessment of selected active pharmaceuticals and metabolites in wastewaters of a swiss university hospital," *Chimia (Aarau)*, vol. 69, no. 11, pp. 684–689, 2015, doi: 10.2533/chimia.2015.684.

[116] H. KAJEIOU, M. SBAA, and A. DARMOUS, "Physico-chemical, chemical and biological characterization of wastewater treatment plant of Oujda (Eastern Morocco) and possibility of reuse in irrigation," *Mater Today Proc*, vol. 72, pp. 3326–3335, 2023, doi: 10.1016/j.matpr.2022.07.355.

[117] M. A. Agoro, A. O. Adeniji, M. A. Adefisoye, and O. O. Okoh, "Heavy metals in wastewater and sewage sludge from selected municipal treatment plants in eastern cape province, south Africa," *Water (Switzerland)*, vol. 12, no. 10, 2020, doi: 10.3390/w12102746.

[118] C. Gómez-Canela, T. Sala-Comorera, V. Pueyo, C. Barata, and S. Lacorte, "Analysis of 44 pharmaceuticals consumed by elderly using liquid chromatography coupled to tandem mass spectrometry," *J Pharm Biomed Anal*, vol. 168, pp. 55–63, 2019, doi: 10.1016/j.jpba.2019.02.016.

[119] C. Gómez-Canela, S. Edo, N. Rodríguez, G. Gotor, and S. Lacorte, "Comprehensive characterization of 76 pharmaceuticals and metabolites in wastewater by LC-MS/MS," *Chemosensors*, vol. 9, no. 10, pp. 1–19, 2021, doi: 10.3390/chemosensors9100273.

[120] B. Subedi and B. Loganathan, "Environmental emission of pharmaceuticals from wastewater treatment plants in the U.S.A.," *ACS Symposium Series*, vol. 1244, pp. 181–202, 2016, doi: 10.1021/bk-2016-1244.ch008.

[121] J. N. Edokpayi, J. O. Odiyo, T. A. M. Msagati, and E. O. Popoola, "Removal Efficiency of Faecal Indicator Organisms, Nutrients and Heavy Metals from a Peri-Urban Wastewater Treatment Plant in Thohoyandou, Limpopo Province, South Africa," *Int J Environ Res Public Health*, vol. 12, no. 7, pp. 7300–7320, 2015, doi: 10.3390/ijerph120707300.

[122] S. K. Gautam, D. Sharma, J. K. Tripathi, S. Ahirwar, and S. K. Singh, "A study of the effectiveness of sewage treatment plants in Delhi region," *Appl Water Sci*, vol. 3, no. 1, pp. 57–65, 2013, doi: 10.1007/s13201-012-0059-9.

[123] J. B. Baranyika, J. Katabarwa, D. K. Nyirimbibi, S. Bakire, and H. Hirwa, "Assessment of the impacts of selected physicochemical and bacteriological parameters of wastewater (hospital effluents) from the University teaching hospital of Butare on the surrounding environment," *J Clean Prod*, vol. 410, no. February, p. 137309, 2023, doi: 10.1016/j.jclepro.2023.137309.

[124] J. Atwebembeire, M. Andama, J. Yatuha, J. B. Lejju, G. K. Rugunda, and J. Bazira, "The Physico-Chemical Quality of Effluents of Selected Sewage Treatment Plants Draining into River Rwizi, Mbarara Municipality, Uganda," *J Water Resour Prot*, vol. 11, no. 01, pp. 20–36, 2019, doi: 10.4236/jwarp.2019.111002.

[125] S. A. Al-Khafaji, W. S. Al-Rekabi, and S. A. Abbas, "Evaluation of the Efficiency of the AL-Mauany Hospital Sewage Treatment Plant in Basrah City," *Journal of Ecological Engineering*, vol. 24, no. 10, pp. 205–213, 2023, doi: 10.12911/22998993/170085.

[126] Y.-L. Cheng *et al.*, "We are Intech Open , the world' s leading publisher of Open Access books Built by scientists, for scientists TOP 1 %," *Intech*, vol. 11, no. tourism, p. 13, 2016, doi: 10.1039/d2va00062h.

[127] J. Rajesh Banu *et al.*, "Trends in Biological Nutrient Removal for the Treatment of Low Strength Organic Wastewaters," *Curr Pollut Rep*, vol. 7, no. 1, pp. 1–30, 2021, doi: 10.1007/s40726-020-00169-x.

[128] L. Alibardi, P. Vale, and Y. Bajón Fernández, "Full-scale trials to achieve low total phosphorus in effluents from sewage treatment works," *Journal of Water Process Engineering*, vol. 40, no. 101981, pp. 1–38, 2021, doi: 10.1016/j.jwpe.2021.101981.

[129] Y. Xie, Q. Zhang, Q. Wu, J. Zhang, M. Dzakpasu, and X. C. Wang, "Bioresource Technology Nitrogen removal efficiency and mechanisms of an improved anaerobic-anoxic – oxic system for decentralized sewage treatment," vol. 393, no. October 2023, pp. 1–9, 2024, doi: 10.1016/j.biortech.2023.129976.

[130] J. Feng *et al.*, "Effluent concentration and removal efficiency of nine heavy metals in secondary treatment plants in Shanghai, China," *Environmental Science and Pollution Research*, vol. 25, no. 17, pp. 17058–17065, 2018, doi: 10.1007/s11356-018-1915-4.

[131] B. B. Dagne, "Determination of Heavy Metals in Wastewater and Their Toxicological Implications around Eastern Industrial Zone, Central Ethiopia," *Journal of*

Environmental Chemistry and Ecotoxicology, vol. 12, no. 2, pp. 72–79, 2020, doi: 10.5897/jece2019.0453.

[132] G. K. Kinuthia, V. Ngure, D. Beti, R. Lugalia, A. Wangila, and L. Kamau, "Levels of heavy metals in wastewater and soil samples from open drainage channels in Nairobi, Kenya: community health implication," *Sci Rep*, vol. 10, no. 1, pp. 1–13, 2020, doi: 10.1038/s41598-020-65359-5.

[133] D. Woldetsadik, P. Drechsel, B. Keraita, F. Itanna, and H. Gebrekidan, "Heavy metal accumulation and health risk assessment in wastewater-irrigated urban vegetable farming sites of Addis Ababa, Ethiopia," *Int J Food Contam*, vol. 4, no. 1, 2017, doi: 10.1186/s40550-017-0053-y.

[134] WHO, "CHILDREN AND NOISE - Children ' s Health and the Environment," *World Health Organization*, p. 50, 2009.

[135] U. S. E. P. A. EPA, "Biosolids Generation, Use and Disposal in the United States. Municipal and Industrial Solid Waste Division, Office of Solid Waste," *Epa*, no. September, p. 74, 1999.

[136] N. Pérez-Lemus, R. López-Serna, S. I. Pérez-Elvira, and E. Barrado, "Analysis of 60 pharmaceuticals and personal care products in sewage sludge by ultra-high performance liquid chromatography and tandem mass spectroscopy," *Microchemical Journal*, vol. 175, Apr. 2022, doi: 10.1016/j.microc.2021.107148.

[137] O. F. S. Khasawneh and P. Palaniandy, "Occurrence and removal of pharmaceuticals in wastewater treatment plants," *Process Safety and Environmental Protection*, vol. 150, pp. 532–556, 2021, doi: 10.1016/j.psep.2021.04.045.

[138] A. Ulvi, S. Aydın, and M. E. Aydın, "Fate of selected pharmaceuticals in hospital and municipal wastewater effluent: occurrence, removal, and environmental risk assessment," *Environmental Science and Pollution Research*, vol. 29, no. 50, pp. 75609–75625, 2022, doi: 10.1007/s11356-022-21131-y.

[139] S. Tripathi, D. Purchase, R. Chandra, A. K. Nadda, and P. Chaturvedi, "Emerging pollutants characterization, mitigation and toxicity assessment of sewage wastewater treatment plant- India: A case study," *J Contam Hydrol*, vol. 254, no. January, p. 104139, 2023, doi: 10.1016/j.jconhyd.2023.104139.

[140] O. A. Alharbi, E. Jarvis, A. Galani, N. S. Thomaidis, M. C. Nika, and D. V. Chapman, "Assessment of selected pharmaceuticals in Riyadh wastewater treatment plants, Saudi Arabia: Mass loadings, seasonal variations, removal efficiency and environmental risk,"

Science of the Total Environment, vol. 882, no. November 2022, p. 163284, 2023, doi: 10.1016/j.scitotenv.2023.163284.

[141] D. U.S. Environmental Protection Agency: Washington, "Effluent Guidelines Program Plan," no. January, 2004.

[142] D. S. Maycock and C. D. Watts, "Pharmaceuticals in Drinking Water," *Encyclopedia of Environmental Health*, pp. 472–484, 2011, doi: 10.1016/B978-0-444-52272-6.00457-8.

[143] K. Balakrishna, A. Rath, Y. Praveenkumarreddy, K. S. Guruge, and B. Subedi, "A review of the occurrence of pharmaceuticals and personal care products in Indian water bodies," *Ecotoxicol Environ Saf*, vol. 137, no. November 2016, pp. 113–120, 2017, doi: 10.1016/j.ecoenv.2016.11.014.

[144] M. Papageorgiou, C. Kosma, and D. Lambropoulou, "Seasonal occurrence, removal, mass loading and environmental risk assessment of 55 pharmaceuticals and personal care products in a municipal wastewater treatment plant in Central Greece," *Science of the Total Environment*, vol. 543, pp. 547–569, 2016, doi: 10.1016/j.scitotenv.2015.11.047.

[145] C. I. Kosma, D. A. Lambropoulou, and T. A. Albanis, "Investigation of PPCPs in wastewater treatment plants in Greece: Occurrence, removal and environmental risk assessment," *Science of the Total Environment*, vol. 466–467, pp. 421–438, 2014, doi: 10.1016/j.scitotenv.2013.07.044.

[146] N. H. Tran and K. Y. H. Gin, "Occurrence and removal of pharmaceuticals, hormones, personal care products, and endocrine disrupters in a full-scale water reclamation plant," *Science of the Total Environment*, vol. 599–600, pp. 1503–1516, 2017, doi: 10.1016/j.scitotenv.2017.05.097.

[147] A. K. Thalla and A. S. Vannarath, "Response to letter to the editor on the paper 'occurrence and environmental risks of nonsteroidal anti-inflammatory drugs in urban wastewater in the southwest monsoon region of India,'" *Environ Monit Assess*, vol. 192, no. 9, pp. 1–13, 2020, doi: 10.1007/s10661-020-08576-9.

[148] M. S. Kostich, A. L. Batt, and J. M. Lazorchak, "Concentrations of prioritized pharmaceuticals in effluents from 50 large wastewater treatment plants in the US and implications for risk estimation," *Environmental Pollution*, vol. 184, pp. 354–359, 2014, doi: 10.1016/j.envpol.2013.09.013.

[149] N. Mohammadian, S. M. Ghoreishi, S. Hafeziyeh, S. Saeidi, and D. D. Dionysiou, "Optimization of synthesis conditions of carbon nanotubes via ultrasonic-assisted

floating catalyst deposition using response surface methodology," *Nanomaterials*, vol. 8, no. 5, pp. 1–14, 2018, doi: 10.3390/nano8050316.

[150] S. K. Kassahun, Z. Kiflie, D. W. Shin, S. S. Park, W. Y. Jung, and Y. R. Chung, "Optimization of sol-gel synthesis parameters in the preparation of N-doped TiO_2 using surface response methodology," *J Solgel Sci Technol*, vol. 82, no. 2, pp. 322–334, 2017, doi: 10.1007/s10971-017-4322-2.

[151] S. Habchi, N. Lahboubi, B. Sallek, and H. El Bari, "Response surface methodology for anaerobic digestion of waste from poultry slaughterhouse: Optimization of load and hydraulic retention time," *Results in Engineering*, vol. 18, no. May, p. 101215, 2023, doi: 10.1016/j.rineng.2023.101215.

[152] I. Trawczyńska and S. Kwiatkowska-Marks, "Application of Response Surface Methodology for Optimization of the Biosorption Process from Copper-Containing Wastewater," *Molecules*, vol. 28, no. 1, 2023, doi: 10.3390/molecules28010444.

[153] M. Saelee *et al.*, "Response-Surface-Methodology-Based Optimization of High-Quality Salvia hispanica L. Seed Oil Extraction: A Pilot Study," *Applied Sciences (Switzerland)*, vol. 13, no. 11, 2023, doi: 10.3390/app13116600.

[154] D. Van Thuan *et al.*, "Adsorption and photodegradation of micropollutant in wastewater by photocatalyst TiO_2/rice husk biochar," *Environ Res*, vol. 236, no. P2, p. 116789, 2023, doi: 10.1016/j.envres.2023.116789.

[155] T. Ayorinde and C. M. Sayes, "An updated review of industrially relevant titanium dioxide and its environmental health effects," *Journal of Hazardous Materials Letters*, vol. 4, no. May, p. 100085, 2023, doi: 10.1016/j.hazl.2023.100085.

[156] J. Arun, S. Nachiappan, G. Rangarajan, R. P. Alagappan, K. P. Gopinath, and E. Lichtfouse, "Synthesis and application of titanium dioxide photocatalysis for energy, decontamination and viral disinfection: a review," *Environ Chem Lett*, vol. 21, no. 1, pp. 339–362, 2023, doi: 10.1007/s10311-022-01503-z.

[157] V. H. Rathi and A. R. Jeice, "Green fabrication of titanium dioxide nanoparticles and their applications in photocatalytic dye degradation and microbial activities," *Chemical Physics Impact*, vol. 6, no. March, p. 100197, 2023, doi: 10.1016/j.chphi.2023.100197.

[158] S. J. Armaković, M. M. Savanović, and S. Armaković, "Titanium Dioxide as the Most Used Photocatalyst for Water Purification: An Overview," *Catalysts*, vol. 13, no. 1, 2023, doi: 10.3390/catal13010026.

[159] F. Abu Bakar and N. S. I. Mohd Foad, "Synthesis of TiO_2 photocatalyst with tunable optical properties and exposed facet for textile wastewater treatment," *Results in Optics*, vol. 13, no. September, p. 100545, 2023, doi: 10.1016/j.rio.2023.100545.

[160] D. R. Eddy *et al.*, "Heterophase Polymorph of TiO_2 (Anatase, Rutile, Brookite, TiO_2 (B)) for Efficient Photocatalyst: Fabrication and Activity," *Nanomaterials*, vol. 13, no. 4, 2023, doi: 10.3390/nano13040704.

[161] M. N. Uddin *et al.*, "An experimental and first-principles study of the effect of B/N doping in TiO_2 thin films for visible light photo-catalysis," *J Photochem Photobiol A Chem*, vol. 254, pp. 25–34, 2013, doi: 10.1016/j.jphotochem.2012.12.024.

[162] Y. Davoodi and M. S. Shafeeyan, "Tailoring photocatalytic performance through Fe-doped TiO_2/ZnO for effective remediation of organic contaminants," *Water Resour Ind*, vol. 31, no. January, p. 100239, 2024, doi: 10.1016/j.wri.2024.100239.

[163] L. Yanneth, D. Pino-sandoval, J. C. Murillo-sierra, J. Luis, E. J. Ruiz-ruiz, and A. Hern, "Hormone Using Boron-Doped TiO_2 Catalyst," *Catalysts*, vol. 43, pp. 1–16, 2023, doi: 10.3390/catal13010043.

[164] Y. Jin *et al.*, "Spent Coffee Grounds Derived Carbon Loading C, N Doped TiO_2 for Photocatalytic Degradation of Organic Dyes," *Materials*, vol. 16, no. 14, pp. 1–14, 2023, doi: 10.3390/ma16145137.

[165] E. Shin *et al.*, "Preparation of K-doped TiO_2 nanostructures by wet corrosion and their sunlight-driven photocatalytic performance," *Appl Surf Sci*, vol. 379, pp. 33–38, 2016, doi: 10.1016/j.apsusc.2016.03.222.

[166] M. Abid *et al.*, "A novel BN/TiO_2/HNT nanocomposite for photocatalytic applications fabricated by electrospinning," *Colloids Surf A Physicochem Eng Asp*, vol. 662, no. December 2022, p. 131043, 2023, doi: 10.1016/j.colsurfa.2023.131043.

[167] X. Li *et al.*, "COS and H_2S simultaneous removal from blast furnace gas over a tailored Cu/Zr co-doped K@TiO_2 bifunctional catalyst under low temperature," *Chemical Engineering Journal*, vol. 471, no. April, p. 144573, 2023, doi: 10.1016/j.cej.2023.144573.

[168] H. Zangeneh, A. A. Zinatizadeh, M. Feyzi, S. Zinadini, and D. W. Bahnemann, "Materials Science in Semiconductor Processing Application of a novel triple metal-nonmetal doped TiO_2 (K-B-N-TiO_2) for photocatalytic degradation of Linear Alkyl Benzene (LAB) industrial wastewater under visible light," *Mater Sci Semicond Process*, vol. 75, no. September 2017, pp. 193–205, 2018, doi: 10.1016/j.mssp.2017.11.040.

[169] H. Zangeneh, A. Akbar, S. Zinadini, M. Feyzi, and D. W. Bahnemann, "A novel photocatalytic self-cleaning PES nano fi ltration membrane incorporating triple metal-nonmetal doped TiO_2 (K-B-N-TiO_2) for post treatment of biologically treated palm oil mill effluent," vol. 127, no. January, pp. 139–152, 2018, doi: 10.1016/j.reactfunctpolym.2018.04.008.

[170] C. Lim *et al.*, "Highly visible-light-responsive nanoporous nitrogen-doped TiO_2 (N-TiO_2) photocatalysts produced by underwater plasma technology for environmental and biomedical applications," *Appl Surf Sci*, vol. 638, no. May, p. 158123, 2023, doi: 10.1016/j.apsusc.2023.158123.

[171] X. Xiao, X. Wang, Y. Li, Y. Li, G. Sun, and Y. Han, "A two-electron migration mechanism co-constructed by K^+ passivation and defect engineering for efficient TiO_2 photocatalytic hydrogen evolution," *Appl Surf Sci*, vol. 631, no. May, p. 157577, 2023, doi: 10.1016/j.apsusc.2023.157577.

[172] D. Wu *et al.*, "Green synthesis of boron and nitrogen co-doped TiO_2 with rich B-N motifs as Lewis acid-base couples for the effective artificial CO_2 photoreduction under simulated sunlight," *J Colloid Interface Sci*, vol. 585, pp. 95–107, 2021, doi: 10.1016/j.jcis.2020.11.075.

[173] X. Zhang, M. Cai, N. Cui, G. Chen, G. Zou, and L. Zhou, "One-step synthesis of b-N-TiO_2/C nanocomposites with high visible light photocatalytic activity to degrade microcystis aeruginosa," *Catalysts*, vol. 10, no. 5, pp. 1–11, 2020, doi: 10.3390/catal10050579.

[174] A. Sapi, I. Arora, S. Sagadevan, A. Chandra, and S. Garg, "Photocatalytic CO_2 reduction using metal and nonmetal doped TiO2 and its mechanism," *Reaction Kinetics, Mechanisms and Catalysis*, no. 0123456789, 2024, doi: 10.1007/s11144-024-02601-5.

[175] J. Musial, D. T. Mlynarczyk, and B. J. Stanisz, "Photocatalytic degradation of sulfamethoxazole using TiO_2-based materials – Perspectives for the development of a sustainable water treatment technology," *Science of the Total Environment*, vol. 856, no. September 2022, p. 159122, 2023, doi: 10.1016/j.scitotenv.2022.159122.

[176] N. Puri and A. Gupta, "Water remediation using titanium and zinc oxide nanomaterials through disinfection and photo catalysis process: A review," *Environ Res*, vol. 227, no. March, p. 115786, 2023, doi: 10.1016/j.envres.2023.115786.

[177] H. Zangeneh, A. A. Zinatizadeh, M. Feyzi, S. Zinadini, and D. W. Bahnemann, "Materials Science in Semiconductor Processing Application of a novel triple metal-

nonmetal doped TiO_2 (K-B-N-TiO_2) for photocatalytic degradation of Linear Alkyl Benzene (LAB) industrial wastewater under visible light," *Mater Sci Semicond Process*, vol. 75, no. September 2017, pp. 193–205, 2018, doi: 10.1016/j.mssp.2017.11.040.

[178] M. B. K. Suhan *et al.*, "Sustainable pollutant removal and wastewater remediation using TiO2-based nanocomposites: A critical review," *Nano-Structures and Nano-Objects*, vol. 36, no. September, p. 101050, 2023, doi: 10.1016/j.nanoso.2023.101050.

[179] Z. Akram, A. Raza, M. Mehdi, A. Arshad, X. Deng, and S. Sun, "Recent Advancements in Metal and Non-Metal Mixed-Doped Carbon Quantum Dots: Synthesis and Emerging Potential Applications," *Nanomaterials*, vol. 13, no. 16, 2023, doi: 10.3390/nano13162336.

[180] P. R. Jubu *et al.*, "Considerations About the Determination of Optical Bandgap from Diffuse Reectance Spectroscopy Using the Tauc Plot," pp. 1–19, 2023, doi: 10.21203/rs.3.rs-2654236/v1.

[181] P. R. Jubu, O. S. Obaseki, A. Nathan-Abutu, F. K. Yam, Y. Yusof, and M. B. Ochang, "Dispensability of the conventional Tauc's plot for accurate bandgap determination from UV–vis optical diffuse reflectance data," *Results in Optics*, vol. 9, no. July, p. 100273, 2022, doi: 10.1016/j.rio.2022.100273.

[182] S. A. Disha, M. Sahadat Hossain, M. L. Habib, and S. Ahmed, "Calculation of crystallite sizes of pure and metals doped hydroxyapatite engaging Scherrer method, Halder-Wagner method, Williamson-Hall model, and size-strain plot," *Results in Materials*, vol. 21, no. December, p. 100496, 2024, doi: 10.1016/j.rinma.2023.100496.

[183] J. He *et al.*, "In situ synthesis of the mesoporous C–TiO_2 microspheres derived from partial hydrolysis tetrabutyl titanate for enhanced photocatalytic degradation under visible light," *Mater Res Bull*, vol. 161, May 2023, doi: 10.1016/j.materresbull.2023.112168.

[184] L. Xia *et al.*, "Porous N-doped TiO_2 nanotubes arrays by reverse oxidation of TiN and their visible-light photocatalytic activity," *Surf Coat Technol*, vol. 365, no. June, pp. 237–241, 2019, doi: 10.1016/j.surfcoat.2018.06.033.

[185] C. Yang, Y. Zhang, Z. Song, Z. Yi, and F. Li, "Novel compound heterozygous mutations in the WWOX gene cause early infantile epileptic encephalopathy," *International Journal of Developmental Neuroscience*, vol. 79, pp. 45–48, 2019, doi: 10.1016/j.ijdevneu.2019.10.003.

[186] S. Zhang, M. Dai, J. Guo, G. Wang, S. Wang, and Z. He, "Stable Ti^{3+} in B-TiO_2/BN based hybrids for efficient photocatalytic reduction," *Chemical Engineering Journal Advances*, vol. 11, Aug. 2022, doi: 10.1016/j.ceja.2022.100333.

[187] Z. He, M. Zhang, H. Yu, Z. Li, B. Deng, and H. Ren, "Multifunctional $BiPO_4$/TiO_2/rGO composite for enhancement removal of malachite green and levofloxacin via adsorption and visible-light photocatalysis synergy," *Mater Sci Semicond Process*, vol. 169, no. August 2023, p. 107891, 2024, doi: 10.1016/j.mssp.2023.107891.

[188] A. Kubiak, "The role of spectral matching in enhancing photocatalytic performance with TiO_2-rGO catalysts for metronidazole wastewater elimination," *Sep Purif Technol*, vol. 355, no. PB, p. 129735, 2025, doi: 10.1016/j.seppur.2024.129735.

[189] C. Han, B. K. Kundu, Y. Liang, and Y. Sun, "Near-Infrared Light-Driven Photocatalysis with an Emphasis on Two-Photon Excitation: Concepts, Materials, and Applications," Feb. 01, 2024, *John Wiley and Sons Inc*. doi: 10.1002/adma.202307759.

[190] C. Srisangari and K. V. Marathe, "Degradation of an emerging organic contaminant via heterogeneous photocatalytic ozonation using V_2O_5 doped ZnO under UV irradiation," *Journal of Water Process Engineering*, vol. 63, Jun. 2024, doi: 10.1016/j.jwpe.2024.105543.

[191] A. H. Navidpour, M. B. Ahmed, and J. L. Zhou, "Photocatalytic Degradation of Pharmaceutical Residues from Water and Sewage Effluent Using Different TiO2 Nanomaterials," *Nanomaterials*, vol. 14, no. 2, Jan. 2024, doi: 10.3390/nano14020135.

[192] S. Kumar (S. Kumar), R. D. Kaushik, and L. P. Purohit, "ZnO-CdO nanocomposites incorporated with graphene oxide nanosheets for efficient photocatalytic degradation of bisphenol A, thymol blue and ciprofloxacin," *J Hazard Mater*, vol. 424, Feb. 2022, doi: 10.1016/j.jhazmat.2021.127332.

[193] P. Dolkar *et al.*, "Challenges and effective tracking down strategies of antibiotic contamination in aquatic ecosystem," *Environmental Science and Pollution Research*, vol. 31, no. 44, pp. 55935–55957, 2024, doi: 10.1007/s11356-024-34806-5.

[194] Y. Tu *et al.*, "Degradation of pharmaceuticals and personal care products (PPCPs) in municipal wastewater by white rot fungi: Neutral environment exploitation and degradation mechanisms," *Chemical Engineering Journal*, vol. 507, no. December 2024, p. 160794, 2025, doi: 10.1016/j.cej.2025.160794.

[195] S. Xie, N. Hamid, T. Zhang, Z. Zhang, and L. Peng, "Unraveling the nexus: Microplastics, antibiotics, and ARGs interactions, threats and control in aquaculture – A

review," *J Hazard Mater*, vol. 471, no. January, p. 134324, 2024, doi: 10.1016/j.jhazmat.2024.134324.

[196] X. Shan, Z. Shan, H. Guo, and F. Ma, "Biodegradation of cephalexin in wastewater by Glutamicibacter sp. S2 and Herbaspirillum sp. S8: Performance, pathway, genomes and synergistic bio-augmentation," *Chemical Engineering Journal*, vol. 507, no. December 2024, p. 160783, 2025, doi: 10.1016/j.cej.2025.160783.

[197] C. X. Chen, A. Aris, E. L. Yong, and Z. Z. Noor, "A review of antibiotic removal from domestic wastewater using the activated sludge process: removal routes, kinetics and operational parameters," *Environmental Science and Pollution Research*, vol. 29, no. 4, pp. 4787–4802, 2022, doi: 10.1007/s11356-021-17365-x.

[198] T. Macsek *et al.*, "Long-term application of ozonation for removal of pharmaceuticals from wastewater treatment plant effluent: Effectiveness, control strategies, ecotoxicity," *J Hazard Mater*, vol. 489, no. December 2024, 2025, doi: 10.1016/j.jhazmat.2025.137703.

[199] J. Qiu, Z. Xu, B. Dong, and M. Wang, "Co-occurrence of cadmium and ciprofloxacin in environmental media decreases ciprofloxacin degradation by biogenic manganese oxides," *Environmental Pollution*, vol. 366, no. October 2024, p. 125488, 2025, doi: 10.1016/j.envpol.2024.125488.

[200] M. Ullah, S. Rana, and M. Hossain, "A Cost-Effective, Eco-Friendly and Functional Wastewater Pre-Treatment Procedure Development for the Degradation of $β$-Lactam Antibiotic Residues Discharged from Cephalosporin Drug Manufacturing Plant," *Water Air Soil Pollut*, vol. 236, no. 1, pp. 1–25, 2025, doi: 10.1007/s11270-024-07606-3.

[201] B. Kanwar, M. Koli, and S. P. Singh, "Antibiotic amoxicillin degradation by electrochemical oxidation process: effects of process parameters and degradation pathway at environmentally relevant concentrations," *Environmental Science and Pollution Research*, vol. 32, no. 2, pp. 575–586, 2024, doi: 10.1007/s11356-024-35780-8.

[202] K. Liu *et al.*, "Facile fabrication metal Cu-decorated g-C_3N_4 photocatalyst with Schottky barrier for efficient pollutant elimination," *Diam Relat Mater*, vol. 126, no. March, p. 109116, 2022, doi: 10.1016/j.diamond.2022.109116.

[203] E. Seliverstova, T. Serikov, A. Sadykova, N. Ibrayev, and N. Nuraje, "Enhanced photocatalytic properties of TiO_2/rGO nanocomposites Doped with CdS," *Mater Lett*, vol. 379, no. October 2024, p. 137660, 2025, doi: 10.1016/j.matlet.2024.137660.

[204] Q. Khan, M. Sayed, and I. Gul, “Titania/reduced graphene oxide nanocomposites (TiO_2/rGO) as an efficient photocatalyst for the effective degradation of brilliant green in aqueous media: effect of peroxymonosulfate and operational parameters,” *Environmental Science and Pollution Research*, vol. 30, no. 27, pp. 71025–71047, 2023, doi: 10.1007/s11356-023-27316-3.

[205] M. Ruid, A. Á. Miguel, G. Cruz-quesada, J. Rivera-utrilla, and S. Manuel, “Ethylparaben Degradation,” *Journal of Catalysts*, 2020.

[206] N. Xiong *et al.*, “An Efficient Photocatalytic Material, rGO-TiO_2, That Can Be Industrially Produced: Fabrication and Structural Characterization,” *Water (Switzerland)*, vol. 17, no. 2, pp. 1–14, 2025, doi: 10.3390/w17020161.

[207] B. Anusha, M. Anbuchezhiyan, R. Sribalan, and N. Srinivasan alias Arunsankar, “Synergistic effect of TiO_2-rGO nanocomposites with Fenton’s reagent for the enhanced photocatalytic degradation of nitrophenols in solar light,” *Appl Phys A Mater Sci Process*, vol. 128, no. 5, pp. 1–14, 2022, doi: 10.1007/s00339-022-05554-5.

[208] R. Yan *et al.*, “Inhibition of Salmonella typhimurium and Listeria monocytogenes in coconut juice by graphene-doped photocatalyst rGO/TiO_2,” *Food Chem*, vol. 463, no. P1, p. 141103, 2025, doi: 10.1016/j.foodchem.2024.141103.

[209] Z. Liu, G. Wang, Y. Li, H. Li, and N. Deng, “Carboxymethyl-$β$-cyclodextrin functionalized TiO_2@Fe_3O_4@RGO magnetic photocatalyst for efficient photocatalytic degradation of tetracycline under visible light irradiation,” *J Environ Chem Eng*, vol. 12, no. 5, p. 113303, 2024, doi: 10.1016/j.jece.2024.113303.

[210] Z. He, M. Zhang, H. Yu, Z. Li, B. Deng, and H. Ren, “Multifunctional $BiPO_4$/TiO_2/rGO composite for enhancement removal of malachite green and levofloxacin via adsorption and visible-light photocatalysis synergy,” *Mater Sci Semicond Process*, vol. 169, no. August 2023, p. 107891, 2024, doi: 10.1016/j.mssp.2023.107891.

[211] N. Feng *et al.*, “Boron environments in B-doped and (B, N)-codoped TiO_2 photocatalysts: A combined solid-state NMR and theoretical calculation study,” *The Journal of Physical Chemistry C*, vol. 115, no. 6, pp. 2709–2719, Feb. 2011, doi: 10.1021/jp108008a.

[212] A. L. Al-Otaibi *et al.*, “Pulsed laser ablation-mediated facile fabrication of MoO_3/TiO_2/rGO nanocomposite as a photocatalyst for dye degradation,” *Opt Laser Technol*, vol. 170, no. October 2023, 2024, doi: 10.1016/j.optlastec.2023.110156.

[213] G. Yang, J. Kim, B. Lee, J. E. Jang, and H.-J. Kwon, “One-Step Laser-Induced Oxidation and Doping for Tailored p-Type Conversion of Al-Doped TiO_2,” *Small*, vol. n/a, no. n/a, p. 2502139, May 2025, doi: 10.1002/smll.202502139.

[214] X. Zhang *et al.*, “One-step synthesis of oxygen vacancy-rich BiOBr/TiO_2 composite: Ultrafast adsorption-photocatalytic performance and mechanism,” *Chemical Engineering Journal*, vol. 495, no. June, p. 153261, 2024, doi: 10.1016/j.cej.2024.153261.

[215] P. Pal, Z.-F. Lin, and R.-A. Doong, “Synergistic adsorption and photocatalytic degradation of ciprofloxacin in aqueous medium using advanced g-C_3N_4/MoS_2 heterostructures,” *Chemical Engineering Journal*, vol. 502, no. July, p. 157884, Dec. 2024, doi: 10.1016/j.cej.2024.157884.

[216] J. Wang *et al.*, “Study on the adsorption mechanism of ciprofloxacin in wastewater by modified fly ash under the coexistence of copper,” *J Environ Chem Eng*, vol. 12, no. 6, p. 114336, 2024, doi: 10.1016/j.jece.2024.114336.

[217] R. Tang *et al.*, “$π$-$π$ stacking derived from graphene-like biochar/g-C_3N_4 with tunable band structure for photocatalytic antibiotics degradation via peroxymonosulfate activation,” *J Hazard Mater*, vol. 423, no. PA, p. 126944, 2022, doi: 10.1016/j.jhazmat.2021.126944.

[218] L. Tan, Z. Liu, C. Zhou, and L. Ding, “Combined factors influencing the surface charge and aggregation behaviors of TiO_2 nanoparticles in the presence of humic acid and UV irradiation,” *Journal of Nanoparticle Research*, vol. 23, no. 8, 2021, doi: 10.1007/s11051-021-05315-0.

[219] J. Wang *et al.*, “Synergistic adsorption-degradation of NOR-Pb(II) composite pollutants using Bi_2WO_6/TiO_2/BC ternary bifunctional composite material: Performance, mechanisms, and DFT calculation,” *Chemical Engineering Journal*, vol. 504, no. September 2024, p. 158892, 2025, doi: 10.1016/j.cej.2024.158892.

[220] A. Paul, A. S. Suneesh, and N. Ramanathan, “A sulfur-based adsorbent for the removal of palladium from aqueous waste: Comprehensive study on the preparation, characterization, adsorption and breakthrough modeling,” *Colloids Surf A Physicochem Eng Asp*, vol. 714, no. September 2024, p. 136577, 2025, doi: 10.1016/j.colsurfa.2025.136577.

[221] A. Kutuzova, T. Dontsova, and W. Kwapinski, "Application of TiO_2-based photocatalysts to antibiotics degradation: Cases of sulfamethoxazole, trimethoprim and ciprofloxacin," *Catalysts*, vol. 11, no. 6, 2021, doi: 10.3390/catal11060728.

[222] R. Tai *et al.*, "Defect Engineering of Bi2WO6 for Enhanced Photocatalytic Degradation of Antibiotic Pollutants," *Small*, vol. 20, no. 29, pp. 1–10, 2024, doi: 10.1002/smll.202310785.

[223] H. Liang *et al.*, "A novel vacancy-strengthened Z-scheme g-C_3N_4/Bp/MoS_2 composite for super-efficient visible-light photocatalytic degradation of ciprofloxacin," *Sep Purif Technol*, vol. 272, no. March, p. 118891, 2021, doi: 10.1016/j.seppur.2021.118891.

[224] Y. Lu *et al.*, "Highly efficient photodegradation of ciprofloxacin by dual Z-scheme Bi_2MoO_6/GQDs/TiO_2 heterojunction photocatalysts: mechanism analysis and pathway exploration," *J Alloys Compd*, vol. 924, p. 166533, 2022, doi: 10.1016/j.jallcom.2022.166533.

[225] X. Hu *et al.*, "Mechanisms underlying the photocatalytic degradation pathway of ciprofloxacin with heterogeneous TiO_2," *Chemical Engineering Journal*, vol. 380, no. July 2019, 2020, doi: 10.1016/j.cej.2019.122366.

[226] X. Mu *et al.*, "Impact of antibiotics on microbial community in aquatic environment and biodegradation mechanism: a review and bibliometric analysis," *Environmental Science and Pollution Research*, vol. 30, no. 25, pp. 66431–66444, 2023, doi: 10.1007/s11356-023-27018-w.

[227] Q. Yuan *et al.*, "Synthesis of a novel TiO_2/HA/RGO composite material with photocatalytic activity for dye degradation," *Mater Chem Phys*, vol. 304, no. March, p. 127847, 2023, doi: 10.1016/j.matchemphys.2023.127847.

[228] M. A. Flórez-Restrepo, X. López-Legarda, and F. Segura-Sánchez, "Bioremediation of emerging pharmaceutical pollutants acetaminophen and ibuprofen by white-rot fungi – A review," *Science of The Total Environment*, vol. 977, p. 179379, May 2025, doi: 10.1016/J.SCITOTENV.2025.179379.

[229] S. Zhu *et al.*, "Magnetic Co/Fe nanocomposites derived from ferric sludge as an efficient peroxymonosulfate catalyst for ciprofloxacin degradation," *Chemical Engineering Journal*, vol. 432, p. 134180, Mar. 2022, doi: 10.1016/J.CEJ.2021.134180.

[230] Q. Sun *et al.*, "Bioaccumulation and sources of typical emerging pollutants via farming activities: Insight from risk assessment and mitigation," *Environ Int*, vol. 198, p. 109399, Apr. 2025, doi: 10.1016/J.ENVINT.2025.109399.

[231] N. Geremia *et al.*, “Fluoroquinolones and Biofilm : A Narrative Review,” 2024.

[232] Y. Yang *et al.*, “Research on the mechanism of flumequine degradation by ultraviolet light activated trichloroisocyanuric acid,” *Environ Res*, vol. 281, p. 121976, Sep. 2025, doi: 10.1016/J.ENVRES.2025.121976.

[233] M. Li, X. Sun, L. Zhao, W. Du, and D. Shang, “The antibacterial activity and mechanisms of Trp-containing peptides against multidrug-resistant Pseudomonas aeruginosa persisters,” *Biochimie*, vol. 225, pp. 133–145, Oct. 2024, doi: 10.1016/J.BIOCHI.2024.05.019.

[234] G. Ferrari, M. Junghans, M. Korkaric, and I. Werner, “FA_Junghans_MidRes,” *Aqua & Gas*, no. 6, pp. 52–59, 2019.

[235] J. Wang *et al.*, “Effects of co-loading of polyethylene microplastics and ciprofloxacin on the antibiotic degradation efficiency and microbial community structure in soil,” *Science of The Total Environment*, vol. 741, p. 140463, Nov. 2020, doi: 10.1016/J.SCITOTENV.2020.140463.

[236] D. G. Kim, D. Choi, S. Cheon, S. O. Ko, S. Kang, and S. Oh, “Addition of biochar into activated sludge improves removal of antibiotic ciprofloxacin,” *Journal of Water Process Engineering*, vol. 33, p. 101019, Feb. 2020, doi: 10.1016/J.JWPE.2019.101019.

[237] S. Huang *et al.*, “Enhanced Degradation of Ciprofloxacin through an Intimately Coupled Photocatalysis and Biodegradation System: Performance and Mechanistic Insights,” *Process Safety and Environmental Protection*, p. 107173, Apr. 2025, doi: 10.1016/J.PSEP.2025.107173.

[238] P. Jing *et al.*, “Optimization of wear resistance and wear mechanism analysis of laser melted nickel-based/diamond composite coatings using response surface methodology,” *Tribol Int*, vol. 212, p. 111009, Dec. 2025, doi: 10.1016/J.TRIBOINT.2025.111009.

[239] A. Khataee, S. Jabbarvand Behrouz, M. Ashrafian Nansa, and Y. Orooji, “Titanium germanium carbide-doped polyethersulfone nanofiltration membrane for various dyes-contaminated water treatment,” *Sep Purif Technol*, vol. 381, p. 135567, Feb. 2026, doi: 10.1016/J.SEPPUR.2025.135567.

[240] L. Kang, Y. Xing, H. Yu, and J. Lu, “Photo-enzyme synergistic catalysis by nitrogen-doped titanate nanotubes for efficient microplastic degradation: Acceleration of Ti valence cycle under visible light irradiation,” *J Environ Chem Eng*, vol. 13, no. 6, p. 119417, Dec. 2025, doi: 10.1016/J.JECE.2025.119417.

[241] F. Nazer, Z. Khakpour, A. Maghsoudipour, and S. Hajati, “Synthesis and characterization of black hydrogenated TiO_2-rGO nanocomposites with enhanced photocatalytic activity,” *Int J Hydrogen Energy*, vol. 78, pp. 148–156, Aug. 2024, doi: 10.1016/J.IJHYDENE.2024.06.260.

[242] S. Landi, I. R. Segundo, E. Freitas, M. Vasilevskiy, J. Carneiro, and C. J. Tavares, “Use and misuse of the Kubelka-Munk function to obtain the band gap energy from diffuse reflectance measurements,” *Solid State Commun*, vol. 341, p. 114573, Jan. 2022, doi: 10.1016/J.SSC.2021.114573.

[243] H. Peng *et al.*, “Enhanced removal of Cr(VI) from wastewater by dielectric barrier discharge plasma coupled with TiO_2/rGO nanocomposites: Catalytic performance and reduction mechanism,” *Sep Purif Technol*, vol. 298, p. 121609, Oct. 2022, doi: 10.1016/J.SEPPUR.2022.121609.

[244] Z. N. Kayani, A. Iqbal, Z. Bashir, S. Riaz, and S. Naseem, “Effect of K contents on the efficiency of K-doped TiO_2 thin films for smart window applications,” *Inorg Chem Commun*, vol. 151, p. 110560, May 2023, doi: 10.1016/J.INOCHE.2023.110560.

[245] M. A. Al Masud, S. Annamalai, and W. S. Shin, “Remediation of ciprofloxacin in soil using peroxymonosulfate activated by ball-milled seaweed kelp biochar: Performance, mechanism, and phytotoxicity,” *Chemical Engineering Journal*, vol. 465, p. 142908, Jun. 2023, doi: 10.1016/J.CEJ.2023.142908.

[246] H. G. Gomaa, “Interaction forces and suspension characteristics in an oscillatory membrane photocatalytic reactor,” *Chemical Engineering Research and Design*, vol. 185, pp. 301–308, Sep. 2022, doi: 10.1016/J.CHERD.2022.07.021.

[247] J. Iyyappan, B. Gaddala, R. Gnanasekaran, M. Gopinath, D. Yuvaraj, and V. Kumar, “Critical review on wastewater treatment using photo catalytic advanced oxidation process: Role of photocatalytic materials, reactor design and kinetics,” *Case Studies in Chemical and Environmental Engineering*, vol. 9, p. 100599, Jun. 2024, doi: 10.1016/J.CSCEE.2023.100599.

[248] M. Zhang *et al.*, “Insights into adsorption and high photocatalytic oxidation of ciprofloxacin under visible light by intra-molecular Donor-Acceptor like p-n isotype heterojunction: Performance and mechanism,” *Chemical Engineering Journal*, vol. 464, p. 142533, May 2023, doi: 10.1016/J.CEJ.2023.142533.

[249] L. Li *et al.*, "Mechanism of dual-pathway peroxymonosulfate activation via Co-Nx coordination-regulated broad-pH-adaptive carbon aerogel for ciprofloxacin degradation," *Environ Res*, vol. 285, p. 122617, Nov. 2025, doi: 10.1016/J.ENVRES.2025.122617.

[250] D. Sagir *et al.*, "Investigation of different activation methods in peroxymonosulfate oxidation for the treatment of chemical industry wastewater," *J Environ Chem Eng*, vol. 13, no. 6, p. 119861, Dec. 2025, doi: 10.1016/J.JECE.2025.119861.

[251] M. Yin, W. Yu, S. Nie, K. Wang, X. Xiao, and B. Chen, "Humic acid inhibits hydroxyl radical generation during oxygenation of Fe(II) on goethite surface," *Science of The Total Environment*, vol. 966, p. 178581, Feb. 2025, doi: 10.1016/J.SCITOTENV.2025.178581.

[252] Y. J. Lee, Y. Jae Jeong, I. Sun Cho, C. G. Lee, S. J. Park, and P. J. J. Alvarez, "The inhibitory mechanism of humic acids on photocatalytic generation of reactive oxygen species by TiO_2 depends on the crystalline phase," *Chemical Engineering Journal*, vol. 476, p. 146785, Nov. 2023, doi: 10.1016/J.CEJ.2023.146785.

[253] Y. Li *et al.*, "Effect of antibiotics on diverse aquatic plants in aquatic ecosystems," *Aquatic Toxicology*, vol. 281, p. 107289, Apr. 2025, doi: 10.1016/J.AQUATOX.2025.107289.

[254] Z. Liu *et al.*, "Quenching should be used with caution to evaluate the role of reactive oxygen species in the degradation of pollutants by electro-advanced oxidation technology," *Process Safety and Environmental Protection*, vol. 195, p. 106823, Mar. 2025, doi: 10.1016/J.PSEP.2025.106823.

[255] I. Ijaz *et al.*, "Activation of persulfate, peroxymonosulfate, and peroxydisulfate using metal-organic framework catalysts for degradation of antibiotics: Identification, quantification, interconversion, and transformation of reactive species," *J Environ Chem Eng*, vol. 12, no. 3, p. 112838, Jun. 2024, doi: 10.1016/J.JECE.2024.112838.

[257] X. Hu *et al.*, "Mechanisms underlying the photocatalytic degradation pathway of ciprofloxacin with heterogeneous TiO_2," *Chemical Engineering Journal*, vol. 380, p. 122366, Jan. 2020, doi: 10.1016/J.CEJ.2019.122366.

[258] X. yi Wang, C. liang Dong, K. Xu, R. long Xiao, and X. juan Feng, "Ciprofloxacin (CIP)-polluted water treatment via a facile mechanochemical route: Influencing factors and mechanism insights," *Water Science and Engineering*, vol. 18, no. 1, pp. 21–29, Mar. 2025, doi: 10.1016/J.WSE.2024.03.004.

[259] V. Patilea and C. Sánchez-Sellero, "Testing for lack-of-fit in functional regression models against general alternatives," *J Stat Plan Inference*, vol. 209, pp. 229–251, Dec. 2020, doi: 10.1016/J.JSPI.2020.04.002.

[260] M. Song, Y. Hua, Y. Liu, X. Xiao, H. Yu, and X. Deng, "Design, Synthesis, and Antimicrobial Activity Evaluation of Ciprofloxacin—Indole Hybrids," *Molecules*, vol. 28, no. 17, Sep. 2023, doi: 10.3390/molecules28176325.

[261] F. Hernández *et al.*, "High resolution mass spectrometry-based screening for the comprehensive investigation of organic micropollutants in surface water and wastewater from Pasto city, Colombian Andean highlands," *Science of the Total Environment*, vol. 922, Apr. 2024, doi: 10.1016/j.scitotenv.2024.171293.

[262] P. Y. Nguyen, G. Carvalho, M. A. M. Reis, and A. Oehmen, "A review of the biotransformations of priority pharmaceuticals in biological wastewater treatment processes," *Water Res*, vol. 188, Jan. 2021, doi: 10.1016/j.watres.2020.116446.

[263] D. R. Eddy *et al.*, "Heterophase Polymorph of TiO_2 (Anatase, Rutile, Brookite, TiO_2 (B)) for Efficient Photocatalyst: Fabrication and Activity," *Nanomaterials*, vol. 13, no. 4, 2023, doi: 10.3390/nano13040704.

[264] M. Abid *et al.*, "A novel BN/TiO_2/HNT nanocomposite for photocatalytic applications fabricated by electrospinning," *Colloids Surf A Physicochem Eng Asp*, vol. 662, no. December 2022, p. 131043, 2023, doi: 10.1016/j.colsurfa.2023.131043.

[265] C. Yu *et al.*, "Construction of a visible-light-driven p-BNMF/TiO_2 composite photocatalyst for effective ofloxacin contaminant removal," *J Alloys Compd*, vol. 970, no. October 2023, p. 172548, 2024, doi: 10.1016/j.jallcom.2023.172548.

[266] L. T. Nguyen *et al.*, "UV–Visible Light Driven Photocatalytic Degradation of Ciprofloxacin by N,S Co-doped TiO_2: The Effect of Operational Parameters," *Top Catal*, vol. 63, no. 11–14, pp. 985–995, 2020, doi: 10.1007/s11244-020-01319-7.

[267] J. Yuan, Y. Zhang, X. Zhang, J. Zhang, and S. Zhang, "N-doped graphene quantum dot-decorated N-TiO_2/P-doped porous hollow g-C_3N_4 nanotube composite photocatalysts for antibiotic photodegradation and H_2 production," *International Journal of Minerals, Metallurgy and Materials*, vol. 31, no. 1, pp. 165–178, 2024, doi: 10.1007/s12613-023-2678-6.

[268] N. A. A. A. Rahman, A. Khasri, N. H. M. Salleh, and M. R. M. Jamir, "Enhanced adsorption-photodegradation of tetracycline using Ce-N-co-doped AC/TiO_2 photocatalyst: isotherms, kinetics, mechanism, and thermodynamic insight,"

Environmental Science and Pollution Research, vol. 31, no. 49, pp. 59398–59415, 2024, doi: 10.1007/s11356-024-34948-6.

[269] C. Appel, L. Q. Ma, R. D. Rhue, and E. Kennelley, "Point of zero charge determination in soils and minerals via traditional methods and detection of electroacoustic mobility," *Geoderma*, vol. 113, no. 1–2, pp. 77–93, 2003.

[270] F. Wang, X. Yu, M. Ge, and S. Wu, "One-step synthesis of TiO_2/γ-Fe_2O_3/GO nanocomposites for visible light-driven degradation of ciprofloxacin," *Chemical Engineering Journal*, vol. 384, no. July 2019, pp. 2–9, 2020, doi: 10.1016/j.cej.2019.123381.

[271] W. Li *et al.*, "$Bi_2Ti_2O_7$/TiO_2/RGO composite for the simulated sunlight-driven photocatalytic degradation of ciprofloxacin," *Mater Chem Phys*, vol. 256, no. February, p. 123650, 2020, doi: 10.1016/j.matchemphys.2020.123650.

[272] J. Zuo *et al.*, "Preparation of Au-RGO/TiO_2 nanotubes and study on the photocatalytic degradation of ciprofloxacin," *Analytical Methods*, vol. 15, no. 4, pp. 519–528, 2023, doi: 10.1039/d2ay01497a.

[273] H. S. Ngo, T. L. Nguyen, N. T. Tran, and H. C. Le, "Experimental Study on Kinetics and Mechanism of Ciprofloxacin Degradation in Aqueous Phase Using Ag-TiO_2/rGO/Halloysite Photocatalyst," *Catalysts*, vol. 13, no. 2, 2023, doi: 10.3390/catal13020225.

[274] C. Sanchez Tobon, I. Panžić, A. Bafti, G. Matijašić, D. Ljubas, and L. Ćurković, "Rapid Microwave-Assisted Synthesis of N/TiO_2/rGO Nanoparticles for the Photocatalytic Degradation of Pharmaceuticals," *Nanomaterials*, vol. 12, no. 22, 2022, doi: 10.3390/nano12223975.

[275] M. Abid, I. Iatsunskyi, E. Coy, G. Lesage, A. Ben Haj Amara, and M. Bechelany, "Ag-BN/HNT-TiO_2 nanofibers produced by electrospinning as catalysts to remove acetaminophen," *Heliyon*, vol. 10, no. 2, p. e24740, 2024, doi: 10.1016/j.heliyon.2024.e24740.

[276] D. Van Thuan *et al.*, "Photodegradation of ciprofloxacin antibiotic in water by using ZnO-doped g-C_3N_4 photocatalyst," *Chemosphere*, vol. 308, p. 136408, Dec. 2022, doi: 10.1016/j.chemosphere.2022.136408.

[277] A. Khan, A. A. Shah, S. O. Allehabi, F. Ahmed, A. Alsulami, and A. Azam, "Enhanced degradation of Ciprofloxacin (CIP) antibiotic and methylene blue (MB) dye using

ZnO/GO nanocomposites under solar irradiation," *Sci Rep*, vol. 14, no. 1, p. 30696, Dec. 2024, doi: 10.1038/s41598-024-78636-4.

[278] A. Bamisaye, O. A. Oluboyede, N. O. Etafo, M. O. Bamidele, O. T. Abiola-Kuforiji, and M. A. Idowu, "Synthesis of zinc oxide nanoparticles using Syzygium malaccense leaf extract: photocatalytic decomposition of ciprofloxacin and antimicrobial studies," *Nanotechnology for Environmental Engineering*, vol. 10, no. 3, p. 54, 2025, doi: 10.1007/s41204-025-00459-z.

[279] Y. Lin *et al.*, "Degradation of ciprofloxacin by a constitutive g-C_3N_4 /BiOCl heterojunction under a persulfate system," *RSC Adv*, vol. 13, no. 7, pp. 4361–4375, 2023, doi: 10.1039/D2RA06500B.

[280] I. Mukherjee, V. Cilamkoti, and R. K. Dutta, "Sunlight-Driven Photocatalytic Degradation of Ciprofloxacin by Carbon Dots Embedded in ZnO Nanostructures," *ACS Appl Nano Mater*, vol. 4, no. 8, pp. 7686–7697, Aug. 2021, doi: 10.1021/acsanm.1c00883.

[281] M. Chen, J. Yao, Y. Huang, H. Gong, and W. Chu, "Enhanced photocatalytic degradation of ciprofloxacin over Bi_2O_3/$(BiO)_2CO_3$ heterojunctions: Efficiency, kinetics, pathways, mechanisms and toxicity evaluation," *Chemical Engineering Journal*, vol. 334, pp. 453–461, Feb. 2018, doi: 10.1016/j.cej.2017.10.064.

[282] F. Rong, Q. Lu, H. Mai, D. Chen, and R. A. Caruso, "Hierarchically Porous WO_3 /$CdWO_4$ Fiber-in-Tube Nanostructures Featuring Readily Accessible Active Sites and Enhanced Photocatalytic Effectiveness for Antibiotic Degradation in Water," *ACS Appl Mater Interfaces*, vol. 13, no. 18, pp. 21138–21148, May 2021, doi: 10.1021/acsami.0c22825.

[283] O. Mertah, A. Gómez-Avilés, A. Kherbeche, C. Belver, and J. Bedia, "Peroxymonosulfate enhanced photodegradation of sulfamethoxazole with TiO_2@$CuCo_2O4$ catalysts under simulated solar light," *J Environ Chem Eng*, vol. 10, no. 5, p. 108438, Oct. 2022, doi: 10.1016/J.JECE.2022.108438.

[284] O. Oyegbeda, S. O. Akpotu, and B. Moodley, "Performance of a veil-like reduced graphene oxide modified with covalent triazine framework – titania (CTF-TiO_2/rGO) for ciprofloxacin removal: H_2O_2 activation, mechanism and toxicity insights," *Journal of Water Process Engineering*, vol. 78, p. 108742, Oct. 2025, doi: 10.1016/J.JWPE.2025.108742.

[285] F. Wang, X. Yu, M. Ge, and S. Wu, “One-step synthesis of TiO_2/γ-Fe_2O_3/GO nanocomposites for visible light-driven degradation of ciprofloxacin,” *Chemical Engineering Journal*, vol. 384, p. 123381, Mar. 2020, doi: 10.1016/J.CEJ.2019.123381.

LIST OF APPENDICES

Appendix A. Supplementary Information for Chapter Three

The experiments presented demonstrate the presence of the most commonly prescribed medications in samples of municipal wastewater (influent and effluent) from Kality. As the sample point as seen in **Figure S3.1,** shows, all specified chemicals were detected in influent and effluent samples taken from the Kality municipal wastewater treatment plant.

Table S3.1: Targeted emerging contaminants for this study.

Compounds	**Molecular formula** [a]	**Charge**	**MW** [a]	**Precursor theoretical m/z**[258]	**Fragment theoretical m/z**[147]
Amoxicillin	$C_{16}H_{19}N_3O_5S$	$[M+H]^+$	365.4 g/mol	365.1	349.1, 208.1
Ciprofloxacin	$C_{17}H_{18}FN_3O_3$	$[M+H]^+$	331.3 g/mol	332.1	314.1, 231.1
Carbamazepine	$C_{15}H_{12}N_2O$	$[M+H]^+$	236.3 g/mol	237.1	194.1,192.1
Caffeine	$C_8H_{10}N_4O_2$	$[M+H]^+$	194.2 g/mol	195.1	138.1,110.1
Ibuprofen	$C_{13}H_{18}O_2$	$[M+H]^+$	206.3 g/mol	207.1	161.1,119.1
Diclofenac	$C_{14}H_{11}C_{l2}NO_2$	$[M+H]^+$	296.1 g/mol	296.0	214.0, 250.0
Tetracycline	$C_{22}H_{24}N_2O_8$	$[M+H]^+$	444.4 g/mol	445.2	410.2,154.1

Data are taken from [a]https://pubchem.ncbi.nlm.nih.gov

The theoretical m/z values for the above-listed compounds and their common fragments when they lose common fragments: amoxicillin has two common fragment values (m/z=349.1 and 208.1) when it loses NH_3 and $C_8H_9NO_3$, respectively. Similarly, ciprofloxacin also has two m/z values of 314.1 and 231.1 when it loses H_2O and $C_6H_5NO_2$, respectively. Caffeine also has 138.1 and 110.1 theoretical m/z values when its loss of $C_2H_4N_2O$ and $C_3H_5N_2O$, respectively.

Table S3.2 High-performance liquid chromatography detection details.

Compounds	Mobile phase	Detection wavelength (nm)	Retention time (min)	Temperature (°C)	R^2
Amoxicillin	30% Methanol, 80% Formic acid 1%	228	1.05	40	0.9983
Ciprofloxacin	70% is 1% formic acid. 30% of acetonitrile	278	2.22	40	0.9982
Carbamazepine	70% is 1% formic acid. 30% of acetonitrile	285	3.90	40	0.9925
Caffeine	70% is 1% formic acid. 30% of acetonitrile	273	1.53	40	0.9924
Ibuprofen	70% is 1% formic acid. 30% of acetonitrile	220	3.41	40	0.9971
Diclofenac	70% is 1% formic acid. 30% of acetonitrile	275	2.03	40	0.9954

Table S3.3 LC-MS/MS identified pollutants based on mass-to-charge (m/z) values

Compounds	**m/z Value**	**Uses**
Paracetamol	117	A common pain reliever and fever reducer.
Caffeine	149	A stimulant is found in coffee, tea, and various energy drinks.
Metoprolol	158	A beta-blocker is used to treat high blood pressure and heart conditions.
Sulfamethoxazole	186	An antibiotic used to treat bacterial infections.
Ibuprofen:	205	A nonsteroidal anti-inflammatory drug is used to

		reduce fever and treat pain or inflammation.
Dibutyl phthalate	279	A plasticizer used in various industrial applications
Diclofenac	305	Used to treat mild to moderate pain
Carbamazepine	231	Used to manage and treat epilepsy, trigeminal neuralgia.
Amoxicillin	377	Used to treat bacterial infections
Ciprofloxacin	325	Used to treat many bacterial infections
Tetracycline	409	Used to treat infections caused by bacteria
Doxorubicin	393	A chemotherapy medication used to treat cancer.
Verapamil	425	A medication used to treat high blood pressure and control angina (chest pain)
Rituximab	651	A monoclonal antibody is used to treat certain autoimmune diseases and types of cancer.

These identifications are tentative and based on common m/z values for fragment ions in mass spectrometry.

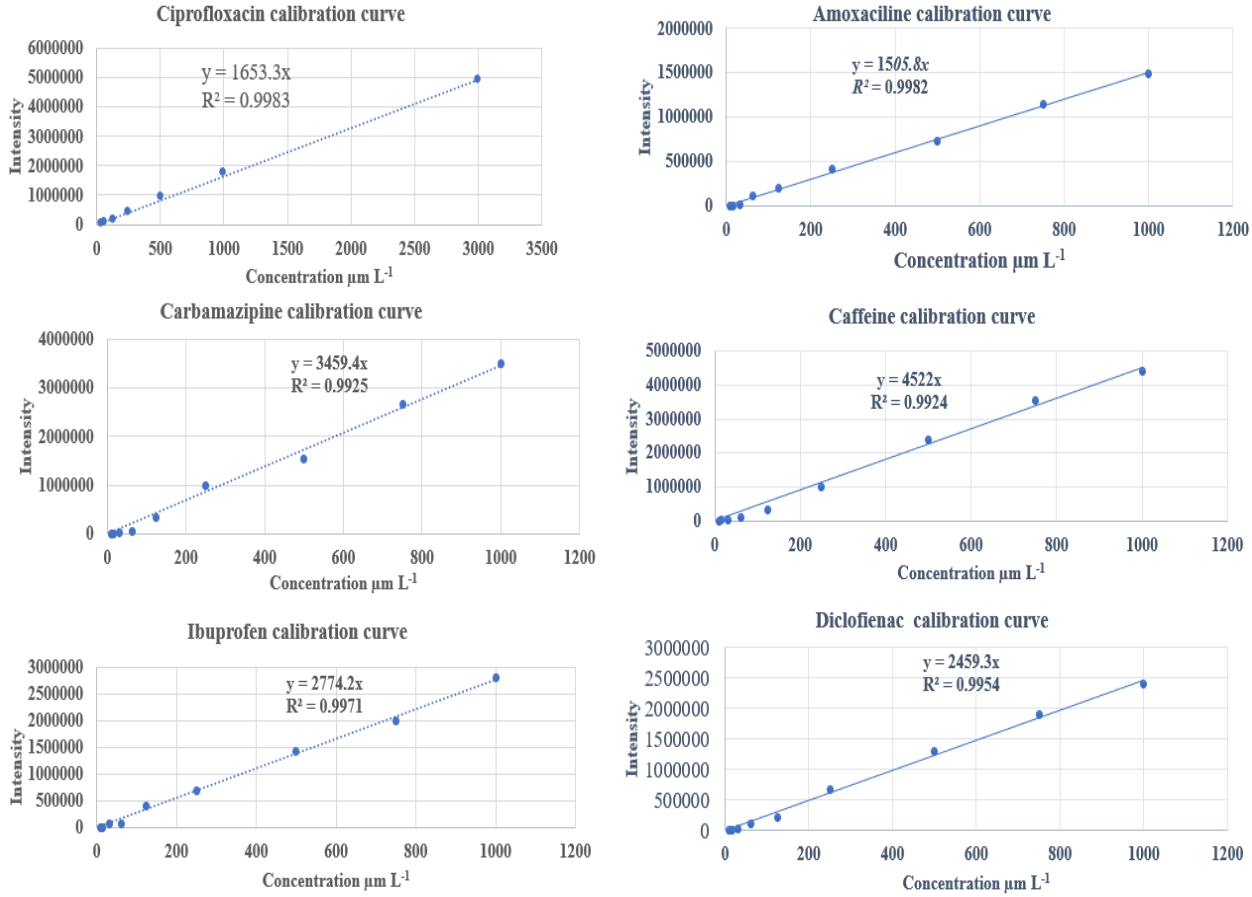

Figure S3.1. Calibration curves of selected Pharmaceutical organic compounds, Experimental conditions: Concentration range 10-1000µm L^{-1} of each sample with 0.3mL methanol.

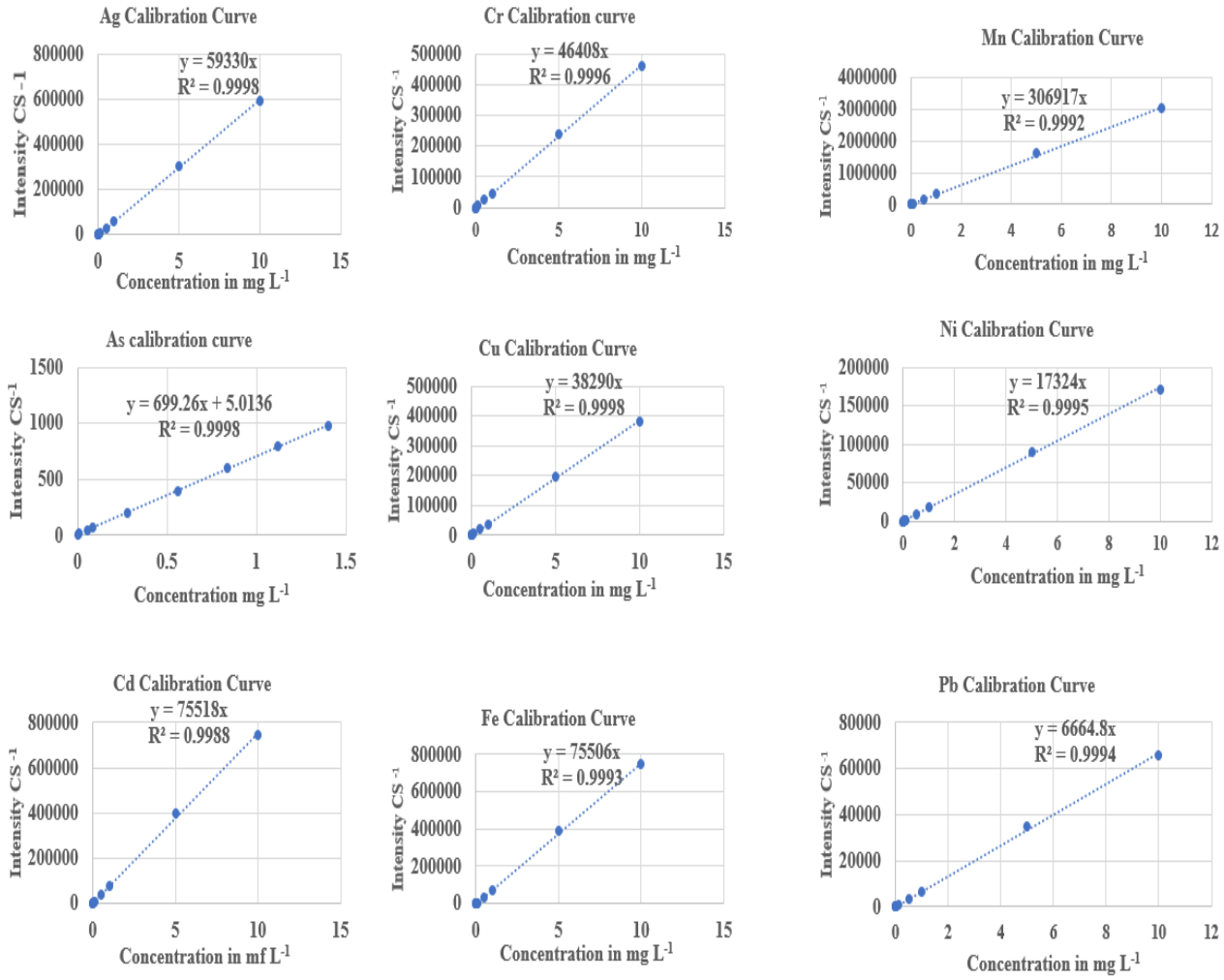

Figure S3.2 Calibration curve of selected heavy metals, Experimental conditions 1000 mg L^{-1} stock solution for each metal in 50 mL volumetric flask, with concentration range (0.001-10 mg L^{-1}) 12% nitric acid dilution and analysis by ICP-OES. Based on the above calibration curve, the concentrations of all heavy metals were calculated accordingly.

Target identification of emerging pollutants based on mass spectra LC-MS/MS results

Emerging pollutants, particularly pharmaceutical compounds, were detected in both wastewater samples. Samples for the influent and effluent were taken before the coarse screening and chlorination process, respectively. As an illustrative example, Figure S3 shows the detection and identification of the antibiotic's amoxicillin, ciprofloxacin, and tetracycline confirmed with the reference standard. These compounds were found at the expected retention time (1.07, 2.22, and 3.6), respectively, as seen in Figure S3.

Anti-inflammatory/ analgesics, like diclofenac and ibuprofen, were also found as well as the main metabolites of the analgesic metamizole. The presence of the anti-hypertensive losartan

and the anti-epileptic and mood-stabilizing drug carbamazepine was confirmed in the wastewater samples.

In addition to the wide group of pharmaceuticals, other compounds were also identified in the samples: caffeine and its main human metabolite, paraxanthine, and the sweeteners sucralose and saccharin. All these findings reveal the impact of the ineffectiveness of conventional municipal wastewater treatment technologies on the quality of discharged wastewater.

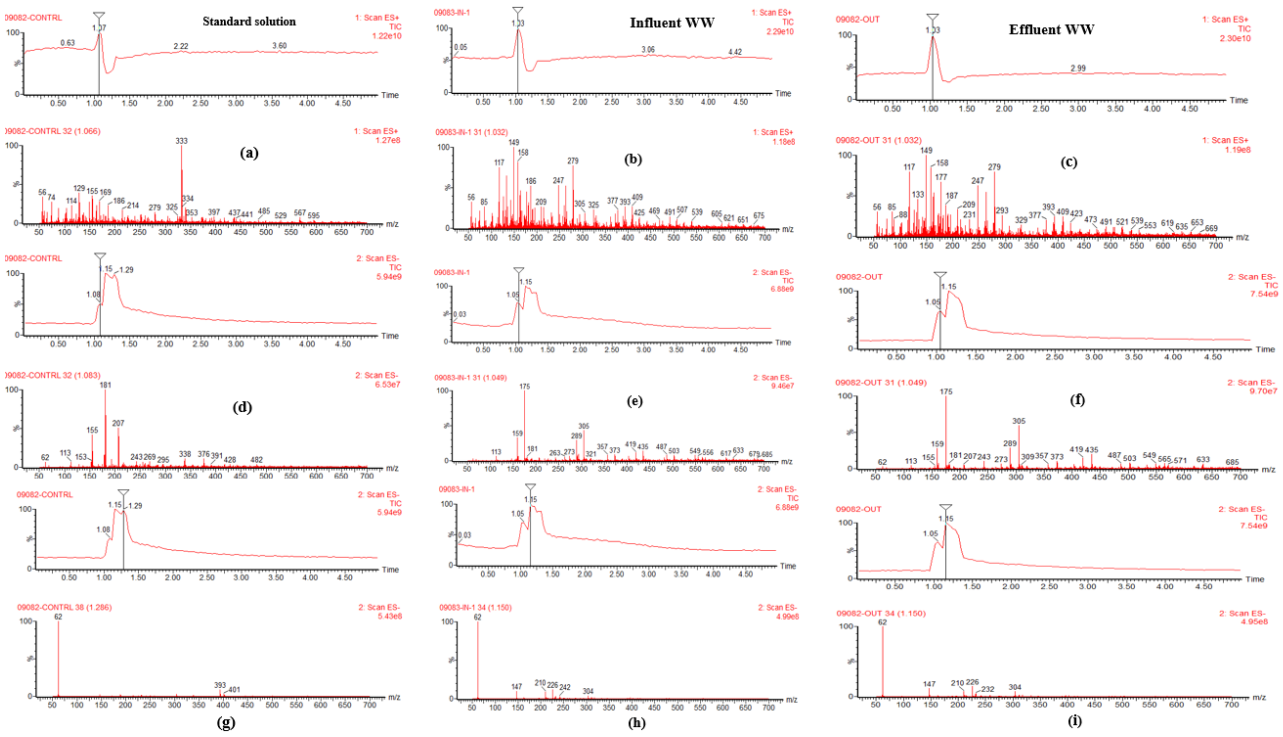

Figure S3.3. Mass spectra of Influent and Effluent of municipal wastewater to identify emerging pollutants from Kality municipal wastewater using m/z ratio and standard solutions, experimental conditions: 5mg L^{-1} of each (amoxicillin, ciprofloxacin, Tetracycline, carbamazepine, Ibuprofen, and diclofenac in (a)), caffeine, amoxicillin, ciprofloxacin in (d) and amoxicillin, ciprofloxacin, and Tetracycline (g).

Biological treatment, advanced oxidation, coagulation/flocculation, advanced filtration, and hybrid technologies are some of the technologies commonly used in WWTPs to treat water effluents [259]. Several global environmental indicators, including chemical and biological oxygen demands, follow the efficiency of WWTPs. Although these metrics typically indicate high organic matter removal efficiency in WWTPs (>85%), there was limited information available on molecular composition [162]. Numerous studies have shown that while the

majority of common WWTP treatments are inefficient in removing pharmaceuticals, some of these treatments contribute to the production of transformation products.

Based on the m/z values, researchers may identify the pollutants from the mass spectra diagram by comparing them with known values for common contaminants. Some possible matches for the m/z values are provided under. As an example, as indicated in Figure (S3a, S3d, S3g), the standard solution mass spectra value at m/z:333 approximately for the ciprofloxacin, ibuprofen (m/z:207), tetracycline, and (m/z: 393). The above-specified indicators to be present in the influent and effluent of the Kality municipal wastewater treatment plant (Figure S3b and S3c) can be compared to these mass spectra in the actual wastewater.

Appendix B. Supplementary Information for Chapter Four

Text S4.1: Doping technique to modify TiO_2

The photocatalytic activity of titanium dioxide (TiO_2) is greatly affected by doping K, B, and N elements. Let's examine the rationale behind the wide selection of potassium (K), boron (B), and nitrogen (N) dopants: By adding energy levels close to the conduction band, **nitrogen (N) doping** enables TiO_2 to absorb visible light [214]. The practical applications of pure TiO_2 are constrained by its main reaction to ultraviolet (UV) light and rapid charge recombination. Enhanced Photocatalysis: For processes such as CO_2 reduction and water splitting, N-doped TiO_2 shows enhanced photocatalytic activity [260]. N-doping and surface heterojunctions work together to improve electron hole separation and performance [105].

Boron (B) Doping: Enhanced Charge Separation: By improving the separation of photoinduced electron-hole pairs, B-doping boosts the photocatalytic activity [202] and decreases the band gap energy. Applications of B-doped TiO_2 include the degradation of organic pollutants and photocatalytic water and air purification [163].

Potassium (K) Doping: Surface Modification: K-doping alters the surface properties of TiO_2 thereby influencing its interactions with reactants. Decreased recombination by trapping electrons generated by advanced oxidation process (AOPs): K-doping improves photocatalysis more efficiently by lowering charge carrier recombination [42]. Applications: K-doped TiO_2 is used in self-cleaning surfaces, antimicrobial applications, and organic pollutant degradation [261].

In conclusion, incorporating these dopants improves the photocatalytic performance of TiO_2 by modifying its electrical structure, surface characteristics, and light absorption capabilities. Ongoing research continues to explore new dopants and techniques to optimise TiO_2 for various

applications. The detailed synthesised modified TiO_2 procedure and analysis information are presented in **Figure S4.1**.

Text S4.2: Reaction Mechanism

Under visible light, photocatalysis using KBN-TiO_2 (potassium boron nitrogen-modified TiO_2) can enhance the breakdown of organic pollutants by triggering a series of oxidative and reductive reactions. The reaction mechanism describes how the process typically performs and the various reactions that could occur.

Visible Light Activation: The modification of KBN effectively reduces the bandgap of TiO_2, thereby facilitating its capacity to absorb visible light. Visible light stimulates the excitation of electrons (e^-) from the valence band (VB) to the conduction band (CB), which leads to the formation of holes (h^+) within the VB:

$$KBN@TiO_2 + hv \rightarrow e^-(CB) + h^+(VB) \quad \text{(S4.1)}$$

The KBN modification enhances charge separation, reducing the recombination of e^- and h^+. Reactive oxygen species (ROS) are produced when electrons and holes interact with water, oxygen, or hydroxide ions:

$$h^+ + H_2O \rightarrow {}^{\bullet}OH + H^+ \quad \text{(S4.2)}$$

$$e^- + O_2 \rightarrow O_2^{\bullet -} \quad \text{(S4.3)}$$

Again $O_2^{\bullet -} + H^+ \rightarrow H_2O_2$ and with a high possibility of ${}^{\bullet}OH$ is formed (S4.4)

Organic pollutants are attacked by the generated ROS, which reduces them to smaller molecules such as CO_2, H_2O, and other harmless by-products. The stepwise possibility of degradation of ciprofloxacin in this study is described below:

Oxidation of ciprofloxacin by hydroxyl radicals (${}^{\bullet}OH$): The aromatic and heterocyclic rings are attacked by hydroxyl radicals, resulting in ring cleavage and the production of intermediates.

$$C_{12}H_{18}FN_3O_3 + {}^{\bullet}OH \rightarrow \text{ Intermediates that have been oxidised} \quad \text{(S4.5)}$$

Breakdown of functional Groups: The amine groups (NH) and fluorine atom (F) initiate oxidisation.

$$F \rightarrow F^- \quad \text{(S4.6)}$$

$$NH \rightarrow NH_4^+ \text{ or } NO_3^- \quad \text{(S4.7)}$$

Mineralisation: Water and carbon dioxide are generated by further breaking down the organic intermediates.

$$Intermediates + {}^{\bullet}OH + O_2 \rightarrow CO_2 + H_2O \quad \text{(S4.8)}$$

In general, the final proposed reaction equation can be described as follows:

$$C_{17}H_{18}FN_3O_3 + {}^{\bullet}OH + H_2 \xrightarrow[KBN@TiO_2]{Light} 17CO_2 + 9H_2O + F^- + NH_4^- + NO_3^- \quad \text{(S4.9)}$$

Table S4.1 ANOVA of the S_{BET} characterisation

Source	Sum of Squares	df	Mean square	F-value	p-value	
Model	997.63	9	110.85	39.00	0.0004	Significant
X_1	567.51	1	567.51	199.67	<0.0001	
X_2	210.64	1	210.69	74.11	0.0003	
X_3	41.09	1	41.09	14.46	0.0126	
X_1X_2	28.30	1	28.30	9.96	0.0252	
X_1X_3	12.46	1	12.46	4.38	0.0905	
X_2X_3	3.63	1	3.63	1.28	0.3098	
X_{12}	15.17	1	15.17	5.34	0.0689	
X_{22}	38.39	1	38.39	13.51	0.0144	
X_{32}	96.59	1	96.59	33.98	0.0021	
Residual	14.21	5	2.84			
Lack of Fit	13.23	3	4.41	8.96	0.1021	Not significant
Pure Error	0.98	2	0.49			
Cor Total	1011.84	14				

The model F-value of 39.00 indicates that the model is significant, with only a 0.04% probability that such a large F-value could occur due to noise. P-values less than 0.0500 suggest that the corresponding model terms are significant. In this case, x_1, x_2, x_3, x_1x_2, x_{22}, and x_{32} are significant model terms. Conversely, P-values exceeding 0.1000 indicate that the model terms are not significant. If a model contains numerous insignificant terms (excluding those required to support hierarchy), model reduction could enhance its performance. The lack of fit F-value of 8.96 implies that the lack of fit is not significant relative to the pure error, with a 10.21% likelihood of such a high F-value occurring due to noise. For a model to fit well, a non-significant lack of fit is desirable.

Table S4.2 ANOVA of the ciprofloxacin degradation efficiency

Source	Sum of Squares	df	Mean square	F-value	P-value	
Model	1819.25	9	202.14	98.51	<0.0001	Significant
X_1	73.63	1	73.63	35.88	0.0019	
X_2	171.03	1	171.03	83.35	0.0003	
X_3	236.97	1	236.97	115.48	0.0001	
X_1X_2	586.37	1	586.37	285.76	<0.0001	
X_1X_3	7.13	1	7.13	3.47	0.1214	
X_2X_3	167.70	1	167.70	81.73	0.0003	
X_{12}	278.11	1	278.11	135.53	<0.0001	
X_{22}	57.43	1	57.43	27.99	0.0032	
X_{32}	203.22	1	203.22	99.03	0.0002	
Residual	10.26	5	2.05			
Lack of Fit	4.65	3	1.55	0.5535	0.6980	not-significant
Pure Error	5.61	2	2.80			
Cor Total	1829.51	14				

The model F-value of 98.51 indicates that the model is significant, with only a 0.01% probability that such a large F-value could occur due to noise. P-values less than 0.0500 suggest that the corresponding model terms are significant. In this case x_1, x_2, x_3, x_1x_2, x_2x_3, x_1^2, x_2^2, and x_3^2 are significant model terms. Conversely, P-values exceeding 0.1000 indicate that the model terms are not significant. If the model contains numerous insignificant terms (excluding those required to support hierarchy), the model reduction could improve its performance. The lack of fit F-value of 0.55 suggests that the lack of fit is not statistically significant compared to the pure error, with a 69.45% probability that a lack of fit F-value of this magnitude could occur due to random variation. A non-significant lack of fit is desirable when aiming for a good fit of the model.

Table S4.3 Fit Statistics model for specific surface area (S_{BET})

Std. Dev.	1.69	R^2	0.9860
Mean	25.81	Adjusted R^2	0.9607
C.V. %	6.52	Predicted R^2	0.7887
		Adeq Precision	19.6925

The **predicted R^2** of 0.7887 is in reasonable agreement with the adjusted R^2 of 0.9607, with a difference of less than 0.2. **Adeq Precision** measures the signal-to-noise ratio. A ratio greater than 4 is desirable, and the obtained ratio of 19.693 indicates an adequate signal. This model can be used to navigate the design space.

Table S4.4 Fit Statistics models for Ciprofloxacin degradation (R%)

Std. Dev.	1.43	**R^2**	0.9944
Mean	74.79	**Adjusted R^2**	0.9843
C.V. %	1.92	**Predicted R^2**	0.9524
		Adeq Precision	31.7104

The **predicted R^2** of 0.9524 is in reasonable agreement with the adjusted R^2 of 0.9843; i.e. the difference is less than 0.2. **Adeq Precision** measures the signal-to-noise ratio. A ratio greater than 4 is desirable, and the obtained ratio of 31.71 indicates an adequate signal. This model can be used to navigate the design space.

Table S4.5 Peak List Only TiO_2

No	2Θ	FWHM (left 2Θ)	Area (cts*2Θ)	d-Spacing (Å)	Height (cts)
1	25.43	0.2362	28.13	3.50	120.74
2	38.03	0.4723	13.53	2.37	29.04
3	48.51	0.2326	14.50	1.88	62.22
4	54.31	0.5314	23.00	1.69	43.88
5	55.39	0.5904	23.64	1.66	40.59
6	63.07	0.4323	19.13	1.47	41.05
7	69.03	0.4323	8.05	1.36	17.29
8	70.68	0.5904	10.18	1.33	17.48
9	75.31	0.5904	14.77	1.26	25.35
10	76.44	0.4723	3.52	1.25	7.55

Table S4.6 Peak List 5%B-2%K-5%N-TiO_2

No	2Θ	FWHM (left 2Θ)	Area (cts*2Θ)	d-Spacing (Å)	Height (cts)
1	25.52	0.3247	46.11	3.49	143.96
2	27.95	0.1771	16.22	3.19	92.83
3	38.01	0.3542	14.59	2.37	41.76
4	48.42	0.4133	28.60	1.88	70.15
5	54.21	0.4327	25.54	1.69	54.81
6	55.29	0.4327	25.80	1.66	55.47
7	62.96	0.4327	20.60	1.48	44.20
8	69.03	0.7085	10.50	1.36	15.03
9	70.55	0.7085	11.58	1.34	16.56
10	75.32	0.4723	16.42	1.26	35.24

Table S4.7 BET, UV-Vis, and CIP removal results

Run	x_1 (%)	x_2 (°C)	x_3 (h)	S_{BET} m^2/g	UV-Vis (eV)	R%
1	2	300	3	69.67	3.21	85.76
2	8	300	3	46.01	3.22	54.45
3	2	500	3	55.76	3.28	51.23
4	8	500	3	42.74	3.14	68.32
5	2	400	2	67.77	3.15	82.89
6	8	400	2	48.89	3.32	80.55
7	2	400	4	58.45	3.16	74.74
8	8	400	4	46.63	3.37	77.02
9	5	300	2	65.19	2.82	84.12
10	5	500	2	51.35	2.42	88.92
11	5	300	4	60.01	3.08	86.12
12	5	500	4	49.98	2.86	65.02
13	5	400	3	48.24	2.67	79.45
14	5	400	3	47.62	2.68	77.02
15	5	400	3	49.02	2.64	76.24
Only TiO_2	0	500	2	50.56	3.21	56.12

Table S4.8 Elemental distribution of the synthesised photocatalyst estimated using SEM-EDS elemental mapping.

Catalysts	Elements	Atomic %	Intensity corn.
Undoped -TiO_2	Ti	35.31	0.2263
	O	64.69	0.9282
Doped-TiO_2	Ti	50.32	0.886
	O	47.10	0.2936
	B	0.75	0.2089
	N	0.45	0.4211
	K	0.69	1.1986

Table S4.9 Comparison of the synthesised KBN@TiO_2 nanoparticles' photocatalytic effectiveness with reported research.

Photocatalyst	Catalyst dose (g/L)	Concentration (C_o) (mg/L)	Irradiation time (min)	Degradation efficiency (%)	Kinetic coefficient (min^{-1})	Ref.
BN@TiO_2	0.5	ACT (10)	180	99.0	0.0132	[264]
p-BNMF/TiO_2	0.1	OFL (20)	120	99.8%	Not given	[265]
N, S-TiO_2	0.5	CIP (30)	150	78.7	0.0065	[266]
N-TiO_2/PCN	0.5	CIP (10)	120	89.6	0.0142	[267]
Ce/N-AC/TiO_2	0.2	TC (10)	120	93.1	0.0687	[268]
KHB-TiO_2	0.1	Methylene (10)	120	91.4	Not given	[13]
KBN@TiO_2	0.5	CIP (10)	120	98.2	0.1336	This study

Table S4.9 presents some of the earlier efforts that addressed photo-degradation in comparison with the present study. While comparing the degradation efficiency and kinetic coefficient obtained for the current system, it is worthwhile to point out that modified KBN@TiO_2 exhibited excellent photocatalytic performances, thereby providing a better platform for highly efficient and affordable organic pharmaceutical removal.

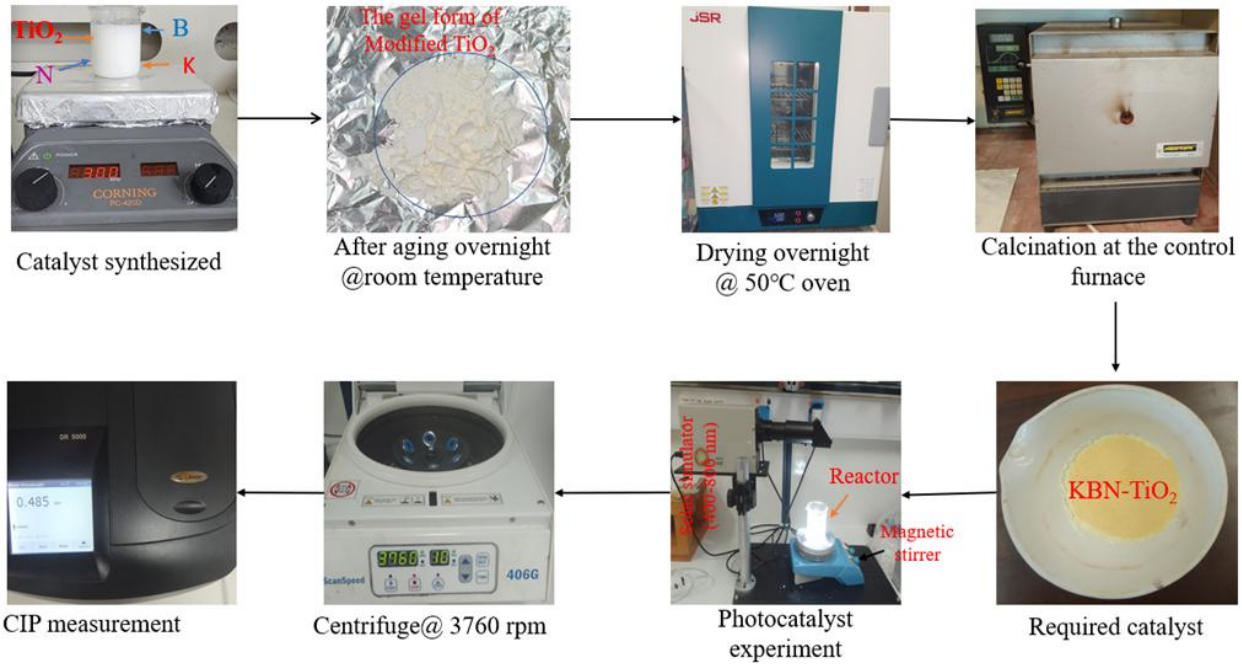

Figure S4.1. General experimental procedures of KBN-TiO_2 synthesis and performance testing

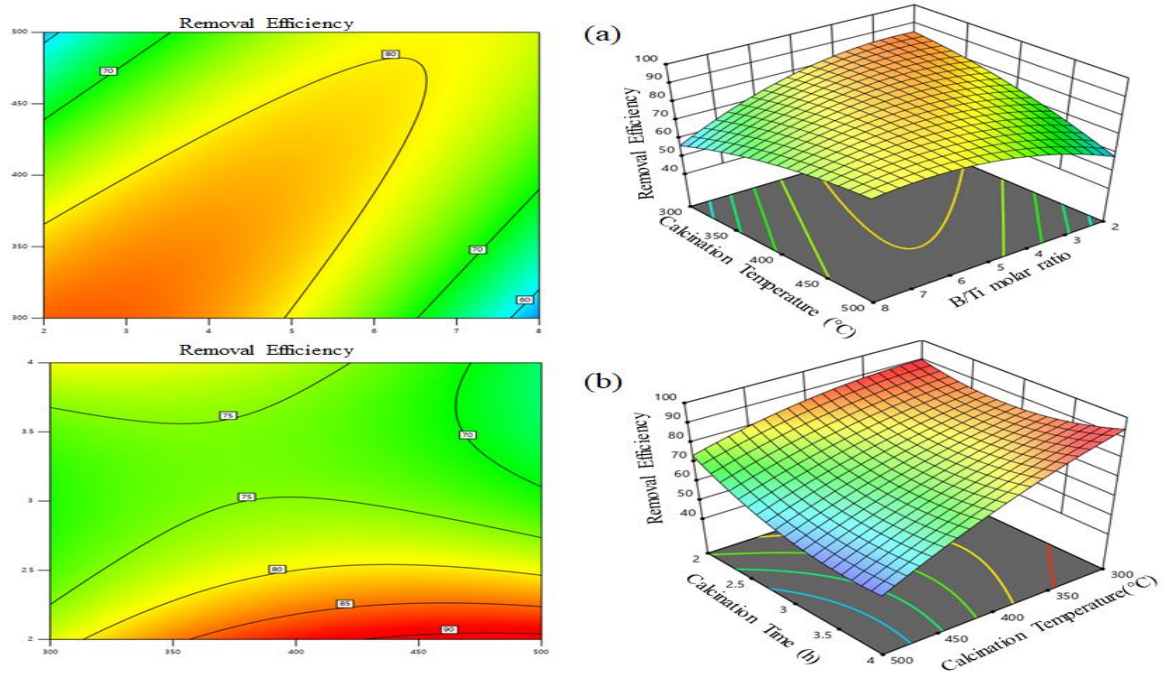

Figure S4.2. Interaction effect on optimum operation counter and 3D graphs for degradation of ciprofloxacin, (a) calcination temperature (°C) and B/Ti molar ratio, (b) calcination time (h) and calcination temperature (°C). Experimental conditions [CIP] = 10 mg L^{-1}, Natural pH = 5.67, KBN-TiO_2 = 0.5g L^{-1}, and time = 120 min.

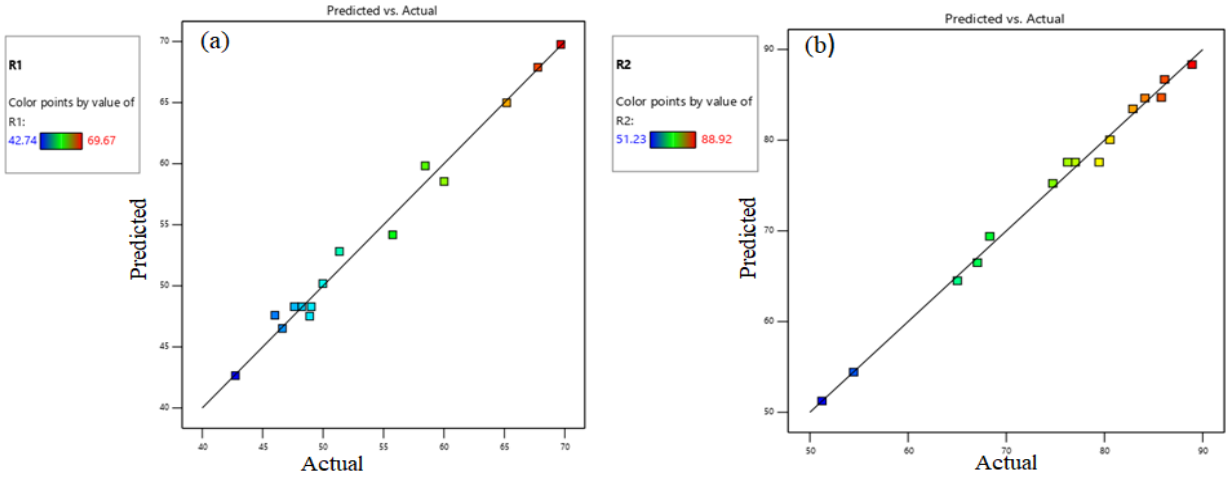

Figure S4.3. Predicted vs actual model diagnostics (a) specific surface area (S_{BET}) and (b) CIP removal efficiency (R%).

Appendix C. Supplementary Information for Chapter Five

Text S5.1. Chemicals and reagents

Titanium tetra-isopropoxide (TTIP, ≥ 97.0%), ciprofloxacin (CIP, $C_{16}H_{18}FN_3O_3$, 98%), norfloxacin (NORF, $C_{16}H_{18}FN_3O_3$, ≥98%), tetracycline hydrochloride (TC, $C_{22}H_{24}N_2O_8$·HCl, ≥99%), humic acid (sodium salt), monobasic sodium phosphate (≥99%), 5,5-dimethyl-pyrroline N-oxide (DMPO, 99%), and 4-amino-2,2,6,6-tetramethylpiperidine (TEMP, 98%) were purchased from Sigma-Aldrich (USA). Water (HPLC grade) and acetonitrile (HPLC grade, LiChrosolv®, Germany) were used as mobile phases. Sodium chloride (NaCl, 99%), sodium bicarbonate ($NaHCO_3$, 99%), sodium sulfate anhydrous (Na_2SO_4, 99%), dibasic sodium phosphate (NaH_2PO_4, 99%), sodium nitrate ($NaNO_3$, >99%), potassium nitrate (KNO_3, 99%), ascorbic acid ($C_6H_8O_6$, ≥98%) were supplied by Duksan Pure Chemicals, Korea. Benzoquinone ($C_6H_4O_2$, 98%) and ammonium solution (NH_3, 28%) were purchased from Junsei Chemical Co., Ltd, Japan. Boric acid (H_3BO_3, 99.5%), triethanolamine ($C_6H_{15}NO_3$, 99%), absolute ethanol (C_2H_5OH, 99%), furfuryl alcohol ($C_5H_6O_2$, ≥98%), and isopropyl alcohol ($(CH_3)_2CHOH$, 99.5%) were obtained from Daejung Chemicals and Metal Co., Ltd., Korea. Potassium permanganate ($KMnO_4$, >99%), hydrogen peroxide (H_2O_2, 30%), and sulfuric acid (H_2SO_4, 98%) were purchased from DC Chemical Co., Ltd, Korea. Sodium hydroxide (1N NaOH) and hydrochloric acid (1N HCl), used to adjust the pH of the reaction solutions, were purchased from Duksan Pure Chemicals Co., Ltd., Korea. All reagents used in this study were of at least ACS grade and were utilized without further purification. All chemical solutions were prepared using double-distilled and de-ionized (DDI) water (Millipore

Sigma TM Synergy TM Ultrapure Water Purification System, Thermo Fisher Scientific, USA, resistivity >18.25 M).

Text S5.2. Material characterization

The morphological properties of the samples were examined using scanning electron microscopy (SEM) (Zeiss Evo 18-20-45). The elemental composition and distribution of the catalyst were determined through energy-dispersive X-ray (EDX). A Micromeritics ASAP 2020 physisorption analyzer (Norcross, USA) was employed to calculate the Brunauer–Emmett–Teller (BET) surface area and pore size distribution of the catalysts using the N_2 adsorption–desorption isotherm. X-ray diffraction (XRD) patterns were recorded using a Rigaku D/Max-B (High-Power) powder diffraction equipment to investigate the crystalline structure of the synthesized KBN@TiO_2@rGO composite and other materials. The Senterra II (Bruker, Billerica, USA) confocal Raman microscope was stimulated with a 10 W laser source set to 532 nm to produce the Raman spectra. Furthermore, X-ray photoelectron spectroscopy (XPS; Thermo Fisher Scientific, USA) was used to obtain surface elemental data. The point of zero charge (pH_{PZC}) was determined using the method proposed by Appel et al. [270], which is briefly explained in **Text S5.5**.

Text S5.3. Analytical methods

A high-performance liquid chromatography (HPLC) system (Agilent Technologies, 1200 series, USA), equipped with an ultraviolet diode array detector (DAD, G1315B) and a Zorbax-eclipse XDB-C18 column (Agilent Technologies, 5 µm particle size, 4.6 × 150 mm, USA), was used to analyze aqueous solutions containing the antibiotics ciprofloxacin (CIP), norfloxacin (NORF), and tetracycline (TC). The mobile phase comprised acetonitrile, formic acid (1%), and phosphoric acid (1%), with a flow rate of 1.0 mL min^{-1}, an injection volume of 20 µL, and a column temperature of 30 °C **(Table S5.2).** Standard calibration curves for CIP, NORF, and TC are presented in **Figure S5.1,** and their physicochemical properties are summarized in **Table S5.3**.

Total organic carbon (TOC) was measured using a Shimadzu TOC analyzer (ASI-L series, Japan). For UPLC-MS/MS analysis, the electrospray ionization (ESI) method was employed in both positive and negative ionization modes (ESI +/–) between 50 m/z and 500 m/z. The mobile phase, comprising 0.1% formic acid and acetonitrile in a 1:1 ratio (v/v), was delivered at a flow rate of 0.2 mL min^{-1}.

Text S5.4. Electron spin resonance (ESR) spectroscopy

ESR spectroscopy (Bruker BioSpin GmbH, Germany) was performed using a microwave frequency of 9.424 GHz, microwave power of 2.000 mW, field sweep of 100 G, modulation amplitude of 4.00 G, conversion time of 30.000 ms, time constant of 163.840 ms, and receiver gain of 5.64×10^2. DMPO and TEMP were employed as spin-trapping agents for $^{\bullet}OH$ and $O_2^{\bullet-}$, and $^1O_2$, respectively. A 1.0 mL sample was collected from the reactor (40 mL amber vial) and mixed thoroughly with 1.0 mL of either DMPO or TEMP, which were prepared using 10 mM phosphate buffer (pH = 7.02) (5.8 mM Na_2HPO_4 and 4.2 mM NaH_2PO_4).

Text S5.5. Determination of point of zero charge (pH_{PZC})

The point of zero charge (pH_{PZC}) was determined using the method proposed by Appel et al. [270]. Briefly, 0.1 g of the KBN@TiO_2@rGO was added to 40 mL polypropylene conical tubes (SPL Co., Korea). The pH of the solution was adjusted from 2 to 12 using 0.1 M HCl or 0.1 M NaOH, followed by the addition of 30 mL of deionised (DI) water. The samples were then shaken for 24 hours at 200 rpm and 25 °C to reach equilibrium. The final solution pH was measured after incubation.

Text S5.6. Adsorption mechanism analysis

The rate of adsorption is described by adsorption kinetic models such as the pseudo-first-order and the pseudo-second-order models. The equilibrium relationship between the concentration of adsorbate in solution at a constant temperature and the amount adsorbed is described by isotherms. The most common isotherm models used for adsorption isotherms are the Langmuir and the Freundlich isotherms.

Typically, the pseudo-first-order kinetic model and the pseudo-second-order kinetic model are described by Eqs. **(S5.1)** and **(S5.2)**, respectively.

$$q_t = q_e(1 - \exp(-k_1 t)) \tag{S5.1}$$

$$q_t = \frac{q_e^2 k_2 t}{(1 + q_e k_2 t)} \tag{S5.2}$$

where q_t (mg g^{-1}) and q_e (mg g^{-1}) represent the adsorption capacity at time t and at equilibrium, respectively; k_1 (min^{-1}) and k_2 (g mg^{-1} min^{-1}) denote the reaction rate constants of the pseudo-first-order and the pseudo-second-order kinetic models, respectively.

Langmuir and Freundlich adsorption isotherm models are commonly used to analyze the adsorption thermodynamics, as expressed in Eqs. (S5.3) and (S5.4), respectively.

$$q = \frac{q_m K_L C}{1 + K_L C} \tag{S5.3}$$

where q (mg g^{-1}) is the amount of adsorbate adsorbed per unit mass of adsorbent, C (mg L^{-1}) is the equilibrium concentration of adsorbate in the solution, q_m (mg g^{-1}) is the maximum adsorption capacity, and K_L (L mg^{-1}) is the Langmuir constant.

$$q = K_F C^{1/n} \tag{S5.4}$$

where K_F [(mg g^{-1})/(mg L^{-1})$^{1/n}$] is the Freundlich constant, and $1/n$ (–) is the non-uniform factor.

Text S5.7. Generation rate of reactive oxygen species (ROS)

Based on **Eq. S5.5**, ROS quantification during oxidation was performed as follows:

$$\text{Generation rate of ROS (mg min}^{-1}) = (k - k_s) \times C_{CIP} \times V \tag{S5.5}$$

where C_{CIP} (mg L^{-1}) is the CIP concentration, V (L) is the volume of the reactor, and k and k_s (min^{-1}) are the first-order rate constants for CIP degradation without and with a scavenger, respectively.

Text S5.8. Total organic carbon (TOC)

TOC was measured to estimate CIP mineralisation (%) using Eq. (S6):

$$Mineralization\,(\%) = \frac{[TOC]_i - [TOC]_f}{[TOC]_i} \times 100 \tag{S5.6}$$

where $[TOC]_i$ and $[TOC]_f$ are the initial and final TOC concentrations in the KBN@TiO_2@ rGO system, respectively.

Table S5.1. High-performance liquid chromatography detection details.

Compound	Molecular structure	Mobile phase	Detection wavelength (nm)	Retention Time (min)	Column Temperature (°C)	R^2
Ciprofloxacin	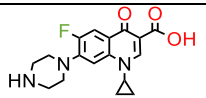	Formic acid (1%) = 70% Acetonitrile = 30%	277	1.7 ± 0.1	30	0.9989
Norfloxacin	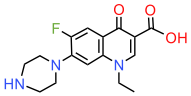	Phosphoric acid (1%) = 40% Acetonitrile = 60%	278	1.3 ± 0.1	28	0.9983
Tetracycline	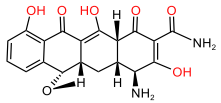	Phosphoric acid (1%) = 80% Acetonitrile = 20%	360	3.6 ± 0.1	30	0.9999

Table S5.2(a). Comparisons of the efficacy of various modified (metal and non-metal) doped TiO_2/rGO composite catalysts in the degradation of organic pollutants.

Photocatalysts materials	**[CIP] (mg L^{-1})**	**Catalyst dosage (g L^{-1})**	**Light Source**	**Reaction time (min)**	**Removal efficiency (%)**	**Reaction rate constant (min^{-1})**	**Reference**
KBN@TiO_2@rGO	10	0.2	500W Xenon lamp ($\lambda > 420$)	120	99.21	0.0337	This study
KBN@TiO_2	10	0.2	500W Xenon lamp ($\lambda > 420$)	120	85.04	0.0156	This study
TiO_2/γ-Fe_2O_3/GO	10	0.4	300W Xenon lamp ($\lambda > 420$)	140	99.00	0.015	[271]
$Bi_2Ti_2O_7$/TiO_2/rGO	10	0.1	500W Xenon lamp ($\lambda > 420$)	180	95.00	0.0158	[272]
Au-rGO/TiO_2	0.2	0.5	35W mercury lamp	180	96.93	-	[273]
Ag-TiO_2/rGO/HNT	20	0.1	UV irradiation	300	90	0.0013	[274]
N/TiO_2/rGO	10	0.25	1266.6W UVA lamp	120	98.01	0.0407	[275]
Ag-BN/HNT-TiO_2	10	0.5	Halogen linear lamp	120	99.00	0.0346	[276]
rGO/TiO_2/g-C_3N_4	20 (MB)	0.05	500W Tungsten lamp	120	98.5	0.00015	[19]

MB = methylene blue pollutant

Table S5.2(b). Comparison of photocatalytic performance of various non-TiO_2-based catalysts for CIP degradation.

Photocatalysts materials	**[CIP] (mg L^{-1})**	**Catalyst dosage (g L^{-1})**	**Light Source**	**Reaction time (min)**	**Removal efficiency (%)**	**Reference**
KBN@TiO_2@rGO	10	0.2	500W Xenon lamp ($\lambda > 420$)	120	99.21	This study
KBN@TiO_2	10	0.2	500W Xenon lamp ($\lambda > 420$)	120	85.04	This study
ZnO/g-C_3N_4	10	0.5	32W compact fluorescent bulb	120	89.00	[277]
ZnO/GO	10	0.1	Natural sun light	80	95.00	[278]
ZnO NPs	10	8	UV irradiation	120	~90.00	[279]
g-C_3N_4/BiOCl	20	0.3	300W Xenon lamp (visible region)	90	86.50	[280]
ZnO/CD NCs	12	0.6	30W UV light (λ = 365 nm)	110	98.00	[281]
Bi_2O_3/$(BiO)_2CO_3$	10	0.5	300 W Xenon lamp	30	93.40	[282]
WO_3/$CdWO_4$	20	0.57	500 W Xenon lamp	90	93.40	[283]
g-C_3N_4/MoS_2	10	0.5	8 × 8 W LED lamps (465 ± 40 nm)	90	90.00	[214]

Table S5.3. Effect of catalyst dosage and initial [CIP] on CIP degradation performance.

	Dosage	**Removal efficiency (%)**	k_{deg} **(min^{-1})**	$t_{1/2}$ **(min)**	R^2
Catalyst dosage (g L^{-1})	0.025	76.23	0.0113	61.33	0.9179
	0.05	82.10	0.0123	56.34	0.9435
	0.1	95.79	0.0208	33.32	0.9401
	0.15	97.04	0.0238	29.12	0.9140
	0.2	99.59	0.0325	21.32	0.9720
	0.25	97.33	0.0275	25.20	0.8254
CIP conc. (mg L^{-1})	1	100	0.1807	3.84	0.9266
	3	100	0.1652	4.19	0.9575
	5	99.09	0.0897	7.73	0.9198
	7	98.84	0.0352	19.69	0.9653
	10	96.03	0.0337	20.56	0.9321

Table S5.4. Effect of pH on CIP removal in the KBN@TiO_2@rGO system.

pH	**Removal efficiency (%)**	k_{deg} **(min^{-1})**	$t_{1/2}$ **(min)**	R^2
3	83.60	0.0130	53.31	0.9820
Unadjusted 5.23	99.21	0.0363	19.09	0.9280
7	99.99	0.0711	9.75	0.9567
9	99.94	0.0590	11.75	0.9444
11	97.96	0.0345	20.09	0.9190

Table S5.5. Effect of cations and anions on CIP degradation in KBN@TiO_2/rGO system.

Types	Ions	Removal efficiency (%)	k_{deg} (min^{-1})	$t_{1/2}$ (min)	R^2
Cations	Control	97.24	0.0325	21.32	0.9740
	Na^+	94.96	0.0221	31.36	0.9577
	K^+	91.88	0.0179	38.72	0.9541
	Mg^{2+}	93.59	0.0204	33.97	0.9903
	Ca^{2+}	88.47	0.0158	43.86	0.9298
Anions	Cl^-	96.20	0.0226	30.66	0.9589
	SO_4^{2-}	92.82	0.0164	42.26	0.7260
	NO_3^-	97.40	0.0251	27.61	0.9563
	HCO_3^-	92.97	0.0183	37.87	0.7145
	PO_4^{3-}	72.81	0.0100	69.3	0.9527

Table S5.6. Effect of water matrix and multi-pollutants on CIP degradation in KBN@TiO_2/rGO system.

	Types	Removal efficiency (%)	k_{deg} (min^{-1})	$t_{1/2}$ (min)	R^2
Water matrix	Distilled water	99.46	0.0375	18.48	0.9628
	Mineral water	96.66	0.0244	28.40	0.8163
	Tap water	95.22	0.0230	30.13	0.8252
	Municipal wastewater	93.28	0.0211	32.84	0.8337
	Ground water	89.37	0.0195	35.54	0.8103
	River water	89.59	0.0082	86.45	0.8520
Multi-pollutants	CIP	99.46	0.0379	18.28	0.9655
	NORF	95.56	0.0221	31.36	0.8746
	TC	100	0.0636	10.90	0.9228
	CIP/NORF	98.30	0.0292	23.73	0.9079
	NORF/CIP	97.50	0.0257	26.96	0.9274

Table S5.7. Physicochemical characterisation of wastewater used in this study.

Source	pH	TOC (mg L^{-1})	HCO_3^- (mg L^{-1})	Cl^- (mg L^{-1})	NO_3^- (mg L^{-1})	SO_4^{2-} (mg L^{-1})	HPO_4^{2-} (mg L^{-1})
Municipal	7.35	10.94	76.24	3.09	36.62	0.56	4.23
River	7.75	19.86	82.56	20.28	13.91	100.16	1.76
Groundwater	7.54	20.37	121.03	20.31	20.27	50.55	1.43

Table S5.8. First-order rate constants calculated from the data in **Fig. 9d.**

First-order rate constant	Removal efficiency (%)	k_{deg} (min^{-1})	Generation of ROS (mg min^{-1})
k	99.21	0.0337	0
k_{TEOA}	55.56	0.0061	2.76×10^{-2}
k_{FFA}	86.38	0.0130	2.07×10^{-2}
k_{IPA}	89.69	0.0155	1.82×10^{-2}
$k_{p\text{-}BQ}$	75.52	0.0084	2.50×10^{-2}

Generation of reactive oxygen species (ROS) (mg min^{-1}): calculated from **Eq. S5.5**.

Table S5.9. Estimated acute and chronic toxicity of CIP and its byproducts using ECOSAR program.

Compounds	Acute toxicity (mg L^{-1})			Chronic toxicity (mg L^{-1})		
	Fish 96 h (LC50)	Daphnid 48 h (LC50)	Algae 96 h (EC50)	Fish (ChV)	Daphnid (ChV)	Algae (ChV)
CIP	1.71E+05	8.05E+04	2.79E+04	1.34E+04	4.69E+03	4.85E+03
P2	2.61E+06	1.10E+06	2.36E+05	1.79E+05	4.63E+04	3.16E+04
P3	2.85E+07	1.07E+07	1.46E+06	1.72E+06	3.34E+05	1.53E+05
P4	7.36E+06	2.65E+06	2.98E+05	4.20E+05	7.23E+04	2.28E+04
P5	6.84E+04	3.36E+04	1.36E+04	5.63E+03	2.17E+03	2.56E+03
P6	4.93E+03	2.43E+03	1.02E+03	409	161	195
P7	2.30E+05	1.08E+05	3.59E+04	1.79E+04	6.11E+03	6.10E+03
P8	4.36E+06	1.78E+06	3.40E+05	2.89E+05	6.95E+04	4.28E+04
P9	1.01E+06	4.40E+05	1.08E+05	7.21E+04	2.03E+04	1.56E+04
P10	1.04E+04	5.53E+03	3.14E+03	942	449	710
P11	1.48E+04	7.71E+03	4.05E+03	1.31E+03	595	880
P12	4.01E+05	1.83E+05	5.50E+04	3.02E+04	9.69E+03	8.85E+03
P13	9.36E+04	4.54E+04	1.76E+04	7.60E+03	2.86E+03	3.25E+03
P14	1.06E+04	5.59E+03	3.10E+03	950	447	694
P15	1.50E+03	861	679	149	87.2	183
P16	4.51E+05	2.03E+05	5.85E+04	3.36E+04	1.05E+04	9.18E+03
P17	5.76E+05	2.58E+05	7.20E+04	4.26E+04	1.30E+04	1.11E+04
P18	1.34E+05	6.38E+04	2.29E+04	1.06E+04	3.81E+03	4.06E+03
P19	1.49E+04	7.73E+03	3.98E+03	1.31E+03	588	854
P20	1.16E+04	6.20E+03	3.57E+03	1.06E+03	508	812
P21	299	187	210	32.8	24	68.3
P22	1.88E+04	9.83E+03	5.16E+03	1.67E+03	758	1.12E+03
Toxicity levels		Very toxic			Harmful	
		Toxic			Not harmful	

Table S5.10. XPS spectra peak results of fresh KBN@TiO_2@rGO and used KBN@TiO_2@rGO.

Name	KBN@TiO_2@rGO (Fresh)			Name	KBN@TiO_2@rGO (used)		
	B.E (eV)	Content (%)	FWHM (eV)		B.E (eV)	Content (%)	FWHM (eV)
B 1s	191.6	1.08	0.67	B 1s	190.72	0.67	0.53
C 1s	283.9	28.61	3.3	C 1s	283.45	35.56	2.70
K 2p	292.4	0.2	1.29	K 2p	291.5	0.18	1.08
N 1s	400.76	0.37	1.92	N 1s	399.24	0.89	3.14
O 1s	529.48	49.91	1.44	O 1s	529.52	44.91	1.43
Ti 2p	458.19	19.83	1.24	Ti 2p	458.21	17.79	1.24

B.E: Binding Energy (eV), and FWHM: Full Width at Half Maximum (eV)

Table S5.11. Physicochemical properties of antibiotics.

Parameter	Ciprofloxacin	Norfloxacin	Tetracycline
Molecular structure [a]	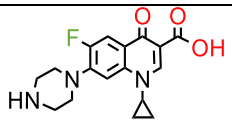	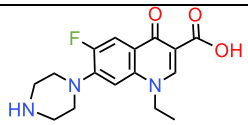	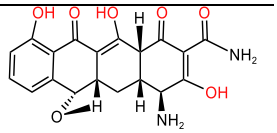
Molecular formula [a]	$C_{17}H_{18}FN_3O_3$	$C_{16}H_{18}FN_3O_3$	$C_{22}H_{24}N_2O_8$
Molar mass (g mol^{-1}) [a]	331.34	319.33	444.4
pKa [b]	5.9, 8.8	6.3, 8.8	3.3, 7.8, 9.6
Solubility in water (mg L^{-1}) [a]	35	280	231
log K_{ow} [a]	0.28	–0.5	-1.37

Data are from [a] https://pubchem.ncbi.nlm.nih.gov and [b] http://www.chemspider.com/.

Table S5.12. Effect of multi-pollutants on CIP degradation in KBN@TiO_2/rGO system.

Types	Removal efficiency (%)	k (min^{-1})	$t_{1/2}$ (min)	R^2
CIP	99.46	0.0379	18.28	0.9655
NORF	95.56	0.0221	31.36	0.8746
TC	100	0.0636	10.90	0.9228
CIP/NORF	98.30	0.0292	23.73	0.9079
NORF/CIP	97.50	0.0257	26.96	0.9274

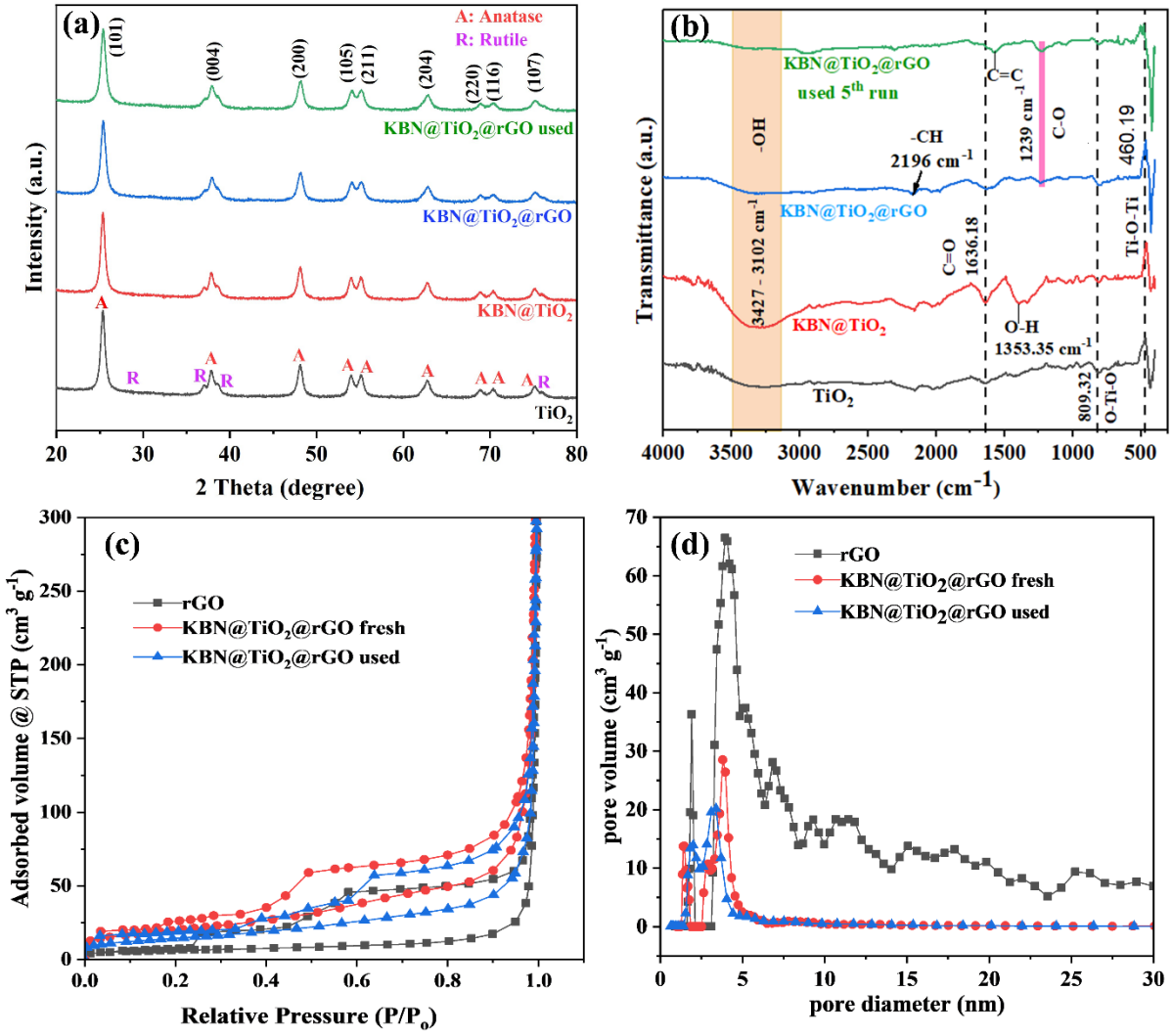

Figure S5.1. XRD patterns of the synthesised (a) TiO_2, KBN@TiO_2, fresh KBN@TiO_2@rGO, and used KBN@TiO_2@rGO, (b) FTIR spectra of TiO_2, KBN@TiO_2, fresh KBN@TiO_2@rGO,

and used KBN@TiO_2@rGO, (c) N_2 adsorption–desorption isotherms, and (d) pore size distribution curves for rGO, fresh KBN@TiO_2@rGO, and used KBN@TiO_2@rGO.

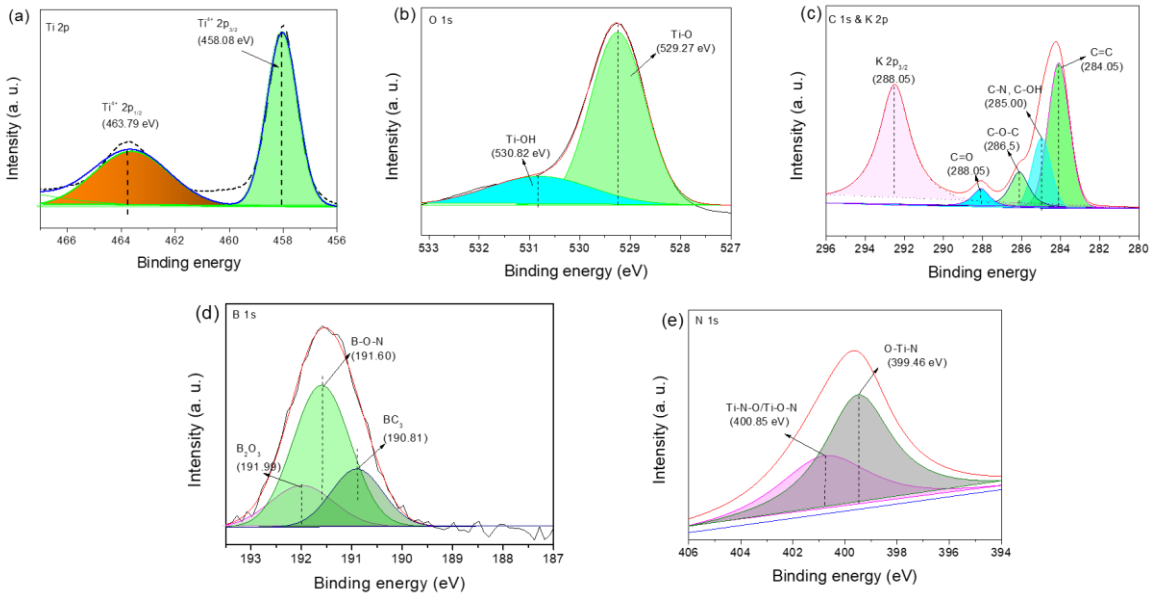

Figure S5.2. XPS analysis of used KBN@TiO_2: (a) Ti 2p, (b) O 1s, (c) C 1s + K 2p, (d) B 1s, and (e) N 1s.

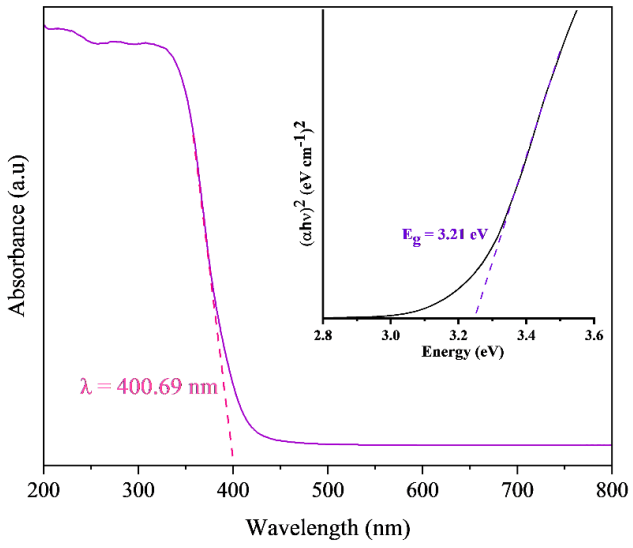

Figure S5.3. UV-Vis diffuse reflectance spectra and Tauc plot of TiO_2.

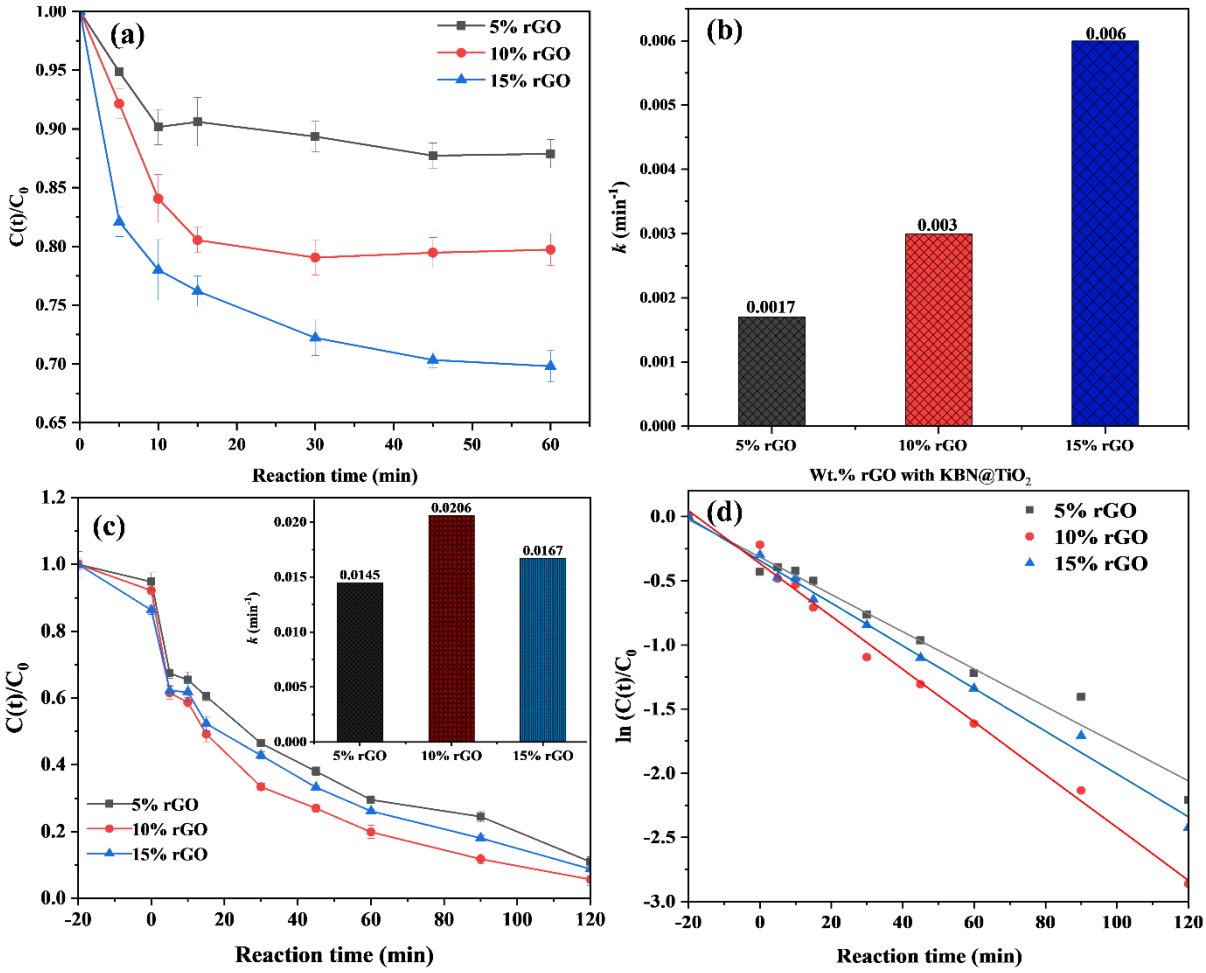

Figure S5.4. Effect of x% rGO (x = 5, 10, and 15) composite with modified KBN@TiO_2 nanoparticles on CIP removal efficiency in the KBN@TiO_2@rGO system. Adsorption performance (a), Pseudo-first-order rate constants (b), Photocatalytic performance (c), Pseudo-first-order rate constants (d). Experimental conditions: catalyst dosage = 0.2 g L^{-1}, $[CIP]_0$ = 10 mg L^{-1}, unadjusted pH = 5.23.

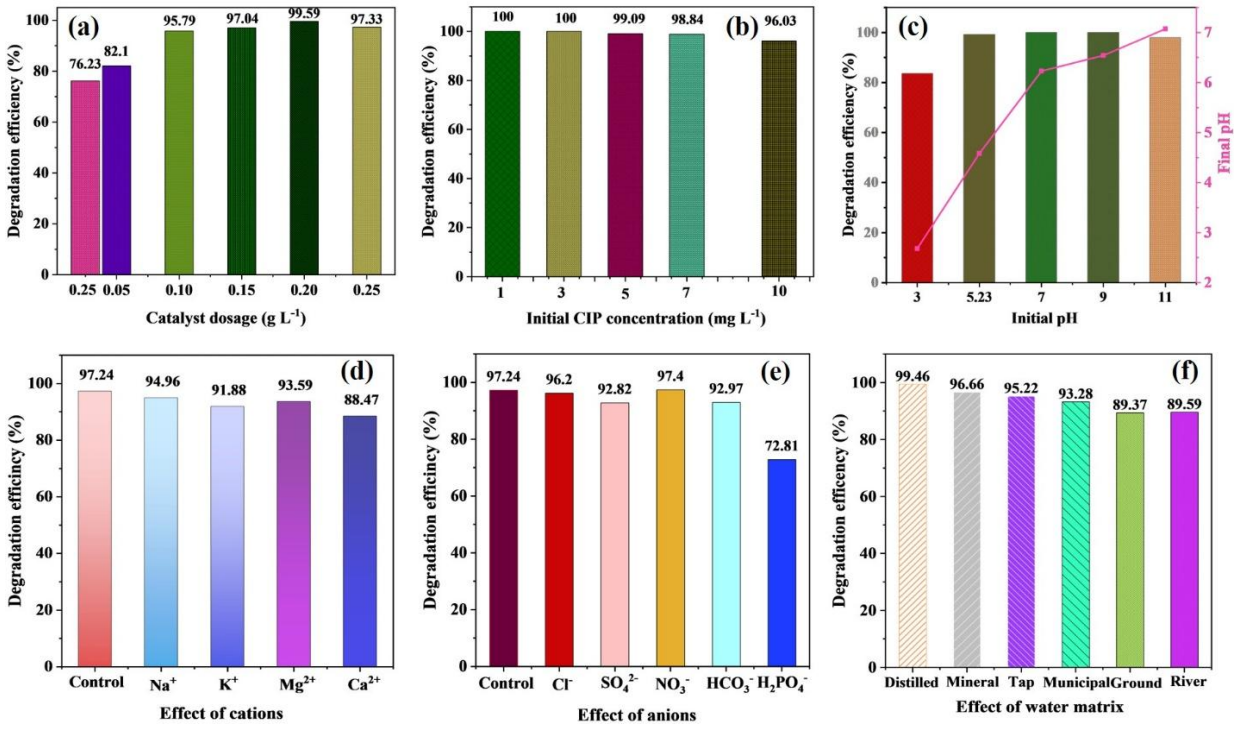

Figure S5.5. Effects of catalyst dosage (a), initial CIP concentration (b), initial pH (c), anions (d), cations (e), and different water matrices (f) for degradation efficiency of CIP on KBN@TiO_2@rGO system. Experimental conditions: $[CIP]_0 = 10$ mg L^{-1}, $[cations]_0 = [anions]_0 = 200$ mg L^{-1}, unadjusted pH = 5.23, catalyst dose = 0.2 g L^{-1}.

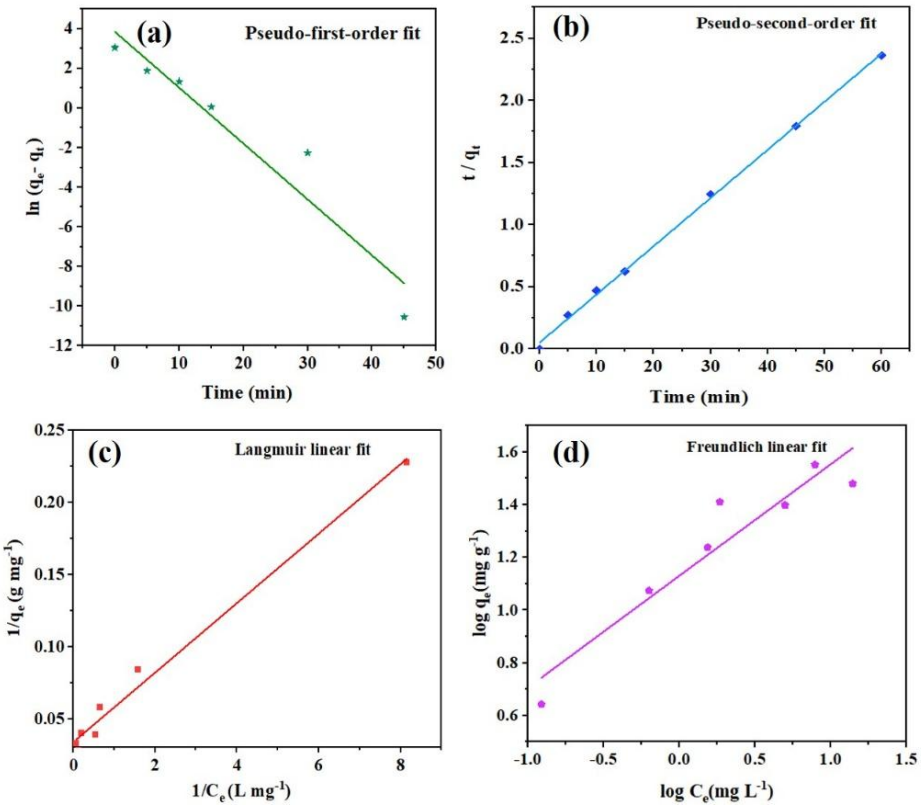

Figure S5.6. Kinetic linear fitting: (a) Pseudo-first-order, (b) Pseudo-second-order, and Adsorption isotherm models: (c) Langmuir, (d) Freundlich.

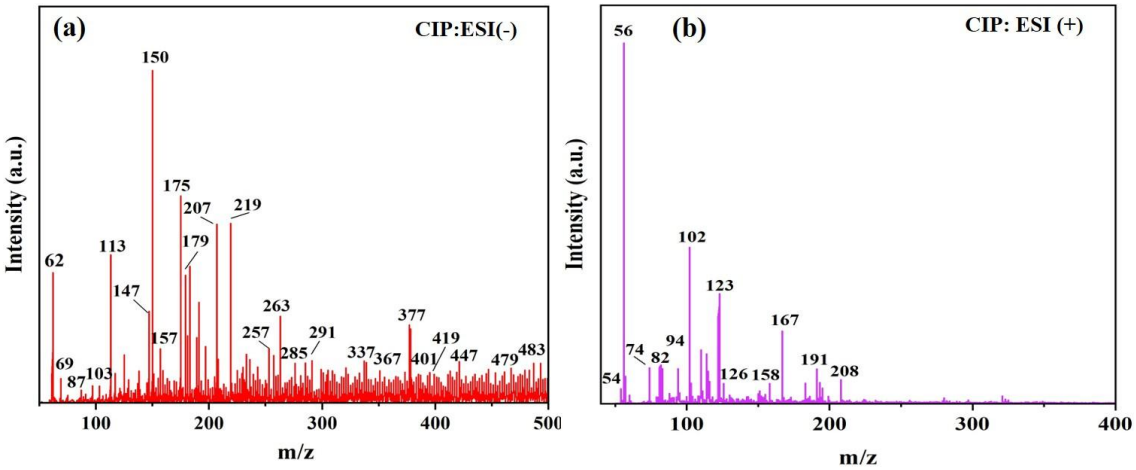

Figure S5.7. Mass spectra of CIP compounds (a) ESI (–) detector, and (b) ESI (+) detector after 120 min oxidation using UPLC-MS/MS analysis in the KBN@TiO_2@rGO system.

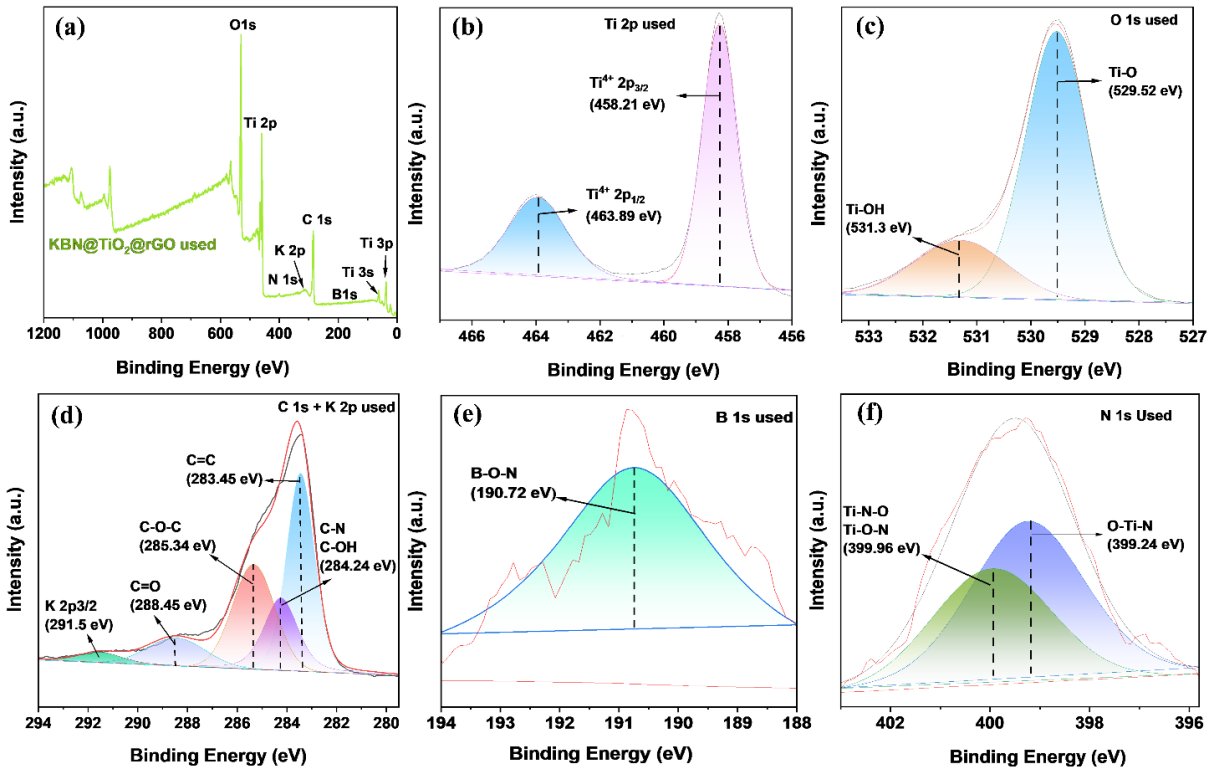

Figure S5.8. XPS analysis of used KBN@TiO_2@rGO: (a) overall survey, (b) Ti 2p, (c) O 1s, (d) C 1s + K 2p, (e) B 1s, and (f) N 1s.

Appendix D. Supplementary Information for Chapter Sex

Text S6.1. Chemicals and Reagents

Titanium tetra-isopropoxide (TTIP, ≥ 97.0%), potassium peroxymonopersulfate ($2KHSO_5 \cdot KHSO_4 \cdot K_2SO_4$, ≥4.0% active oxygen basis), ciprofloxacin (CIP, $C_{16}H_{18}FN_3O_3$, 98%), norfloxacin (NORF, $C_{16}H_{18}FN_3O_3$, ≥98%), tetracycline hydrochloride (TC, $C_{22}H_{24}N_2O_8 \cdot HCl$, ≥99%), humic acid (sodium salt), monobasic sodium phosphate (≥99%), 5,5-dimethyl-pyrroline N-oxide (DMPO, 99%), and 4-amino-2,2,6,6-tetramethylpiperidine (TEMP, 98%) were purchased from Sigma-Aldrich (USA). Water (HPLC grade) and acetonitrile (HPLC grade, LiChrosolv®, Germany) were used as mobile phases. Sodium chloride (NaCl, 99%), sodium bicarbonate ($NaHCO_3$, 99%), sodium sulfate anhydrous (Na_2SO_4, 99%), dibasic sodium phosphate (NaH_2PO_4, 99%), sodium nitrate ($NaNO_3$, >99%), potassium nitrate (KNO_3, 99%), ascorbic acid ($C_6H_8O_6$, ≥ 98%) were supplied by Duksan Pure Chemicals, Korea. Benzoquinone ($C_6H_4O_2$, 98%) and ammonium solution (NH_3, 28%) were purchased from Junsei Chemical Co., Ltd, Japan. Boric acid (H_3BO_3, 99.5%), triethanolamine ($C_6H_{15}NO_3$,

99%), absolute ethanol (C_2H_5OH, 99%), furfuryl alcohol ($C_5H_6O_2$, ≥98%), and isopropyl alcohol ($(CH_3)_2CHOH$, 99.5%) were obtained from Daejung Chemicals and Metal Co., Ltd., Korea. Potassium permanganate ($KMnO_4$, >99%), hydrogen peroxide (H_2O_2, 30%), and sulfuric acid (H_2SO_4, 98%) were purchased from DC Chemical Co., Ltd, Korea. Sodium hydroxide (1N NaOH) and hydrochloric acid (1N HCl), used to adjust the pH of the reaction solutions, were purchased from Duksan Pure Chemicals Co., Ltd., Korea. All reagents used in this study were at least ACS grade and were utilised without further purification. All chemical solutions were prepared using double-distilled and de-ionised (DDI) water (Millipore Sigma TM Synergy TM Ultrapure Water Purification System, Thermo Fisher Scientific, USA, resistivity >18.25 M).

Text S6.2. Material characterisation

The morphological properties of the samples were examined using scanning electron microscopy (SEM) (Zeiss Evo 18-20-45). The elemental composition and distribution of the catalyst were determined through energy-dispersive X-ray (EDX). A Micromeritics ASAP 2020 physisorption analyser (Norcross, USA) was employed to calculate the Brunauer–Emmett–Teller (BET) surface area and pore size distribution of the catalysts using the N_2 adsorption–desorption isotherm. X-ray diffraction (XRD) patterns were recorded using a Rigaku D/Max-B (High-Power) powder diffraction equipment to investigate the crystalline structure of the synthesised KBN@TiO_2@rGO composite and other materials. The Senterra II (Bruker, Billerica, USA) confocal Raman microscope was stimulated with a 10 W laser source set to 532 nm to produce the Raman spectra. Furthermore, X-ray photoelectron spectroscopy (XPS; Thermo Fisher Scientific, USA) was used to obtain surface elemental data.

Text S6.3. Analytical methods

A high-performance liquid chromatography (HPLC) system (Agilent Technologies, 1200 series, USA), equipped with an ultraviolet diode array detector (DAD, G1315B) and a Zorbax-eclipse XDB-C18 column (Agilent Technologies, 5 µm particle size, 4.6 × 150 mm, USA), was used to analyze aqueous solutions containing the antibiotics ciprofloxacin (CIP), norfloxacin (NORF), and tetracycline (TC). The mobile phases and working conditions for ciprofloxacin (CIP), tetracycline (TC), norfloxacin (NORF), diclofenac (DCF), and sulfamethoxazole (SMX) are presented in **Table S6.1**. Standard calibration curves for CIP, NORF, DCF, SMX, and TC are presented in **Figure S6.1.**

Total organic carbon (TOC) was measured using a Shimadzu TOC analyser (ASI-L series, Japan). For UPLC-MS/MS analysis, the electrospray ionisation (ESI) method was employed in both positive and negative ionisation modes (ESI +/–) between 50 m/z and 500 m/z. The mobile phase, comprising 0.1% formic acid and acetonitrile in a 1:1 ratio (v/v), was delivered at a flow rate of 0.2 mL min^{-1}.

Text S6.4. Electron spin resonance (ESR) spectroscopy

ESR spectroscopy (Bruker BioSpin GmbH, Germany) was performed using a microwave frequency of 9.424 GHz, microwave power of 2.000 mW, field sweep of 100 G, modulation amplitude of 4.00 G, conversion time of 30.000 ms, time constant of 163.840 ms, and receiver gain of 5.64×10^2. DMPO and TEMP were employed as spin-trapping agents for $^{\bullet}OH$ and $O_2^{\bullet-}$, and $^1O_2$, respectively. A 1.0 mL sample was collected from the reactor (40 mL amber vial) and mixed thoroughly with 1.0 mL of either DMPO or TEMP, which were prepared using 10 mM phosphate buffer (pH = 7.02) (5.8 mM Na_2HPO_4 and 4.2 mM NaH_2PO_4).

Text S6.5. Electrochemical Analysis

An electrochemical electrode was developed. Approximately 10 mg of KBN@TiO_2@rGO was mixed with 120 µL of a 5.0 wt.% Nafion® solution, and the resulting mixture was diluted with 1 mL of deionised water (DW) obtained using a cyclone ultrapure water still (WSCO44 MH3.4, Fistreem International, UK). The mixture was then ultrasonicated for 30 min to create a suspension. Next, the drop-casting method was used to coat the mixture onto a glassy carbon (GC) electrode. The catalyst-coated GC electrode was then allowed to dry at 25 ℃ overnight (approximately 9h). After drying, it was employed as the working electrode. In contrast, a silver/silver chloride (Ag/AgCl) electrode. This study utilised 0.1 M Na_2SO_4 as the supporting electrolyte. Chronoamperometry analysis was performed using a Corrtest potentiostat (CS350, Wuhan Corrtest Instruments Corp., Ltd., China). The current was measured under open-circuit potential conditions, and the current response was measured by adding an oxidant (PMS) and pollutant CIP at specific time intervals. Linear sweep voltammetry (LSV) was measured with a potential sweep ranging from 0 to 1.6 vs. Ag/AgCl at a scan rate of 50 mVs^{-1}.

Text S6.6. Generation rate of reactive oxygen species (ROS)

Based on **Eq. S1**, the ROS quantification during oxidation was performed as follows:

$$\text{Generation rate of ROS } (\text{mg min}^{-1}) = (k - k_s) \times C_{CIP} \times V \quad \text{(S6.1)}$$

where C_{CIP} is the CIP concentration (mg L^{-1}); V is the volume of the reactor (L); k and k_s are the first-order rate constants (min^{-1}) for CIP degradation without a scavenger and with a scavenger, respectively.

Text S6.7. Total organic carbon (TOC)

TOC was measured to estimate CIP mineralisation (%) using Eq. (S2):

$$Mineralization\,(\%) = \frac{[TOC]_i - [TOC]_f}{[TOC]_i} \times 100 \qquad \text{(S6.2)}$$

where $[TOC]_i$ and $[TOC]_f$ are the initial and final TOC concentrations in the KBN@TiO_2@rGO system.

Table S6.1. High-performance liquid chromatography detection details.

Compound	**Molecular structure**	**Mobile phase**	**Detection wavelength (nm)**	**Retention Time (min)**	**Column Temperature (°C)**	**R^2**
Ciprofloxacin	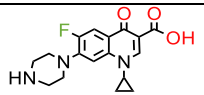	Formic acid (1%) = 70% Acetonitrile = 30%	277	1.7 ± 0.1	30	0.9989
Tetracycline	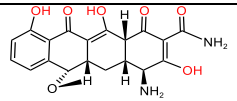	Phosphoric acid (1%) = 80% Acetonitrile = 20%	360	3.6 ± 0.1	30	0.9999
Norfloxacin	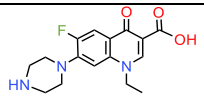	Phosphoric acid (1%) = 40% Acetonitrile = 60%	278	1.3 ± 0.1	28	0.9983
Diclofenac	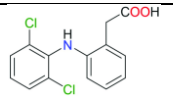	Phosphoric acid (1%) = 40% Acetonitrile = 60%	276	4.5 ± 0.1	30	0.9998
Sulfamethoxazole	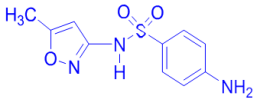	Formic acid (1%) = 70% Acetonitrile = 30%	259	1.5 ± 0.1	28	0.9991

Table S6.2. Comparisons of the efficacy of various modified (metal and non-metal) doped TiO_2@rGO/PMS composite catalysts in the degradation of organic pollutants.

Photocatalysts materials	**[CIP] (mg L^{-1})**	**Catalyst dosage (g L^{-1})**	**Light Source**	**Reaction time (min)**	**Removal efficiency (%)**	**Reaction rate constant (min^{-1})**	**Reference**
KBN@TiO_2@rGO/PMS	10	0.1	500W Xenon lamp (λ > 420nm)	90	100	0.06625	This study
KBN@TiO_2@rGO	10	0.2	500W Xenon lamp (λ > 420nm)	120	99.21	0.0337	[44]
TiO_2@$CuCo_2O_4$/PMS	5 (SMX)	0.25	500W Xenon lamp (λ > 300nm)	180	80	0.10	[284]
$CoTiO_3$/TiO_2NTs/Ti/PMS	10	0.1	UV irradiation	720	95.2	0.0158	[84]
CTF-TiO_2/rGO	10	0.05	100W LED (λ > 400nm)	120	99.83	0.0188	[285]
TiO_2/ γ-Fe_2O_3/GO	10	0.1	UV irradiation	140	99	-	[285]
N/TiO_2/rGO	10	0.25	1266.6W UVA lamp	120	98.01	0.0407	[275]
Ag-BN/HNT-TiO_2	10	0.5	Halogen linear lamp	120	99.00	0.0346	[278]

Table S6.3. Effects of different catalysts on CIP degradation efficiency.

Oxidation	Catalyst Type	Removal (%)	k (min^{-1})	$t_{1/2}$ (min^{-1})	R^2
Chemical Oxidation	TiO_2/PMS	24.35 ± 0.05	0.0037	187.30	0.3384
	TiO_2@rGO/PMS	32.31 ± 0.02	0.0047	147.45	0.3617
	BN@TiO_2/PMS	28.92 ± 0.05	0.0045	154.00	0.3823
	BN@TiO_2@rGO/PMS	31.84 ± 0.02	0.0060	115.50	0.4684
	KBN@TiO_2/PMS	25.42 ± 0.05	0.0056	123.75	0.4838
	KBN@TiO_2@rGO/PMS	35.44 ± 0.04	0.0063	110.00	0.4811
Photo Oxidation	TiO_2/PMS	51.11 ± 0.04	0.0056	47.14	0.9080
	TiO_2@rGO/PMS	63.09 ± 0.01	0.0074	37.06	0.9167
	BN@TiO_2/PMS	81.13 ± 0.01	0.0139	35.54	0.8598
	BN@TiO_2@rGO/PMS	96.10 ± 0.04	0.0276	23.33	0.8650
	KBN@TiO_2/PMS	98.15 ± 0.01	0.0330	23.33	0.8821
	KBN@TiO_2@rGO/PMS	100.0 ± 0.00	0.0490	14.14	0.9278

Table S6.4. Effect of catalyst dosage and initial [CIP] on CIP degradation performance.

	Dosage	Removal efficiency (%)	k_{deg} (min^{-1})	$t_{1/2}$ (min)	R^2
Catalyst dosage (g L^{-1})	0.05	95.67	0.0273	25.38	0.9865
	0.1	100	0.0490	14.14	0.9278
	0.15	98.39	0.0371	18.68	0.9306
	0.2	97.09	0.0301	23.02	0.8499
CIP conc. (mg L^{-1})	5	100	0.0676	10.25	0.9494
	10	100	0.0490	14.14	0.9213
	15	96.82	0.0326	21.26	0.9137
	20	95.38	0.0265	26.15	0.9719

Table S5. Effect of pH on CIP removal in KBN@TiO_2@rGO/PMS system.

pH	Removal efficiency (%)	k_{deg} (min^{-1})	$t_{1/2}$ (min)	R^2
3	93.27	0.0245	28.29	0.9720
Unadjusted 5.23	100	0.0490	14.14	0.9213
7	100	0.0425	16.31	0.9692
9	100	0.0421	16.46	0.9740
11	96.29	0.0259	26.76	0.7787

Table S6.6. First-order rate constants calculated from the data in **Fig. 5a.**

First-order rate constant	Removal %	k (min^{-1})	Generation of ROS (mg min^{-1})
k	100.00	0.06625	0
k_{MeOH}	65.14	0.0086	5.77×10^{-2}
k_{TBA}	83.02	0.0140	5.23×10^{-2}
$k_{p\text{-}BQ}$	75.42	0.0109	5.54×10^{-2}
k_{FFA}	80.34	0.0107	5.56×10^{-2}
k_{IPA}	91.57	0.0226	4.44×10^{-2}

The generation of ROS quantified using equation Eq. S1.

Table S6.7. XPS spectra peak results of fresh KBN@TiO_2@rGO and used KBN@TiO_2@rGO.

Name	KBN@TiO_2@rGO (Fresh)			Name	KBN@TiO_2@rGO (used)		
	B.E (eV)	Content (%)	FWHM (eV)		B.E (eV)	Content (%)	FWHM (eV)
B 1s	191.6	1.08	0.67	B 1s	190.72	0.67	0.53
C 1s	283.9	28.61	3.3	C 1s	283.45	35.56	2.70
K 2p	292.4	0.2	1.29	K 2p	291.5	0.18	1.08
N 1s	400.76	0.37	1.92	N 1s	399.24	0.89	3.14
O 1s	529.48	49.91	1.44	O 1s	529.52	44.91	1.43
Ti 2p	458.19	19.83	1.24	Ti 2p	458.21	17.79	1.24

B.E: Binding Energy (eV), and FWHM: Full Width at Half Maximum (eV)

Table S6.8. Fit statistical values

	CIP removal	TOC removal
Std.Dev.	0.7109	0.7322
Mean	94.05	68.39
C.V. %	0.7559	1.07
R^2	0.9942	0.9908
Adjusted R^2	0.9884	0.9817
Predicted R^2	0.9688	0.9548
Adequate Precision	44.0719	34.5417
Lack of fitness (P-value)	0.0947	0.3385

The predicted R^2 value for CIP removal (0.9688) shows good agreement with the adjusted R^2 (0.9884), as their difference is less than 0.2. Adequate precision represents the signal-to-noise ratio, where a value greater than 4 is considered desirable. The obtained ratio of 44.072 indicates a strong signal, confirming that the model is suitable for navigating the design space.

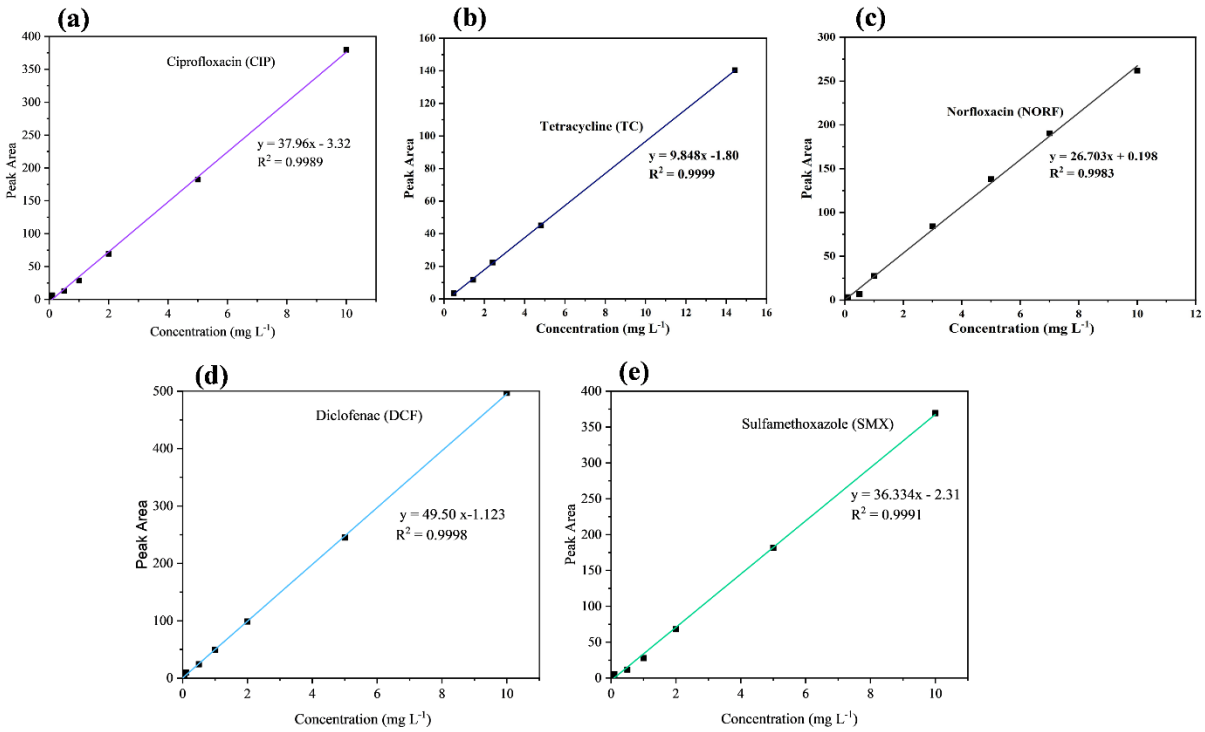

Figure S6.1. HPLC standard calibration curves for (a) ciprofloxacin, (b) tetracycline, (c) norfloxacin, (d) diclofenac, and (e) sulfamethoxazole.

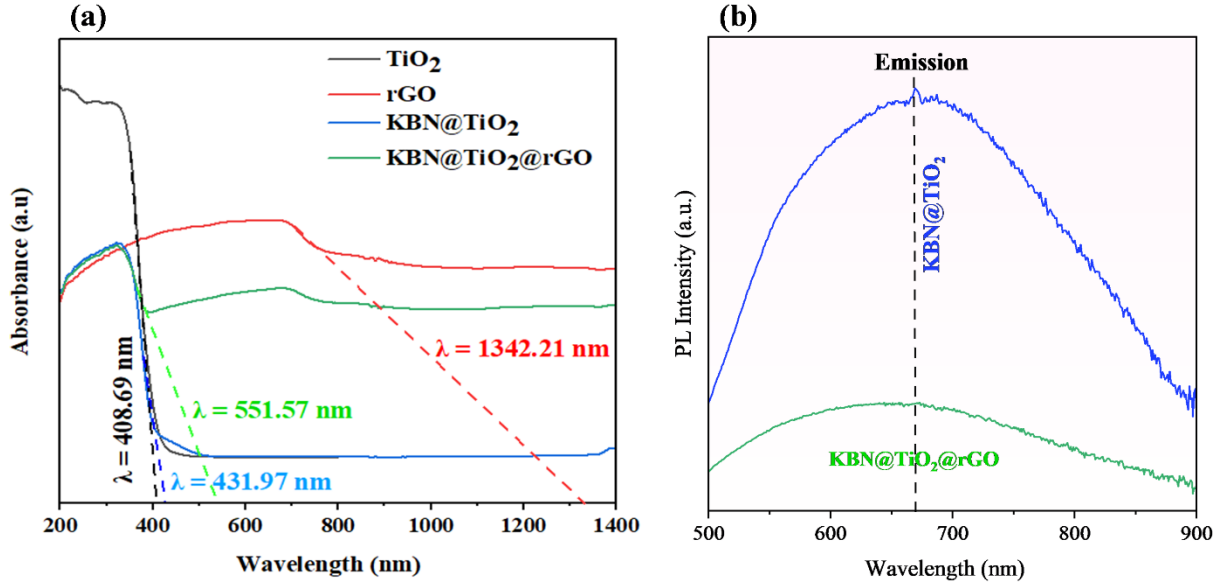

Figure S6.2. UV-Vis diffuse reflectance spectra of (a) TiO_2, rGO, KBN@TiO_2, and KBN@TiO_2@rGO, and (b) PL spectra of KBN@TiO_2@rGO.

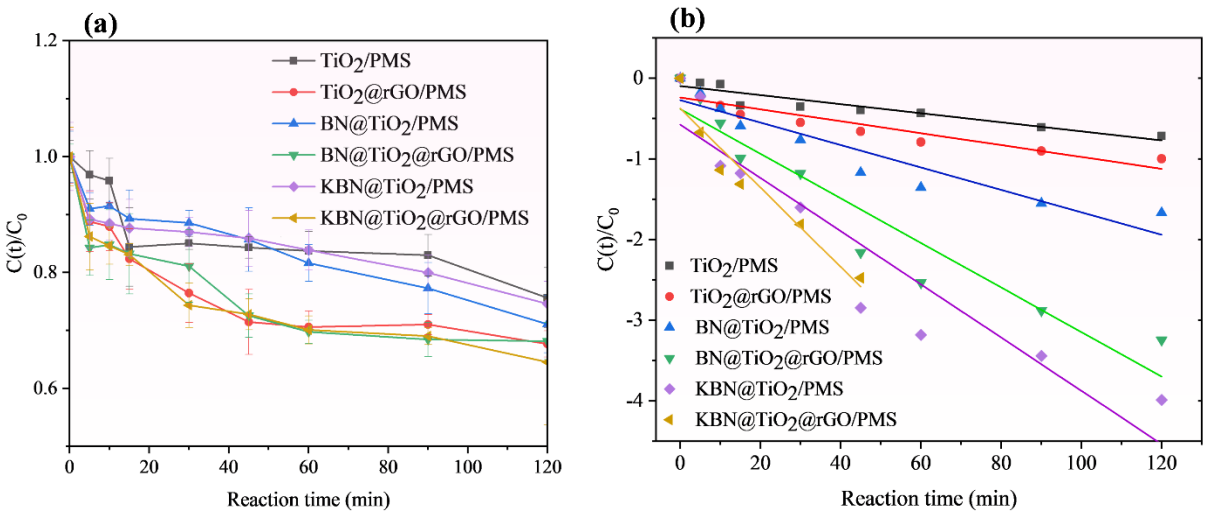

Figure S6.3. CIP removal by (a) adsorption, (b) First-order rate constants comparison of common catalysts on PMS activation. (Experimental conditions: [CIP] = 10 mg L^{-1}, [catalyst concentration]$_0$ = 0.1 g L^{-1}, [PMS] = 0.5 mM, pH unadjusted = 5.23).

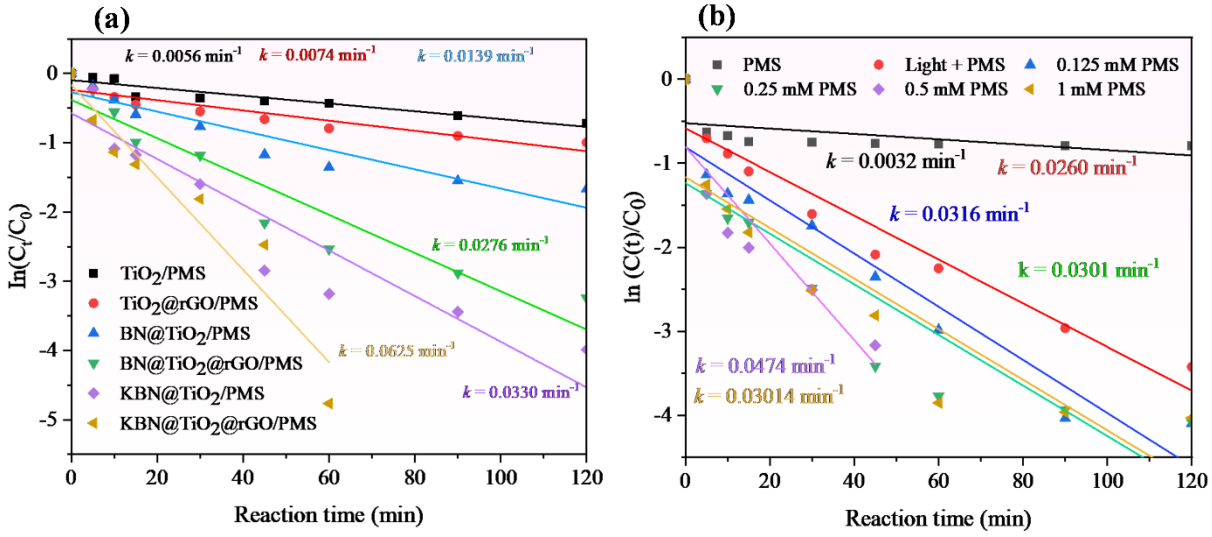

Figure S6.4. CIP removal based on (a) first-order constants of photocatalytic degradation and (b) first-order rate constants under varying PMS doses. Experimental conditions: [CIP]$_0$ = 10 mg L^{-1}, [catalyst concentration]$_0$ = 0.1 g L^{-1}, [PMS]$_0$ = 0.5 mM, pH unadjusted = 5.23).

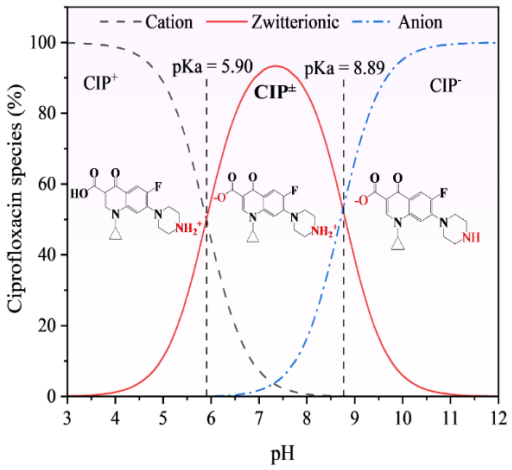

Figure S6.5. Distribution of CIP speciation with pH range values.

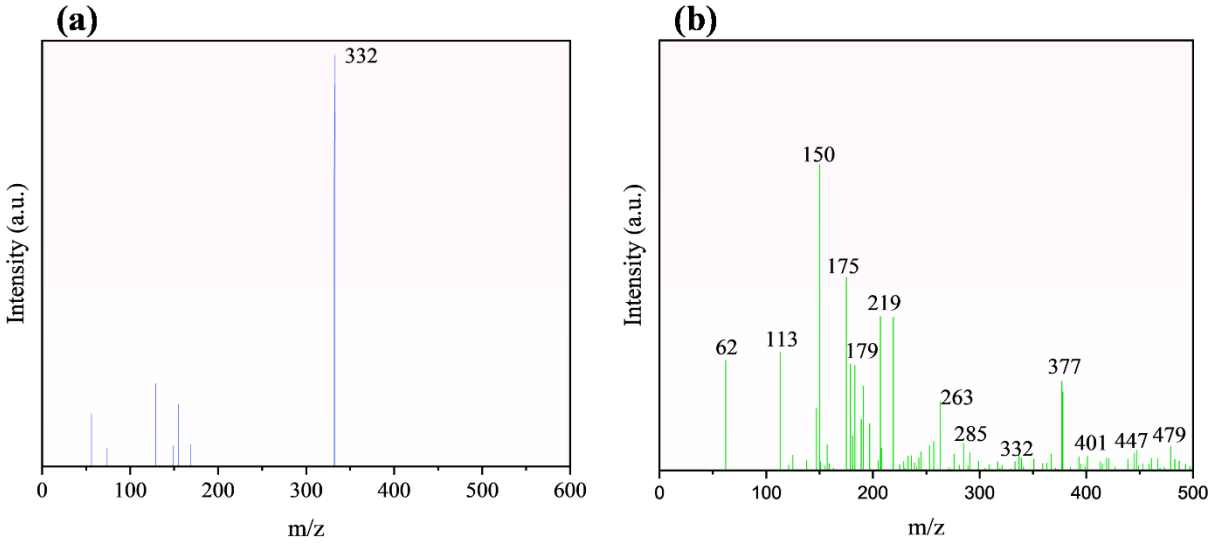

Figure S6.6. UPLC–MS/MS mass spectra of ciprofloxacin compounds recorded (a) before and (b) after photooxidation in the KBN@TiO_2@rGO/PMS system.